On the Role of the Agulhas Current on weather and climate of South Africa

By

Arielle Stela NKWINKWA NJOUODO

Department of Oceanography

University of Cape Town

Thesis submitted for the degree of

Doctor of Philosophy

University of Cape Town **10/10/2018**

Dedication

I dedicate this thesis to my Father Robert Nkwinkwa and my Mother Désirée Kombou for all the love, support and blessings you always give me. To my brothers and sisters Yonkeu Nkwinkwa Didier Patrice, Noizi Nkwinkwa Willy Stéphane, Nkwinkwa Tchoumé Ida Manuela, Nkwinkwa Nana Vanessa Laura, Dr. Kamdom François Kevin, Nkwinkwa Minkeza Christelle Flora and Nkwinkwa Yangue Carla Yoan, for all the love and support you always bring to my life.

Plagiarism declaration

I, **Arielle Stela Nkwinkwa Njouodo**, hereby declare that the content of this thesis is my own work, upon the guidance of my PhD advisors Professor Mathieu Rouault and Professor Noel Keenlyside. This dissertation has been submitted to the Turnitin module and I confirm that my supervisors have seen my report and any concerns revealed by such have been resolved with my supervisors. I therefore authorise the University to reproduce for the purpose of research the content of this thesis.

Signature: Signed by candidate Date: 10/10/2018

Declaration

I confirm that I have been granted permission by the University of Cape Town's Doctoral Degrees Board to include the following publication in my thesis, and where co-authorships are involved, my co-authors have agreed that I may include the publication:

Nkwinkwa Njouodo, A.S., Koseki, S., Keenlyside, N. and Rouault, M. (2018). Atmospheric signature of the Agulhas Current. *Geophysical Research Letters*. https://doi.org/10.1029/2018GL077042.

Student name: Arielle Stela Nkwinkwa Njouodo Student number: NKWARI001

Signature: Signed by candidate Date: 10/10/2018

Acknowledgements

I am thankful to the Almighty God for the grace, and strength he gave me to complete my PhD project.

I am extremely grateful to my supervisors Professor Mathieu Rouault and Professor Noel Keenlyside for having trust in me and for giving me the opportunity to do my PhD Thesis. I really appreciated your advice and guidance throughout this thesis.

I thank all the Members and academic staff of the Department of Oceanography at the University of Cape Town.

I am very grateful to the Nansen TuTu Centre, WRC and ACCESS NRF for the funding I received to do my PhD project in South Africa and Norway.

I acknowledge the German Deutscher Akademischer Austauschdienst (DAAD) South Africa through which, I obtained part of my scholarship during my PhD.

I express my gratitude to Prof. Noel Keenlyside from the University of Bergen, and Prof. Johnny Johanessen from the Nansen Environmental and Remote Sensing Research Center of Bergen, who gave me the opportunity to spend time in Norway, where part of the work has been done.

I thank Dr. Shunya Koseki from the University of Bergen, who helped me with the WRF model data, and from whom I gained more knowledge in Atmospheric Sciences.

I thank Prof. John Field for his help in reviewing the grammar of this thesis.

A very special thanks to my lovely husband Dr. Rodrigue Anicet Imbol Koungue for your spontanous and fruitfull help during our PhD journey at University of Cape Town, South Africa.

I express my appreciation to the big family Yangue Thomas and Njououndou Isaac, for the encouragements and support I received during this PhD project.

Madame Koungue Jeanne, Madame Nfonbeu Odette, I am greatful for all your prayers and support you always formulate for me.

My childhood friends Yondo Nfonbeu Winnie Stella Aurelie epse Fanmey, Nana Dibatchou Arlette Corine, and Yamedji Tchoua Eldrige, I thank you for the encouragements I always receive from you.

Abstract

The Agulhas Current is the strongest western boundary current of the Southern Hemisphere. The aim of this thesis is to understand the impact of ocean-atmosphere interaction in the Agulhas Current on the atmosphere and to investigate its importance for Southern African rainfall. This warm Current creates a high temperature gradient with the surrounding ocean, leading to a large turbulent flux of moisture from ocean to atmosphere (also called the turbulent latent heat flux). The dynamics of ocean-atmosphere interaction above the Agulhas Current and its impact on the weather and climate of Southern Africa are not well known. This is due to a) climate reanalyses that do not include the Agulhas Current and b) the lack of regional capacity in ocean-atmosphere modeling. I use ocean observations, various climate reanalyses, and several satellite remote sensing data sets to find out if the new reanalyses (cited below) do represent the intense exchange of moisture that occurs above the Agulhas Current and the Agulhas Retroflection region. The largest turbulent latent heat flux is found in the Retroflection region in winter, while the lowest is off Port Elizabeth in summer. The Climate Forecast System Reanalysis (CFSR) and the Modern-Era Retrospective analysis for Research and Applications version-2 (MERRA-2) do represent the turbulent latent heat flux well when compared to high-resolution satellite data. ERA-Interim Reanalysis underestimates the turbulent latent heat flux due to reduced wind speeds. The observation-based National Oceanography Centre Southampton (NOCS) is different from the satellites and the reanalysis products because its annual cycle is reversed, and NOCS underestimates the turbulent latent heat flux compared to the former products. The study of the satellite product air-sea turbulent fluxes (SEAFLUX) shows that east of the Agulhas Current, the specific humidity difference is the main driver of the annual cycle variations of turbulent latent heat flux, while the main driver in the Retroflection is the wind speed and both the specific humidity difference and the wind speed in between (around Port Elizabeth). I use high-resolution annual mean observations from satellites, atmospheric reanalysis, and the Weather Research and Forecasting (WRF) model to show that the warm core of the Agulhas Current drives a band of precipitation along the east coast of South Africa when the Current is adjacent to the coast. To do that, I conduct a classic modeling experiment with one configuration representing the sea surface temperature (SST) of the Agulhas Current relatively well. This WRF experiment reproduces the

turbulent latent heat flux well. The second simulation is with SST of the Agulhas Current reduced by up to 2°C compared to the first experiment. From a diagnostic of the pressure adjustment mechanism, results show that the warm SST of the Agulhas Current enhances the formation of coastal precipitation along and above the Current. Finally, I look at the seasonality of ocean-atmosphere interaction in the Agulhas Current and its impact on Southern African precipitation. In winter, the impact of the Agulhas Current is confined to the atmosphere above it and mechanisms are similar to those described for annual mean. In summer and autumn, SST differences between the two simulations where the Agulhas Current system is more than 25°C, leads to differences in geopotential height above the ocean, extending along the eastern coast and over the land area. The higher temperature of the control simulation leads to cyclonic circulation anomalies and larger moisture flux anomalies from the Agulhas Current to the continent from the south. The analysis of the high-level moisture flux indicates that the Agulhas Current influences the rainfall and humidity flux of Southern Africa. More moisture flux is then brought inland at a higher level. In the northeast of the region, there is an export of moisture anomalies from land to the ocean, and an import of moisture anomalies from above the Agulhas Current to the landmass. This is due to the wind anomalies between the two simulations. However, the overall result leads to more precipitation over the interior of the continent. The study shows that it is important to integrate the fine structure of the ocean temperature of the Agulhas Current in modeling studies and climate reanalyses. Results of this thesis have implications for the prediction of South African weather and climate, and for understanding past and present climate.

TABLE OF CONTENTS

LIST OF FIGURES

LIST OF TABLES

LIST OF ACRONYMS

AVHRR: Advanced Very High-Resolution Radiometer

BVW: Bourassa-Vincent-Wood

BVWN: Bourassa-Vincent-Wood neutral

CFSR: Climate Forecast System Reanalysis

ECMWF: European Centre for Medium-Range Weather Forecast

HOAPS: Hamburg Ocean Atmosphere Parameters and Fluxes

LHF: Latent Heat Flux

MERRA: Modern-Era Retrospective analysis for Research and Applications

MODIS: Moderate Resolution Imaging Spectroradiometer

NCEP: National Centers for Environmental Prediction

NOCS: National Oceanography Centre Southampton

SEAFLUX: air-sea turbulent fluxes

SLP: Sea Level Pressure

SST: Sea Surface Temperature

SCOW: Scatterometer Climatology of Ocean Winds

TRMM PR: Tropical Rainfall Measuring Mission Precipitation Radar

OISST: Optimal Interpolation Sea Surface Temperature

Qa: specific humidity of air

Qsst: specific humidity at the sea surface

VIMF: Vertically Integrated Moisture Flux

VIMFC: Vertically Integrated Moisture Flux Convergence

VIMFD: Vertically Integrated Moisture Flux Divergence

WRF: Weather Research and Forecasting

CHAPTER 1

1 INTRODUCTION

1.1 OVERVIEW OF THE WESTERN BOUNDARY CURRENTS (WBCS)

1.1.1 Description of the WBCs

Subtropical western boundary currents (WBC) are warm, fast flowing, deep and narrow currents that form on the western side of ocean basins. They include the Kuroshio Current, the Gulf Stream, the Brazil Current, the East Australian Current, and the Agulhas Current. These oceanic currents constitute the western branches of the subtropical gyres and are identifiable in **Figure 1.1** by the huge amount of the upward ocean surface heat flux released compared to the surrounding water. In WBC regions, the low-level atmosphere becomes unstable above warm sea surface temperature (SST), due to large sensible and latent heat fluxes. This had been observed globally in regions with strong SST gradients: Kuroshio and its Extension (*Xie,* 2004; *Tokinaga et al.* 2009; *Koseki and Watanabe*, 2010), Gulf Stream (*Chelton et al.* 2004; *Xie et al.* 2004; *Minobe et al.* 2008; 2010), Brazil–Malvinas Currents (*Tokinaga et al.* 2005), and Agulhas Return Current (*O'Neill et al.* 2005).

The WBCs play a tremendous role in the climate system by carrying warm tropical water to the mid-latitudes and by transporting heat and moisture to the atmosphere, affecting storms, atmospheric jet streams, as well as ocean carbon uptake (*Rouault et al.* 2002; *Nakamura et al.* 2004; *Takahashi et al.* 2009; *Minobe et al.* 2008; *Kwon et al.* 2010; *Nkwinkwa Njouodo et al.* 2018). However, the WBCs have considerably warmed up over the past twenty years (*Wu et al.* 2012; *Yang et al.* 2016). *Wu et al.* (2012) show that the enhanced warming of these currents could be due to the poleward shift of their mid-latitude extensions and/or intensification in their strength. The aim of our study is to assess the impact of the strongest Southern Hemisphere WBC, on the regional climate.

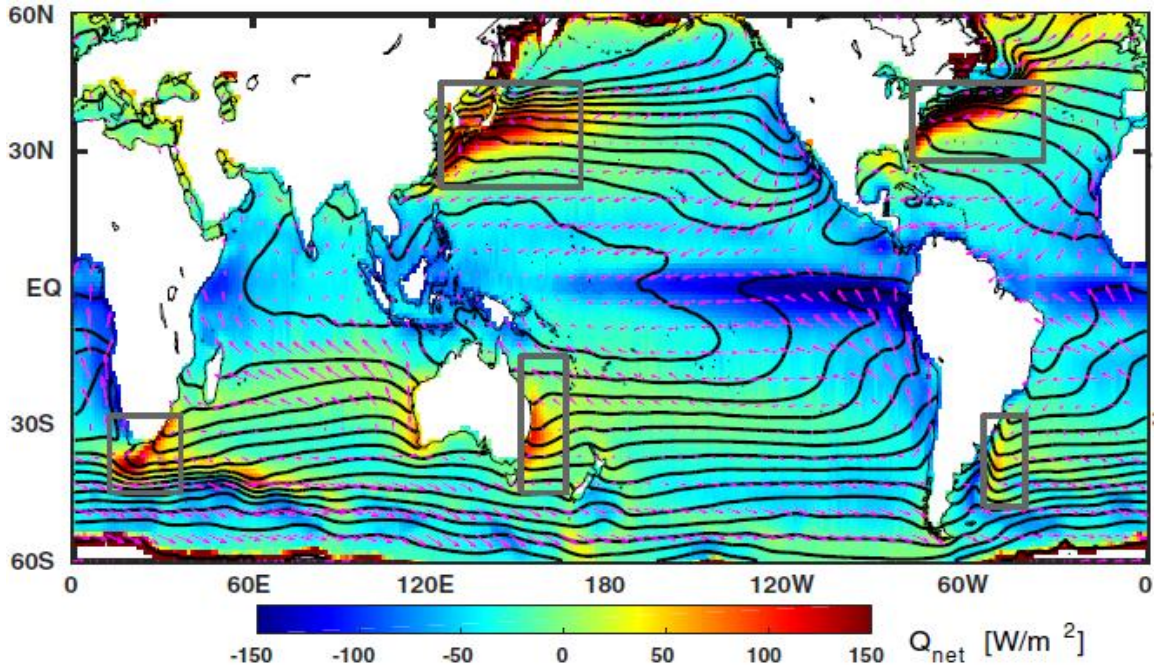

Figure 1.1: Annual climatology from 1984 to 2009 of the net heat flux (shaded, positive upward) from the Objectively Analyzed Air-Sea Fluxes (OAFlux), with the HadISST version 1 (black contours) and the NCEP/NCAR wind direction (pink arrows) overlaid (*Yang et al.* 2016). The grey boxes represent the western boundary currents. From top to bottom and from left to right the Kuroshio Current, the Gulf Stream, the Agulhas Current, the East Australian Current, and the Brazil Current.

1.1.2 Processes affecting the SST variability in the WBC regions

Warm SSTs are good indicators of WBCs at the ocean surface. The SST is relevant for the weather and climate measurement, and is retrieved by satellite microwave radiometers, infrared radiometers, *in-situ* moored or drifting buoys, and research or opportunity ships. Several processes cause changes in SST: oceanic advection (via heat fluxes), frontal shifts, Ekman transport and Ekman pumping, Rossby waves, the thermocline depth and surface wind or wind stress curl. Oceanic advection over the WBCs is marked by the release of heat fluxes from the ocean to the atmosphere. *Cayan,* (1992) showed that the SST anomaly tendency and the monthly heat flux

anomalies are significantly correlated over the ocean. They found that anomalous positive fluxes (upward) are linked to anomalous cooling, and anomalous negative fluxes to anomalous warming of the ocean. *Cayan,* (1992) concluded that ocean heat content and SSTs are relevant to determine the heat flux anomalies in WBCs with positive local SST (*Frankignoul and Kestenare* 2002; *Tanimoto et al.* 2003; *Park et al.* 2005). Thus, the SST variability is huge around regions of strong SST gradients along oceanic fronts associated with WBCs (*Frankignoul et al.* 2001; *Nakamura and Kazmin,* 2003). *Nakamura and Kazmin,* (2003) observed that the axis of the North Pacific subarctic frontal zones was displaced from 42.58°N around 1970 to 40.58°N in the mid-1980s, yielding to an SST decrease of around 2°C. For example, the Gulf Stream shift is influenced by changes in the North Atlantic Oscillation. It moves north during positive phases of the North Atlantic Oscillation (*Frankignoul et al.* 2001). In the Southern Hemisphere, the strengthening and the poleward shift of the Agulhas Current also induce an increase in SST (*Yang et al.* 2016; *Rouault et al.* 2009; *Wu et al.* 2012). The SST variability in WBC regions is also induced by the Rossby waves through the vertical displacement of the thermocline and the horizontal displacement of the WBC's fronts. This process is at the origin of the observed low-frequency variability of the SST and thermocline close to the Kuroshio Extension (*Qiu,* 2003; *Taguchi et al.* 2007) and the Gulf Stream (*Frankignoul et al.* 1997; *Sturges et al.* 1998; *Sirven et al.* 2002). On the other hand, SST variability is affected both by the wind speed and the wind stress curl. Many authors showed using satellite observations (*Chelton et al.* 2001, 2004; *O'Neill et al.* 2003, 2005; *Chelton and Wentz,* 2005; *Maloney and Chelton,* 2006) a linear relationship between the wind speed perturbations and SST perturbations, and between the wind stress curl and the crosswind SST gradient. Moreover, *Small et al.* (2008) found that SST perturbations are linearly related to wind speed change across SST fronts mainly for SST perturbations ranging from -1 to 1°C. However, *Park et al.* (2006) did not found a linear relationship between change in wind speed, wind stress curl and SST change greater than 1°C across the Gulf Stream. The recent study in the Agulhas region by *Rouault et al.* (2016) reveals that when the wind is enhanced above warm eddies, there is no relationship between the enhancement in surface wind speed and the SST perturbations, but the decrease in wind speed from the centre to the edge of the eddies downstream, and the SST perturbations are linealy related. A summary of the processes affecting changes in SST over the WBCs is in **Figure 1.2.**

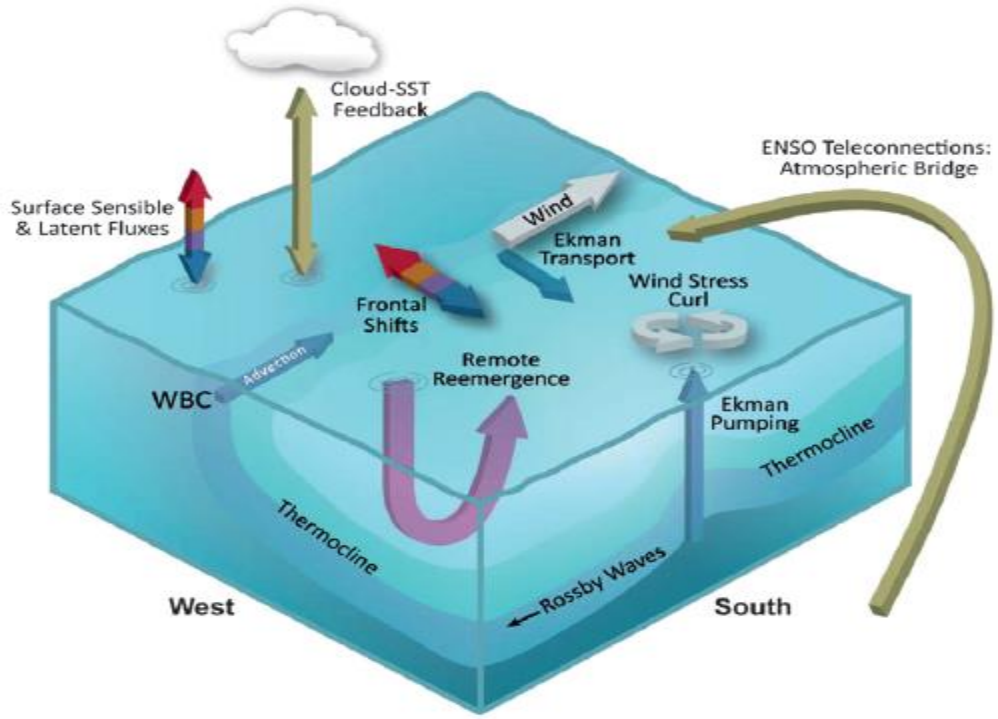

Figure 1.2: Summary of the oceanic and atmospheric processes affecting the SST changes in the Western boundary current regions (*Kwon et al.* 2010).

1.2 THE AGULHAS CURRENT AND ITS IMPORTANCE FOR THE CLIMATE

The Agulhas Current is the strongest western boundary current in the Southern Hemisphere (*Stramma and Lutjeharms,* 1997). It flows along the continental shelf of the southeast Africa, from about 27°S up to 40°S and retroflects back to the Indian Ocean, in an eastward direction (*Bryden et al.* 2005; *Lutjeharms,* 2006). Like the Gulf Stream or the Kuroshio, the Agulhas Current is marked by intensive heat loss, and sharp sea surface temperature gradient, up to 10°C warmer than the surrounding ocean (**Fig. 1.3**). The greater Agulhas Current system has 3 principal components (**Fig. 1.3**): the core of the Agulhas Current which is about 200 km wide from the shore near 32°S (*Bryden et al.* 2005), or 219 km wide near 34°S (*Beal et al.* 2015); the Agulhas Retroflection region, lying between 16 and 20°E and between 38° and 41°S, with a loop diameter of about 340 km (*Lutjeharms and Van Ballegooyen,* 1988); and the Agulhas Return Current that meanders back

to the indian ocean (*Beal et al.* 2011). The core of the Agulhas Current is steered by the shelf break (200 m isobath) along the southeast coast of South Africa and is important because of its thermal contrast with the surrounding water.

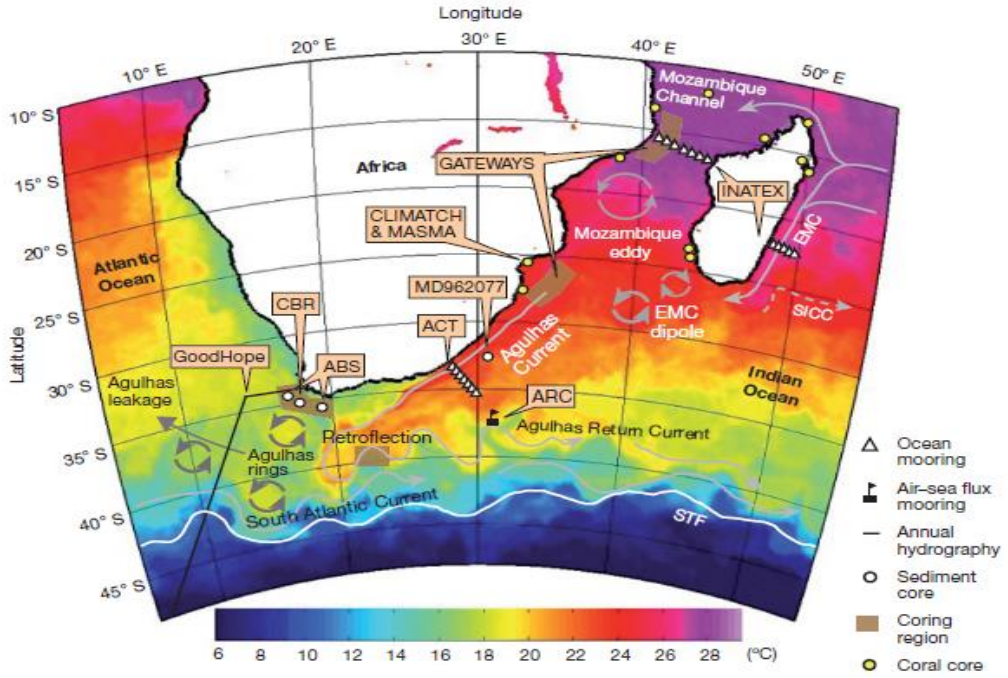

Figure 1.3: Sea surface temperature for 23 May 2009, representing the great Agulhas system. The Agulhas Current and the Retroflection region are marked by SST between 23 and 25°C, and the Agulhas leakage with SST between 18 and 20°C (*Beal et al.* 2011).

1.2.1 Sources of the Agulhas Current

The sources of the Agulhas Current have been extensively documented. *Stramma and Lutjeharms* (1997) suggested that the mean flow of the Agulhas Current is composed of 25 Sverdrups (1Sv = 10^6 m^3s^{-1}) from east of Madagascar Current, 35 Sv due to the recirculation in a subgyre of the southwest Indian Ocean south of Madagascar, and 5 Sv contribution of the Mozambique Channel. All in all, *Stramma and Lutjeharms* (1997) calculated the maximum transport of the Agulhas Current in the upper 1000 m of the ocean to be 65 Sv, using historical data. *Biastoch and Krauss*, (1999) found a similar result using the Modular Ocean Model, with a 1/3° x 1/3° horizontal

resolution, while *Beal and Bryden*, (1999) estimated that the Agulhas Current transports around 70 Sv by using *in-situ* measurements by Lowered Acoustic Doppler Current Profilers (LADCP). Past studies showed that the Red and Arabian Seas provide some of the Agulhas Current flow (*Toole and Warren,*1993; *Valentine et al.* 1993; *Beal and Bryden*, 1997*; Beal et al.* 2000; 2006). Moreover, the study of *Beal et al.* (2011) revealed that the Agulhas Current takes its sources from the subtropical gyre waters, from the Red and Arabian Seas, from the Indonesian throughflow and from the equatorial Indian Ocean via the Mozambique Channel eddies and the East Madagascar Current.

The flow of the Agulhas Current is directed by the topography. Upstream, the dominant mode of the Agulhas Current's variability is in the form of large, solitary meanders, called Natal Pulses (*Lutjeharms and Roberts*, 1988; *Bryden et al.* 2005). Moreover, the Agulhas Current has been linked upstream to variation in the Indonesian throughflow and the Pacific El Niño–Southern Oscillation (*De Ruijter et al.* 2005; *Le Bars et al.* 2013), while downstream it transports warm and saline waters into the South Atlantic Ocean (*Peeters et al.* 2004), forming part of the meridional overturning circulation which can influence the climate.

Our region of study is mainly focused on the Agulhas Current system region (**Fig. 1.4**). **Figure 1.4** (top panel) illustrates the mean SST derived from the Moderate Resolution Imaging Spectroradiometer (MODIS, *Kilpatrick et al.* 2015) over the period 2003-2007, with the overlaid wind direction of the Scatterometer Climatology of Ocean Winds (SCOW, *Risien and Chelton,* 2008). SCOW is a climatology from 1999 to 2007. MODIS and SCOW have a different climatological period because of the availability of the data. More details are found in **Chapter 2**. The pattern of warm waters (> 22°C) of the Agulhas Current south of Africa, originating in the Indonesian throughflow is well defined (**Fig. 1.4**). The wind speed is landward in this region.

The leakage of water from the Agulhas Current into the South Atlantic Ocean manifests in the eddy corridor, whereby relatively warm water (18 °C < t < 20 °C) extends northwestward from the Retroflection region. The 18°C isotherm defines the southern boundary of the meandering structure of the Agulhas Return Current. This region is dominated by westerly winds. Colder water (< 16 °C) is visible in the Antarctic Circumpolar Current (ACC) to the south and in the Benguela coastal upwelling region west of South Africa. **Figure 1.4** (bottom panel) shows the mean surface geostrophic current field derived from the GlobCurrent data for the period 2003-2007. The core of the Agulhas Current that can be up to 219 km wide near 34°S (*Beal et al.* 2015), with a mean

velocity of around 1.5 m.s^{-1} in the region south of Port Elizabeth is well defined. The Return Current, in comparison, displays distinct large-scale meanders and eastward surface currents of around 1 m.s^{-1}.

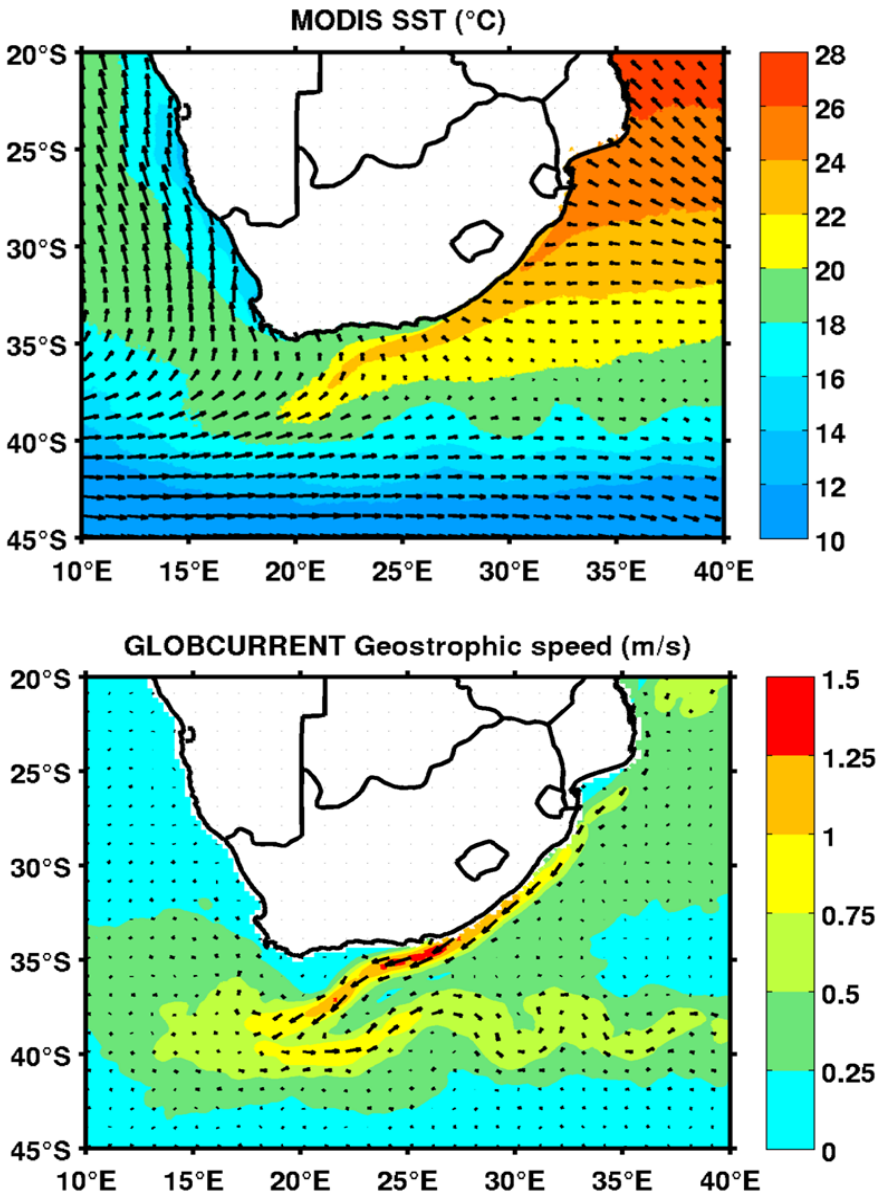

Figure 1.4: top) MODIS SST (°C) annually averaged over the period 2003-2007 (background colour), with overlaid SCOW wind direction (arrows) (1999-2007), **bottom)** GlobCurrent geostrophic current speed at 0 m depth (background colour) with overlaid current speed (arrows), averaged over the same period as MODIS SST. One arrow represents the mean direction of four grid points.

1.2.2 Importance of the Agulhas Current

The Agulhas Current is very important for the ocean and climate system. In terms of global ocean circulation, *Gordon,* (1986) was the first to find that the interocean exchange of water between the South Indian and Atlantic Oceans could be relevant to maintain the Atlantic surface salinities, known as the Agulhas leakage. Later, more studies showed that the Agulhas Current supplies the upper branch of the Atlantic Meridional Overturning Circulation (AMOC) through this transport of warm and saline water from the Indian to the Atlantic Ocean (*Gordon et al.* 1992; *Donners and Drijfhout,* 2004; *Lutjerhams,* 2006). Model experiments suggest that changes in Agulhas leakage may impact the strength and stability of the AMOC (*Weijer et al.* 2002; *Knorr & Lohmann,* 2003; *Biastoch et al.* 2008). As the Agulhas leakage is relevant to balance the global thermohaline circulation (*Gordon et al.* 1992; *Lutjeharms,* 2006; *Beal et al.* 2011), the increase or reduction of its strengh will lead to strengthening or weakening the AMOC and the corresponding variations of the North Atlantic Deep Water formation (*Biastoch et al.* 2009; *Beal et al.* 2011). Moreover, large anticyclonic eddies formed due to the Agulhas Return Current are known as the largest in the world ocean and are believed to play an important role in the general thermohaline circulation (*Gordon et al.* 1992).

In addition to the influence of the Agulhas Current on ocean circulation through the Agulhas leakage, *Lutjerhams et al.* (2000) present evidence for upwelling along the landward side of the Agulhas Current. This upwelling occurs in a constrained area, centered at Port Alfred (~33.6°S). *Rouault et al.* (2000) suggested two mechanisms for the origin of this local upwelling: the Ekman transport in the bottom edge of the Agulhas Current, and a topographically induced upwelling, expected when the current passes from a narrow to a wide shelf. Intermittent upwelled waters occur more than 40% of the time and change the SST dramatically (*Lutjeharms et al.* 2000). This process can impact nutrient availability, stratification, and primary productivity of the eastern part of the Agulhas Bank.

The Agulhas Current system plays a significant role in the climate, via the Agulhas leakage (*Gordon,* 1992; *Beal et al.* 2011; *Biastoch et al.* 2009;), the Agulhas Current (*Lutjeharms,* 1986; *Jury,* 1993, 1994; *Rouault et al.* 2000, 2013; *Catto et al.* 2012), and the Agulhas Return Current (*Shimada and Minobe,* 2011). *Lutjeharms et al.* (1986) observed a cloud line above the Agulhas Current. They concluded that cumulus and stratocumulus clouds unveil the location of the warmest

waters due to the Agulhas Current upstream of the Agulhas Retroflection region (*Lee-Thorp et al.* 1998; *Lutjeharms and Rouault*, 2000). However, the impact of the Agulhas Current on the climate of South Africa still needs to be fully assessed. Scatterometer wind observations have revealed that wind divergence or convergence at the ocean surface are related to SST fronts that are linked to ocean currents (*Chelton et al.* 2004; *Xie*, 2004; *Small et al.* 2008). This highlights the importance of western boundanry currents (e.g. Agulhas Current) while estimating the surface wind, or the mean stress through the current feedback (*Chelton et al.* 2001; *Renault et al.* 2016). Over the Agulhas region, *Renault et al.* (2017) show that the current feedback slows down the oceanic mean circulation and acts as an oceanic eddy killer. Moreover, over the warm side of the Agulhas Current, the turbulent latent and sensible heat fluxes increase considerably (*Jury*, 1994; *Rouault and Lee-Thorp*, 1996; *Rouault et al.* 2000; *Rouault and Lutjeharms*, 2000; *Bentamy et al.* 2017), up to 5 times increase compared to the surrounding ocean (*Jury*, 1994). As winds blow from cool to warm SST, this enhances the turbulent fluxes and destabilize the boundary layer over the warmer SST than the cooler SST. This process will increase the vertical mixing, that deepens the boundary layer above the warmer SST compared to the cooler SST.

1.3 LITERATURE REVIEW

1.3.1 Impact of the Gulf Stream and the Kuroshio on the regional climate

In the Northern hemisphere, the Gulf Stream and the Kuroshio Current have an impact on the climate and weather of the surrounding countries. Patches of low clouds formed over warm meanders are observed across the Gulf Stream front (*Young and Sikora*, 2003). *Minobe et al.* (2008) revealed that the Gulf Stream affects the entire troposphere above it. Using observations, reanalysis and an Atmospheric General Circulation Model, they suggested that atmospheric pressure adjustments to sharp SST gradients lead to wind convergence at the ocean surface, which anchors a band of rainfall along the Gulf Stream. In the corresponding region, upward motion and cloud formation unphold up to the upper troposphere as illustrated by **Figure 1.5**. *Kuwano-Yoshida et al.* (2010) suggested that the model experiments simulate a tight band of precipitation, surface wind convergence, and evaporation over the Gulf Stream pathway. However, recent studies

propose that the low-level wind convergence and the narrow band of precipitation over the Gulf Stream region are the results of interexchange between atmospheric variability and the sharp SST front (*Parfitt et al.* 2016; *O'Neill et al.* 2017; *Sheldon et al.* 2017).

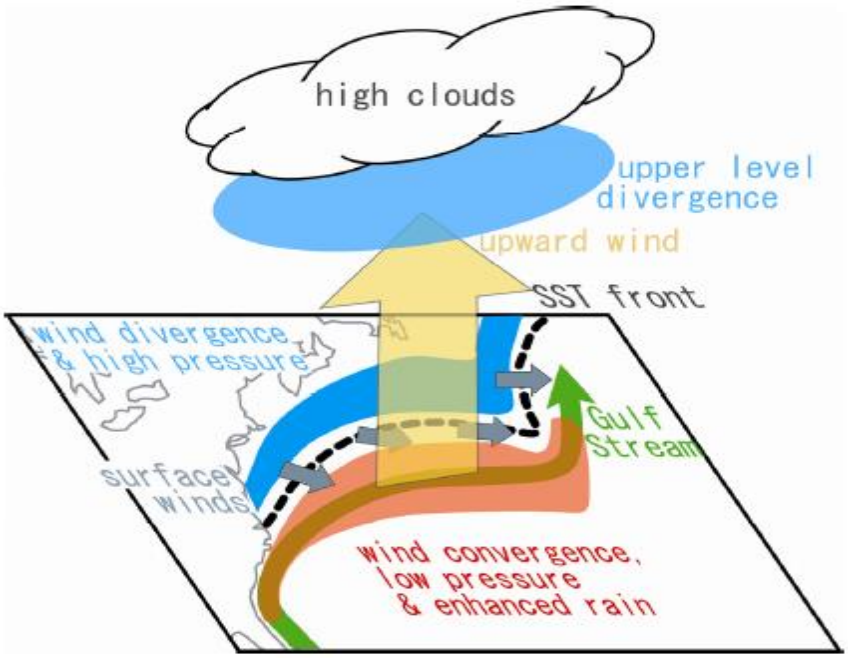

Figure 1.5: Atmospheric responses in the Gulf Stream region. Rainfall (red shade) and wind convergence related to low pressure are formed on the offshore side of the SST front (black dashed curve) of the Gulf Stream (green long arrow). Onshore, surface wind divergence associated with high pressure occurs (blue shade). Upward motion extends to the upper troposphere (yellow arrow) and is related to the upper-level horizontal divergence (blue oval) and high-level clouds (*Minobe et al.* 2008).

Minobe et al. (2010) studied the atmospheric feedback to the Gulf Stream SST front using high-resolution satellite observation data sets and operational analysis and forecasts. They proposed two atmospheric response modes in this region. One in wintertime is a shallow-heating mode dominating the Gulf Stream with strong latent heating in the lower troposphere. The other, in summertime, is a deep-heating mode over the western side of the Gulf Stream, depicted by latent heating in the middle and upper troposphere due to deep convection. As for the Gulf Stream,

several studies have been made on the Kuroshio Current. These WBCs are linked to a band of concentrated heat and moisture (*Kwon et al.* 2010) which impact the mean state of the atmosphere by allowing frequent formation of cyclones and storm tracks.

The influence of the Kuroshio and Oyashio Extension on the regional overlying atmosphere is shown in *Taguchi et al.* (2009). They compared monthly high-resolution satellite and reanalysis SSTs with historical temperatures. *Taguchi et al.* (2009) found that the locally enhanced of heat fluxes and air temperature at the ocean surface across the frontal zones favour the formation of storm track during the winter and the spring. Using satellite observations, reanalysis data sets and a regional atmospheric model, *Sasaki et al.* (2012) investigated the impact of the Kuroshio Current in the East China Sea on the baiu rainfall. They showed that the highest amount of precipitation over the Kuroshio is in June. During this period of the year, the band of precipitation spread out over the East China Sea. Thus heavy precipitation is collocated to the warmer waters of the Kuroshio which enhances rainfall in the corresponding region. Locally, the strong oceanic fronts created by the Gulf Stream and the Kuroshio are known to increase the height of MABL, and to anchor the low-level baroclinicity (*Nakamura et al.* 2004). Recent studies present several mechanisms to explain the influence of these WBCs on precipitation (*Xu et al.* 2011; *Minobe et al.* 2008; *Sasaki et al.* 2012; *Parfitt and Czaja*, 2016; *O'Neill* et al. 2017; *Vannière et al.* 2017). However, the influence of the Agulhas Current is less known than that of the Gulf Stream and the Kuroshio.

In the Southern hemisphere, most of the studies to date have encountered the problem of the low-resolution of reanalysed climate data sets. For example, the latent heat fluxes measured by *Rouault et al.* (2000) above the Agulhas Current were not well reproduced in models (e.g. the National Centers for Environmental Prediction Reanalysis 2 (NCEP2) and the ECMWF second-generation reanalysis (ERA-40)). The data used by *Gimeno et al.* (2010) may have caused underestimation of the ocean-atmosphere exchanges in the Agulhas region, due to a low spatial resolution (2.5° x 2.5°) in both model and reanalysis. Nevertheless, *Gimeno et al.* (2010) presented the Agulhas Current region as a moisture source for South Africa (**Fig. 1.6**).

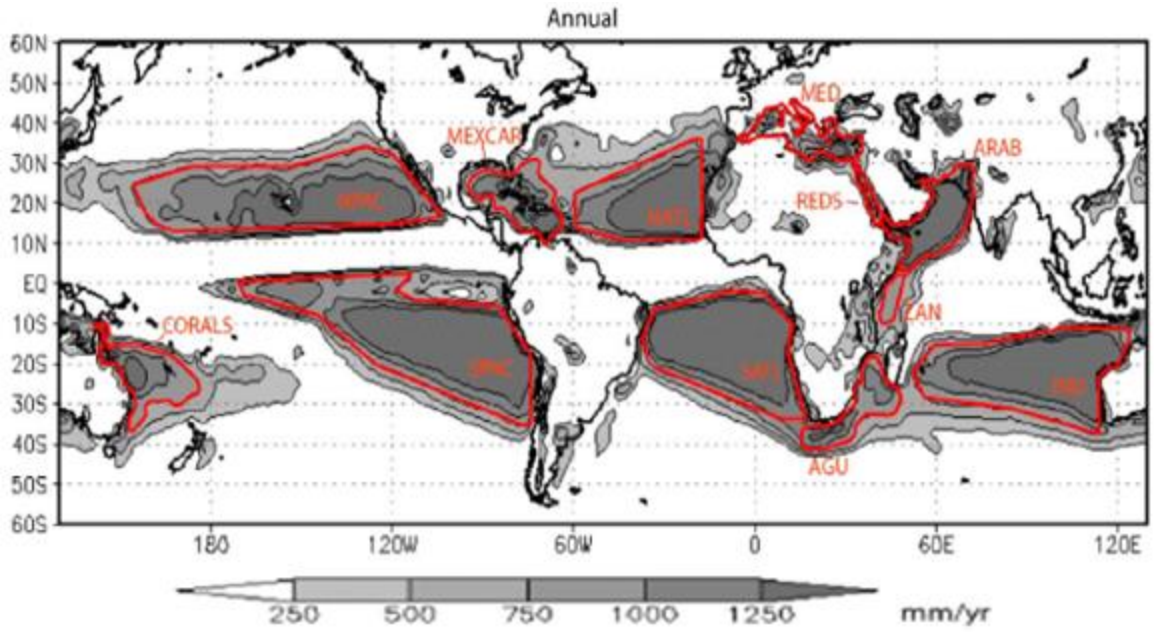

Figure 1.6: Climatological annual vertically integrated moisture flux divergence (mm/yr). Areas inside the red contour lines indicate moisture source regions for the continent (*Gimeno et al.* 2010). The Agulhas Current is a source of moisture for South Africa.

1.3.2 Impact of the Agulhas Current on the regional climate

The climatic influences of Agulhas Current have probably been tremendous for the existence of *Homo sapiens* in Africa in the Middle ages (*Marean et al.* 2007). Substantial turbulent latent heat fluxes (as known as turbulent flux of moisture), as well as marine boundary layer modification, have been measured above the core of the Agulhas Current, the Retroflection region and the Agulhas Return Current (*Mey et al.* 1990; *Lee-Thorp et al.* 1999; *Rouault et al.* 1995, 2000, 2003; *Rouault and Lutjeharms*, 2000). These measurements show that the turbulent latent heat flux is higher in the Agulhas Current system compared to the surrounding ocean. *Rouault et al.* (2002) provided evidence that low-level moisture from the Agulhas Current played a major role in the development of a convective storm and associated tornado across the southern part of South Africa. They hypothesed that moisture produced over the Current was associated to an extreme weather system. In addition, the Agulhas Current has considerably warmed up since the 1980s, which has increased the transfer of moisture from the ocean to the atmosphere (*Rouault et al.* 2009).

Moreover, *Gimeno et al. (2010)* showed that the core of the Agulhas Current system is a source of moisture for Southern Africa (**Fig. 1.6**). The core of the Agulhas Current that is about 200 km wide from the shore near 32°S (*Bryden et al.* 2005) is important because of the SST difference between the Agulhas Current and the surrounding water. This thermal contrast leads to a five-fold increase in turbulent fluxes compared to the surrounding ocean. Radiosondes launched during the Agulhas Current air-sea exchange experiment (ACASEX) cruise show that the core of the current produces a wall of moisture (*Rouault et al.* 1995, 2000; *Lee-Thorp et al.* 1999) that can reach up to 2000 m above the Agulhas Current. This flux of moisture is directed towards the coast when the wind blows from the Agulhas Current to the coast (*Jury et al.* 1997; *Lee-thorp et al.* 1999; *Rouault et al.* 2000). Cloud lines above the Agulhas Current are the results of the strong exchange of moisture occurring in this region at the time of fair-weather (*Rouault et al.* 1995, 2000; *Lutjeharms et al.* 1986; *Lutjeharms and Rouault*, 2000). A major issue in the Agulhas Current region is the underestimation of the latent heat fluxes estimated over the Agulhas Current. In this region, the heat fluxes were not well reproduced in first-generation climate reanalyses (NCEP1, *Kalnay et al. (*1996), and ERA-40 (*Uppala et al.* 2005). However, recent reanalyses like the Climate Forecast System Reanalysis (CFSR, *Saha et al.* 2010), the Modern-Era Retrospective analysis for Research and Applications version 2 (MERRA-2, *Gelaro et al.* 2017) are now available at a higher resolution. Similarly, numerous new air-sea interaction data sets derived from satellite remote sensing such as SEAFLUX ((air-sea turbulent fluxes), *Curry et al.* 2004) have been produced at a resolution that allows a good representation of the Agulhas Current.

In addition to the impact of the Agulhas Current on heat fluxes, few studies found an influence of this warm western boundary current on South Africa rainfall. They suggested that precipitation along the eastern coast of South Africa is influenced by the vicinity of the Agulhas Current (*Jury et al.* 1993; *Rouault et al.* 2013). *Reason,* (2001) investigated the climatic effect of the greater Agulhas Current on South Africa region, but the author used a low-resolution model. *Jury,* (2015) suggested that the El Niño–Southern Oscillation, the Southern Africa rainfall, and the SST are related, by considering the Agulhas Current system as a whole. As for the latent heat fluxes, former climate reanalyses (ERA-40, NCEP2) were not accurate to properly study the climatic impacts of the western boundary currents, because of they coarse horizontal resolution (*Rouault et al.* 2003; *Rouault & Lutjeharms,* 2003). Meanwhile, recent studies recommend that for the investigation of ocean-atmosphere interaction over WBCs, it is better to have a model with a spatial resolution of

at least 0.25° x 0.25° (*Smirnov et al.* 2015; *Parfitt et al.* 2016). Several processes are suggested to explain the role of the Gulf Stream and the Kuroshio on precipitation. However, the impact of the Agulhas Current on the Southern Africa rainfall is not well known compared to that of the Gulf Stream and the Kuroshio Current.

1.4 OBJECTIVES AND OUTLINE OF THE THESIS

1.4.1 Aims of the study

The climatic impact of the strongest WBC of the southern hemisphere on South Africa has been studied using coarse resolution satellite data sets and/or reanalyses (*Rouault et al.* 2003; *Reason,* 2001; *Gimeno et al.* 2010). Thus these were not able to take into account the impact of the core of the Agulhas Current that can be up to 200 km wide, with a speed of 1.5 $m.s^{-1}$. However, the new generation of satellite data sets and climate reanalysis integrate the core of the Agulhas Current. The use of this new version of data will lead to improvements in the weather, climate prediction, and services for South Africa. The aim of this study of air-sea exchange above the Agulhas Current is divided into two parts:

- Provide an improved understanding of ocean-atmosphere interaction in Southern Africa at relevant spatial and temporal scales;
- Investigate the impact of the Agulhas Current on Southern Africa rainfall, on a seasonal and annual timescale.

1.4.2 Outline of the thesis

I will use the new generation of high-resolution satellites and reanalyses data sets that integrate the effect of the core of the Agulhas Current. Moreover, I will analyse the outputs of the Weather Research and Forecasting model (WRF, *Skamarock and Klemp*, 2008), version 3.7.1 to investigate the influence of the Agulhas Current on rainfall. My study will be structured as follow:

- Chapter 2 will give an overview of satellites, observations and reanalyses data sets used for this study, as well as a description of the atmospheric WRF model used. The methods applied to reach my objectives will be detailed in this part.
- Chapter 3 will document the ocean-atmosphere interactions above the Agulhas Current, with a focus on the representation of latent heat flux by numerous sets of products. In this section, I will intercompare the first and second generation of climate data sets, by:

1) exploring whether the new climate reanalyses and satellite-derived data sets adequately represent the high latent heat flux (LHF) or exchange of moisture above the Agulhas Current,
2) examining the magnitude of uncertainties in the basic parameters used to derive the LHF, and
3) quantifying the annual cycle of the LHF and its drivers in the Agulhas Current system. This chapter will be relevant for choosing a good high-resolution reanalysis for the next study.

- Chapter 4 will access using a set-of-art data, and a numerical model experiments how the warm waters associated with the Agulhas Current affects the regional precipitation and the associated low-level atmosphere, east of South Africa on an annual timescale. The WRF numerical model will provide two simulations: the control run driven with high-resolution observed SST and a sensitivity experiment driven with a smoothed SST in order to remove the sharp SST gradients associated with the Agulhas Current. This second experiment is otherwise identical to the control run. This chapter has been published in *Nkwinkwa Njouodo et al.* (2018).
- Chapter 5 will be similar to the previous study but on a seasonal timescale. This section will have an overview of the period of the year when the rainfall is at the maximum or minimum over the southern Africa, and the mechanisms driving these seasonal differences.
- Chapter 6 will provide a discussion of the results, a summary and suggestions for future work.

CHAPTER 2

2 DATA AND METHODS

To study the ocean-atmosphere interaction over the Agulhas Current and its impact on South Africa weather and climate, numerous sets of high-resolution satellite observations, ship observations, high and low-resolution reanalyses are used and compared. The comparison allows us to quantify the differences between products. Moreover, to investigate the impact of the strongest western boundary current of the southern hemisphere on precipitation in eastern South Africa, we perform and analyse two sensitivity experiments of the Weather Research and Forecasting model (WRF, *Skamarock & Klemp*, 2008). The data and the atmospheric WRF model are described in this Chapter.

2.1 DATA

2.1.1 Observations

2.1.1.1 *In-situ* observations

The National Oceanography Centre Southampton (NOCS, *Berry and Kent*, 2011) version 2 data set is analysed. NOCS is based on Voluntary Observing Ship (VOS) and is obtained from the International Comprehensive Ocean-Atmosphere Data Set (ICOADS) (*Woodruff et al.* 1987; *Berry and Kent*, 2009, 2011). This product is presented on a 1° x 1° spatial grid and uses optimal interpolation (OI) of daily estimates of ship data from 1973 to 2006. The interpolation method is essentially based on the approach developed by *Reynolds and Smith* (1994) and by *Lornec* (1981). The wind speed over the oceans is estimated visually by the VOS from anemometers (*Berry and Kent*, 2011) or using the Beaufort Equivalent Scale (*Thomas et al.* 2008). To have the same climatology as the anemometer winds, the WMO1100 is used thereafter to correct the visual wind

reports. Surface meteorological fields have been adjusted to account for varying measurement heights and for known biases. For example, the anemometer observations were adjusted to a standard reference height of 10 m using the bulk formulae and parameterizations of *Smith* (1980, 1988). To measure the SST, the water samples were collected using a bucket or from the engine-intake measurement (ERI). Buckets can have a cold bias when there is heat loss from the water sample. ERIs can have a warm bias due to the proximity of the intake to the engine (*Kent and Taylor*, 2006). Corrections were applied for the different types of measurements using the method given by *Josey et al.* (1999). Humidity observations were made using wet and dry bulb thermometers (*Berry and Kent*, 2011). The bias method applied is from *Josey et al.* (1999), after being adjusted to 10 m using *Smith* (1980, 1988). The flux estimates in the NOCS data are based on the bulk formulas of *Reed*, (1977); *Clark et al.* (1974); *Smith*, (1980, 1988). A correction method is then used to develop the monthly NOCS flux fields (*Josey et al.* 1999) which is available at www.noc.soton.ac.uk/noc_flux/. The monthly mean data set is calculated from daily estimates of each variable and the standard deviation of these daily values within each month is also presented in the link above. It is important to note that the tropical and the southern oceans are poorly sampled. Thus, the uncertainties in these regions are much larger than the interpolation uncertainties estimate. This is probably due to the measurement uncertainties included in NOCS v2.0 (*Berry and Kent*, 2011).

To validate the seasonal precipitation over land, we use the gridded climatology of *Hewitson and Crane* (2005) based on observations. This climatology of South African precipitation is a high-resolution climatology (0.1° x 0.1°) of gridded-average daily precipitation computed from 1950 to 2000, using the conditional interpolation method (*Hewitson and Crane* 2005).

2.1.1.2 Satellite observations

The Moderate Resolution Imaging Spectroradiometer data set (MODIS, *Kilpatrick et al.* 2015) is analysed. MODIS is derived from instruments aboard Terra and Aqua satellites, both part of NASA's Earth Observing System. The spatial resolution of MODIS SST is 4 x 4 km and is available from June 2002 to the present. MODIS represents the fine spatial structures of the Agulhas Current quite well, especially near the coast. MODIS SST has a viewing swath width of 2.3 km. It views the entire surface of the Earth every one to two days

(https://modis.gsfc.nasa.gov/about/). Its detectors measure 36 spectral bands between 0.4 and 14.4 μm. MODIS is the first spacecraft radiometer to have multiple infrared bands in the mid-infrared atmospheric transmission window (*Kilpatrick et al.* 2015). The Level 2 product is produced daily and consists of global day and night coverage every 24 hours. The algorithm used to retrieve the SST skin is similar to the Advanced Very High-Resolution Radiometer (AVHRR) algorithm used for SST (*Kilpatrick et al.* 2001). MODIS data is freely available at ftp://podaac.jpl.nasa.gov/OceanTemperature.

Another SST product used is the AVHRR-based Optimal Interpolation Sea Surface Temperature (OISST, *Reynolds et al.* 2007). The daily AVHRR OISST is measured from a single sensor and is available on a horizontal grid of 0.25° x 0.25°. OISST extends from late 1981 onward and can be freely downloaded from https://www.ncdc.noaa.gov/oisst/.

The GlobCurrent surface geostrophic current (*Johannessen et al.* 2016) is another satellite product used in this study, to resolve the structure of the Agulhas Current, as shown in **Figure 1.4**. GlobCurrent is a recently released global ocean current product derived from combined Ekman and geostrophic current estimates and is available at (http://www.globcurrent.org). GlobCurrent extends from 1993 to 2015, with a spatial resolution of 0.25° x 0.25°. Further details of this product are provided by *Rio et al.* (2014) and *Johannessen et al.* (2016) and validation is found in *Hart-Davis et al.* (2018). The former authors found that on average, the GlobCurrent underestimates the ocean velocity by around 27% in the Agulhas Retroflection region, but this product could be used for the representation of the Agulhas Current.

The Tropical Rainfall Measuring Mission Precipitation Radar (TRMM PR, (*Biasutti et al.* 2012) is a climatology, available from 1998 to 2007. This satellite product is based on the version 6 of TRMM 2A25 obtained from measurements made with the TRMM PR. A feature of TRMM PR is its very high horizontal resolution (0.05° x 0.05°). The data are monthly climatologies from daily-mean (*Biasutti et al.* 2012). The PR has a view swath width of 247 km. The data are retrieved up to 123.5 km poleward of 35° latitude, meaning that the PR satellite covers the region 36°N to 36°S. TRMM PR Climatology is available on http://kage.ldeo.columbia.edu:81/SOURCES/.LDEO/.ClimateGroup/.DATASETS/.TRMM_PR/

The Scatterometer Climatology of Ocean Winds (SCOW, *Risien and Chelton,* 2008) is used as reference for the 10 m wind speed and direction. The relative high-resolution (0.25° x 0.25°) resolves the small-scale features that are dynamically important for both the ocean and the

atmosphere (*Risien and Chelton,* 2008). SCOW is a climatology based on 122 months from September 1999 to October 2009 that includes the NASA Quick scatterometer (QuikSCAT) data set. SCOW can be retrivied at http://cioss.coas.oregonstate.edu/scow/. SCOW wind is based on harmonic analyis described in *Risien and Chelton,* (2008). The authors compared SCOW wind to NCEP–NCAR (*Kalnay et al.* 1996; *Kistler et al.* 2001) and the ECMWF (*Gibson et al.* 1997) reanalysis winds. They concluded that these reanalyses have a much coarser grid spacing of 2.5° and 1.875° respectively, resulting in a poor ability to resolve features at scales below 1000-1500 km. NCEP and ECMWF reanalyses are often used to force ocean models, and can underestimate some basic parameters such as SST, air temperature or wind speed.

The high-resolution air-sea turbulent fluxes (SEAFLUX, *Curry et al.* 2004) are used to evaluate the LHF in the Agulhas Current region. With a spatial resolution of 0.25° x 0.25°, SEAFLUX covers the global ice free ocean and is available from January 1998 to December 2007. SEAFLUX benefits from an international effort under the GEWEX and CLIVAR umbrella (*Curry et al.* 2004) and can be downloaded at http://SEAFLUX.org. This product is three-hourly (averaged from 0000-0300Z, 0300-0600Z...) and provides sufficient parameters to calculate the turbulent fluxes (fluxes of moisture). It was compared at the global scale with various satellite-derived products and reanalyses (*Chou et al.* 2004; *Smith et al.* 2011). SEAFLUX wind speed is an equivalent neutral wind valid at 10 m, based on the Cross-Calibrated MultiPlatform wind and the neural network algorithm (*Roberts et al.* 2010). Moreover, SEAFLUX wind speed is formed by assimilation of wind retrievals from SSM/I, TMI, AMSR-E, QuikSCAT, and SeaWinds onboard ADEOS-2. NCEP and ECMWF are used to fill in data gaps (*Curry et al.* 2004). The SST is taken from the Reynolds Optimally Interpolated Version 2.0 AVHRR-only, a NOAA SST (*Reynolds et al.* 2007). The air specific humidity is obtained using a neural network algorithm based on *Roberts et al.* (2010). This parameter is valid at 10 m above the sea surface. The final value of the LHF is computed using the bulk algorithm developed by *Fairall et al.* (2003) for TOGA COARE3.0. A general discussion of SEAFLUX product is given in *Curry et al.* (2004).

The last satellite flux product used is the third version of the Hamburg Ocean Atmosphere Parameters and Fluxes (HOAPS3, *Clayson et al.* 2013). The HOAPS3 (0.5° x 0.5°) provides fields of turbulent heat fluxes over the global ice-free ocean, and covers the time period July 1987 to December 2005. It is a completely reprocessed data set (*Andersson et al.* 2010; 2011). The HOAPS3 wind speed is based on the neural network approach, and is measured at 10 m. The

advantage of this method is to take into account the atmospheric conditions (cloud, clear sky), and the non-linearity of the problem. HOAPS3 SST is based on the AVHRR Oceans Pathfinder SST (*Casey* 2004). Thus, the AVHRR day and night-time data are averaged to daily mean SST maps. The HOAPS3 specific humidity at the sea surface is calculated from the saturation humidity, using the Magnus formula (*Murray*, 1967). The air specific humidity at 10 m is computed using the method given by *Bentamy et al.* (2003).

Type	*In-situ* observation		Satellite						
Product	**NOCS** (*Berry and Kent,* 2011)	**Climatology** of *Hewitson and Crane* (2005)	**MODIS** (*Kilpatrick et al.* 2015)	**OISST** (*Reynold et al.* 2007)	**GlobCurrent** (*Johannessen et al.* 2016)	**TRMM PR** (*Biasutti et al.* 2012)	**SCOW** (*Risien and Chelton,* 2008)	**SEAFLUX** (*Curry et al.* 2004)	**HOAPS3** (*Clayson et al.* 2013)
Horizontal resolution	1°x1°	0.1° x 0.1°	0.04°x 0.04°	0.25°x 0.25°	0.25° x 0.25°	0.05°x 0.05°	0.25°x 0.25°	0.25°x 0.25°	0.5°x 0.5°
Period available	1973 2006	1950 to 2000	June 2002 to present	1981 to present	1993 to present	1998 2007	1999 2007	Jan 1998 to Dec 2007	Jul 1987 Dec 2005
Averaging period of study	2003 2006	1950 to 2000	2003 2007	2001 2005	2003 2007	1998 2007	1999 2007	2003 2007	2003 2005
SST	X		X	X				X	X
Geostrophic current					X				
Precipitation		X				X			
Wind speed	X						X	X	X
Latent heat flux	X							X	X
Specific humidity (Qsst)	X		X					X	X
Specific humidity of air (Qa)	X							X	X

Table 2.1: Summary of observation data sets used for the study, along with their original spatial grid, the available period, the averaging period and the available sea surface parameters (marked by a cross).

The heat fluxes of HOAPS3 are calculated from swath retrievals and parameterized using the Coupled Ocean-Atmosphere Response Experiment bulk flux algorithm version 3 (COARE3.0, *Fairall et al.* 2003). The monthly HOAPS3 data product is available at http://www.hoaps.org/. A recent comparative study of *Bentamy et al.* (2017) between SEAFLUX, HOAPS3 and some products (ERA-Interim, OAFlux) shows large sensible heat fluxes variations south of 40°S in SEAFLUX and HOAPS3 compared to other products. They concluded that these large variations are indicative of spurious differences in the air-sea temperature difference. A summary of the eight satellite products used is given in **Table 2.1**.

2.1.2 Climate reanalysis

2.1.2.1 Old generation Reanalysis (1st and 2nd generation)

Two old generation reanalyses are used for the ocean-atmosphere comparison with observations and new generation reanalyses. One is the National Centers for Environmental Prediction (NCEP-DOE) reanalysis version 2 (NCEP2, *Kanamitsu et al.* 2002), and the other is the ERA-40 reanalysis (*Uppala et al.* 2005) from the European Centre for Medium-Range Weather Forecast reanalysis (ECMWF). NCEP2 is a first-generation reanalysis. It has an irregular grid of 1.87° x 1.90° and is available from 1979 to present. NCEP2 is an improved version of NCEP1. The improvements include an updated model with better physical parameterizations compared to NCEP1. The limitation of NCEP2 is its low spatial resolution and the poor representation of the Southern Hemisphere. ERA-40 is a second-generation reanalysis product, with a spatial resolution of 2.5° x 2.5° from September 1957 to August 2002. ERA-40 is the first reanalysis to assimilate satellite radiances directly. We use only two parameters of these reanalysis, the SST and the latent heat flux, to evaluate whether the new finer-resolution reanalyses have a better representation of the Agulhas Current than the low-resolution reanalyses. NCEP2 is provided by the NOAA–CIRES Climate Diagnostics Center and is available at http://www.cdc.noaa.gov/. ERA-40 can be downloaded at http://apps.ecmwf.int.

2.1.2.2 New Generation Reanalysis (3rd generation)

Nowadays, it is recommended to use the 3rd generation reanalysis, to better quantify the air-sea interactions. Three reanalysis products are used for this study. The Climate Forecast System Reanalysis (CFSR, *Saha et al.* 2010), the Modern-Era Retrospective analysis for Research and Applications (MERRA-2, *Gelaro et al.* 2017) and the ERA-Interim reanalysis (*Dee et al.* 2011) from the ECMWF.

CFSR is provided by NCEP and is available from 1979 to 2010 (http://rda.ucar.edu/). CFSR is a global coupled atmosphere-ocean-land-sea-ice system and outputs are available at an hourly temporal resolution. The horizontal and vertical model resolution is T382 L64 (i.e. around 38 km with 64 vertical levels) (*Saha et al.* 2010). CFSR is based on the Global Forecast System (GFS) that is a weather forecast model produced by NCEP. Moreover, CFSR uses the Gridded Statistical Interpolation (GSI) data assimilation system for the atmosphere. The oceanic model used is the Modular Ocean Model version 4p0d (MOM4p0d, *Griffies et al.* 2004) at a 0.5° horizontal resolution with 40 levels in the vertical to a depth of 4737 m. The CFS model runs on multiple processes and uses a parallel programming model MPMD (Multiple Program Multiple Data). There are three executable programs: the GFS model, the MOM4 model and the coupler (*Saha et al.* 2010), each program has its own outputs and runs automously. They are linked by the exchange of data between them as follows: the GFS runs on the atmospheric time step (3 mins), MOM4 runs on a fast sea ice time step (3 mins), and a slow ocean time step (30 minutes), while the coupler runs on its own time step and receives data from the GFS and MOM4. CFSR wind speed is composed of the SSM/I brightness temperature converted to wind speeds by a neural approach (*Saha et al.* 2010); the scatterometer wind data sets from ESA ERS 1, ESA ERS 2, QuickSCAT and the WindSat. These scatterometer winds were assimilated in CFSR but after being degraded to 100 by 100 km resolution. CFSR SST used the AVHRR-only product from November 1981 through May 2002 and is replaced by the AMSR+AVHRR product from June 2002 to present day. In addition, CFSR is composed of *in-situ* ship and buoy SST. Thus, all observations used for CFSR SST are bias-corrected with buoy data sets. Missing grid points were filled in via interpolation (*Saha et al.* 2010). The specific humidity in CFSR is an instantaneous passing variable from the GFS to the sea ice model. For the specific humidity, CFSR used AQUA-AIRS, AMSU-a, AMSRE data and Microwave Humidity Sounder (MHS) instruments. In addition to ocean surface

parameters, we use some CFSR atmospheric variables for **Chapter 4**, such as the horizontal and vertical wind velocity from 1000 to 650 hPa.

MERRA-2 is a NASA atmospheric reanalysis available from 1980 to the present (http://disc.sci.gsfc.nasa.gov/uui/search/MERRA-2). This 3rd generation reanalysis replaces the original MERRA reanalysis (*Rienecker et al.* 2011). The data assimilation system for MERRA-2 is the upgraded version of the Goddard Earth Observing System Model Version 5 (GEOS-5), produced in NASA GMAO (Global Modeling and Assimilation Office). It is a 3-dimension variational analysis (3D-VAR), with incremental update including aerosol data assimilation. The horizontal grid is a native cubed-sphere grid, and outputs are interpolated to 0.62° longitude, with 0.5° lat., on 72 sigma levels from the surface to 0.01 hPa (*Gelaro et al,* 2017). A detailed description of input observations assimilated in MERRA-2 is given in *McCarty et al.* (2016). The wind data assimilated in MERRA-2 is a combination of SSM/I surface wind speed, ESA ERS-1, ESA ERS-2, QuikSCAT and ASCAT (Advanced scatterometer) surface wind vectors. MERRA-2 wind speed is stability dependent. MERRA-2 SST is a combination data of CMIP mid-monthly 1° from 1 January 1980 to 31 December 1981; NOAA OISST daily 0.25° (AVHRR) from 1 January 1982 to 31 December 2002; NOAA OISST daily 0.25° (AVHRR and AMSR-E) from 1 January 2003 to 31 March 2006; and OSTIA daily 0.05° from 1 April 2006 to the present. The processing of these products into a grid set of daily SST boundary conditions for MERRA-2 is described in *Bosilovich et al.* (2016). The air specific humidity at 10 m height is estimated as diagnostic outputs based on the computed fluxes and transfer coefficients.

The European Centre for Medium-Range Weather Forecasts (ECMWF, *Dee et al.* 2011) ERA-Interim is another 3rd generation reanalysis used for this study. ERA-Interim is a new atmospheric reanalysis to replace the 1st generation ERA-40. ERA-Interim provides a 0.75° x 0.75° spatial resolution and is available from 1979 to the present day (http://apps.ecmwf.int). The horizontal resolution of the data set is approximately 80 km at 60 vertical levels from the surface up to 0.1 hPa. ERA-Interim is the first reanalysis product to apply the 4D-Var data assimilation scheme. The wind speed is directly assimilated in ERA-Interim, compared to ERA-40. A comparison of ERA-Interim surface wind speed with QuickSCAT and ERS is given in *Dee et al.* (2011) from 1992 to 2002. They found that ERA-Interim wind speed is underestimated by approximately 0.1 $m.s^{-1}$ compared to these satellite products. After 2002, *Dee et al.* (2011) found an increase of ERA-Interim wind speed over the oceans. They suggested that this increase is due to the evolution

of the observing system. ERA-Interim SST is obtained by using the prescribed SST data from NCEP 2D-Var (January 1989–June 2001), NCEP OISST V2 (July 2001–December 2001), NCEP Real-Time Global (RTG, from January 2002 to January 2009), and Operational Sea Surface Temperature and Sea-Ice Analysis (OSTIA from February 2009). ERA-Interim humidity is a combination of pilot balloons, aircraft, and radiosondes in extremely cold conditions and at high altitude. Thus, the analysis scheme for the specific humidity is developed by *Holm*, (2003). **Table 2.2** provides an overview of the fifth monthly reanalyses used for this study.

Product	**NCEP2** (*Kanamitsu et al.* 2002)	**ERA-40** (*Uppala et al.* 2005)	**MERRA-2** (*Gelaro et al.* 2017)	**ERA-Interim** (*Dee et al.* 2011)	**CFSR** (Saha et al. 2012)
Horizontal resolution	1.90°x 1.87°	2.5°x 2.5°	0.50°x 0.66°	0.75°x 0.75°	0.31°x 0.31°
Period available	1979 to present	Sep 1957 to Aug 2002	1981 to present	1979 to present	1979 to 2010
Averaging period of study	2003 2007	1997 2001	2003 2007	2003 2007	2003 2007
Latent heat flux	X	X	X	X	X
SST	X	X	X	X	X
Wind speed			X	X	X
Specific humidity (Qsst)			X	X	X
Specific humidity of air (Qa)			X	X	X
SLP			X	X	X

Table 2.2: Summary of climate reanalysis used for the study, along with their original spatial grid, the available period, the averaging period and the available sea surface parameters (marked by a cross).

2.1.3 Atmospheric Model (Weather Research and Forecasting)

The Weather Research and Forecasting model (WRF, *Skamarock and Klemp,* 2008) system version 3.7.1 is forced laterally by the reanalysis ERA-Interim (0.75°, *Simmons et al.* 2007; *Dee et al.* 2011), that is a 6-hourly reanalysis data set. The model is forced at the surface by the Optimum Interpolated Sea Surface Temperature (OISST, 0.25°x0.25°, *Reynolds et al.* 2007) daily data. The model domain is 17°S-43°S and 8°E-52°E (Figure 2.1), and the resolution is 25×25 km, with 56 vertical eta-coordinate levels. A relaxation zone is implemented in the first four lateral grid points to avoid discontinuity between forcing data and the model. The simulation extends from 1st December 2000 to 1st January 2006. The first month is considered as spin-up and only the remaining 5 years are analyzed. Two WRF simulations are analysed: a control experiment (CTL) with lower boundary condition taken from advanced very high-resolution radiometer (Reynolds et al., 2007), and lateral boundary conditions from ERA-Interim reanalysis and a sensitivity experiment (SMTH) with smoothed SST boundary conditions but otherwise identical configuration. After the successful simulation of the annual and diurnal cycles of rainfall over South Africa by a regional climate model (*Pohl et al.* 2014), we use the following physical schemes: the WRF Single-Moment (WSM) 6-class for microphysics scheme (*Hong and Lim,* 2006), the Yonsei University parameterization for the Planetary Boundary Layer (PBL, *Hong et al.* 2006) and the Rapid Radiative Transfer Model (*Mlawer et al. 1997; Dudhia,* 1989) for long and shortwave radiative forcing. In addition, the 4-layer NOAH land surface model is active (*Chen and Dudhia,* 2001a; *Chen and Dudhia,* 2001b). *Kain-Fritch* scheme (KF, Kain, 2004) is used for cumulus convective parameterization. We evaluated the performance of three cumulus convective scheme: KF, *Betts-Miller-Janjic* (BMJ, Betts, 1986) and *Grell-Freitas* (GF, *Grell and Freitas,* 2013) with the same settings of other physical parameterizations with 45 x 45 km horizontal resolution. The KF scheme resolved the rain band produced above the Agulhas Current better, as well as the whole atmosphere compared to the BMJ and GF schemes. To construct our SMTH experiment, we smoothed the SST using a spatial filter based on a 9-neighbour grid method. The result at each grid point is a weighted average of the grid point plus the 8 surrounding points. The center point receives a weight of 1.0, the points at each side, above and below receive a weight of 0.5, and corner points receive a weight of 0.3. All 9 points are multiplied by their weights and summed, then divided by the total weight to obtain the smoothed value. Any missing data points

are not included in the sum; points beyond the grid boundary are considered to be missing. Thus the final result may be the result of an averaging with less than 9 points. The difference in SST between the CTL and SMTH experiments is seen in **Figure 2.1**. The WRF model is widely used in the community for the study of storms (*Kain et al.* 2006); low level airstream jets (*Storm et al.* 2009); snowfall (*Wang et al.* 2011); diurnal cycle of rainfall (*Rouault et al.* 2013; *Pohl et al.* 2014)... The validation of WRF is addressed in **Chapters 4** and **5**.

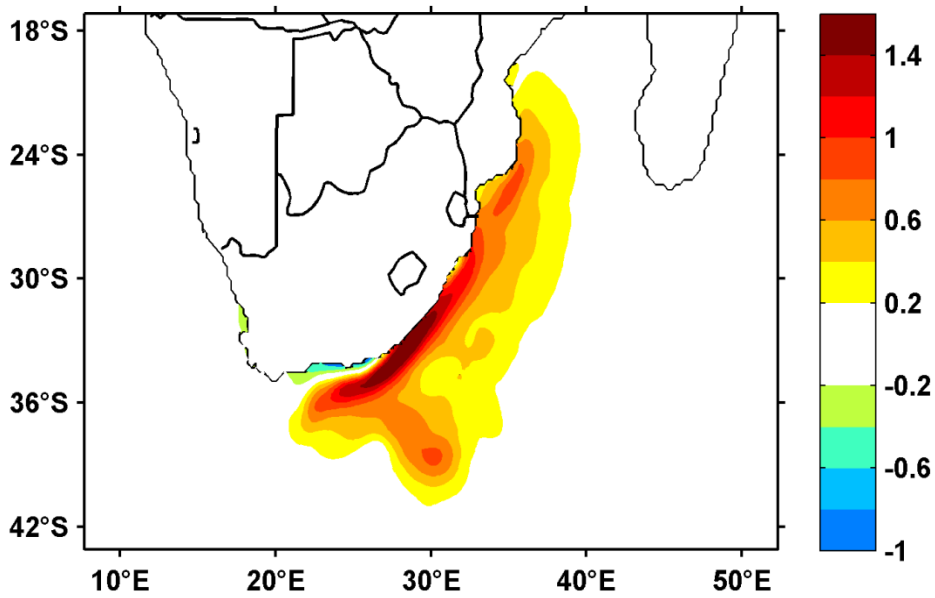

Figure 2.1: Annual climatology of the SST difference between WRF CTL and WRF SMTH. A maximum of ~1.5°C is seen in the core of the Agulhas Current.

2.2 METHODOLOGY

The averaging periods of our analysis are from 2003 to 2007 in **Chapter 3** and from 2001 to 2005 in **Chapter 4** and **5.** The data range from monthly to seasonal and are constrained by the availability of satellite data sets. Because products are not available over the same period, we use the same common period (5 years) for the averaging in order to have consistent results. The data we use in **Chapter 3** are the observations NOCS, the satellites data MODIS, GlobCurrent, SCOW, SEAFLUX, HOAPS3, and the reanalyses CFSR, MERRA-2, ERA-Interim, NCEP2 and ERA-40.

They all have a common period, except for NOCS, SCOW, HOAPS3 and ERA-40 (see **Table 2.1**). The data used in **Chapters 4** and **5** are the satellite data sets TRMM PR, OISST, GlobCurrent, SCOW, the reanalysis CFSR, and the numerical model WRF. We chose CFSR reanalysis because of its good representation of the ocean-atmosphere interaction in the Agulhas region (LHF, wind speed, SST), compared to other reanalyses.

2.2.1 Bourassa-Vincent-Wood algorithm

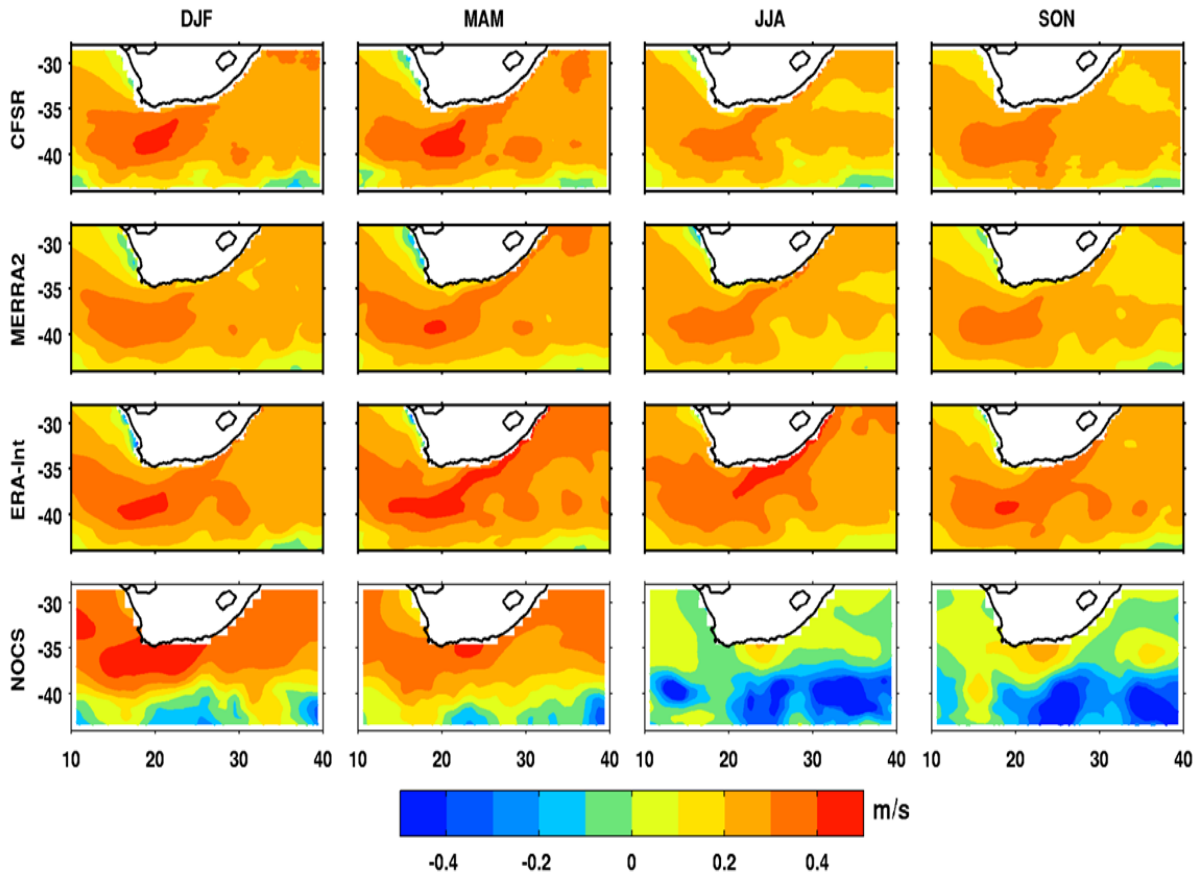

Figure 2.2: Mean seasonal differences of wind speed ($m.s^{-1}$) between Equivalent Neutral wind speed and real wind speed calculated using the BVW height adjustment code, for CFSR, MERRA-2, ERA-Interim and NOCS products: austral summer (DJF), autumn (MAM), winter (JJA) and spring (SON). Equivalent Neutral wind speed is between 0.1 and 0.5 $m.s^{-1}$ more than the recalculated real wind speed.

Geernaert and Katsaros (1986) defined the equivalent neutral wind speed as the mean wind speed observed in a neutral atmospheric stratification. In the case of stable atmospheric stratification the equivalent neutral wind is smaller than the real wind, and is larger in an unstable atmospheric stratification. Thus, near the ocean surface when the air is stable the wind speed is smaller and larger when the air is unstable.

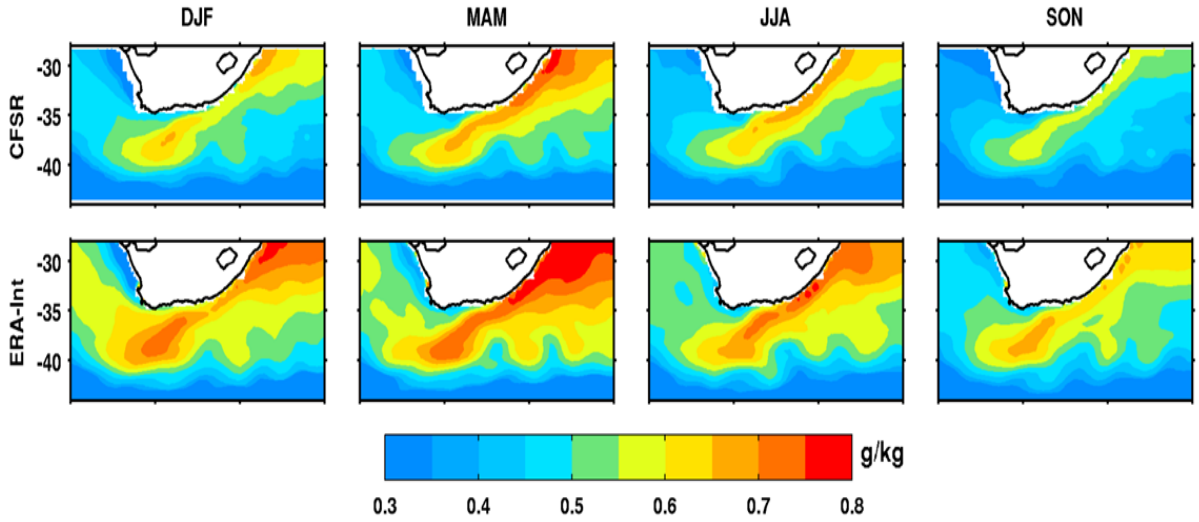

Figure 2.3: Mean seasonal differences of air specific humidity (Qa, $g.kg^{-1}$) between Qa at 2 m and Qa at 10 m calculated using the BVW height adjustment code for CFSR and ERA-Interim. Qa at 2 m is between 0.3 and 0.8 $g.kg^{-1}$ more than the recalculated Qa at 10 m.

The new generation reanalysis CFSR, MERRA-2, ERA-Interim and the observation NOCS use stability dependent winds. Therefore we re-calculate these winds to equivalent neutral winds at 10 m, using the Bourassa-Vincent-Wood neutral (BVWN) algorithm (*Bourassa et al.* 1999) for a better comparison with satellite remote sensing SCOW, SEAFLUX, and HOAPS3 wind speeds that are equivalent neutral at 10 m. Note that the real wind may reflect the unstable condition found above the Agulhas Current, leading to wind differences at 10 m between neutral and unstable conditions. The Bourassa-Vincent-Wood algorithm has an option of calculating both equivalent neutral winds and winds based on the air-sea stability. We calculate the seasonal difference between the equivalent neutral wind speed and the real wind speed for CFSR, MERRA-2, ERA-Interim and NOCS (**Fig. 2.2**). In the Agulhas system, the 10 m equivalent neutral wind speeds for CFSR, MERRA-2, and ERA-Interim are up to 0.5 $m.s^{-1}$ higher than the real wind speeds on

average, particularly in the Retroflection region during the austral summer (DJF) and autumn (MAM). Meanwhile, the 10 m equivalent neutral wind speed is 0.5 $m.s^{-1}$ lower for NOCS in the retroflection region, and the Agulhas Return Current in winter (JJA) and spring (SON) (**Fig. 2.2**).

Moreover, we compute the 2 m specific humidity of air to a height of 10 m using the BVW for height adjustment for the reanalyses CFSR and ERA-Interim, because satellite remote sensing estimates provide values at 10 m and CFSR and ERA-Interim at 2 m. We calculate the differences between the 2 m and the 10 m specific humidity for CFSR and ERA-Interim (**Fig. 2.3**). These differences exhibit a decrease of Qa when the height increases (from 2 to 10 m) for the whole domain, specifically along the coast up to 0.8 $g.kg^{-1}$. In the Southern Ocean and around the Benguela upwelling system, the differences range between 0.3 and 0.5 $g.kg^{-1}$.

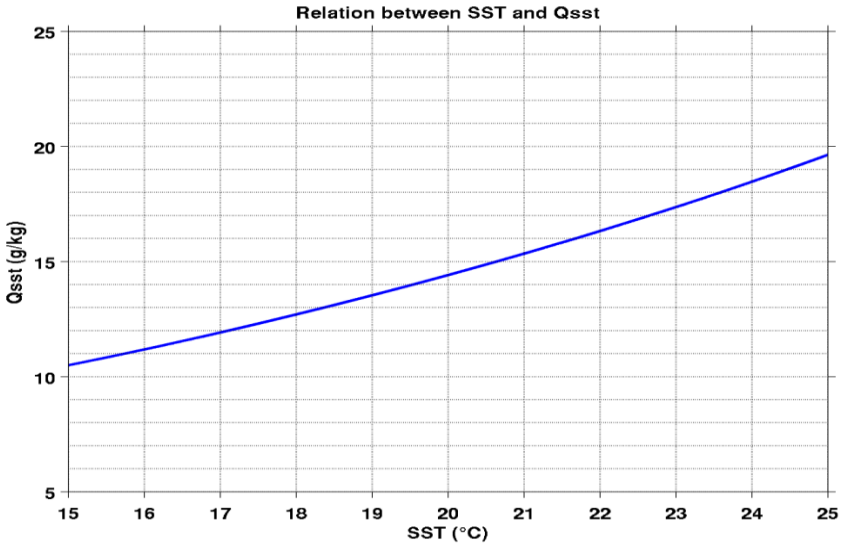

Figure 2.4: Relationship between SST and the sea surface specific humidity (Qsst).

In **Chapter 3**, we compare the specific humidity at the sea surface (Qsst) for numerous products. Qsst is not available for MODIS and ERA-Interim. Therefore, we calculate MODIS and ERA-Interim Qsst using the Clausius-Clapeyron relation and their respective SSTs. Qsst and SST are linked by the Clausius-Clapeyron relation. For example SSTs of 15, 20 and 25°C correspond to saturated specific humidities of around 10.5, 14.5 and 19.5 $g.kg^{-1}$ respectively (**Fig. 2.4**). Warmer SSTs lead to faster evaporation.

2.2.2 Bulk method

The bulk method is used to recalculate the turbulent latent heat flux (LHF) in **Chapter 3**, to evaluate the contribution of the wind speed or the difference in specific humidity. The Bulk formula is the product of the surface wind speed (relative to the sea surface) and the difference between specific humidity of the air and saturated specific humidity at the temperature of the sea surface:

$$Qe = \rho_a C_E l_v |U - U_S|(q_{sst} - q_a) \text{.....(Eq. 2.1)}$$

Here Q_e is the turbulent LHF; ρ_a is the air density; C_E is the transfer coefficient for water vapor; l_v is the latent heat of evaporation; U is the surface wind speed; U_s is the surface current; q_{sst} is the surface specific humidity, usually the saturated specific humidity at the temperature of the sea surface and q_a is the specific humidity of air at 10 m. Note that the reanalysis products do not account for wind speed relative to the surface current which might lead to incorrect estimation of the LHF in the Agulhas Current where the surface current can reach up to 2 m.s^{-1} (*Rouault et al.*, 2000, 2003). The satellite products, on the other hand, account for this effect as the wind speed is retrieved from estimating the sea roughness which is a direct effect of the relative wind speed (*Risien and Chelton*, 2008).

2.2.3 Pressure ajustment mechanism

The pressure adjustment mechanism (*Lindzen and Nigam*, 1987; *Back and Bretherton*, 2009) is a dynamical explanation for the wind response to SST, in which SST modifies the marine atmospheric boundary layer temperature. Therefore, the resultant pressure anomalies induce surface wind convergence over warm SSTs and wind divergence over cool SSTs. *Minobe et al.* (2008) showed the impact of the pressure adjustment mechanism, measured by a relation between surface wind convergence and sea level pressure (SLP) Laplacian in the Gulf Stream. They proposed that the pressure adjustment mechanism plays a role in producing the observed pattern of wind convergence/divergence in the Gulf Stream. A similar study is investigated in **Chapter 4**.

We use a simple Marine Atmospheric Boundary Layer model to investigate the relationship between the near surface wind convergence and SLP Laplacian (*Lindzen and Nigam*, 1987; *Minobe et al.* 2008):

$$\begin{cases} \varepsilon u - fv = -\frac{p_x}{\rho_0} \\ \varepsilon v + fu = -\frac{p_y}{\rho_0} \end{cases} \text{..... (Eq. 2.2)}$$

where x and y are the zonal and meridional coordinates; u and v are the zonal and meridional surface wind (frictional stresses from above the MABL are neglected); ρ_0 and p are the density and pressure in the MABL; ε denotes the constant damping coefficient; and f represents the Corioli's parameter. Surface wind convergence is linked to the SLP Laplacian by a linear relationship,

$$-\rho_0(u_x + v_y) = (p_{xx} + p_{yy})\frac{\varepsilon}{(\varepsilon^2 + f^2)} \text{..... (Eq. 2.3)}$$

SLP and underlying SST are also related (*Lindzen and Nigam,* 1987) according to

$$\varepsilon p + H(u_x + v_y) = -\gamma T \text{..... (Eq. 2.4)}$$

where T is the SST, ɣ is a constant, and H is the equivalent depth of the MABL. Thus a linear relationship between surface pressure and SST may indicate an impact of the ocean on the atmosphere. We compare the Laplacian relationship of these two quantities to isolate the strength of this relation at the finer scale of the warm core of the Agulhas Current. Recent studies have questioned the relevance of this diagnostic model, but it still serves for comparison with previous studies of northern hemisphere western boundary currents.

CHAPTER 3

3 THE ANNUAL CYCLE OF THE LATENT HEAT FLUX IN THE AGULHAS CURRENT SYSTEM

3.1 INTRODUCTION

A large amount of latent heat is released to the atmosphere from the Agulhas Current and its Retroflection region. This part of the ocean is considered to be one of the key regions for air-sea interactions in the mid-latitudes. Therefore, evaluating latent heat flux (LHF) products and understanding mechanisms of annual and seasonal variations in the LHF over the region are tremendous. The turbulent heat fluxes are underestimated in models if the resolution does not represent the SST field within the core of the current (*Rouault et al.* 2003). This makes the study of the impact of the Agulhas Current on weather and climate of South Africa difficult. Therefore, the aims of this study are threefold: (i) to explore whether the new climate reanalyses and satellite-derived data sets do adequately represent the high LHF or exchange of moisture above the Agulhas Current, (ii) to examine the magnitude of uncertainties in the basic variables (wind, SST, surface specific humidity) used to derive the LHF; and (iii) to quantify the annual cycle of the LHF and its drivers in the Agulhas Current. To do so, we represent the horizontal map of the seasonal cycles of various parameters, and the corresponding annual cycles. For the annual cycles, four key locations are selected to better quantify maximum and minimum as well as differences in data sets. We chose three regions (1° x 1°) within the Agulhas Current system: off Durban (31.5-32.5°E; 30-31°S) representing the eastern part of the Agulhas Current; off Port Elizabeth (25-26°E; 34.5-35.5°S), representing the middle of the Agulhas Current and the Retroflection area (19-20°E; 38-39°S) to the west of the Agulhas Current and one location off Cape Town (16-17°E; 33.5-34.5°S) for outlining differences between Agulhas Current and surrounding ocean. These locations are also used to help understand the drivers of the LHF in the Agulhas Current.

3.2 RESULTS

3.2.1 Seasonal mean and annual cycle of LHF

The seasonal LHF averages derived from the different products (presented in **Chapter 2**) are shown in **Figure 3.1** for the Austral summer (December to February -DJF); autumn (March to May -MAM); winter (June to August -JJA) and spring (September to November -SON).

In the Agulhas Current system, the LHF ranges from about 100 to 250 $W.m^{-2}$ with maxima during autumn and winter depending on the product. In comparison, the minimum LHF of about 50 $W.m^{-2}$ is found during summer in the Benguela upwelling region. Towards the colder Southern Ocean, the LHF is also low (around 50 $W.m^{-2}$) for all seasons. The large-scale patterns in the seasonal cycle of the LHF for the HOAPS3 and SEAFLUX satellite-based estimates, and the high-resolution CFSR and MERRA-2 reanalyses products are in fairly good agreement. As HOAPS3 has missing data along the coast it cannot represent the LHF in the Benguela upwelling region and along the Agulhas Current east of Port Elizabeth. The ERA-interim and ERA-40 products have similar seasonality but much lower LHF in autumn and winter than the SEAFLUX, HOAPS3, CFSR, and MERRA-2 products. NOCS is quite different with a distinct maximum of ~250 $W.m^{-2}$ in summer and a minimum in winter (between 125 and 175 $W.m^{-2}$) above the Agulhas Retroflection region. ERA-40 and NCEP2 do not adequately represent the LHF of the Agulhas Current system (compared to others reanalyses products) because they do not have enough resolution to represent the Agulhas Current SST as we will see below (see sections **3.2.3, 3.2.4**). Moreover, ERA-40 and NCEP2 do not reproduce the meandering shape of the Agulhas Return Current (**Fig. 3.1**).

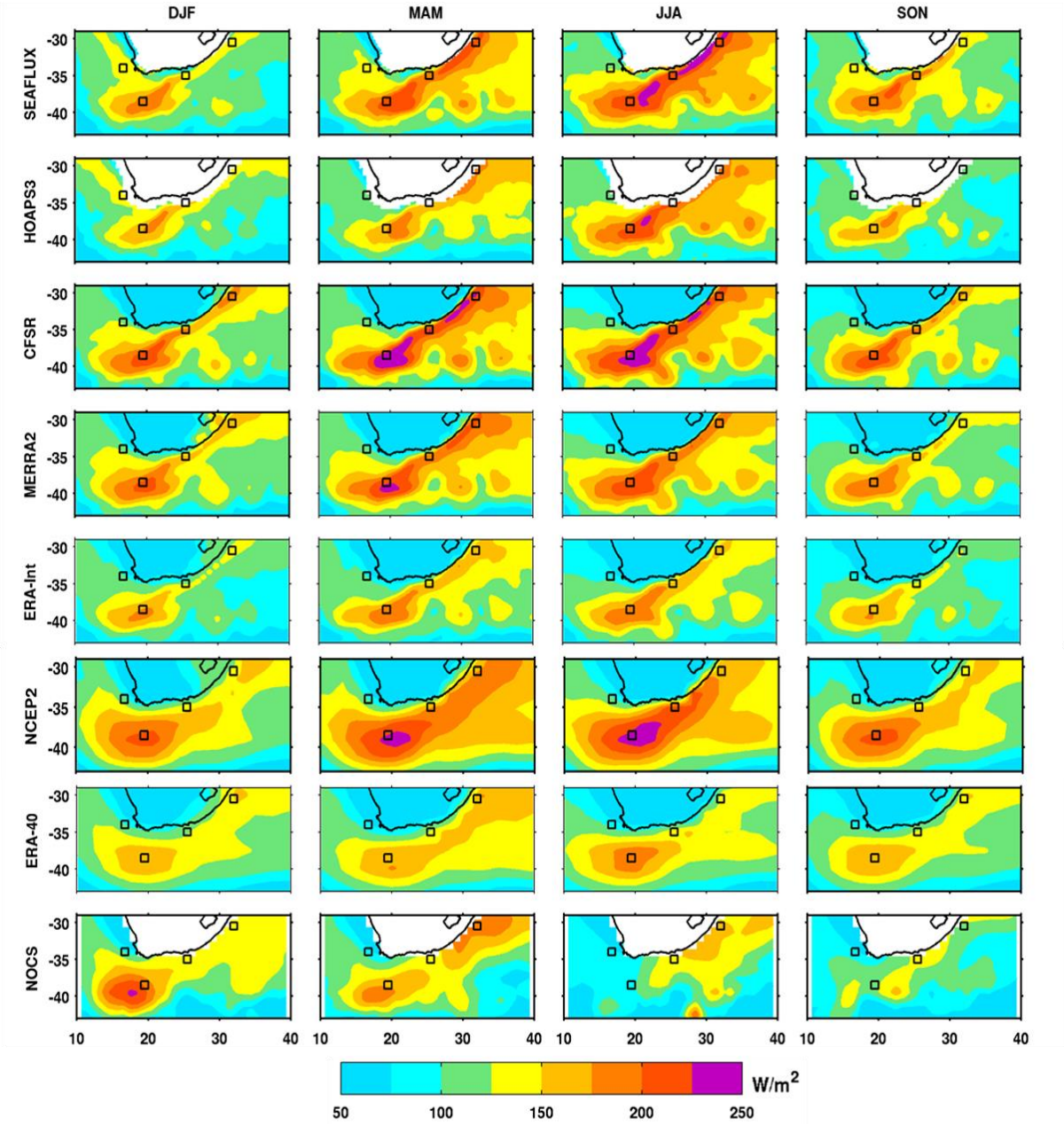

Figure 3.1: Seasonal averages of LHF ($W.m^{-2}$) for SEAFLUX, HOAPS3, CFSR, MERRA-2, ERA-Interim, NCEP2, ERA-40, and NOCS, in austral summer (DJF), autumn (MAM), winter (JJA) and spring (SON). Black squares represent the four locations taken for the study off Durban (31.5-32.5°E; 30-31°S), off Port Elizabeth (25-26°E ; 34.5-35.5°S), Agulhas Retroflection (19-20°E ; 38-39°S) and off Cape Town (16-17°E ; 33.5-34.5°S).

The annual cycles of all the LHF products, except HOAPS3, are shown in **Figure 3.2** for the four locations off Durban, off Port Elizabeth, in the Retroflection, and off Cape Town. HOAPS3 is omitted because of the missing data along the coast. There are differences between the LHF products both in time and space where their standard errors do not overlap. The standard deviation gives an idea of how the amplitude of a time series fluctuates. It is calculated using the MATLAB function std for the standard deviation. The annual LHF is between 40 and 260 $W.m^{-2}$ in the Agulhas system, and between 40 and 175 $W.m^{-2}$ off Cape Town. Off Durban, the SEAFLUX maximum is 230 $W.m^{-2}$ in May; the minimum is nearly 130 $W.m^{-2}$ in January. For the other products, the highest LHF values occur between March and June and the lowest values between November and February. SEAFLUX, CFSR, and MERRA-2 overlap except in May-June. ERA-Interim, NCEP2, ERA-40, and NOCS overlap except in May-June and August where ERA-40 is smaller. All in all, the CFSR has the highest mean annual value (192 $W.m^{-2}$) and ERA-Interim the lowest (141 $W.m^{-2}$) (**Table 3.1**). Off Port Elizabeth the annual cycles are similar (**Fig. 3.2**). In this region, the SEAFLUX product has a maximum in August and a minimum in January. The other products have their maximum values between May and August and minima between September and February. SEAFLUX, CFSR, MERRA-2, and NCEP2 overlap for each month. From April to August ERA-Interim, ERA-40, and NOCS do not overlap with the former products. Lowest values in the Agulhas Current system are found off Port Elizabeth in late summer (~100 $W.m^{-2}$). In the Retroflection, the highest value is found in July for all products except for NOCS which has the lowest value (~80 $W.m^{-2}$) during winter but the highest (210 $W.m^{-2}$) in February. SEAFLUX, CFSR, MERRA-2, ERA-Interim and NCEP2 overlap. NOCS does not overlap with the others for most of the year and its standard error is quite large compared to other products. All in all, CFSR has the highest LHF (217 $W.m^{-2}$) and NOCS the lowest (141 $W.m^{-2}$) (**Table 3.1**).

Averaging the three Agulhas locations CFSR has the highest LHF; ERA-interim, ERA-40, and NOCS have the lowest LHF. Off Cape Town, SEAFLUX is higher than any other product (**Fig. 3.2** and **Table 3.1**). For the whole year, all the products overlap together except for SEAFLUX that overlaps with CFSR and NCEP2 between May and September. To summarize, we find that the LHF exhibit roughly similar space and time patterns as found globally by *Chou et al.* (2004); *Smith et al.* (2011); *Bentamy et al.* (2017) but with differences in magnitude and phasing of maxima and minima.

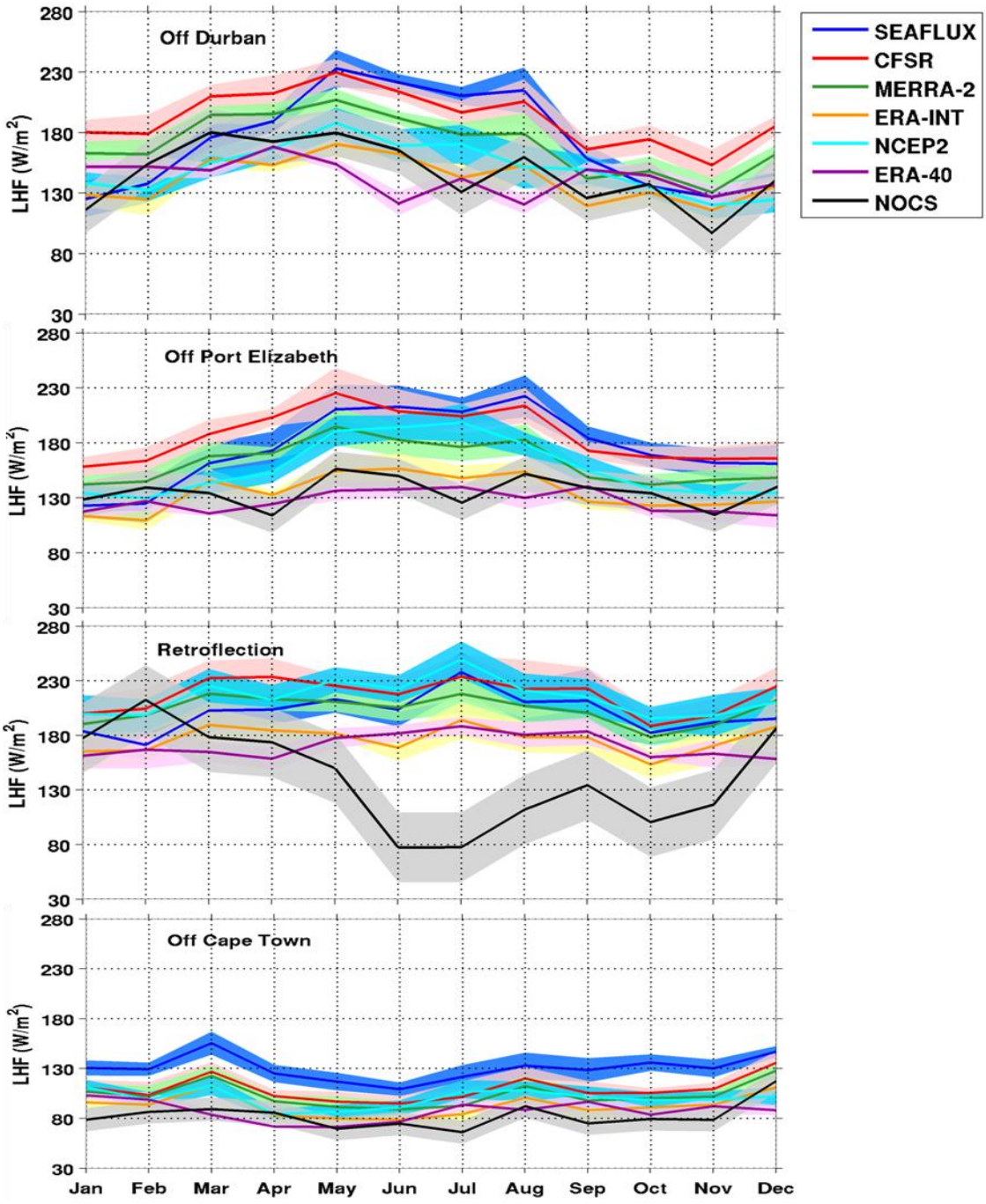

Figure 3.2: Annual cycles of LHF ($W.m^{-2}$). In Agulhas Current off Durban, off Port Elizabeth, Agulhas Retroflection and off Cape Town for SEAFLUX (blue), CFSR (red), MERRA-2 (green), ERA-Interim (yellow), NCEP2 (cyan), ERA-40 (purple) and NOCS (black). Shades areas represent the standard errors calculated as the standard deviation divided by the square root of the number of years.

ZONES	SEAFLUX	CFSR	MERRA-2	ERA-INTERIM	NCEP2	ERA-40	NOCS
Off Durban	172.1	192.0	171.1	141.2	150.0	143.0	146.6
Off Port Elizabeth	175.9	186.2	162.1	134.4	156.9	126.5	135.6
Retroflection	200.5	216.9	203.4	176.5	214.8	170.3	141.4
Mean Agulhas	182.8	198.4	178.9	150.7	173.9	146.6	141.2
Off Cape Town	130.1	109.4	103.5	92.1	100.0	87.3	82.8

Table 3.1: Annual means LHF ($W.m^{-2}$) off Durban, off Port Elizabeth, Retroflection region, the average of the three Agulhas points, and off Cape Town for seven considered data sets.

3.2.2 Differences of LHF between SEAFLUX and other products

The mean seasonal differences in LHF between the observations, the reanalyses, and the satellite-based SEAFLUX are shown in **Figure 3.3**. The LHF products have been re-gridded on the grid of SEAFLUX. The differences range within ±70 $W.m^{-2}$, roughly ±38% of the annual mean value of SEAFLUX LHF for the three Agulhas locations (**Table 3.1**). Differences can be positive or negative and sometimes have the shape of the Agulhas Current which indicates the problem of low-resolution SST. HOAPS3 is around 30 $W.m^{-2}$ lower than SEAFLUX in the Agulhas Return Current for each season. The positive differences between CFSR and SEAFLUX (CFSR - SEAFLUX) are mostly seen in the Agulhas Current system and reach up to 60 $W.m^{-2}$ during summer (DJF). All reanalyses and NOCS underestimate the LHF in the Benguela system by about 70 $W.m^{-2}$. In the Agulhas Current system along the coast during summer, differences between MERRA-2 and SEAFLUX are less than with CFSR. NCEP2 and ERA-40 underestimate the LHF along the coast for all seasons, especially during winter with a difference of 60 $W.m^{-2}$. This is due to the low-resolution of their SST field as further addressed in the next section.

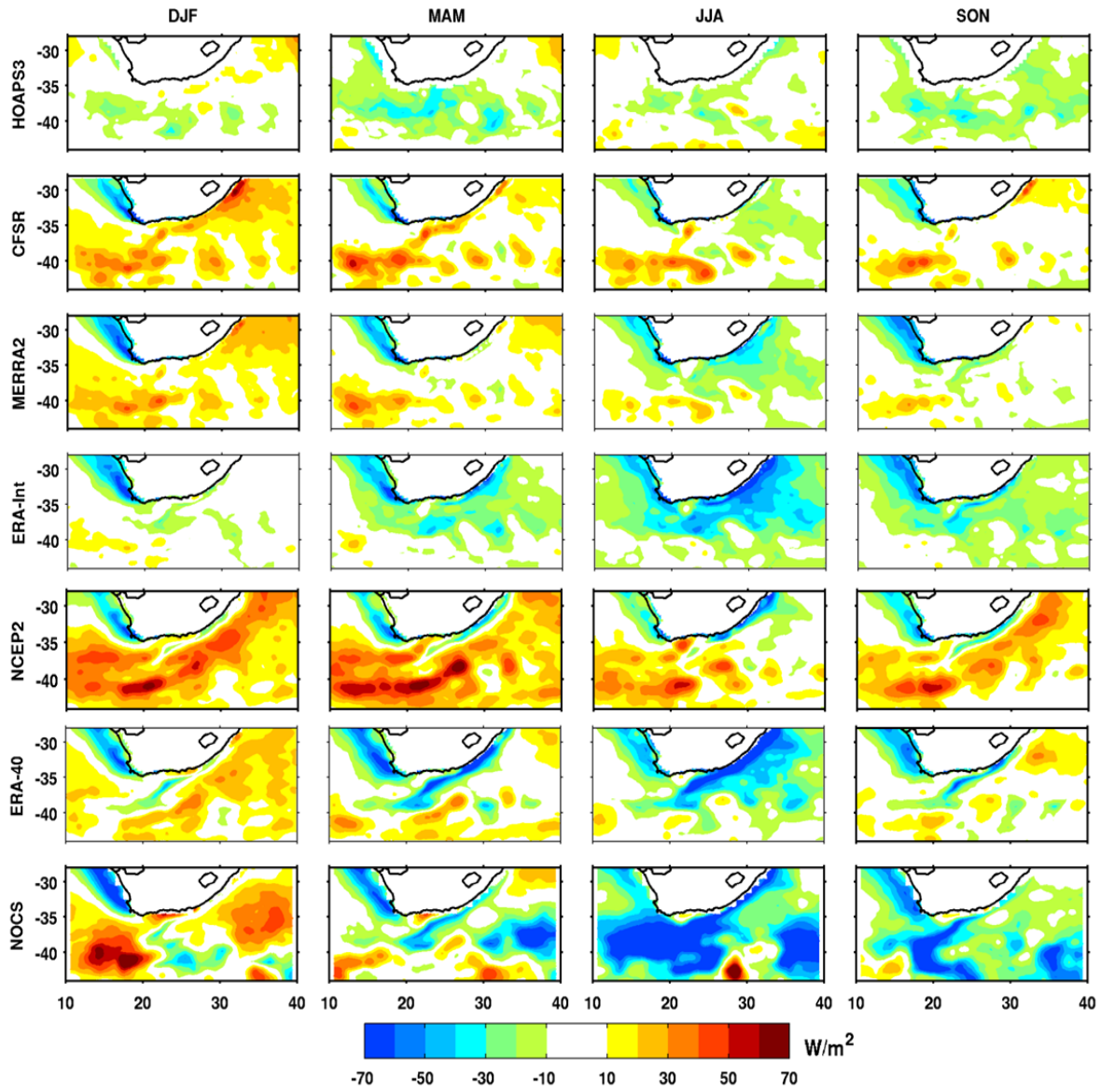

Figure 3.3: Mean seasonal differences of LHF ($W.m^{-2}$) between the observation-based, the reanalysis products, and SEAFLUX product, for the summer (DJF), autumn (MAM), winter (JJA) and spring (SON). The products have been interpolated on the grid of SEAFLUX (0.25° x 0.25°).

In summer, NOCS LHF is almost similar to SEAFLUX from off Durban to off Port Elizabeth. During winter, the difference between NOCS and SEAFLUX is less than $70W.m^{-2}$. This could indicate that too few Voluntary Observing vessels are taking measurements in the Agulhas Current system. Indeed vessels have a tendency to leave the Agulhas Current at the location off Port

Elizabeth cruising close to the shore towards Cape Town or they avoid the southwest flowing Agulhas Current as much as possible when sailing eastwards towards Durban (*Rouault et al.* 2009).

In the coming sections the individual contributions of SST, wind speed and specific humidity to the LHF are examined in order to understand the origin of the LHF differences between products.

3.2.3 Seasonal mean and annual cycle of SST

The seasonal SST averages derived from the different products (presented in **Chapter 2**) are given in **Figure 3.4** for austral summer, autumn, winter, and spring. With its high-resolution (4 x 4 km) MODIS SST is taken as the reference for the comparison of SST. The MODIS SST fields align well with the Agulhas Current velocity structure (**Fig. 1.4**). In the Agulhas Current system (**Fig. 3.4**), the SST magnitude ranges from about 18 to 26°C with the maximum during summer (DJF) and autumn (MAM) and minimum SST in the Retroflection region in winter (JJA). The large-scale patterns of SST for MODIS, SEAFLUX, and HOAPS3 are similar, but HOAPS3 has missing data along the coast (**Fig. 3.4**). CFSR and MERRA-2 have the same horizontal distribution as MODIS. ERA-Interim underestimates the SST in the Agulhas Current. NCEP2 and ERA-40 are around 4°C less than MODIS along the coast. The low-resolution of these reanalyses is clearly apparent as they are not able to adequately resolve the Agulhas Current SST. Moreover, there is a poor representation of the meanders of the Agulhas Return Current in SST for NCEP2 and ERA-40. NOCS also underestimates the SST in the core of the Agulhas Current.

The annual cycles of all SST products except HOAPS3 (with quite small standard errors) are shown in **Figure 3.5** for the four locations of this study. The annual variations of SST are in good agreement with MODIS SST with maxima in late summer and minima in late winter. Off Durban, MODIS SST ranges between 18 and 28°C. SEAFLUX, CFSR, MERRA-2, ERA-Interim, and NOCS are similar to MODIS. NCEP2 and ERA-40 range between 17 and 24°C and they do not overlap with other products. From the annual mean, NCEP2 and ERA-40 are respectively 2 and 4°C lower than MODIS (**Table 3.2**).

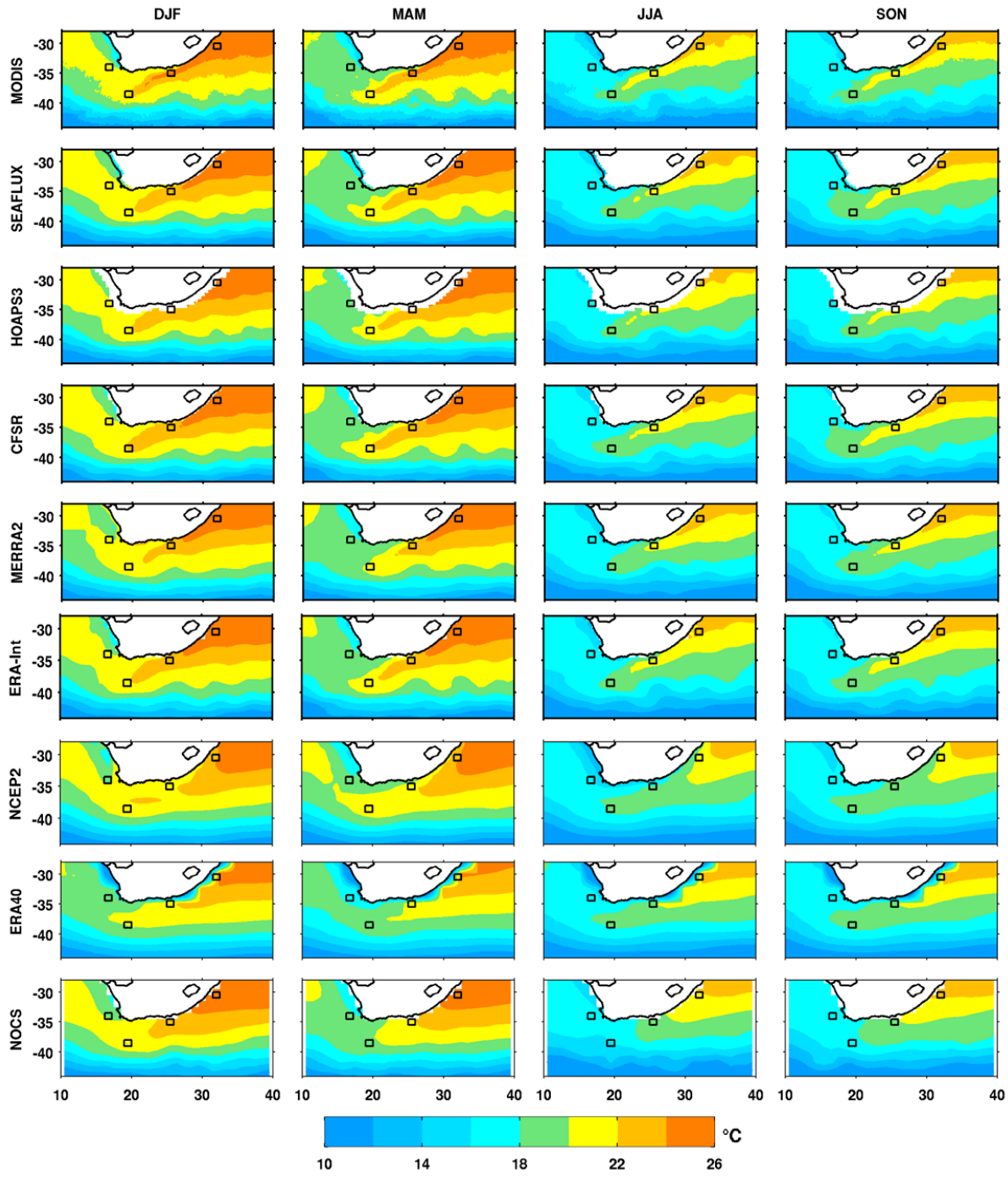

Figure 3.4: Seasonal averages of SST (°C) of MODIS, SEAFLUX, HOAPS3, CFSR, MERRA-2, ERA-Interim, NCEP2, ERA-40, and NOCS. Black squares represent the four locations taken for the study. MODIS SST is the reference for SST. The products have been interpolated on the grid of MODIS (4 km x 4 km).

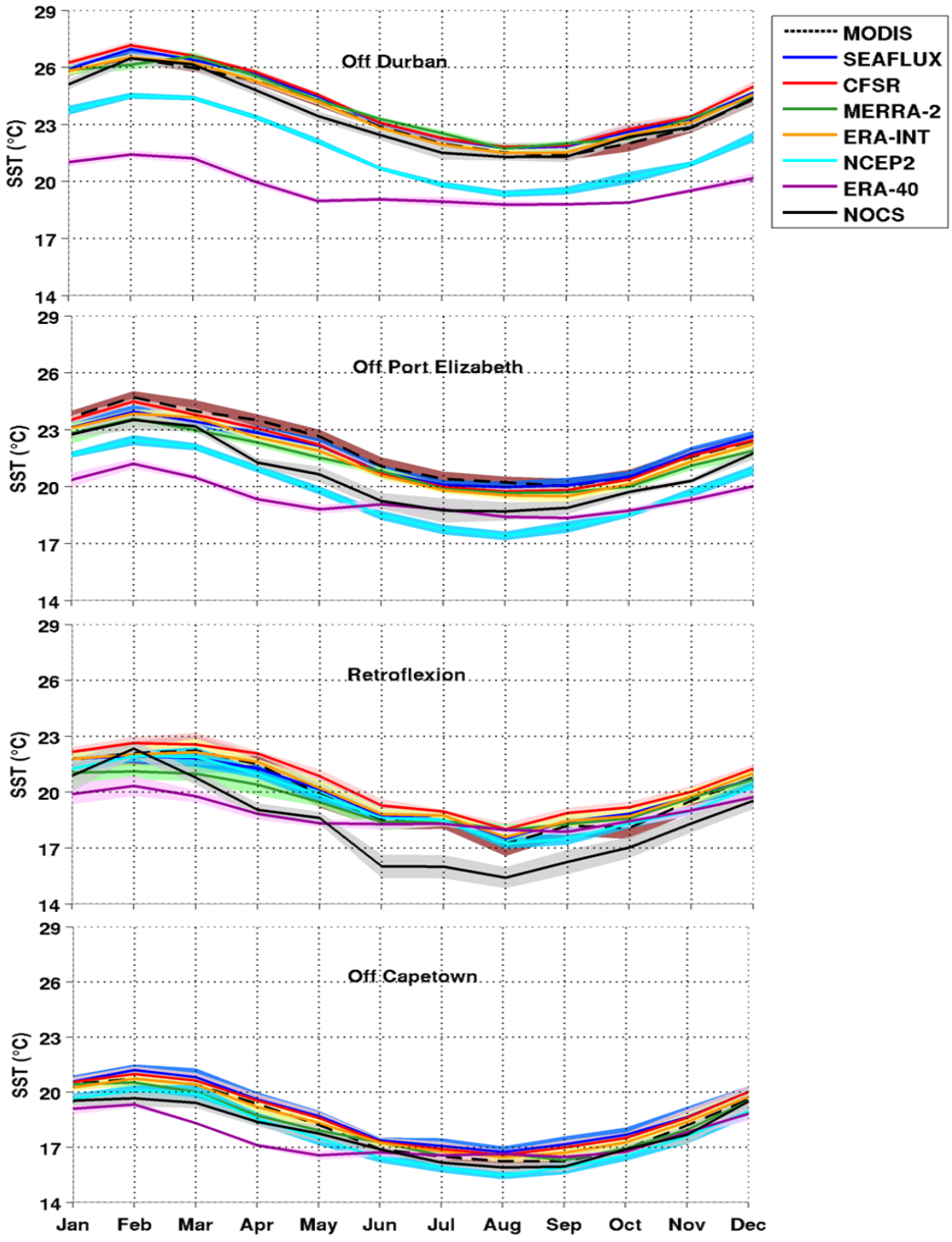

Figure 3.5: Annual cycles of SST (°C) off Durban, off Port Elizabeth, Retroflection region and off Cape Town for MODIS (black dash), SEAFLUX (blue), CFSR (red), MERRA-2 (green), ERA-Interim (yellow), NCEP2 (cyan), ERA-40 (purple) and NOCS (black). Shade areas represent the standard errors.

Off Port Elizabeth, MODIS SST varies between 20 and 25°C. In this region, SEAFLUX, CFSR, MERRA-2, and ERA-Interim overlap with MODIS. NCEP2, ERA-40, and NOCS underestimate the SST. The annual mean MODIS SST is 22.1°C (**Table 3.2**). NCEP2 and ERA-40 are respectively 2.3 and 2.7°C colder than MODIS. In the Retroflection region, MODIS SST is between 16 and 23°C (**Fig. 3.5**). NOCS SST is underestimated and does not overlap with other products for most months. This could explain the lowest value of NOCS LHF in this region. Other products do overlap except ERA-40. All in all, the mean annual value of MODIS is 19.9°C, and NOCS is the coolest (18.4°C). Off Cape Town, the SST is between 15 and 22°C. All SSTs overlap except ERA-40 with a smaller amplitude between February and May. The mean MODIS SST is 18.3°C (**Table 3.2**); ERA-40 is 17.5°C (the coolest).

ZONES	MODIS	SEA FLUX	CFSR	MERRA-2	ERA-INTERIM	NCEP2	ERA-40	NOCS
Off Durban	23.7	24.1	24.2	24.0	23.8	21.7	19.7	23.5
Off Port Elizabeth	22.1	21.8	21.8	21.4	21.5	19.8	19.4	20.7
Retroflection	19.9	20.0	20.5	19.5	20.1	19.6	19.4	18.4
Mean Agulhas	21.9	22.0	22.2	21.6	21.8	20.4	19.5	20.9
Off Cape Town	18.3	18.8	18.7	18.2	18.5	17.7	17.5	17.8

Table 3.2: Annual means SST (°C) off Durban, off Port Elizabeth, Retroflection region, the average of the three Agulhas points, and off Cape Town. The products are averaged using the resampled data on the grid of MODIS (4 x 4 km).

The mean seasonal differences between observations, reanalyses SST and the satellite product MODIS SST are shown in **Figure 3.6**. The SSTs have been re-gridded on the grid of MODIS. The differences range within ±3°C, roughly ±14% of the annual mean MODIS SST in the Agulhas Current system. The spatial discrepancies between the different SST products and the MODIS SST field display the structure of the Agulhas Current that is better resolved in the high-resolution MODIS SST. NCEP2, ERA-40, and NOCS have the lowest SST in the Agulhas Current system.

This will increase errors for the calculation of Qsst. This could partially explain the lowest values of the LHF in this region for the respective products. Differences in SST may also be due to the differences between skin and bulk SST as suggested by *Chan and Gao* (2005).

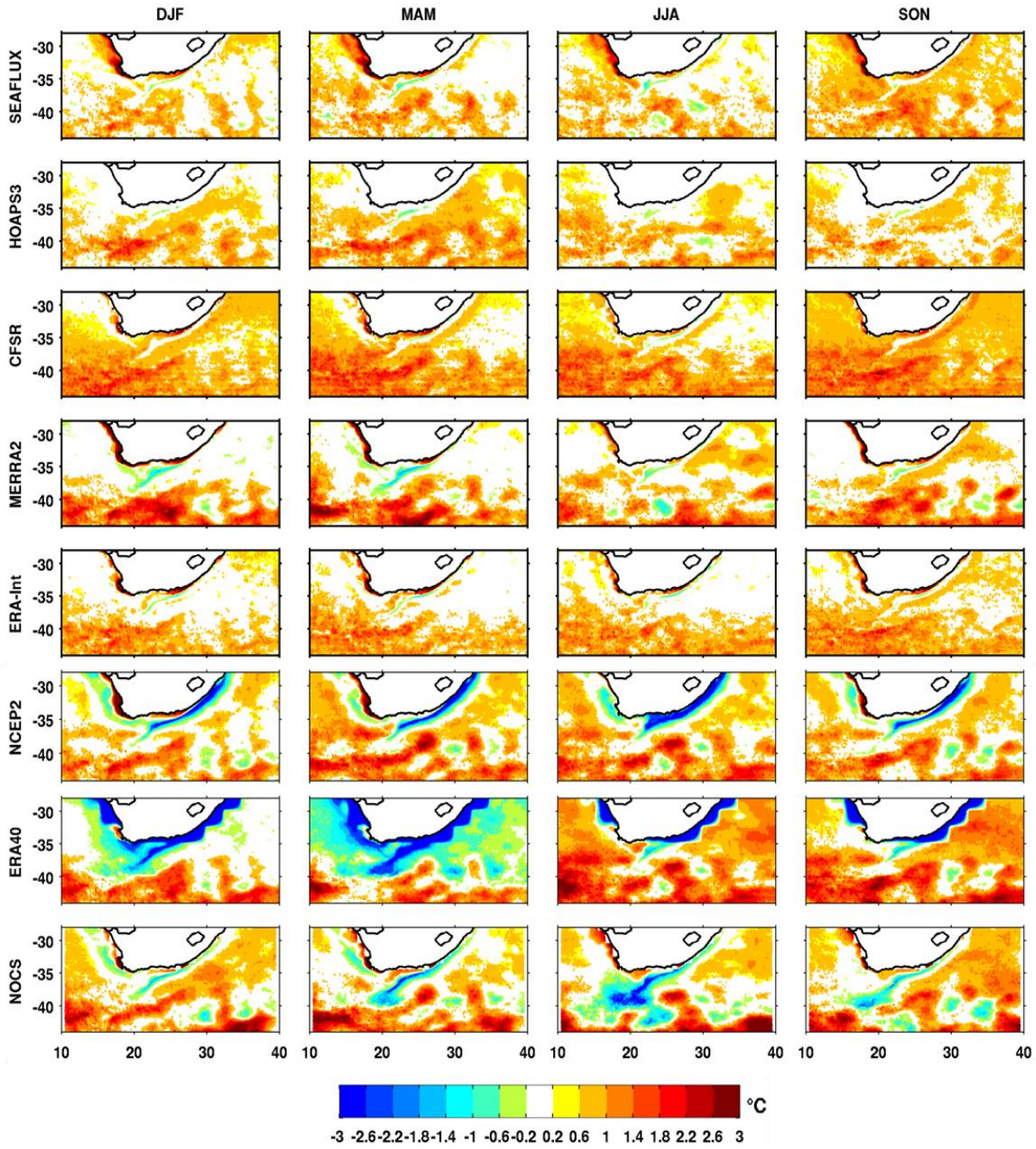

Figure 3.6: Mean seasonal differences of SST (°C) between the observation-based, the reanalysis products, and the satellite product MODIS, for the summer (DJF), autumn (MAM), winter (JJA) and spring (SON).

3.2.4 Seasonal mean and annual cycle of surface wind speed

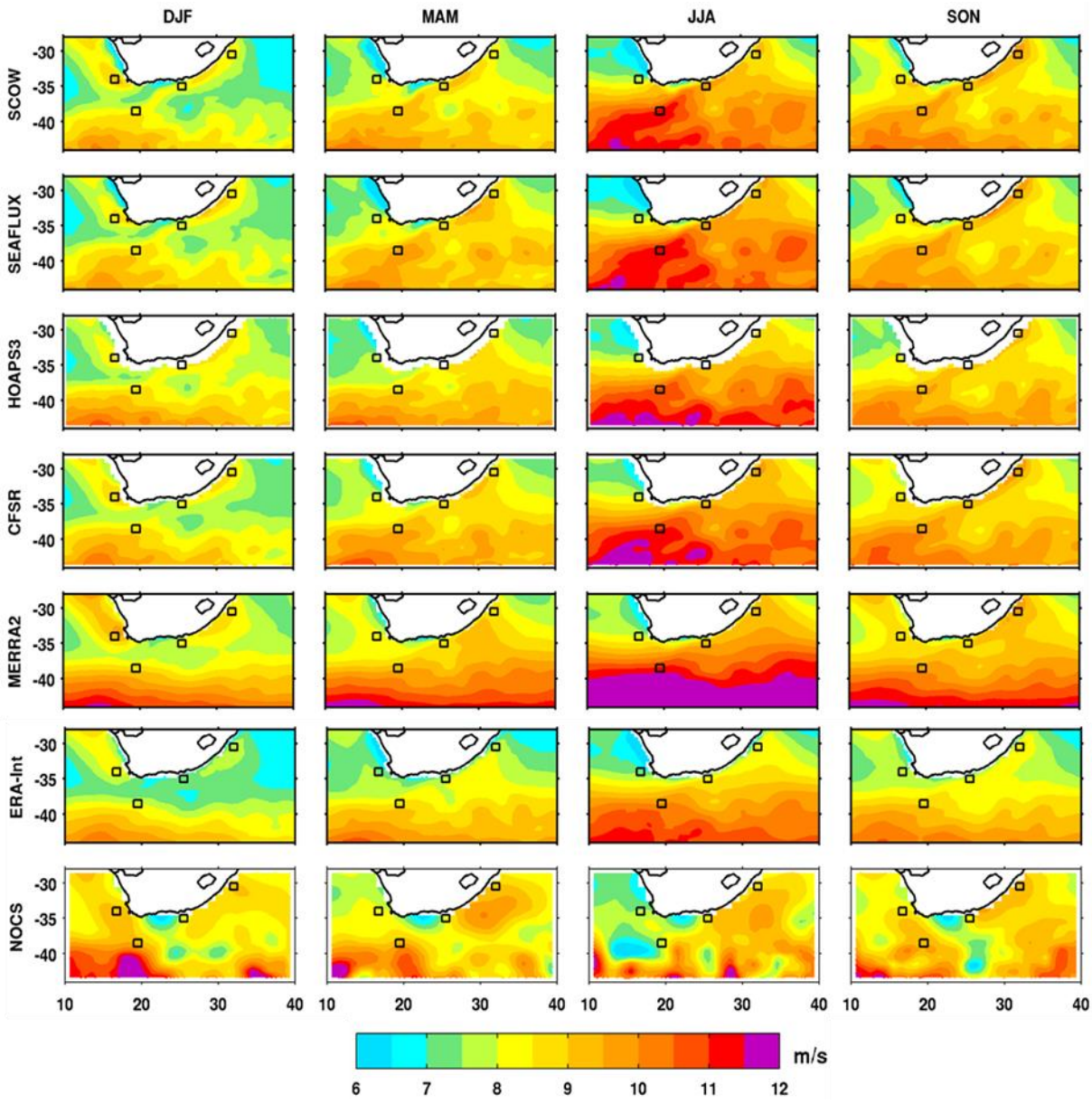

Figure 3.7: Seasonal averages of surface wind speed ($m.s^{-1}$) of SCOW, SEAFLUX, HOAPS3, CFSR, MERRA-2, ERA-Interim, and NOCS. Black squares represent the four locations taken for the study. SCOW wind is the reference for the wind speed. Products have been interpolated on the grid of SCOW (0.25° x 0.25°).

The seasonal surface wind speed averages from the different products presented in **Chapter 2** are shown in **Figure 3.7** for the austral summer, autumn, winter, and spring. NCEP2 and ERA-40 are

not included in the remaining study since their low spatial resolution leads to large errors in SST and therefore LHF in the Agulhas Current system. The satellite-based SCOW is used as the reference for surface wind speed. SCOW wind speed is clearly stronger above the Agulhas Current than in the surrounding water by about 2 $m.s^{-1}$ due to the impact of the unstable stratification in the atmospheric boundary layer, leading to an increase of the near-surface wind speed across the warm SST front (*Chelton et al.* 2004). The wind speed of CFSR, MERRA-2, ERA-Interim, and NOCS are re-calculated to equivalent neutral wind using the BVWN algorithm (*Bourassa et al. 1999*), for the convenience of comparing results.

In the Agulhas Current region, the maximum wind speed for all products is found in the Retroflection region in winter (JJA). We recall that in winter, the LHF reaches its maximum there of around 250 $W.m^{-2}$ (**Fig. 3.1**). In comparison, the minimum wind speed is encountered in the Agulhas Current in summer, corresponding to the minimum LHF there. The large-scale patterns in the seasonal cycle of the wind speed for SEAFLUX, HOAPS3, CFSR and SCOW are in fairly good agreement (**Fig. 3.7**). MERRA-2, ERA-Interim, and NOCS misrepresent the meanders of the Agulhas Return Current for each season. In autumn (MAM) and winter (JJA), MERRA-2 overestimates the wind speed in the Southern Ocean compared to SCOW. ERA-Interim wind speed is weaker than all other products. In the Agulhas Current, the NOCS maximum is found in autumn. In winter, NOCS wind speed appears quite weak compared to other products. This is the likely explanation for the low values of the LHF for ERA-Interim and NOCS (~200 and 150 $W.m^{-2}$ respectively) in the Agulhas Current system.

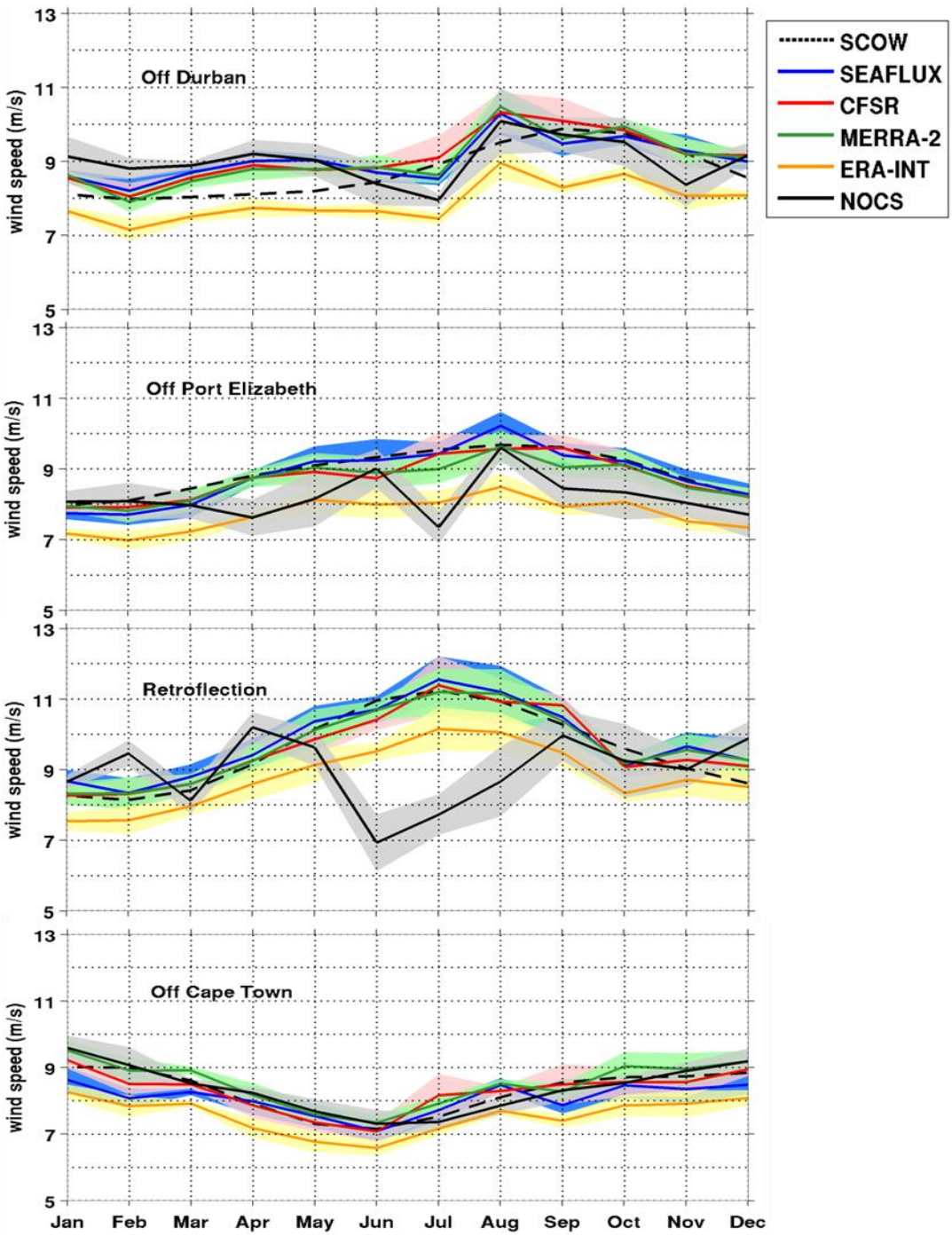

Figure 3.8: Annual cycles of the surface wind speed ($m.s^{-1}$) off Durban, off Port Elizabeth, Retroflection region and off Cape Town for SCOW (black dash), SEAFLUX (blue), CFSR (red), MERRA-2 (green), ERA-Interim (yellow), and NOCS (black). Shade areas represent the standard errors.

The annual cycles of the near-surface wind speed are represented in **Figure 3.8**. The wind speed ranges from 6 to 12 $m.s^{-1}$. Off Durban, the wind starts to increase in July with a maximum in August. All the products are in phase, and their amplitudes overlap except for ERA-Interim that is the weakest. Off Port Elizabeth, the wind has larger seasonal variations compared to Durban, increasing from March until August. This explains why the annual variations of the LHF are more pronounced off Port Elizabeth than off Durban. SEAFLUX is 0.1 $m.s^{-1}$ lower than SCOW (**Table 3.3**). The other products are between 0.2 (MERRA-2, CFSR) and 1.2 $m.s^{-1}$ (ERA-Interim) lower than SCOW.

ZONES	SCOW	SEAFLUX	CFSR	MERRA-2	ERA-INTERIM	NOCS
Off Durban	8.7	9.0	9.1	9.0	7.9	9.0
Off Port Elizabeth	8.9	8.8	8.7	8.7	7.7	8.2
Retroflection	9.6	9.8	9.6	9.7	8.8	8.9
Mean Agulhas	9.1	9.2	9.1	9.1	8.1	8.7
Off Cape Town	8.3	8.1	8.3	8.5	7.6	8.4

Table 3.3: Annual means of surface wind speed ($m.s^{-1}$) off Durban, off Port Elizabeth, Retroflection region, the average of the three Agulhas points, and off Cape Town.

The highest values of the annual cycle of the wind speed are encountered in the Retroflection region (**Figs. 3.7, 3.8**, and **Table 3.3**). All the products overlap except NOCS between May and August. NOCS has some maxima and minima that drive the maxima and minima of the NOCS LHF in February, June, and September (**Fig. 3.2**). The annual mean wind speeds (**Table 3.3**) in the Agulhas Current show that SEAFLUX is 0.2 $m.s^{-1}$ higher than SCOW; while the other products are between 0.1 (MERRA-2) and 0.8 $m.s^{-1}$ (ERA-Interim) lower than SCOW. CFSR is equal to SCOW. Off Cape Town all the products overlap with SCOW. ERA-Interim has the weakest wind

speed, this could explain its lowest LHF in this region (**Fig. 3.3**, **Table 3.1**). To summarize, for the mean Agulhas region, SEAFLUX is 0.1 $m.s^{-1}$ higher than SCOW, CFSR, and MERRA-2 are similar to SCOW, ERA-Interim, and NOCS are respectively 1.0 and 0.4 $m.s^{-1}$ weaker than SCOW.

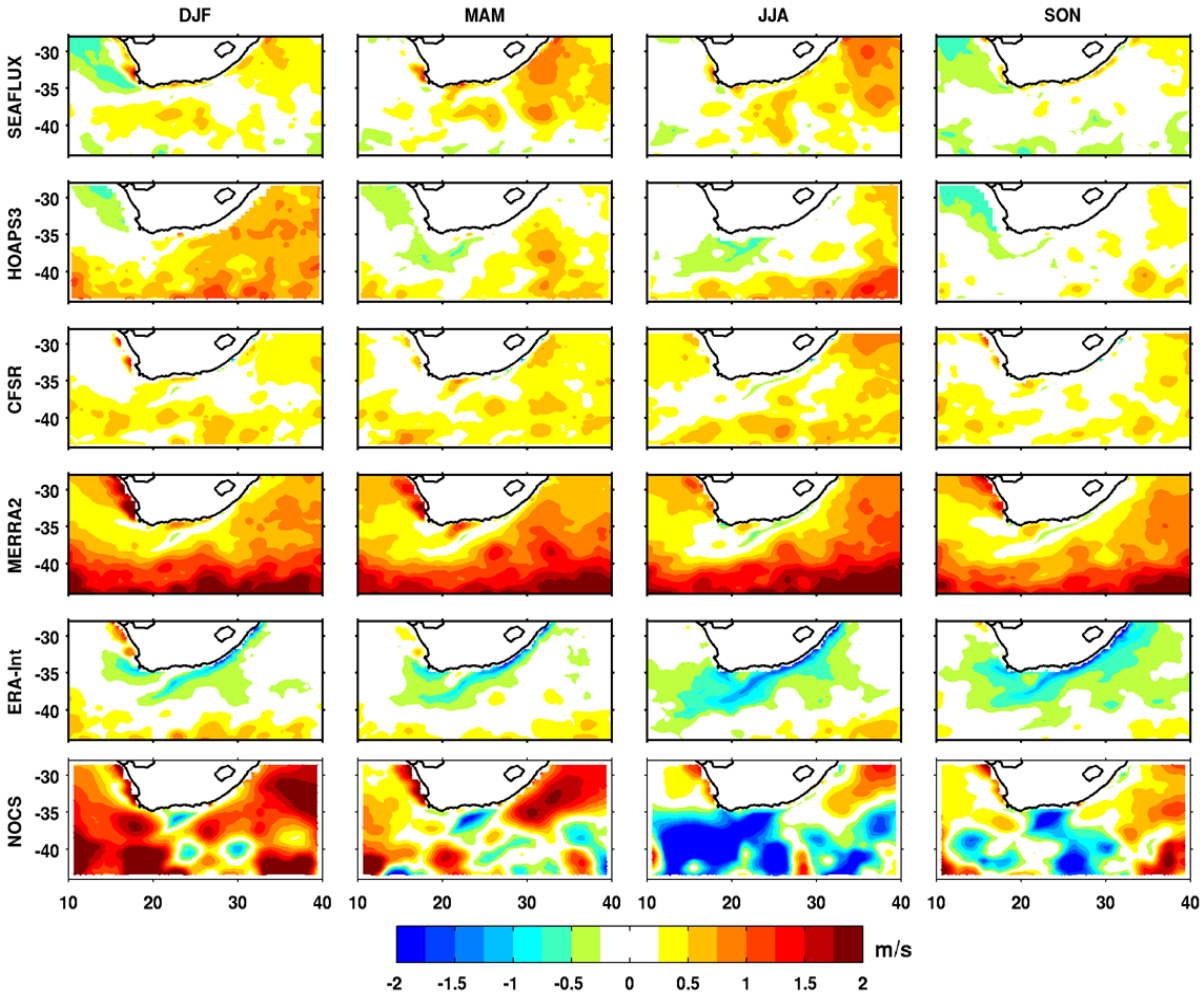

Figure 3.9: Mean seasonal differences of the surface wind speed ($m.s^{-1}$) between the observation-based, the reanalysis products, and the satellite product SCOW wind speed, for the summer (DJF), autumn (MAM), winter (JJA) and spring (SON).

The mean seasonal differences between the different observations and wind speed reanalysis products and the satellite SCOW product are represented in **Figure 3.9**. The differences range within ±2 $m.s^{-1}$, around ±22% of the mean SCOW wind speed in the Agulhas system. In the Agulhas Current region, HOAPS3, CFSR, and MERRA-2 underestimate the wind speed by 0.5

m.s^{-1}, compared to SCOW. Meanwhile, ERA-Interim underestimates the wind speed by 2 m.s^{-1} particularly in the Agulhas Current system (**Figs. 3.8**, **3.9** and **Table 3.3**).

3.2.5 Seasonal mean and annual cycle of specific humidity

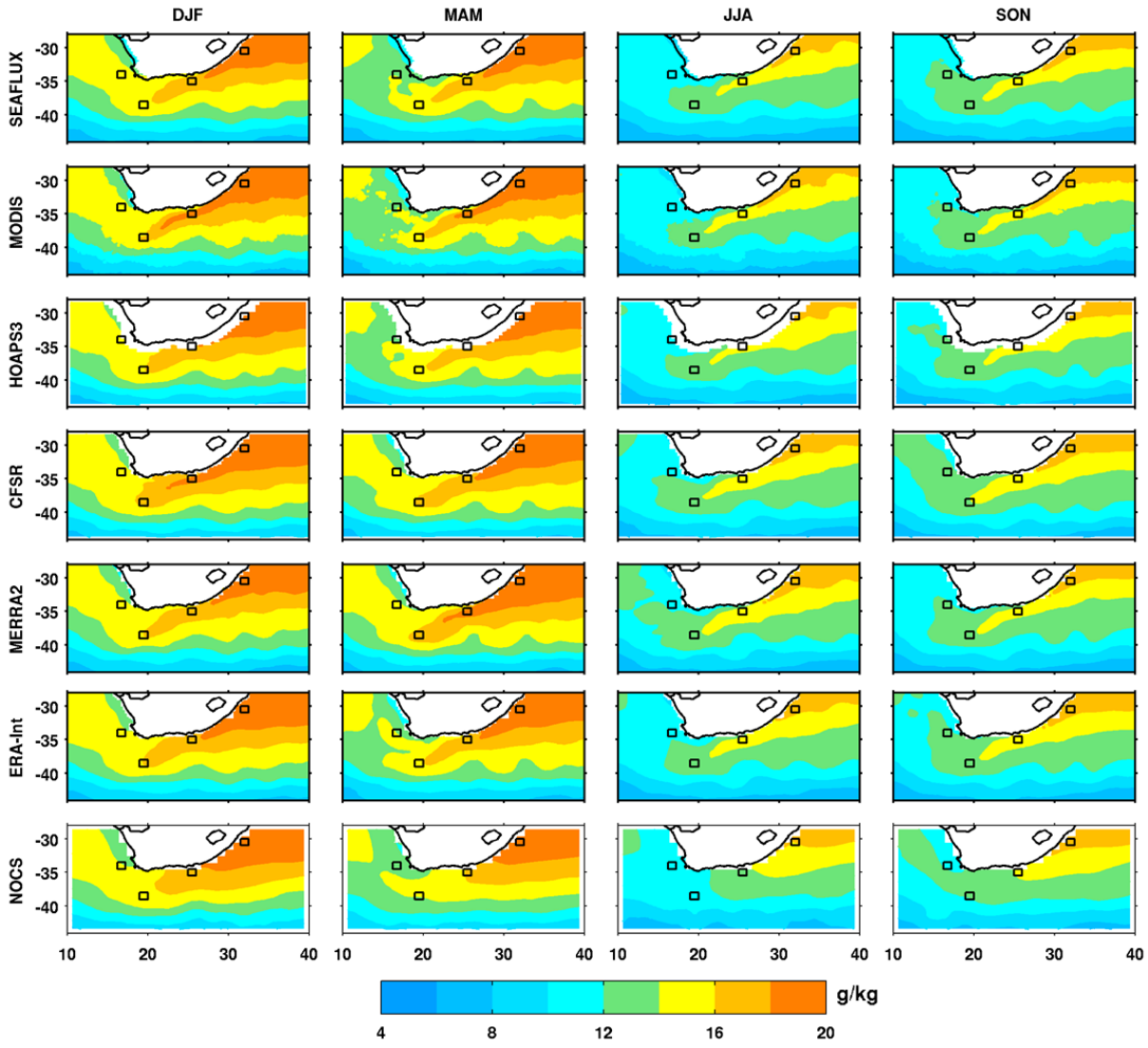

Figure 3.10: Seasonal averages of the surface specific humidity (Qsst, g.kg^{-1}) for MODIS, SEAFLUX, HOAPS3, CFSR, MERRA-2, ERA-Interim, and NOCS. Black squares represent the four locations taken for the study.

The averages surface specific humidity (Qsst) derived from the different products (presented in **Chapter 2**) are shown in **Figure 3.10**. ERA-Interim Qsst is computed using the SST and the surface pressure of ERA-Interim, and the Clausius-Clapeyron relation. MODIS Qsst is computed using MODIS SST, the surface pressure of ERA-Interim and the Clausius-Clapeyron relation. In the Agulhas Current region, the maximum SEAFLUX Qsst ranges from around 16 to 20 $g.kg^{-1}$ in summer (DJF) and autumn (MAM) and the minimum is between 14 and 18 $g.kg^{-1}$ in winter (JJA) and spring (SON) (**Fig. 3.10**). As for the SST field, Qsst decreases poleward and westward following the pathway of the Agulhas Current. The Qsst minimum (~ 4 $g.kg^{-1}$) is observed in the Southern Ocean for all seasons. The large scale-patterns in the seasonal cycle of the Qsst for MODIS, HOAPS3, and ERA-Interim are similar to SEAFLUX Qsst. From Port Elizabeth to the Retroflection region, CFSR and MERRA-2 are in fairly good agreement with SEAFLUX. NOCS fails to capture the sharp maximum in the Agulhas Current and the meanders of the Return Current region in summer and autumn.

The specific humidity of the near-surface air (Qa) at a reference height of 10 m is displayed in **Figure 3.11**. Qa is available for the products presented in **Chapter 2**. The same scale as Qsst (**Fig. 3.10**) is kept for a better comparison. CFSR and ERA-Interim Qa are re-adjusted to 10 m using the BVW algorithm. Qa is lower than Qsst. The Agulhas Current is not shown as distinctly as it is for the SST, Qsst and wind speed. Qa decreases poleward and westward along the pathway of the Agulhas Current like Qsst. The large-scale patterns of CFSR and MERRA-2 are similar compared to the satellite products in summer (DJF) and autumn (MAM). The Qa maximum is found in summer in the eastern part of the Agulhas Current. During winter, the distributions of all products are completely different from one to another. In winter and in the Agulhas Current system, Qa ranges between 6 and 12 $g.kg^{-1}$ for SEAFLUX, HOAPS3, CFSR, MERRA-2, and NOCS, while ERA-Interim Qa ranges between 6 and 10 $g.kg^{-1}$. ERA-Interim has the lowest Qa product for all seasons which would increase ERA-Interim LHF and compensate for its weaker wind speed in the calculation of LHF.

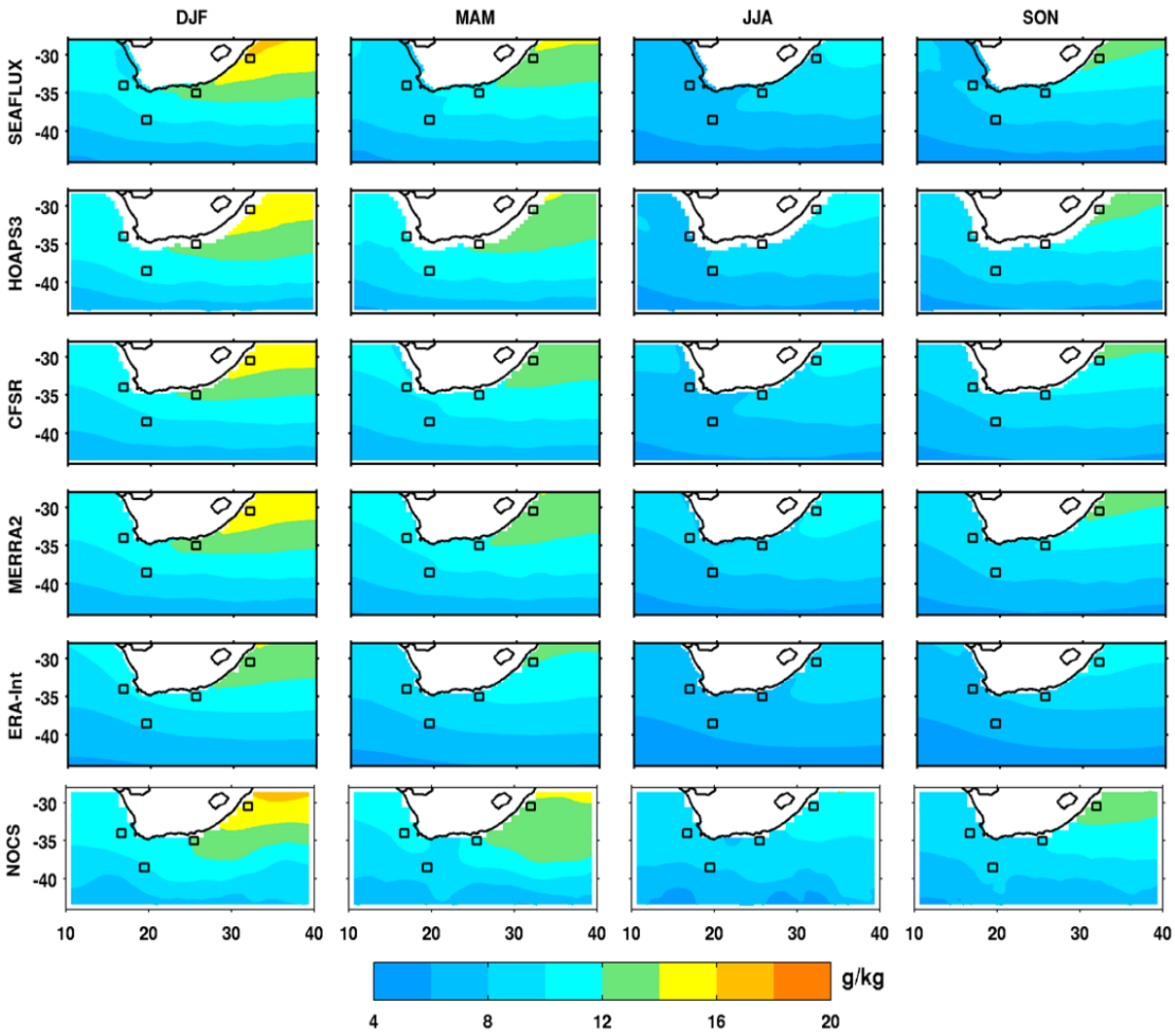

Figure 3.11: Seasonal averages of the specific humidity of air (Qa, g.kg^{-1}) for SEAFLUX, HOAPS3, CFSR, MERRA-2, ERA-Interim, and NOCS. Black squares represent the four locations taken for the study.

3.2.6 Differences between surface and air specific humidity (Qsst – Qa)

According to the bulk formulae (*cf.* **Eq. 2.1**, **Chap. 2**) Qsst-Qa is as important as the near-surface wind speed for calculating the LHF. Qsst-Qa ranges between 0 and 8 g.kg^{-1} which is equivalent in the calculation of LHF to a wind speed of 0 to 8 m.s^{-1}. Positives values of Qsst-Qa imply evaporation in our study. In the Agulhas Current system Qsst-Qa ranges from 4 to 8 g.kg^{-1} (**Fig. 3.12**). In spite of uncertainties in the Qa, the spatial pattern of the Agulhas Current is relatively

well depicted due to Qsst. The satellite-based HOAPS3, the reanalyses CFSR, MERRA-2, and ERA-Interim have their maximum Qsst-Qa in autumn (MAM) and winter (JJA) as for SEAFLUX, but the large scale-patterns do not completely agree with SEAFLUX. NOCS has the lowest Qsst-Qa with a minimum in the Agulhas Current in winter. ERA-Interim has the highest Qsst-Qa followed by CFSR and MERRA-2.

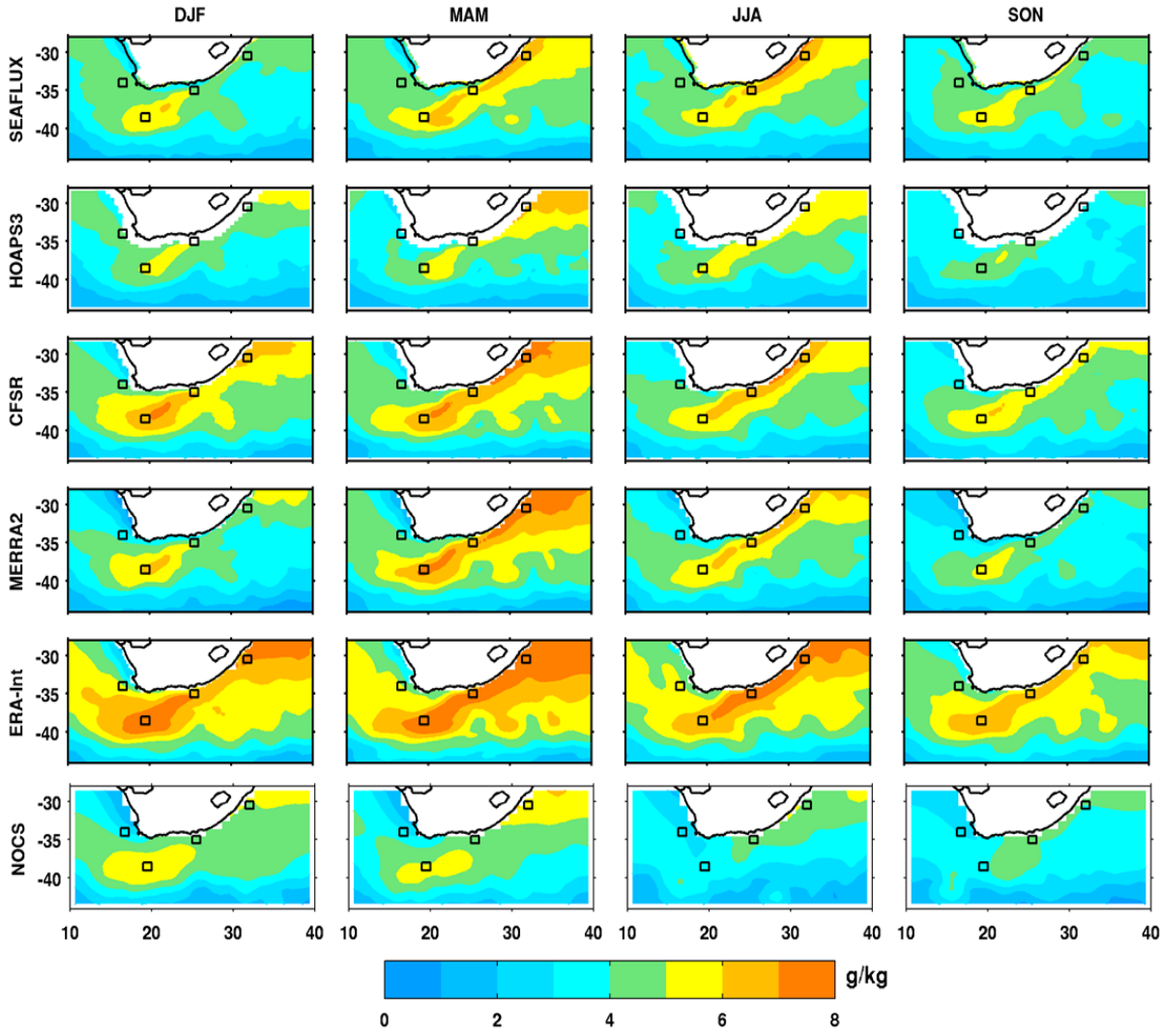

Figure 3.12: Seasonal differences between surface specific humidity and specific humidity of air (Qsst-Qa, $g.kg^{-1}$) for SEAFLUX, HOAPS3, CFSR, MERRA-2, ERA-Interim, and NOCS. Black squares represent the four locations taken for the study.

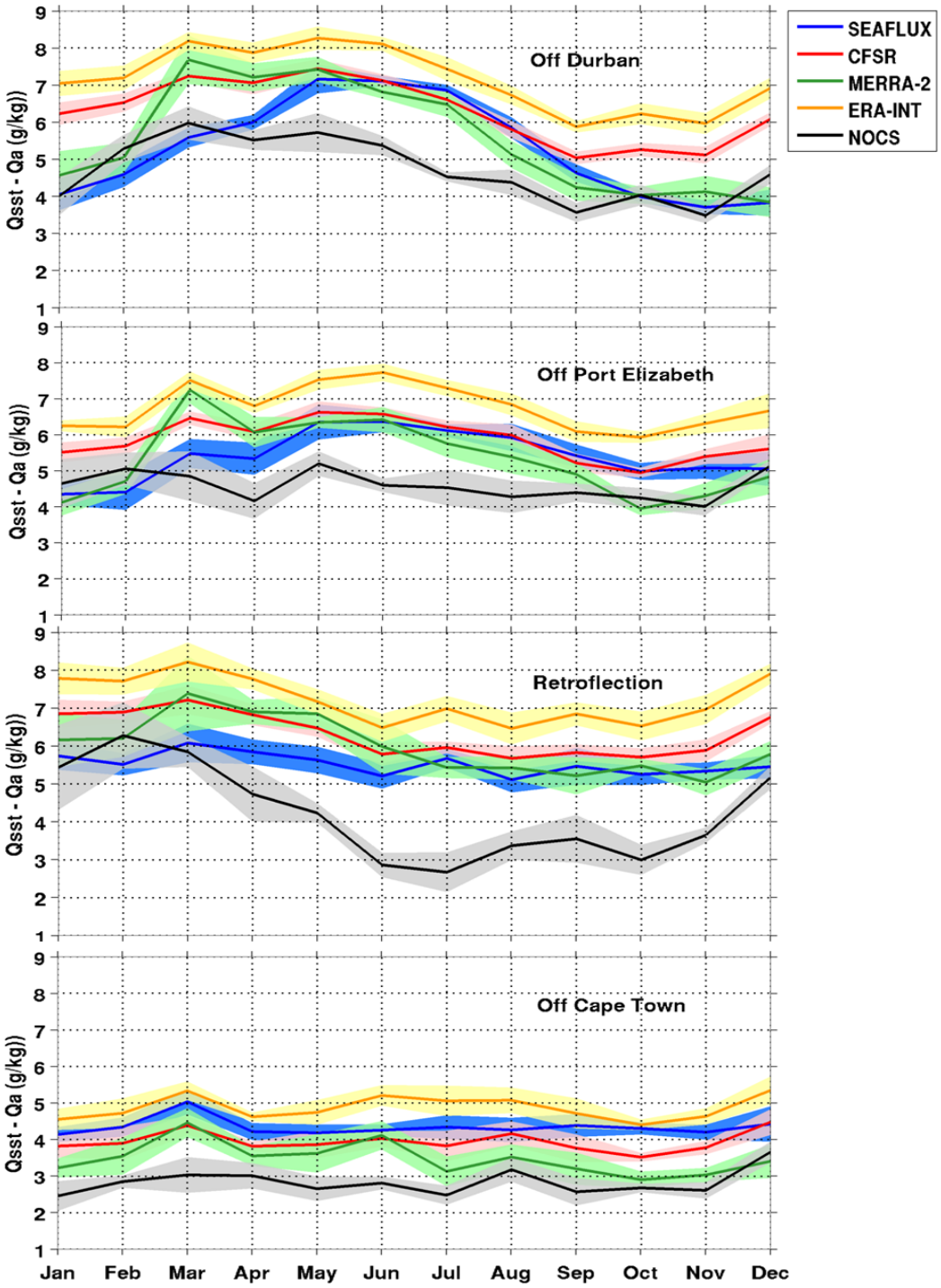

Figure 3.13: Annual cycles of the differences between Qsst and Qa ($g.kg^{-1}$), off Durban, off Port Elizabeth, Retroflection region, and off Cape Town for SEAFLUX (blue), CFSR (red), MERRA-2 (green), ERA-Interim (yellow), and NOCS (black). Shade areas represent the standard errors.

The annual cycles of Qsst-Qa for SEAFLUX, CFSR, MERRA-2, ERA-Interim, and NOCS are displayed in **Figure 3.13** for the four locations of this study. There are considerable differences between the products. The maxima are located off Durban, with values ranging from 3 to 9 $g.kg^{-1}$. The SEAFLUX Qsst-Qa maximum is up to 7 $g.kg^{-1}$ between May and July and decreases thereafter to 3.8 $g.kg^{-1}$ until mid-spring. SEAFLUX overlaps with CFSR and MERRA-2 from May to August, while SEAFLUX, MERRA-2, and NOCS overlap in summer and spring. ERA-Interim has the largest Qsst-Qa and does not overlap with other products (**Fig. 3.13**, **Table 3.4**).

ZONES	SEAFLUX	CFSR	MERRA-2	ERA-INTERIM	NOCS
Off Durban	5.3	6.3	5.5	7.2	4.7
Off Port Elizabeth	5.4	5.9	5.3	6.7	4.6
Retroflection	5.5	6.3	6.0	7.2	4.2
Mean Agulhas	5.4	6.2	5.6	7.0	4.5
Off Cape Town	4.3	3.9	3.5	4.9	2.8

Table 3.4: Annual means of the differences between the surface specific humidity and the specific humidity of air (Qsst-Qa, $g.kg^{-1}$) off Durban, off Port Elizabeth, Retroflection region, the average of the three Agulhas points, and off Cape Town.

Off Port Elizabeth the annual cycles of Qsst-Qa range between 4 and 8 $g.kg^{-1}$. All products have a maximum in March. From May to October, SEAFLUX, CFSR, and MERRA-2 overlap. ERA-Interim is the highest and NOCS the lowest. In the Retroflection region, Qsst-Qa is between 3 and 9 $g.kg^{-1}$ (**Fig. 3.12**, **Table 3.4**). SEAFLUX has small annual variations (between 5.5 and 6 $g.kg^{-1}$) compared to other products. SEAFLUX overlaps with CFSR and MERRA-2 from June to November. As off Durban and off Port Elizabeth, ERA-Interim and NOCS are respectively the largest and the smallest. These former products do not overlap with others. NOCS has a maximum (6 $g.kg^{-1}$) in February and a minimum in July (~3 $g.kg^{-1}$), corresponding to the maximum and minimum of NOCS LHF. In the Retroflection area, the reanalyses are higher than the satellite-based SEAFLUX (**Figs. 3.11, 3.12,** and **Table 3.4**). Offshore Cape Town, Qsst-Qa ranges from 2

to 5 g.kg^{-1}. In summary, ERA-Interim has the largest Qsst-Qa values while NOCS reveals the lowest values.

The mean seasonal differences of Qsst-Qa between HOAPS3, CFSR, MERRA-2, ERA-Interim, NOCS and SEAFLUX product are presented in **Figure 3.14**. The differences range within ±2 g.kg^{-1}, around ±37% of the mean SEAFLUX Qsst-Qa in the Agulhas system. In this region, HOAPS3, CFSR, and MERRA-2 overestimate the Qsst-Qa by around 2 g.kg^{-1} compared to SEAFLUX in summer (DJF) and autumn (MAM), but underestimate Qsst-Qa by ~1 g.kg^{-1} in winter (JJA). ERA-Interim overestimates the Qsst-Qa for all seasons (**Fig. 3.14**, **Table 3.4**), while NOCS overestimates the Qsst-Qa in summer and underestimates the Qsst-Qa by 2 g.kg^{-1} in winter.

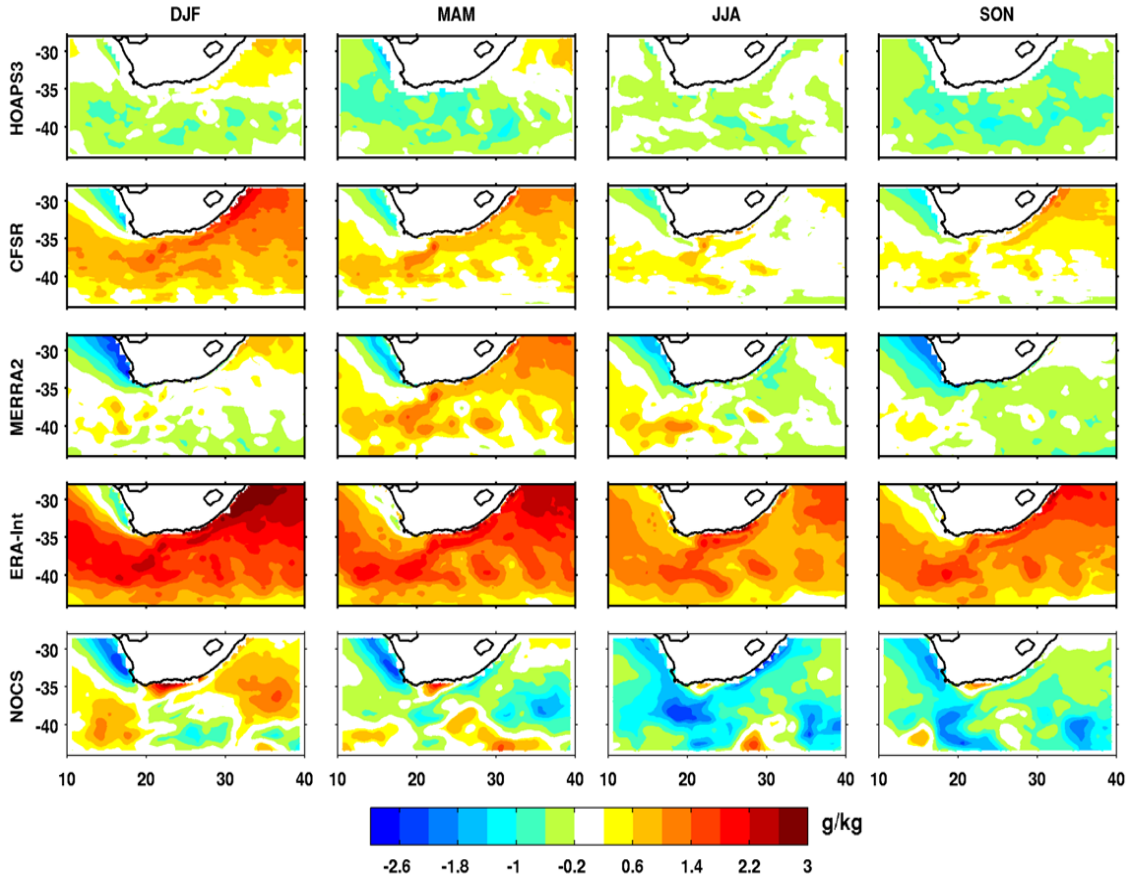

Figure 3.14: Mean seasonal differences of Qsst-Qa (g.kg^{-1}) between HOAPS3, CFSR, MERRA-2, ERA-Interim, NOCS and SEAFLUX for the summer (DJF), autumn (MAM), winter (JJA) and spring (SON).

3.2.7 Drivers of the annual cycle of LHF using SEAFLUX

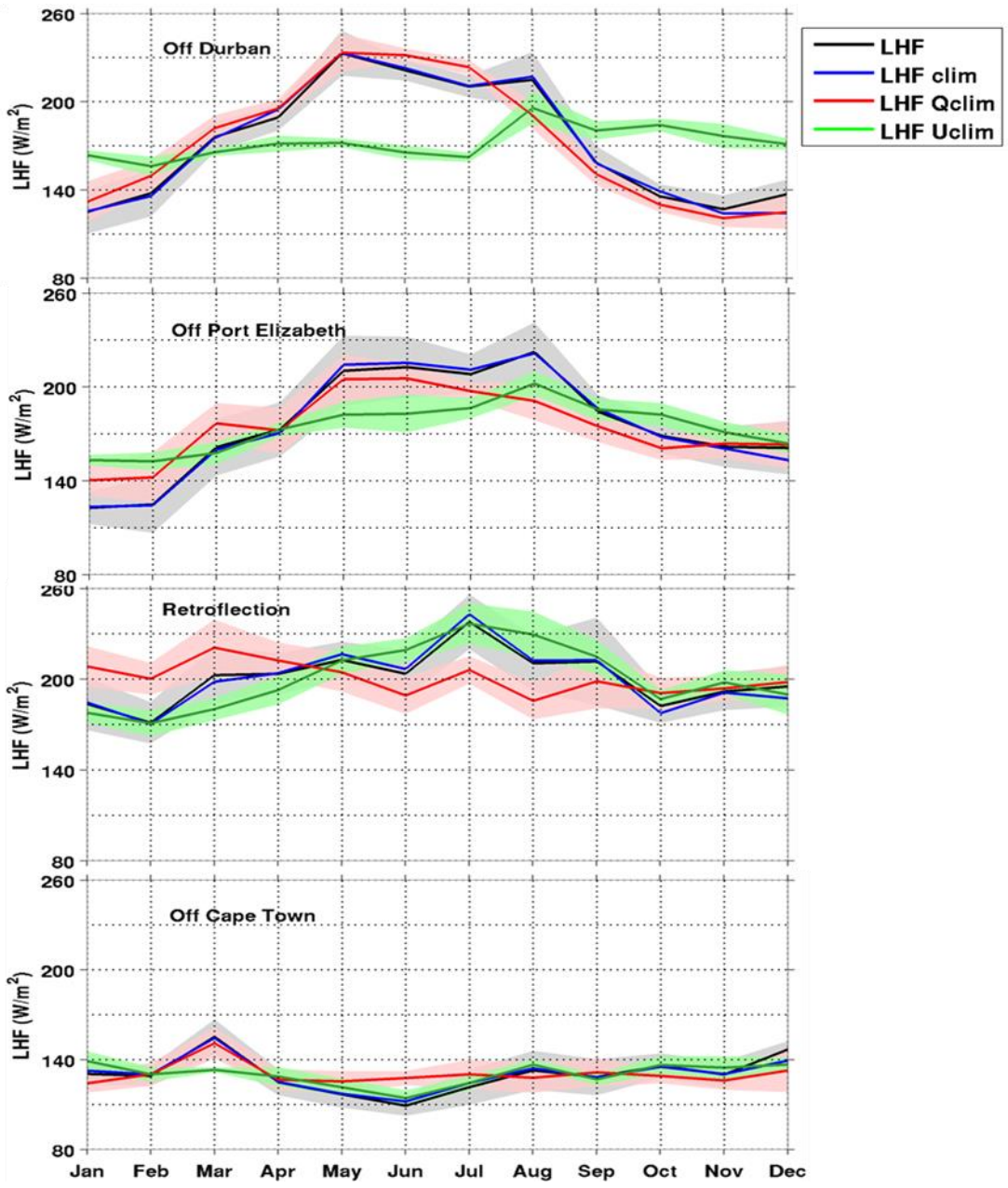

Figure 3.15: SEAFLUX annual cycles of LHF ($W.m^{-2}$) (black) and the recalculated LHF using: a monthly climatology wind speed and Qsst-Qa (LHF_clim, blue); a monthly climatology of Qsst-Qa and the annual mean of wind speed (LHF_Qclim, red), and a monthly climatology of wind speed and the annual mean of Qsst-Qa (LHF_Uclim, green) off Durban, off Port Elizabeth, Retroflection region and off Cape Town. Shade areas represent the standard errors.

In this section, the drivers of the annual cycle of the LHF are studied off Durban, Port Elizabeth, Cape Town and in the Retroflection region using the satellite-based SEAFLUX. We are using this product because SEAFLUX SST agrees rather well with the MODIS SST field (**Figs. 3.4** and **3.5**), SEAFLUX wind speed also compares well with SCOW wind speed (**Figs. 3.7** and **3.8**). SEAFLUX wind speed ranges between 8 and 12 $m.s^{-1}$ in the Agulhas Current system, and Qsst-Qa ranges between 4 and 7 $g.kg^{-1}$ (**Figs 3.8** and **3.13**). Off Cape Town, SEAFLUX wind speed varies between 7 and 9 $m.s^{-1}$ with Qsst-Qa ranging between 4 and 5 $g.kg^{-1}$. To evaluate the contribution of either the wind speed or the difference in specific humidity, we recalculated 3 types of LHF using the SEAFLUX product (**Fig. 3.15**) based on **Eq. 2.1** (**Chap. 2**).

The recalculated LHF are considered with: a) a monthly climatology of wind speed as well as a monthly climatology of Qsst-Qa (LHF_clim), b) a monthly climatology of Qsst-Qa and the annual mean of wind speed (LHF_Qclim), and c) a monthly climatology of wind speed and the annual mean of Qsst-Qa (LHF_Uclim). To recalculate the LHF, we estimate the coefficient $\rho_a C_E l_v$ $(coef)$ of **Equation 2.1** as follows:

$$coef = \frac{rms\ (LHF)}{rms\ (LHF\_clim)} \dots\dots\dots\dots\ (\boldsymbol{Eq.3.1})$$

We find that $coef$ is around 3.6, with $C_E \sim 0.0012$ as found by *Singh et al.* (2005). The authors suggested that C_E values range between 0.00152 and 0.00105 for wind speeds between 2 and 19 $m.s^{-1}$.

The highest value of the LHF is found in the Retroflection area in winter (around 250 $W.m^{-2}$) while the lowest LHF is off Cape Town (100 $W.m^{-2}$, in winter) (**Fig. 3.15**). To illustrate the contribution of the wind speed or the specific humidity to the LHF, and to statistically compare the initial LHF and the recalculated LHF, we show the correlation coefficients, the ratio of variances and the explained variances between LHF and each of the recalculated LHFs (**Table 3.5**). The explained variance ($EXPvar$) is defined as:

$$EXPvar(x) = 100 - 100 \times \left[\frac{var(LHF - LHF\_x)}{var(LHF)}\right] \dots\dots\dots\dots\ (\boldsymbol{Eq.3.2})$$

where LHF_x is LHF_clim, LHF_Qclim or LHF_Uclim.

LHF recalculated	Correlation	Ratio (%)	Explained variance (%)
Off Durban			
LHF_clim	0.99	110	99
LHF_Qclim	0.96	112	48
LHF_Uclim	0.10	7	1
Off Port Elizabeth			
LHF_clim	0.99	109	99
LHF_Qclim	0.94	45	31
LHF_Uclim	0.90	22	21
Retroflection			
LHFclim	0.99	129	95
LHF_Qclim	0.13	34	2
LHF_Uclim	0.85	149	45
Off Cape Town			
LHFclim	0.98	77	95
LHF_Qclim	0.71	32	20
LHF_Uclim	0.75	36	22

Table 3.5: Correlations, ratio of variances and explained variances between SEAFLUX LHF and SEAFLUX recalculated LHF off Durban, off Port Elizabeth, Retroflection region and off Cape Town.

The recalculated LHF_clim compares well with the initial LHF for all the locations (**Fig. 3.15**). The $EXPvar$ is 99% off Durban and off Port Elizabeth (**Table 3.5**), while that in the Retroflection region and off Cape Town $EXPvar$ is 95% indicating that the recalculated LHF_clim represents LHF well, even though its amplitude is smaller than LHF in these regions. This may be due to nonlinearities in using monthly climatology. Off Durban, the correlation between LHF and LHF_Qclim is 0.96, and the ratio of variances is 112% with 48% of the $EXPvar$, while the correlation between LHF and LHF_Uclim is 0.10, with 7% of the ratio of variances (**Table 3.5**). This result indicates that off Durban LHF and probably the eastern part of the Agulhas Current is mostly driven by the monthly climatology of Qsst-Qa. The monthly climatology of the wind speed

only explains 1% of the variance. In the Retroflection region correlation between LHF and LHF_Qclim is 0.13, the ratio of variances is 34% and the $EXPvar$ is 2% while the correlation between LHF and LHF_Uclim is 0.85 with 149% of the ratio of variances and 45% of the $EXPvar$. This result reveals that in this region and probably the West of the Agulhas Current, the LHF is driven by the monthly climatology of the wind speed rather by the Qsst-Qa. Off Port Elizabeth and off Cape Town, the correlation between LHF and LHF_Qclim as well as LHF_Uclim is more than 0.71, statistically significant at the 95% level. This result shows that the LHF is driven by the wind speed and differences in specific humidity for both regions.

3.3 DISCUSSION AND SUMMARY

In this chapter, the first objective was to investigate whether the recent climate reanalyses (CFSR, MERRA-2, ERA-Interim), satellite-based (SEAFLUX, HOAPS3) and in-situ observation-based (NOCS) LHF products give a good representation of the intense turbulent flux of moisture that occurs above the Agulhas Current. The Agulhas Current is not adequately resolved in the coarser-resolution by first generation reanalyses (ERA-40 and NCEP2). SEAFLUX compares quite well with HOAPS3, but HOAPS3 does not have data along the coast. Therefore, HOAPS3 does not represent the Agulhas Current or the Benguela upwelling system adequately. Compared to the SEAFLUX LHF, the ERA-40 and NCEP2 LHF fail to represent the structure of the Agulhas Current (**Figs. 3.1** and **3.3**). The new reanalysis products, on the other hand, give a better representation of the current. CFSR is relatively similar to MERRA-2 but has higher LHF. Between the three new reanalyses, surprisingly ERA-Interim has the lowest fluxes (100-200 $W.m^{-2}$). This result was unexpected in view of the higher spatial resolution of the ERA-Interim products (0.75° x 0.75°) compared to ERA-40 (2.5° x 2.5°). It is most likely due to its low wind speed although the LHF is compensated by large values of Qsst-Qa. The phase of the seasonal cycle of the NOCS LHF is reversed in the Retroflection region compared to other products. This might indicate that too few vessels pass through the Agulhas Retroflection region to sample the area adequately. Another reason for the uncertainties in NOCS is due to measurement uncertainty (*Berry and Kent,* 2011). To conclude, CFSR and MERRA-2 show good representation of the Agulhas Current. CFSR reanalysis will be used for **Chapters 4** and **5** to investigate the relation

between the intense flux of moisture over the Agulhas Current and the weather and climate in Southern Africa, and to validate mesoscale atmospheric models such as the Weather Research and Forecasting model (WRF, *Skamarock and Klemp* 2008).

The second aim of this study was to identify the level of uncertainties introduced by the basic parameters (SST, wind, surface specific humidity) used to estimate the LHF (e.g. **Eq. 2.1**). The differences between each product and the reference products from MODIS are calculated for SST, SCOW for wind speed and SEAFLUX for Qsst-Qa. CFSR SST is higher than MERRA-2 SST compared to MODIS SST. This may explain higher values of the LHF from CFSR compared to MERRA-2, as SST is used to compute Qsst. For a better comparison of the wind speed and Qa between products, we convert the stability-dependent wind speed (CFSR, MERRA-2, ERA-Interim, and NOCS) to the equivalent neutral wind speed using the BVWN algorithm (*Bourassa et al.* 1999). The difference between the real wind speed and the recalculated wind speed is 0.5 $m.s^{-1}$ maximum. We also readjust the 2 m Qa to 10 m Qa using the BVW algorithm, for CFSR and ERA-Interim. This correction removes between 0.3 and 0.8 $g.kg^{-1}$ to the initial 2 m Qa. Between CFSR, MERRA-2, and ERA-Interim, MERRA-2 has the highest wind speed and CFSR the highest Qsst-Qa as provided in **Tables 3.3** and **3.4**. Between CFSR, MERRA-2, and ERA-Interim, ERA-Interim has the weakest wind speed in the Agulhas system compared to SCOW (**Fig. 3.8**, **Table 3.3**), despite the fact that ERA-Interim wind speed is recalculated using the BVWN algorithm. This explains the lowest values of the ERA-Interim LHF. In the Agulhas Current system, CFSR and MERRA-2 wind speed are similar. ERA-Interim has the strongest Qsst-Qa compared to other reanalyses (**Fig. 3.13**, **Table 3.4**). This compensates for the low wind speed in the calculation of ERA-Interim LHF but not enough. Qsst-Qa variability is mostly influenced by the variation of Qa. The comparison of the nine LHF products by *Smith* et al. (2011) indicates that in many regions, the differences in specific humidity of air between the products have a greater impact than the discrepancies in wind speed and SST. The recent study of *Bentamy et al.* (2017) showed that the differences in LHF tend to be strongly related to large differences in surface wind speeds and/or specific air humidity. The differences of LHF can also be explained by the diversity of algorithms: different bulk flux algorithms (e.g., *Brunke et al.* (2003)), different sources of the input meteorological state variables (e.g., *Curry et al.* (2004)), differences in the boundary conditions, and differences in the procedures for *in-situ* data collection.

Finally, the annual cycle of the LHF and its drivers in the Agulhas Current system are investigated using SEAFLUX. SEAFLUX is used to recalculate the LHF using a climatology Qsst-Qa and/or wind speed, as it has a high spatial resolution (0.25° x 0.25°) and reliable SST and wind speed (*Smith et al.* 2011). Three locations, representative of various regions of the Agulhas Current system (off Durban, off Port Elizabeth and Retroflection) and one point outside the Agulhas system (off Cape Town) were selected for the comparison. In the Agulhas Current system, the lowest LHF of 100 $W.m^{-2}$ is found off Port Elizabeth in late summer. In contrast, the largest LHF of ~250 $W.m^{-2}$ is located in the Retroflection region in winter. This is consistent with the analysis of *Rouault* et al. (2003) who showed that large LHF from the Agulhas Current and the Retroflection region occur throughout the year but particularly during winter. In the Agulhas Current Retroflection area, large values of the LHF are due to the stronger wind speed in the Retroflection region. Correlation between LHF and LHF_Uclim is 0.85. Off Durban higher values of the LHF can be explained by the difference of specific humidity. In this region, the correlation between the LHF and LHF_Qclim is 0.96. Off Port Elizabeth and Cape Town, values of LHF can be explained by the combination of Qsst-Qa and the wind speed. To summarize, off Durban, LHF is driven by surface specific humidity. In the Retroflection region LHF is mostly driven by the wind speed. Off Port Elizabeth it is a combination of the specific humidity and the wind speed.

CHAPTER 4

4 ATMOSPHERIC SIGNATURE OF THE AGULHAS CURRENT: ANNUAL CYCLE

4.1 INTRODUCTION

Western boundary currents play an important role in the climate system by influencing extra-tropical storms and oceanic rainfall. However, their coastal influence is less known, particularly in the Southern Hemisphere. Using satellite datasets (see Chapter 2), the Climate Forecast System Reanalysis (CFSR, *Saha* et al. 2010), and the Weather Research and Forecasting model (WRF, *Skamarock and Klemp,* 2008), we investigate whether the Agulhas Current is a driver of the observed band of rainfall along the south-eastern African coast and above the Agulhas Current. The reanalysis CFSR is used because it represents better the ocean-atmosphere interactions above the Agulhas Current, due to its higher resolution, and because CFSR is a partially coupled reanalysis, and therefore estimates better the ocean and the atmosphere over the region. The study period is from 2001 to 2005. Five years of analysis are adequate because the Agulhas current shows little interannual variation (*Krug and Tournadre*, 2012). Moreover, perturbations of the Agulhas Current, Natal Pulse or early retroflection do not occur often (*Krug and Tournadre*, 2012; *Rouault and Penven*, 2011). One control and one sensitivity experiment are performed using the WRF model, to assess whether the sharp sea surface temperature gradient of the Agulhas Current influences the adjacent coastal rainfall.

4.2 ARTICLE'S RESULTS

The results of this study have been published in Geophysical Research Letters (GRL) in April 2018 as: **Nkwinkwa Njouodo, A.S.**, Koseki, S., Keenlyside, N. and Rouault, M. (2018). Atmospheric signature of the Agulhas Current. *Geophysical Research Letters*. https://doi.org/10.1029/2018GL077042.
This analysis has been done by me under the supervision of my PhD Advisors, and the co-authors of the paper.

4.2.1 High-resolution observations over the Agulhas Current

We analyse the annual climatological mean state using satellite observations and modern atmospheric reanalysis to reveal a clear relationship between the Agulhas Current and precipitation (**Fig. 4.1**). The Agulhas Current is 80–100 km wide and runs south-westward along the eastern coast of South Africa, following roughly the continental shelf until it retroflects and flows westward (**Fig. 4.1a**). Here, we focus on the core of the current, which is a few degrees warmer than the surrounding ocean (contours **Fig. 4.1**), and on the region where the current hugs the coast. The SST varies from 27 ^{o}C off the East Coast of South Africa to 23 ^{o}C in the retroflection in late summer and from 22 ^{o}C to 18 ^{o}C in late winter (**Fig. 3.5**). The turbulent latent heat flux (turbulent flux of moisture) above the sharp tongue of SST is high, reaching values of up to 220 W.m^{-2} annually in the Agulhas region. The high flux is caused by the advection of oceanic colder and drier air over the current, together with the destabilising effect of the SST gradient on the surface MABL and the wind speed (*Lee-Thorp et al.* 1999; *Rouault et al.* 2000).

The annual mean rainfall rate of derived observations from the TRMM Precipitation Radar (PR, *Biasutti et al*. 2012) and the CFSR reanalysis (*Saha et al.* 2010) both show a narrow band of precipitation along the eastern coast of South Africa, just over the core of the Agulhas Current (**Figs. 4.1c, d**). TRMM PR derived rainfall frequency show an equally striking relationship (**Fig. 4.1b**). TRMM PR climatology has a high horizontal resolution (0.05° x 0.05°) that allows better definition of the core of the Agulhas Current adjacent to the coast compared to other satellite products, although there are no data south of 36°S (see **Chapter 2**). In the Agulhas region, annual mean precipitation varies from 3 to 4 mm.d^{-1} for TRMM PR, while a few degrees to the east it is about 1 mm.d^{-1} less. CFSR captures the rain band, especially near the coast to the east (**Fig. 4.1d**).

CFSR precipitation differs from TRMM PR by 1 to 2 mm.d^{-1} (and by more over the interior of the continent, which is not our domain of research).

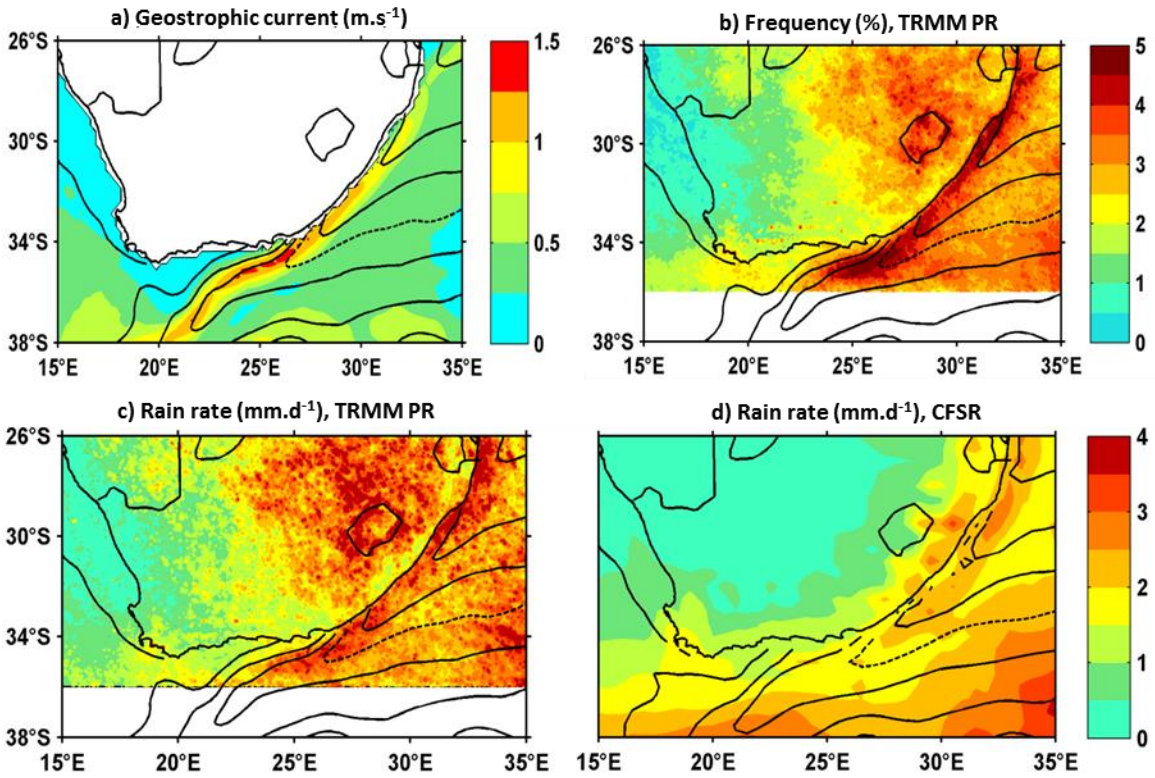

Figure 4.1: Annual climatology: (**a**) surface geostrophic current from GlobCurrent at 0 m depth, (**b**) rain frequency of Tropical Rainfall Measuring Mission Precipitation Radar (TRMM PR) showing the percentage of observations at a given location for which rain was detected and its corresponding rain rate (**c**). (**d**) rain rate of the Climate Forecast System Reanalysis (CFSR). The solid contours represent annual climatology of optimal interpolation sea surface temperature (SST) (**a**), (**b**), (**c**) and CFSR SST (**d**) with 1° intervals; the dashed line is 22°C SST.

4.2.2 Mechanisms for rainfall over the Agulhas Current

The CFSR reanalysis shows that local evaporation exceeds rainfall by between 2 to 5 mm.d^{-1} over the entire region, with the greatest excess over the Agulhas Current (**Fig. 4.2**).

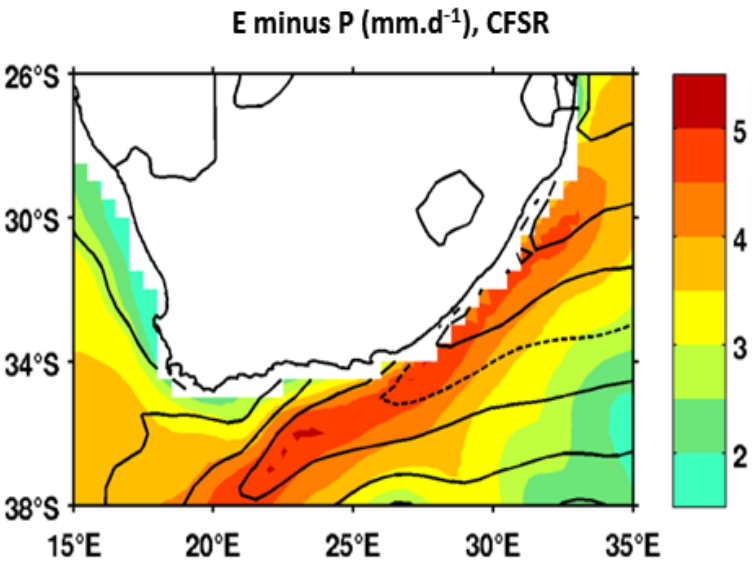

Figure 4.2 : Annual climatology of CFSR evaporation minus precipitation. CFSR annual mean SST is contoured with 1° intervals, the dashed line is 22°C SST.

Thus, local moisture supply is consistent with the broad scale rainfall over the region and with the enhanced rainfall over the Agulhas Current. However, moisture alone does not lead to rainfall: air masses must be lifted to saturation by low-level wind convergence, atmospheric convective processes, or by frontal processes. Frontal processes are probably responsible for the broad scale rainfall occurring south of our region of interest; here sharp SST gradients anchor the storm track of extra-tropical cyclones (*Nakamura et al.* 2004) and thereby cause frontal rainfall (*Hand et al.* 2014; *Parfitt et al.* 2016). This mechanism may explain rainfall patterns over the Agulhas Return Current, where the current and the southern hemisphere storm tracks align (*Hoskins and Hodges*, 2005).

Sharp SST gradients can also influence surface winds and generate lower-level atmospheric convergence and vertical motion, which can penetrate deep into the free troposphere (*Chelton and Xie*, 2010). Vertical mixing is one mechanism for the wind response to SST fronts (*Wallace et al.* 1989); above warm SST, the lower atmosphere becomes unstable due to large turbulent heat fluxes. This mechanism is observed in regions with strong SST gradients (*Xie*, 2004), including the Agulhas Return Current (*O'Neill et al.* 2005, **Chapter 3**). Another dynamical explanation for the wind response to SST is the pressure adjustment mechanism (*Lindzen and Nigam*, 1987; *Back*

and Bretherton, 2009): SST modifies the MABL temperature so that the resultant pressure anomalies induce surface wind convergence over warm SST and wind divergence over cool SST. Earlier studies implicated the pressure adjustment mechanism in producing the observed pattern of wind convergence and divergence over major SST frontal regions (*Minobe et al.* 2008; *Shimada and Minobe*, 2011). Recent studies suggest that the low-level convergence and associated rain band over the Gulf Stream is instead the result of the interaction of synoptic-scale atmospheric variability with the sharp SST front (*Parfitt et al.* 2016; *O'Neill et al.* 2017; *Sheldon et al.* 2017).

To assess whether the increase of rainfall over the core of the Agulhas Current may result from similar mechanisms to those of the Gulf Stream, we compare the annual climatology of SST Laplacian, wind convergence, and SLP Laplacian. According to the pressure adjustment mechanism, a tight relationship among these quantities indicates that warmer (cooler) SST drives lower (higher) SLP, and in turn enhances surface wind convergence (divergence) (*Minobe et al.* 2008) (see section 2.2 of **Chapter 2**). The Laplacian analysis acts as a spatial high-pass filter that highlights sharp gradients. The negative SST Laplacian of the CFSR reanalysis (**Fig. 4.3a**) exhibits a distinct structure along the eastern coast of South Africa, collocated with the rain band. (The SST Laplacian is reversed in sign for the convenience of comparing results.)

The satellite-derived SST Laplacian SST (**Fig. 4.3b**) is similar to the CFSR result (**Fig. 4.3a**), but stronger in amplitude because of the higher resolution data. As the finer resolution data has a smaller-scale structure than coarser-resolution data (in this case, finer: OISST, 0.25°, coarser: CFSR, 0.5°), the high-passed variable can be larger in the finer resolution data. Therefore, the SST Laplacian of OISST fields could have larger values than those of CFSR. Along the eastern coast of South Africa, a predominant narrow band of 10 m wind convergence (**Fig. 4.3c**) is collocated with the rainfall and negative SST Laplacian. CFSR reproduces the band of wind convergence found in the higher resolution satellite-based SCOW climatology (**Fig. 4.3d**) quite well, even though the pattern is shifted poleward compared to the CFSR reanalysis. Convergence and divergence also occur in the retroflection region around 38.5°S, 22°E and downstream along the meandering Agulhas Return Current (not shown). This result has also been observed by *Shimada and Minobe*, (2011) over the same region. The SLP Laplacian shows a positive band along the eastern coast of South Africa (**Fig. 4.3e**) that is co-located with the SST Laplacian, wind convergence and rainfall. This indicates that SLP above the Agulhas Current is linked to the

underlying SST and may be consistent with the pressure adjustment mechanism (*Lindzen and Nigam*, 1987; *Minobe et al.* 2008).

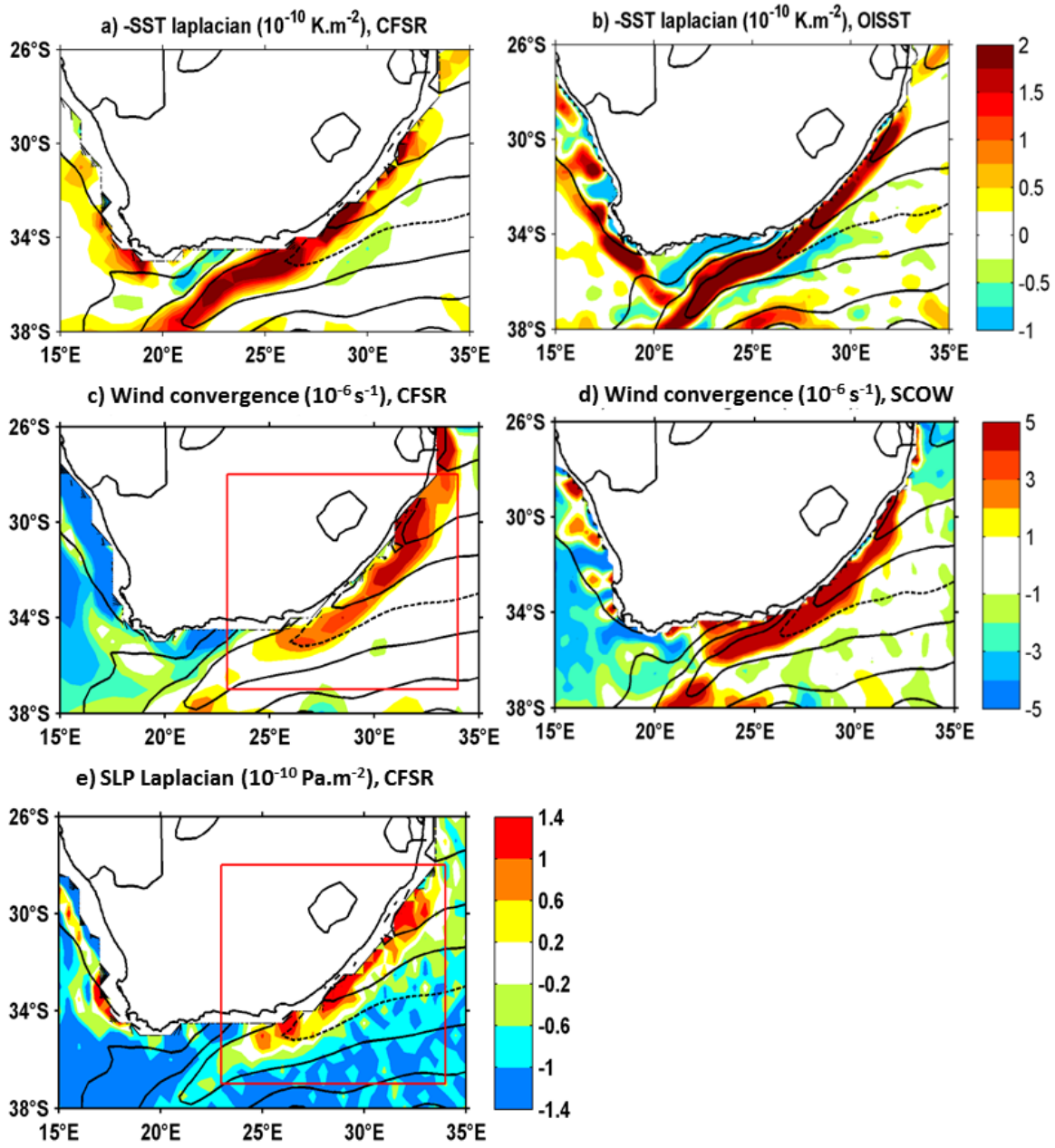

Figure 4.3: Annual mean: sign reversed SST Laplacian **(a)** CFSR and (b) OI SST; wind convergence (positives values) **c)** CFSR, (d) SCOW, (**e**) CFSR sea level pressure (SLP) Laplacian. Solid contours represent annual climatology of: **a**), **c**) and **e**) CFSR SST and **b**) and **d**) OI SST. The dashed line is 22°C.

We quantify the relationship among the terms of the pressure adjustment mechanism for the maritime region over the Agulhas Current (28–37°S, 23–34°E; red boxes in **Figs. 4.3c, e**). The relationship between SLP Laplacian and surface wind convergence exhibits a spatial correlation coefficient of 0.50, statistically significant at the 95% level (**Fig. 4.4a**). The scatter plot shows that the relation between SLP Laplacian and surface wind convergence is approximately linear. However, there is greater scatter among positives values of SLP Laplacian and wind convergence, as compared to negatives values. The negative SST Laplacian and SLP Laplacian exhibit a stronger spatial correlation of 0.71, significant at the 95% level (**Fig. 4.4b**). These significant relations are consistent with those found over the Gulf Stream, indicating that the low-level convergence could be the result of the interaction of synoptic-scale atmospheric variability with the sharp SST front and may drive rainfall over the Agulhas Current.

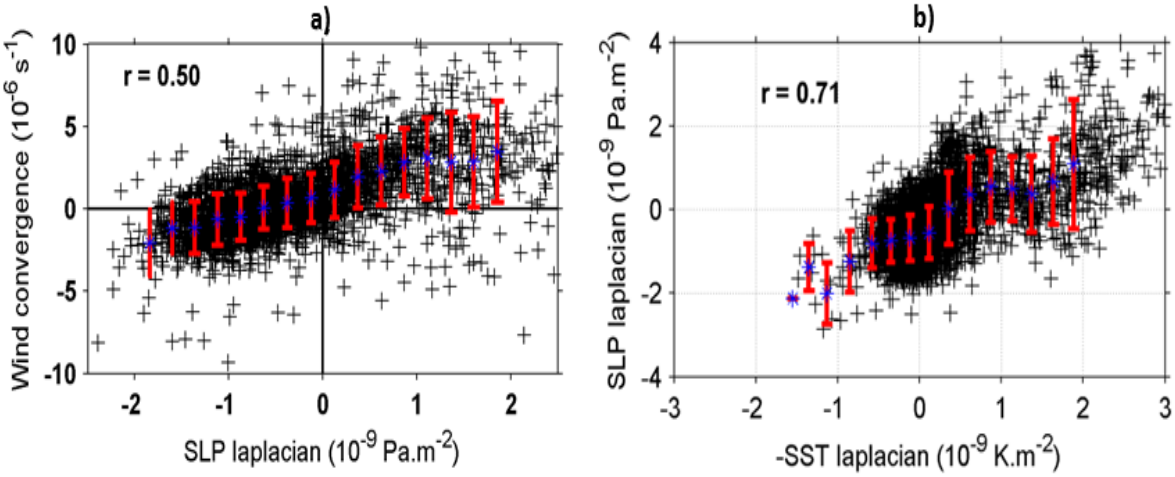

Figure 4.4: Scatter plot showing the relation between **a**) wind convergence and SLP Laplacian and **b**) SLP Laplacian and sign reversed SST Lapacian of CFSR, based on monthly climatology within the region 28–37°S, 23–34°E indicated by the red boxes in (**Figs. 4.3c, e**)). The blue stars represent the mean values for each interval; the error bars in red are ±1 standard deviation.

4.2.3 Influence of the Agulhas Current on regional atmospheric model experiments

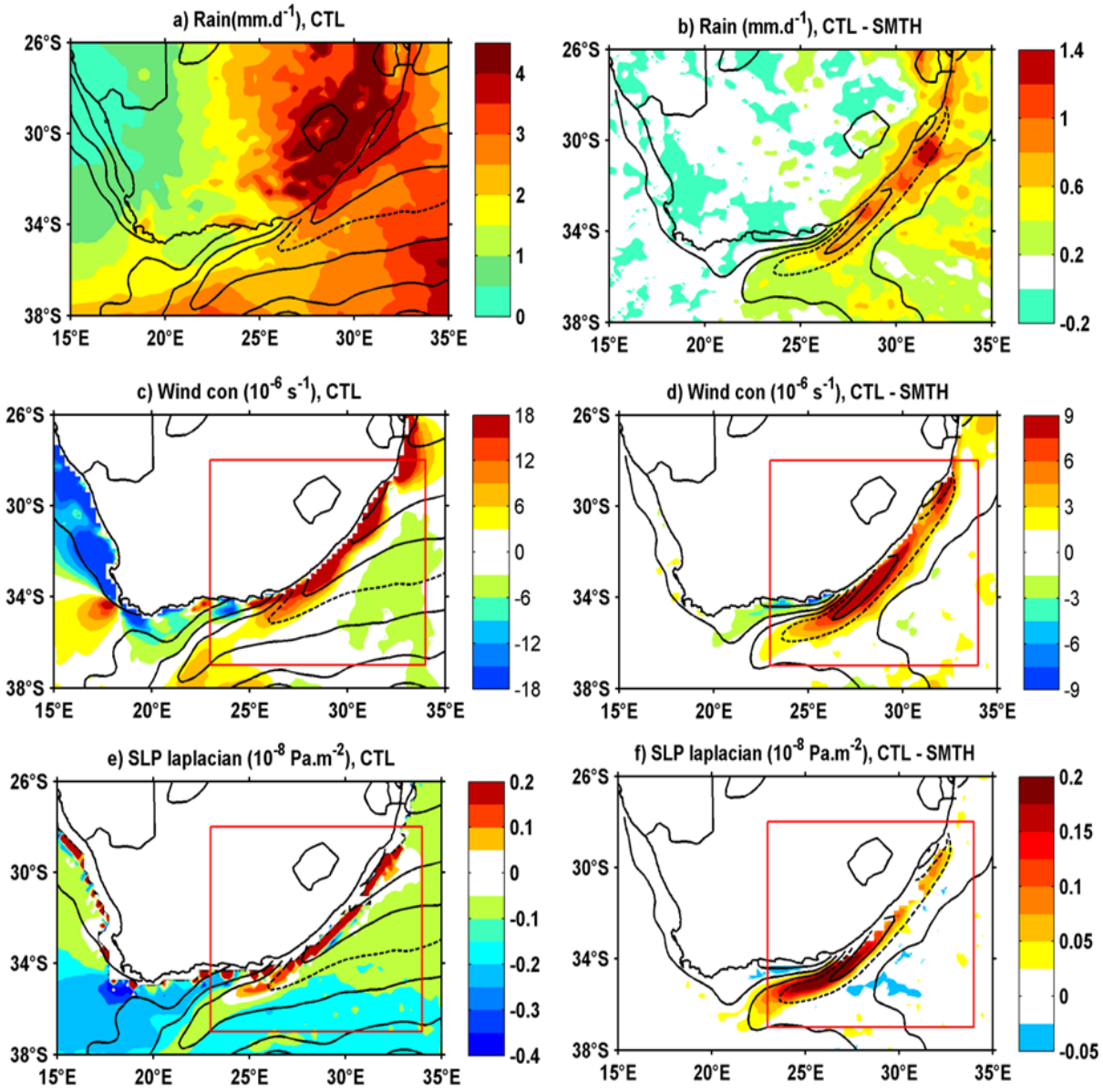

Figure 4.5: The annual mean (a) rainfall, (c) wind convergence, and (e) SLP Laplacian simulated by control (CTL) with the sea surface temperature (SST) contours of CTL overlaid. (b, d, and f) the impact of smoothing the SST gradients in the Agulhas Current region on these quantities is shown by the differences between CTL and smoothed SST (SMTH); the contours show the SST difference between CTL and SMTH (0.5 °C intervals and dashed line for 1 °C).

We perform two regional model experiments (*Skamarock and Klemp*, 2008) to isolate the role of the Agulhas warm core on the atmosphere (**Chapter 2**). The regional model experiment with observed SST (CTL) reproduces the rain band along the Agulhas Current realistically (**Fig. 4.5a**). In the CTL experiment, the Agulhas Current precipitation rate varies between 2 and 4 $mm.d^{-1}$ (**Fig. 4.5a**) and is similar to the TRMM PR observations (**Fig. 4.1b, c**), but is up to 2 $mm.d^{-1}$ more than the CFSR reanalysis (**Fig. 4.1d**). Over land the simulated annual precipitation is stronger than in the observations and reanalysis. This may be due to the strong sensitivity of the cumulus convection schemes to the topography, a common issue with this regional model (*Pohl et al*. 2014).

We represent the differences between the two experiments in **Figure 4.5**. The rain band along the South African coast adjacent to the Agulhas Current is greatly reduced in the experiment with smoothed SST (SMTH) compared to CTL (**Fig. 4.5b**). The difference is up to 1.4 $mm.d^{-1}$ with a maximum offshore Kwazulu-Natal (around 30.5°S; 31.5°E). The wind convergence and the positive SLP Laplacian over the Agulhas Current are relatively well simulated compared to satellite estimates and reanalyzed output (**Figs. 4.5c, e**). (Note that the simulated SLP Laplacian is influenced by inland values along the ocean grid adjacent to land, probably due to orography). The difference of wind convergence between CTL and SMTH shows a well-defined maximum over the Agulhas Current (**Fig. 4.5d**) that is co-located with the corresponding difference of SLP Laplacian (**Fig. 4.5f**). The magnitude of the difference in wind convergence is about half of the magnitude of CTL, while the differences in SLP are of similar magnitude to that of CTL.

The spatial correlation between the SLP Laplacian and wind convergence computed from the difference of the experiments is 0.55 (**Fig. 4.6a**), which is similar to the value from CFSR reanalysis (r = 0.50). The spatial correlation between SLP Laplacian and the negative SST Laplacian computed from the difference of the experiments is 0.70 (**Fig. 4.6b**), which is also similar to that from CFSR reanalysis (r=0.71). These results strongly support the hypothesis that SST gradients anchor the rain band over the Agulhas Current.

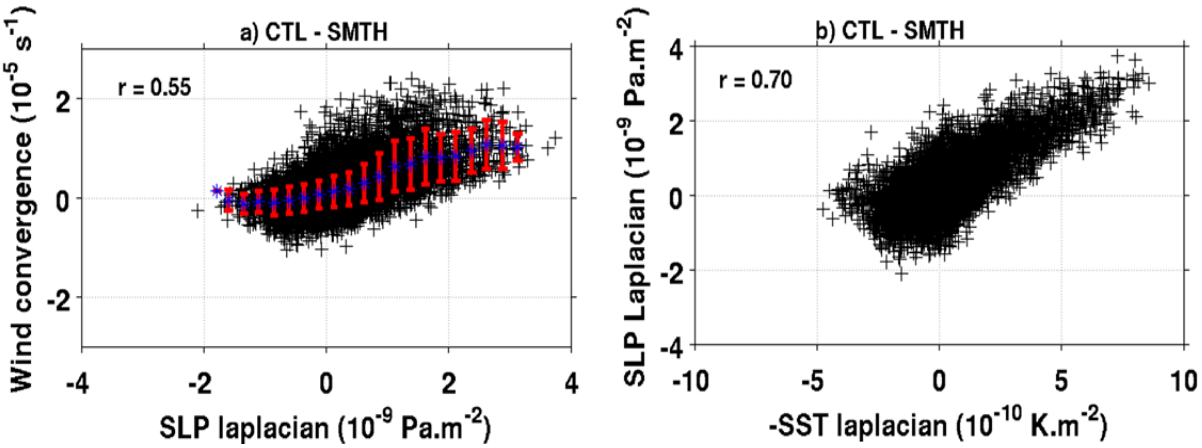

Figure 4.6: Scatter plot showing the relationships between (a) wind convergence and SLP Laplacian and (b) SLP Laplacian and sing inversed SST Laplacian for monthly climatology differences between CTL and SMTH within the region 28–37°S, 23–34°E.

Evaluating the rainfall frequency between the two experiments, we find that the coastal rainfall in SMTH is around 40% less than in CTL (**Fig. 4.7a**). Additional analyses define the type of precipitation due to the warm SST of the core of the Agulhas Current; the coastal rain band is mostly due to convective precipitation, rainfall due to large-scale circulation is almost identical between the two simulations (**Figs. 4.7b, c**), while the coastal convective precipitation is greatly diminished in SMTH (**Figs. 4.7d, e**). Thus, the experiments show that the warmer Agulhas Current SST enhances precipitation along the eastern coast of South Africa.

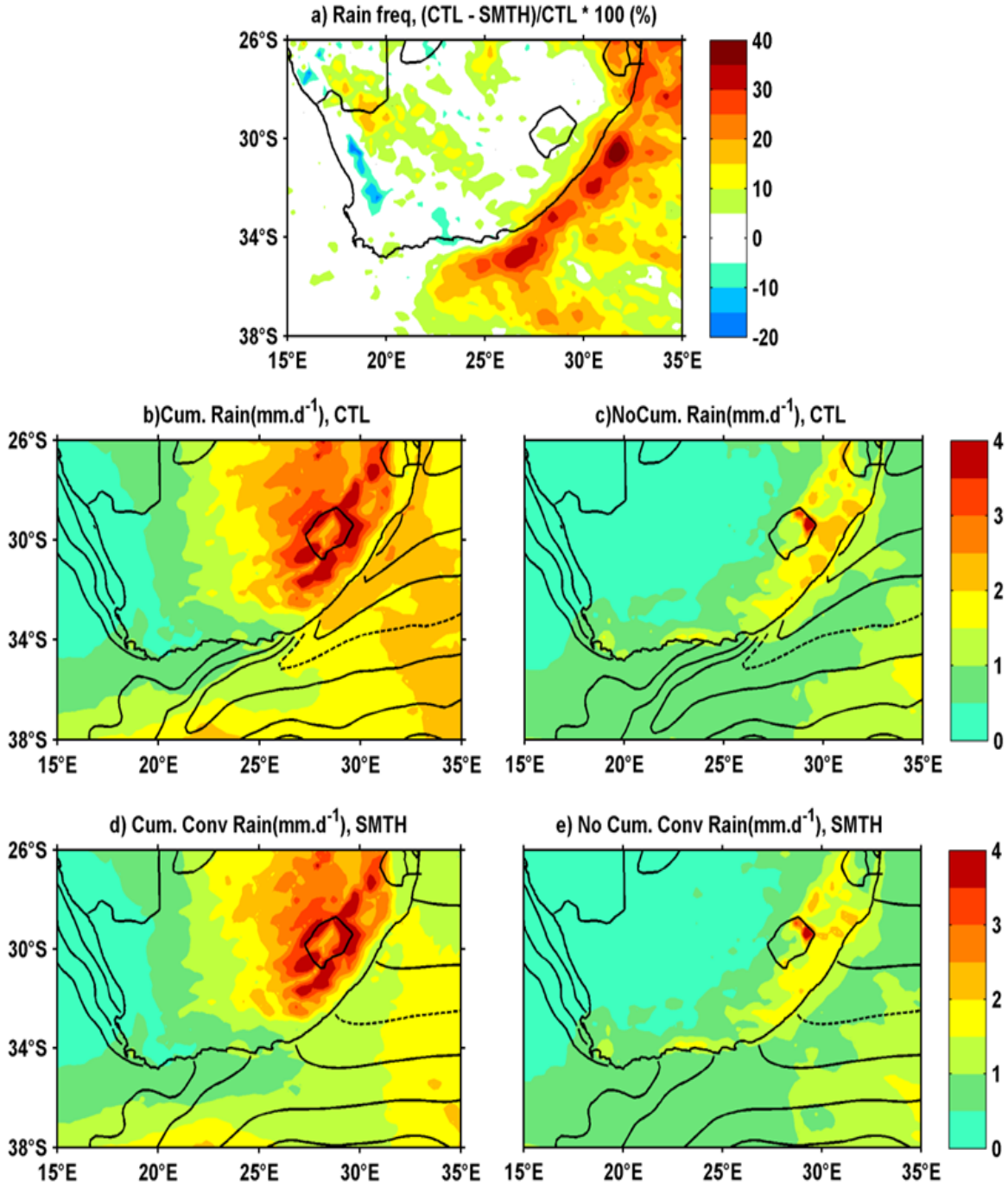

Figure 4.7: Rainfall analysis: a) Rain frequency between CTL rain and the difference between CTL and SMTH rain. b) CTL rainfall, Cum = cumulus convection, c) CTL rainfall, No Cum = without cumulus convection (large scale rainfall). d**)** SMTH rainfall, Cum = Cumulus convection, e) SMTH rainfall, No Cum = without cumulus convection.

4.2.4 Vertical atmospheric structure over the Agulhas Current

The CFSR reanalysis shows strong upward motion in the lower troposphere between 950 and 850 hPa that is co-located with the rainband over the core of the Agulhas Current (**Fig. 4.8a**). Above, there is a distinct structure of the wind divergence between 850 and 700 hPa, and by 650 hPa the upward motion is much reduced and there is mostly large-scale convergence (**Fig. 4.8d**, **Figs. 4.9a, d**). The signature of the Agulhas Current is weak at 650 hPa. At lower-levels there are corresponding narrow bands of subsidence either side of the upward motion that contribute to a local lower tropospheric overturning circulation. Thus, reanalysis suggests that convection reaches only the lower troposphere in accord with measurements made above the Agulhas Current (*Lee-Thorp et al.* 1999; *Rouault et al.* 2000).

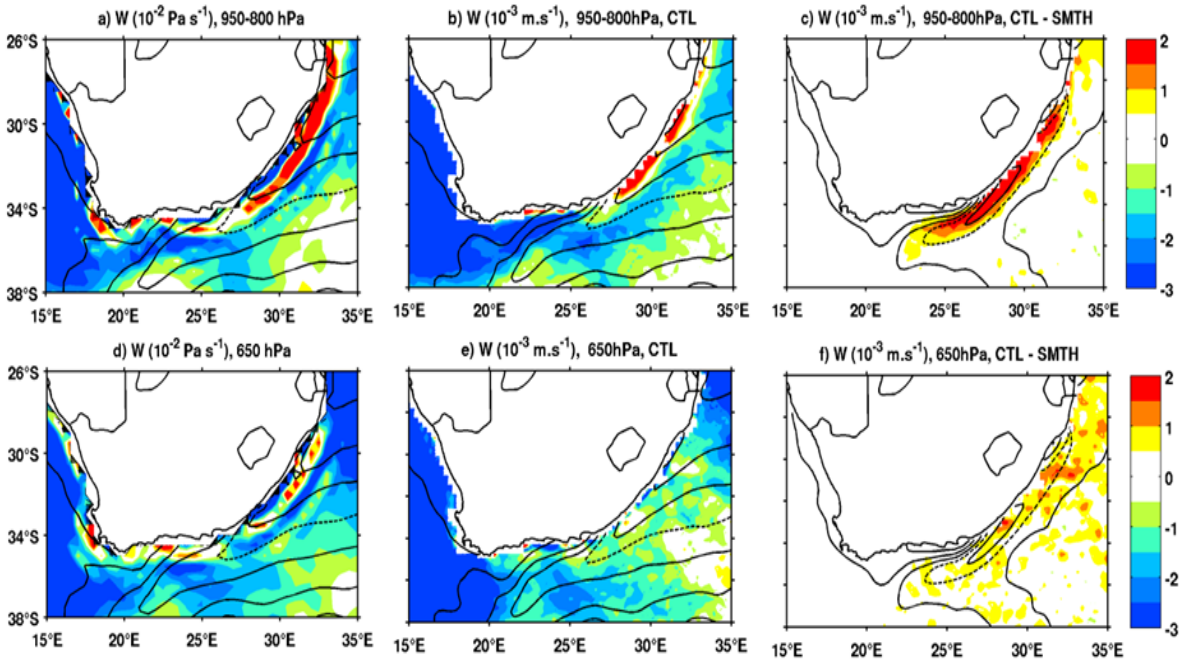

Figure 4.8: The annual mean of vertical velocity vertically averaged between 950 and 800 hPa (a) Climate Forecast System Reanalysis, (b) control (CTL), and (c) the difference between CTL and smoothed SST. (d, e, and f) Their respective 650-hPa vertical velocities with the SST contours overlaid.

The regional model experiments show that the Agulhas Current drives this local overturning circulation. In CTL, the vertical motion at lower levels is weaker and occurs closer to the coast

than in the reanalysis, and there is a broader band of subsidence to the east of the upward motion (**Fig. 4.8b**). Consistent with the weaker upward motion, the horizontal divergence above is weaker and there are few indications of upward motion at 650 hPa (**Fig. 4.8e**; **Figs. 4.9b, e**). The difference between CTL and SMTH confirms that SST associated with the Agulhas Current drives this vertical circulation, which is associated with the rain band along the southern African coast (**Figs. 4.8c, f**; **Figs. 4.9c, f**).

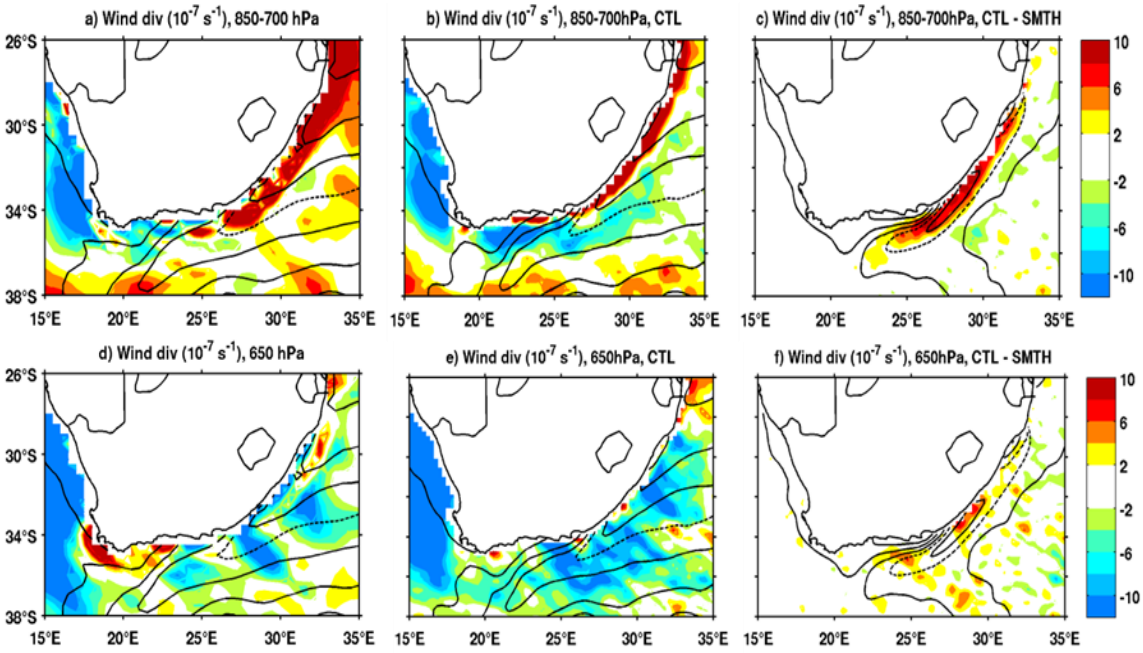

Figure 4.9: The annual mean of the wind divergence averaged between 850 and 700 hPa: a) CFSR, b) CTL and c) the difference between CTL and SMTH. (d,e,f) Their respective 650 hPa wind divergences with the SST contours overlaid.

There are large differences in the rainfall patterns in different seasons, but in all cases there is rainfall over the Agulhas current and coastal regions both in the model and observations (**Fig. 4.10**). Our simulations indicate that the Agulhas current affects terrestrial rainfall most during the austral summer and the least in winter (**Fig. 4.10**). The values of the differences in rainfall range between 0.3 and 1.8 $mm.d^{-1}$ along the coast. It seems that orography and convergence may also be a factor of influencing the regional rainfall, when the flux of moisture created by the current is

advected onshore in summertime. The seasonal mean of the vertical velocity vertically averaged between 950 and 800 hPa (**Fig. 4.11)** shows that the positive anomalies of vertical motion along the inland coast in summer (DJF) are co-located with the increased in rainfall when CTL is compared to SMTH.

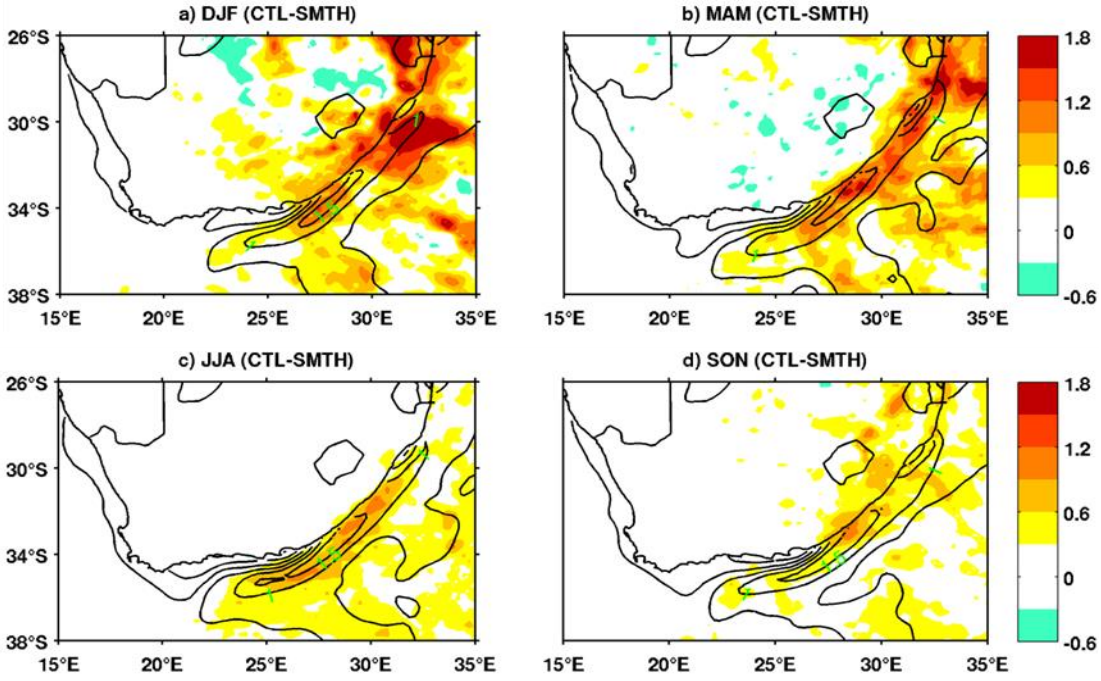

Figure 4.10: Seasonal differences in rainfall between CTL and SMTH: a) DJF (December-January-February), b) MAM (March-April-May), c) JJA (June-July-August), d) SON (September-October-November). There is more rainfall in CTL during summer and spring (DJF, MAM). Solid contours represent annual climatology of OI SST (1° intervals), dashed line is 22°C SST.

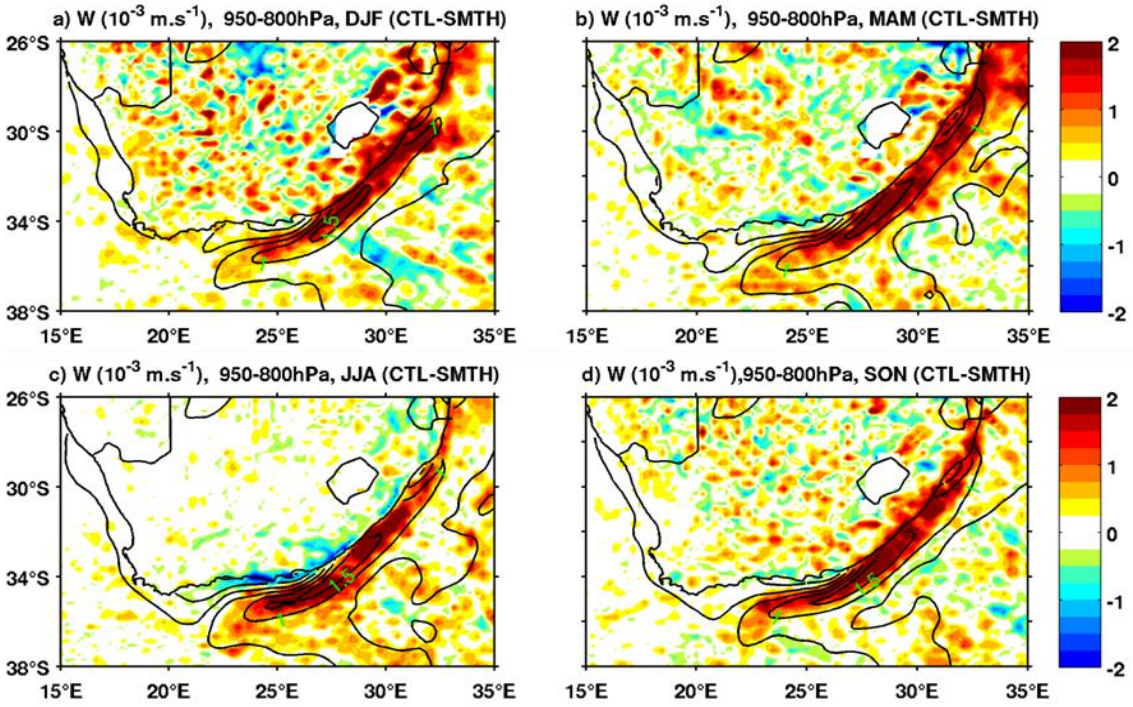

Figure 4.11: As in **Figure 4.10** but for the vertical velocity vertically averaged between 950 and 800 hPa**.**

4.3 DISCUSSION AND SUMMARY

Using high-resolution satellite-derived estimates, climate reanalysis, and regional atmospheric model experiments, we have shown that the warm core of the Agulhas Current drives a band of precipitation along the coast and offshore of South Africa. We found that spatially smoothing the SST leads to a decrease of 50% for wind convergence, of 100% for SLP Laplacian, and a 40% reduction in precipitation over the core of the Agulhas Current.

Diagnosis of the pressure adjustment mechanism identifies a very similar relationship to that of the Gulf Stream (*Minobe et al.* 2008). Recent studies, however, indicate that the anchoring of precipitation over the Gulf Stream front is mainly associated with atmospheric frontal precipitation associated with synoptic-scale extratropical cyclones (*O'Neill et al.* 2017; *Parfitt et al.* 2016, *Sheldon et al.* 2017; *Vannière et al.* 2017). A similar mechanism might act over the Agulhas Current, as a large part of the rainfall here is also related to atmospheric fronts (*Catto et al.* 2012).

Our atmospheric model simulations indicate that up to 20% of the coastal precipitation is related to the warm core of the Agulhas Current. This may represent a lower limit as increasing the model resolution might increase the strength of ocean-atmosphere interaction (*Smirnov et al.* 2015). Thus, it is important to resolve the fine structure of ocean temperature for simulating the climate of the region. This has implications for the prediction of South African weather and climate and for understanding past and present climate. Moreover, the diurnal cycle is an important driver of terrestrial rainfall in summer along the inland coast (*Pohl et al.* 2014; *Rouault et al.* 2013), and low-level convergence associated with orography may also be a factor that enhances summer rainfall. A complete understanding of how the Agulhas Current drives terrestrial precipitation in this region will therefore involve in-depth analysis of both the diurnal cycle and seasonality of various parameters such as the wind speed, the sea surface temperature, the sea level pressure.

CHAPTER 5

5 SEASONAL IMPACT OF THE AGULHAS CURRENT ON SOUTH AFRICA PRECIPITATION

This chapter is a follow up of the previous chapter and focuses on the seasonal impact of the Agulhas Current on Southern Africa rainfall. We use the high-resolution gridded climatology of *Hewitson and Crane* (2005) based on observations, Tropical Rainfall Measuring Mission Precipitation Radar (TRMM PR, *Biasutti et al.* 2012), optimal interpolation sea surface temperature (OISST, *Reynold et al.* 2007), Globcurrent geostrophic currents (*Johannessen et al.* 2016), the Climate Forecast System Reanalysis (CFSR, *Saha et al.* 2010), and two experiments of the Weather Research and Forecasting model (WRF, *Skamarock and Klemp* 2008). Simulations of the regional model are conducted to isolate the effect of the Agulhas warm core on the atmosphere (**Chap. 2**). One experiment represents the sea surface temperature and latent heat flux (WRF control), the other is with SST reduced by 2°C in the core of the Agulhas Current (WRF smoothed). The present chapter gives a hint of the probable seasonal impact of the Agulhas Current on the regional climate.

5.1 HIGH-RESOLUTION SURFACE PARAMETERS

5.1.1 Surface current, sea surface temperature and latent heat flux

Figure 5.1 shows the seasonal cycle of the Agulhas Current derived from the 0 m depth GlobCurrent geostrophic currents (*Johannessen et al.* 2016) for the austral summer (DJF), autumn (MAM), winter (JJA) and spring (SON). The geostrophic current speed ranges between 0.5 to about 1.5 $m.s^{-1}$, with a maximum along the coast in summer (**Fig. 5.1a**). The Current increases in speed in this region between 25 and 38°S, with a maximum off Port Elizabeth (~34°S, 23-26°E). The current speed minimum in the Agulhas region is between 1 to 1.25 $m.s^{-1}$ in winter (32-38°S,

20-30°E) (**Fig. 5.1c**). This is consistent with results from *Krug and Tournadre* (2012) which concluded that there is a seasonality in the Agulhas Current, with a strong flow in summer, and weaker velocities in winter, with a seasonal geostrophic current speeds varying from 1.5 $m.s^{-1}$ in March to 1.3 $m.s^{-1}$ in July. Warm sea surface temperature (SST) are found in the Agulhas Current system, compared to the surrounding region, with a maximum temperature of about 28°C in summer and 22°C in winter (*cf.* **Fig. 3.4**).

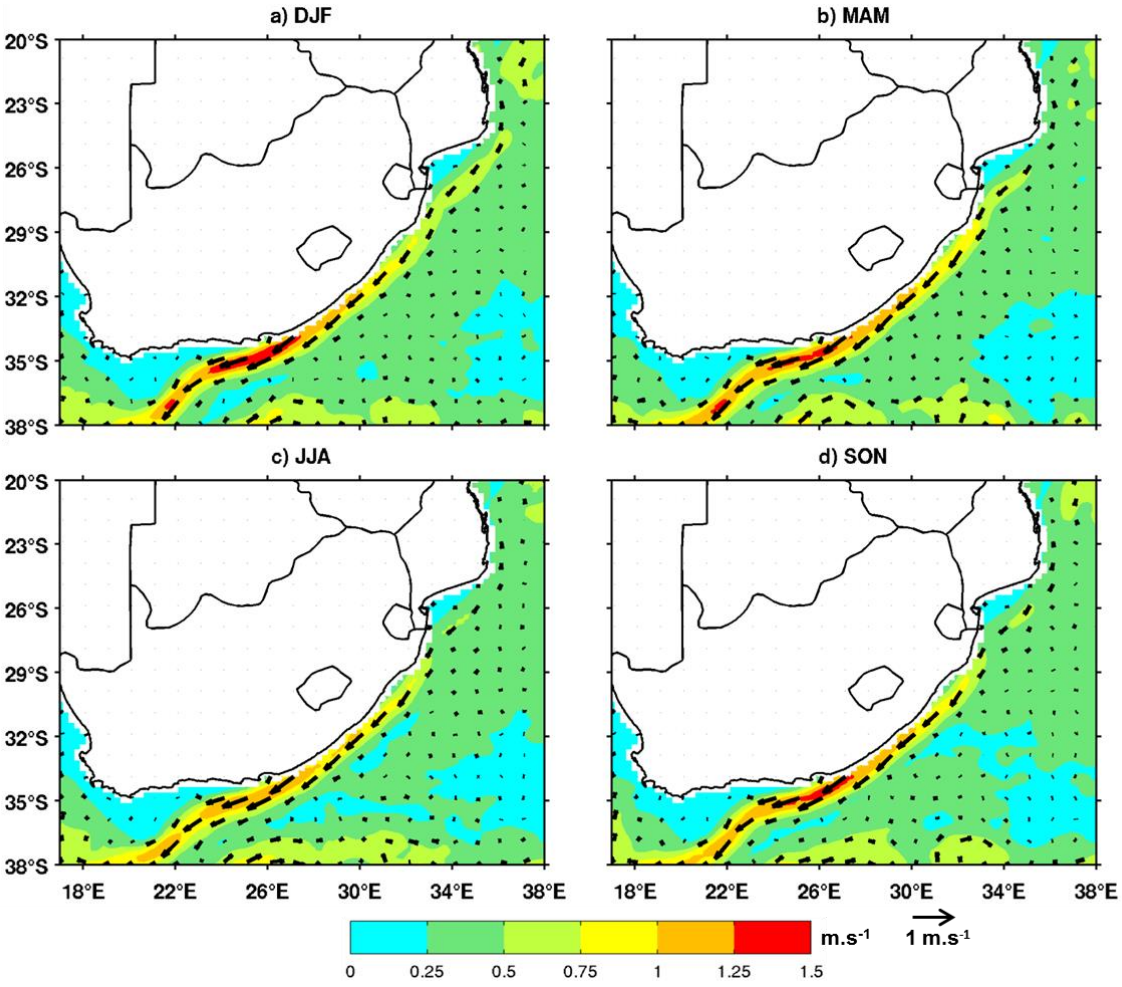

Figure 5.1: Seasonal averages of the surface geostrophic current ($m.s^{-1}$) from GlobCurrent at 0 m depth: a) summer (DJF), b) autumn (MAM), c) winter (JJA) and d) spring (SON). Arrows represent the direction of the current for the respective seasons every 2°. Off Port Elizabeth (~33°S), the current speed accelerates and can reach 1.5 $m.s^{-1}$ in DJF, MAM or SON.

Seasonal SST of WRF control experiment is shown in **Figure 5.2**. SST reaches 28°C in summer (DJF), northeast of South Africa (**Fig. 5.2a**), with the warmest SST occurring in February (*cf* **Fig. 3.5** of **Chap. 3**). There is a temperature gradient along the east coast, due to the Agulhas Current. SSTs above 25°C are found east of 29°E, potentially creating convection. In autumn (MAM), SST is quite similar to summer (DJF) (**Fig. 5.2b**) because the SST is maximum in February and March. Winter (JJA) is the season with the coolest SST in the Agulhas region (**Fig. 5.2c**), with the lowest SST in August. During winter, in the Agulhas region, maximum SST is 23°C and minimum SST is 20°C when the Current separates from the coast (*cf.* **Chapter 3**). Spring (SON) SST is similar to winter SST, with the warmest SST along the coast, in the Agulhas Current (**Fig. 5.2d**).

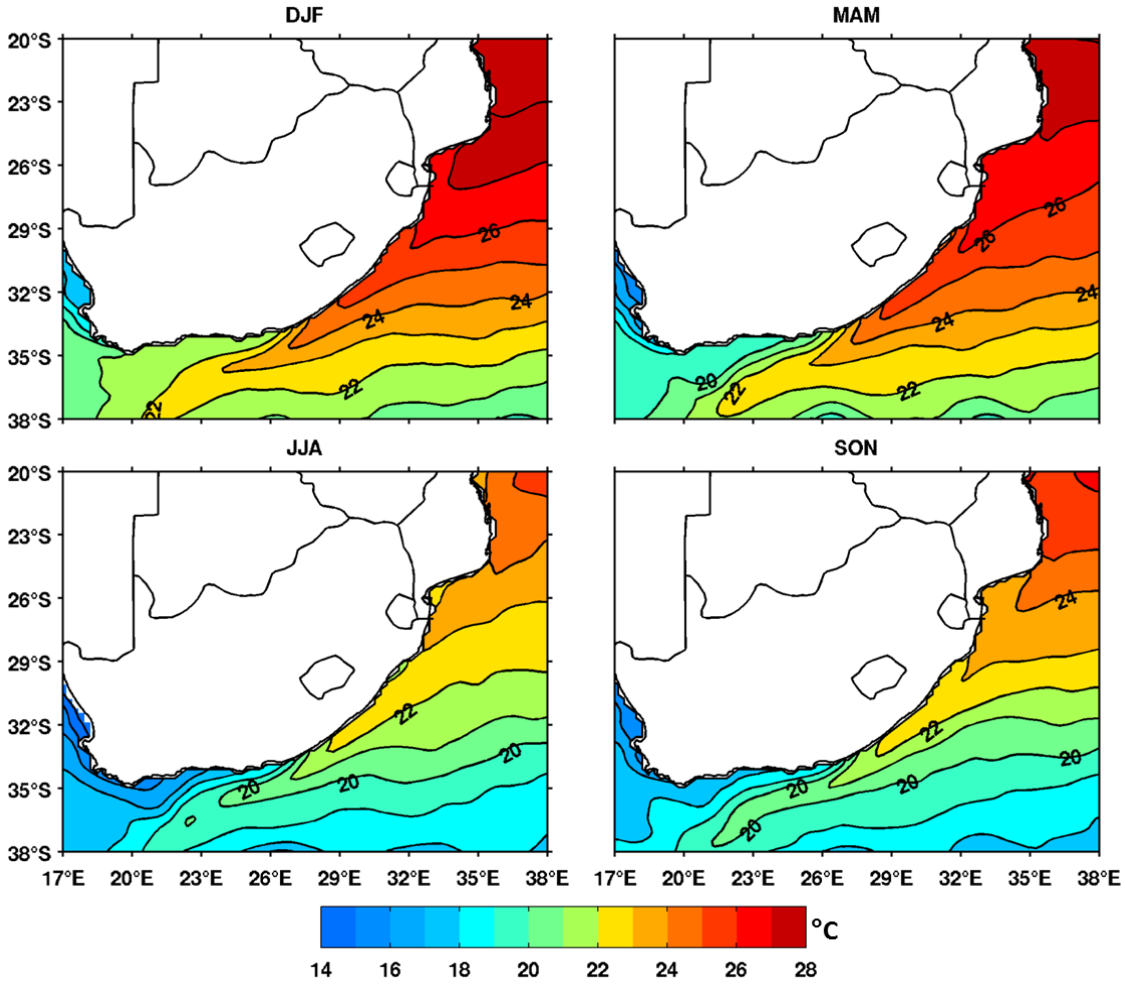

Figure 5.2: Seasonal means SST for WRF control experiment, with 1°C intervals overlaid: a) summer (DJF), b) autumn (MAM), c) winter (JJA) and d) spring (SON).

A warm SST in the Agulhas Current causes a large amount of turbulent flux of moisture (also called turbulent latent heat flux, LHF) from ocean to atmosphere. Above the Agulhas Current LHF is maximum all year long (between 175 and 250 $W.m^{-2}$), but with higher values in winter especially along the coast (**Fig. 5.3c**) and lower values in summer (**Fig. 5.3a**). This result is in accordance with the seasonal cycle of LHF in **Chapter 3**. Over the landmass, the minimum LHF is in winter (~50 $W.m^{-2}$), and maximum LHF is in summer (~150 $W.m^{-2}$) corresponding to ~1.8 $mm.d^{-1}$ in winter and ~5.3 $mm.d^{-1}$ in summer. Note that 1 $mm.d^{-1}$ is approximately 28.36 $W.m^{-2}$.

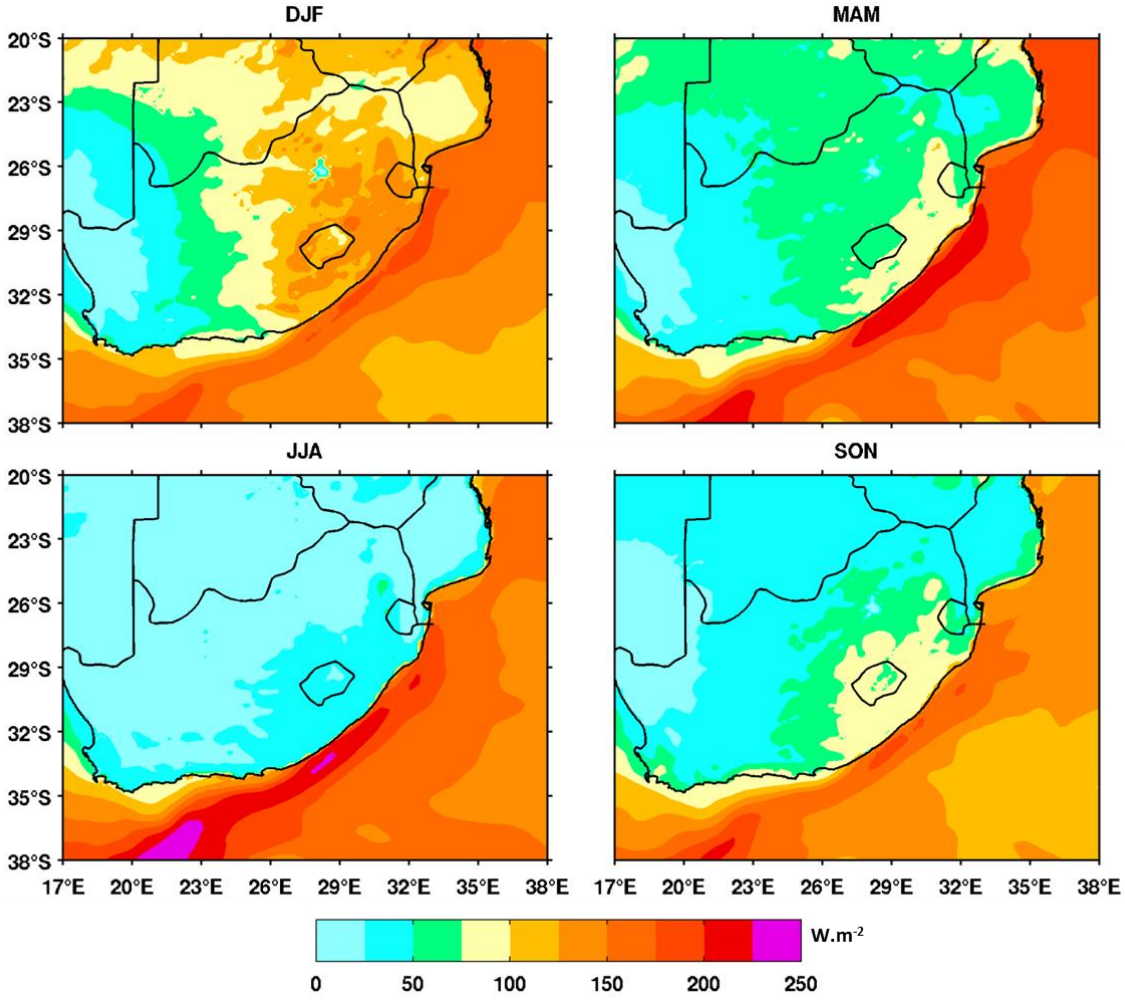

Figure 5.3: Seasonal latent heat flux ($W.m^{-2}$) averages for WRF control experiment: a) summer (DJF), b) autumn (MAM), c) winter (JJA) and d) spring (SON).

5.1.2 Precipitation

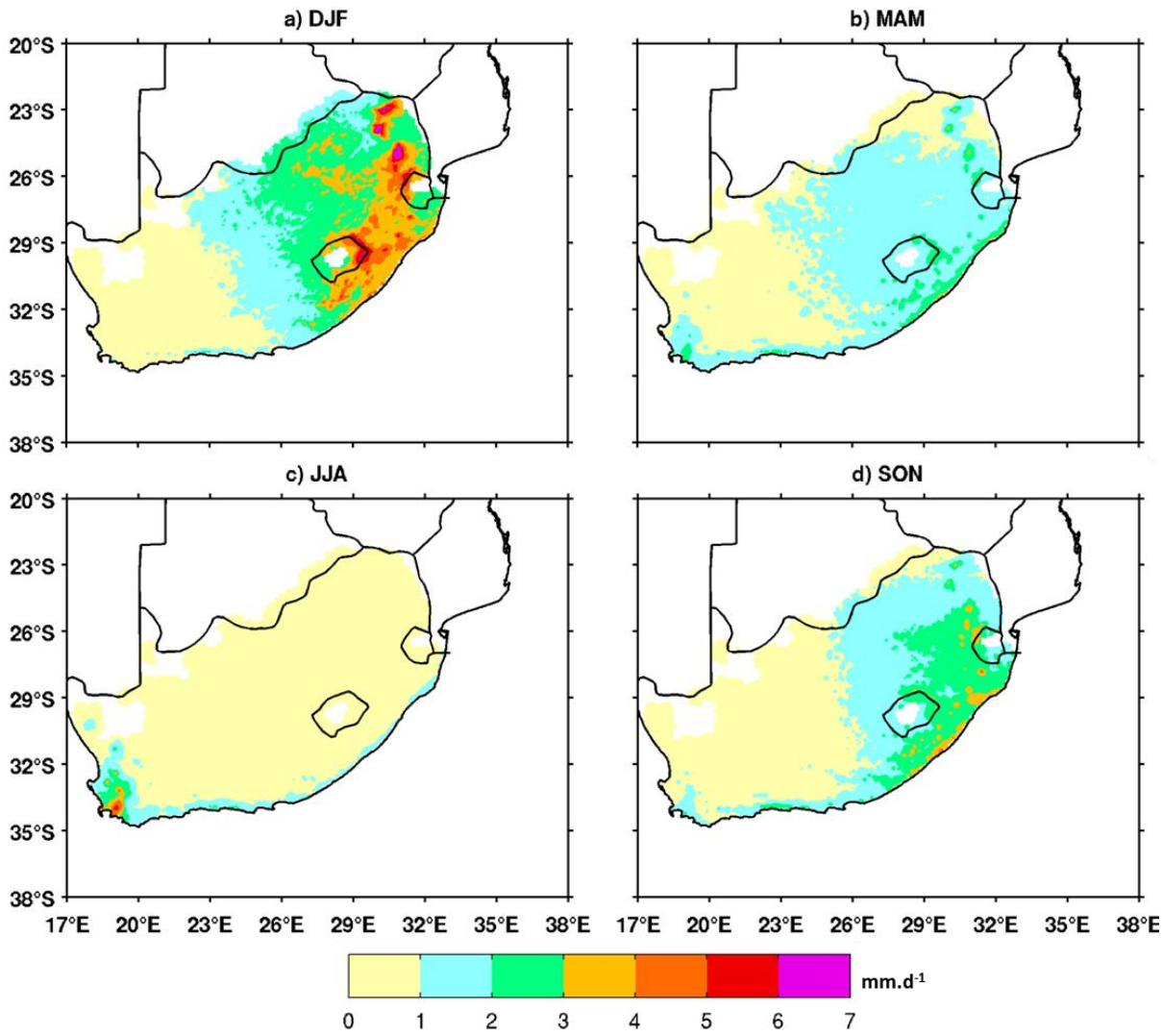

Figure 5.4: Seasonal climatology of South Africa rainfall (mm.d^{-1}) from 1950 to 2000, of the gridded-averaged daily precipitation data from *Hewitson and Crane* (2005): a) summer (DJF), b) autumn (MAM), c) winter (JJA) and d) spring (SON).

We use a 50-year climatology of South African precipitation from *Hewitson and Crane* (2005) to validate the simulated rainfall by WRF control and CFSR over land. This high-resolution climatology (0.1° x 0.1°) is a gridded-average daily precipitation computed from 1950 to 2000, using the conditional interpolation method (*Hewitson and Crane* 2005). South African

precipitation ranges between 0 to 7 mm.d^{-1}, with a maximum in summer (DJF) southeast of the country between 23-26°S and 30-31°E (**Fig. 5.4a**). Another maximum is around the Drakensberg region, between 29-30°S and 29-30°E. Meanwhile, the southwest of the country is arid. Autumn (MAM) is a transitional season between summer (DJF) and winter (JJA). During autumn, precipitation ranges between 0 to 3 mm.d^{-1}, with a maximum along the "garden route" and the east coast of South Africa. This maximum lasts until winter, forming a rainband ranging between 1 and 2 mm.d^{-1} (**Fig. 5.4c**). Winter is the rainy season over the Western Cape (31-34°S and 18-20°E), with precipitation up to 6 mm.d^{-1} due to the effect of the orography. Meanwhile, the rest of the country is arid. *Preston-Whyte and Tyson* (1988) investigated the winter rainfall over the south coast and the southwestern region and concluded that the winter rainfall originates from the cold fronts. Spring (SON) is the transition season between winter-summer and is marked by the increase in precipitation over the southeast of South Africa, with a maximum rainfall along the east coast where the Agulhas Current is adjacent to the coast (**Fig. 5.4d**).

We use the high-resolution (0.05° x 0.05°) TRMM PR to validate the WRF control and CFSR rainfall above the ocean. **Figure 5.5** shows the seasonal mean rainfall of TRMM PR. TRMM PR overestimates the summer terrestrial rainfall by 1 mm.d^{-1} (**Fig. 5.5a**) compared to the climatology of *Hewitson and Crane* (2005). Moreover, TRMM PR the precipitation along the inland coast underestimates by 2 mm.d^{-1} compared to the former climatology, which shows maximum rainfall along the coast. Over the ocean, the highest summer precipitation is northeast of southern Africa. In autumn (MAM), terrestrial precipitation is also overestimated by 1 mm.d^{-1} (**Fig. 5.5b**) compared to the climatology of *Hewitson and Crane* (2005). Above the ocean, highest values of rainfall is over the Agulhas region and the South Indian Convergence Zone (SICZ). TRMM PR underestimates the winter (JJA) rainfall over the Western Cape, and the inland coast to the east (**Fig. 5.5c**). Over the ocean, the influence of the Agulhas Current is clearly apparent in winter precipitation. In spring (SON), precipitation is abundant over the landmass, in the southeast of South Africa (**Fig. 5.5d**).

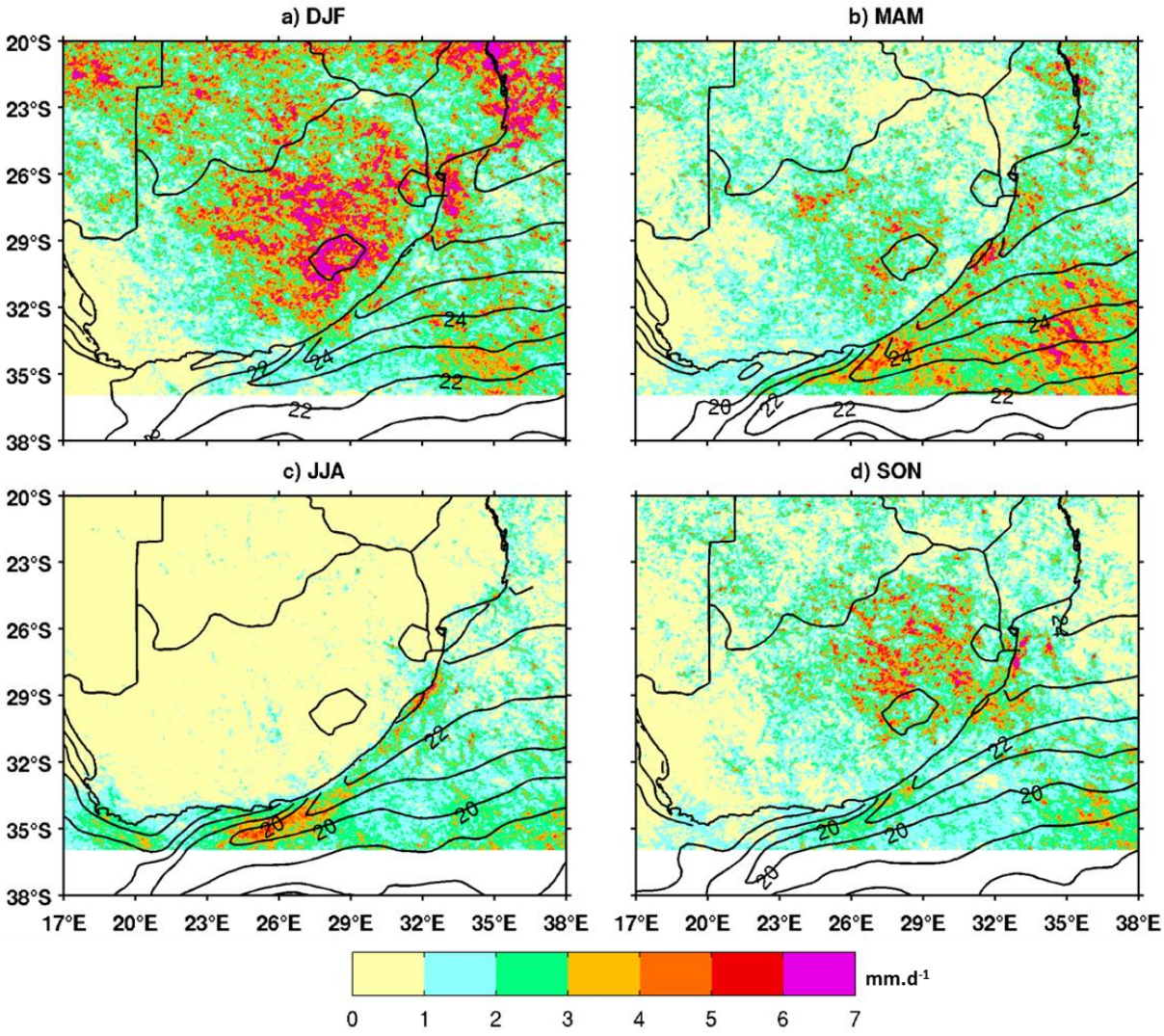

Figure 5.5: Seasonal averages of rain rate (mm.d^{-1}) from Tropical Rainfall Measuring Mission Precipitation Radar, with the overlaid optimal interpolation sea surface temperature (SST) (°C), respectively for: a) summer (DJF), b) autumn (MAM), c) winter (JJA) and d) spring (SON). Summer is the wettest season over the continent, autumn and winter are the wettest above the Agulhas Current region.

The summer WRF control rainfall overestimates the climatology of *Hewitson and Crane* (2005) by 3 mm.d^{-1}, southeast of South Africa (**Fig. 5.6a**). Along the inland coast, WRF control captures the maximum rainfall seen in the former climatology, but overestimates the oceanic rainfall

compared to TRMM PR. This might be due to the orographic effect of the Drakensberg (*Tyson and Preston-White* (2000), **Chap. 4**).

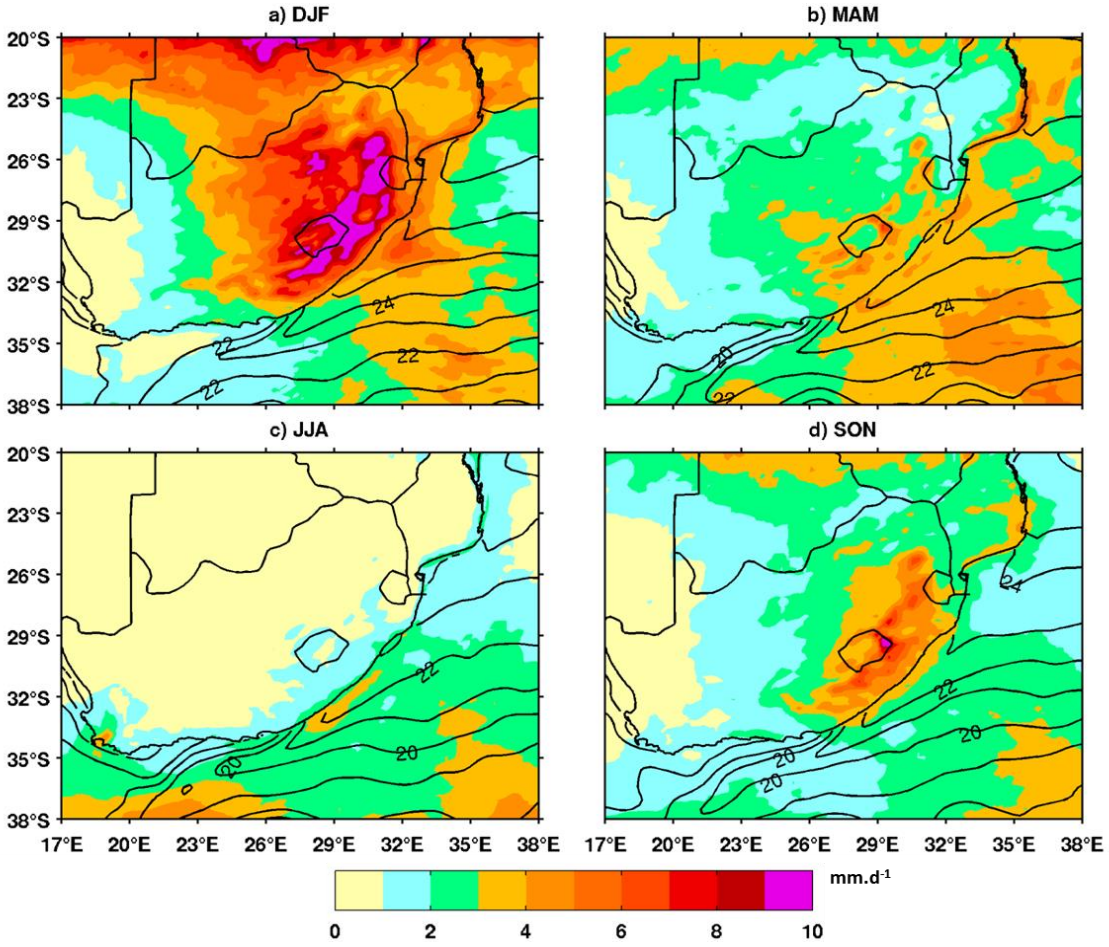

Figure 5.6: Seasonal averages of rain rate for WRF control experiment with the corresponding SST (°C) overlaid: a) summer (DJF), b) autumn (MAM), c) winter (JJA) and d) spring (SON). Summer is the wettest season over the continent.

In winter (JJA) above the Agulhas, precipitation ranges between 3-4 mm.d^{-1}. Thus WRF control underestimates the coastal precipitation by 2 mm.d $^{-1}$ above the Agulhas Current compared to TRMM PR (**Fig. 5.5c**). In spring (SON), WRF control overestimates the terrestrial and maritime precipitation compared to the climatology of *Hewitson and Crane* (2005), and TRMM PR (**Fig. 5.5d**). Generally, the "garden road" also called the South Coast or all year South Africa rainfall region (*Engelbrecht et al.* 2015, 2016) experiences equal rainfall throughout the year and could be

due to air-sea contrasts opposing on one hand the Agulhas Current causing huge latent heat fluxes (see **Chap. 3**), on the other hand the topography of Little Karoo. It is needed to do more experiments to really define the cause of the constant rainfall along the "garden route". To summarise, WRF model overestimates the land precipitation compared to *Hewitson and Crane* (2005) for all seasons. WRF model overestimates the maritime precipitation in summer, autumn, and spring, compared to TRMM PR, but underestimates the winter precipitation above the Agulhas Current. CFSR precipitation underestimates the land and oceanic rainfall by 1 to 3 mm.d^{-1} for all seasons (**Fig. 5.7**), compared to the climatology of *Hewitson and Crane* (2005) for land rainfall and TRMM PR for the maritime precipitation.

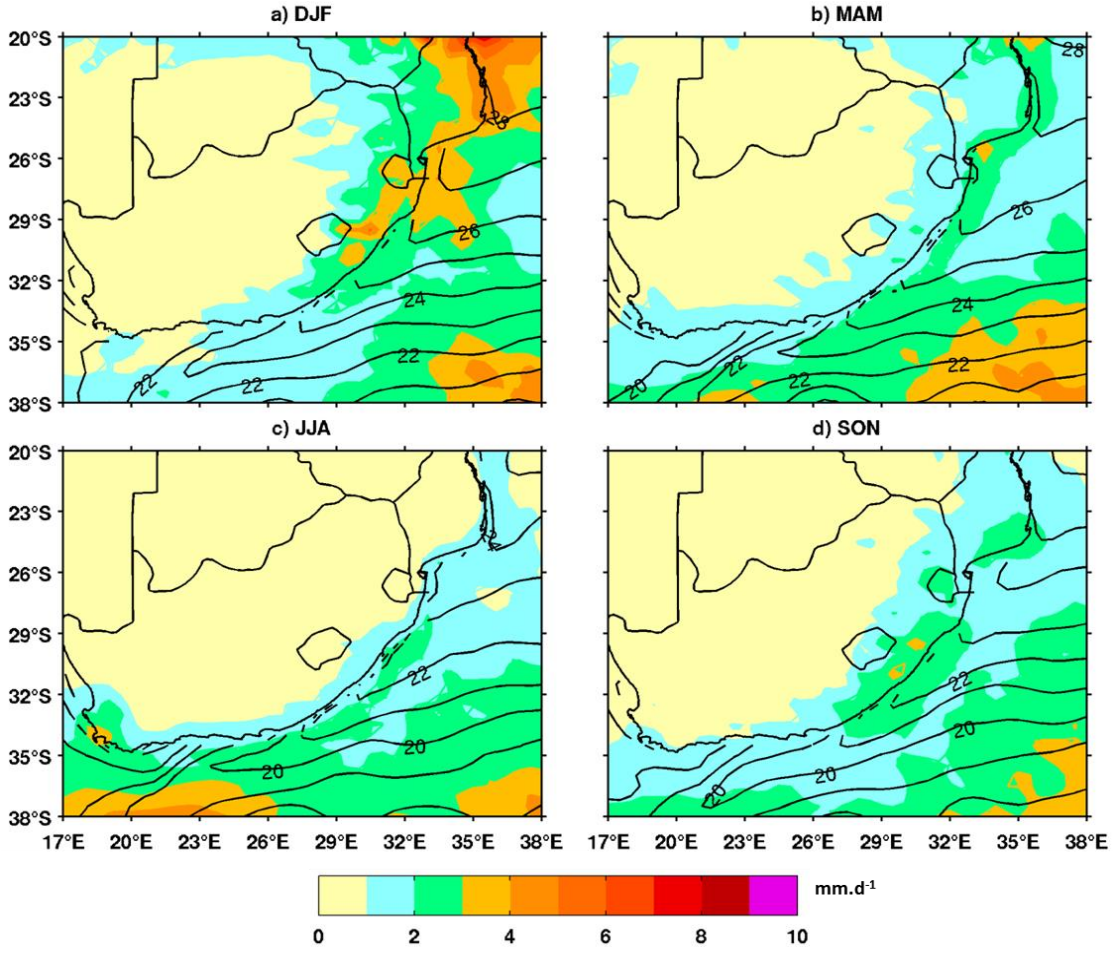

Figure 5.7: Seasonal averages of rain rate of Climate Forecast System Reanalysis (CFSR), with the CFSR sea surface temperature (SST) (°C) overlaid: a) summer (DJF), b) autumn (MAM), c) winter (JJA) and d) spring (SON).

5.1.3 Analysis of the pressure adjustment mechanism

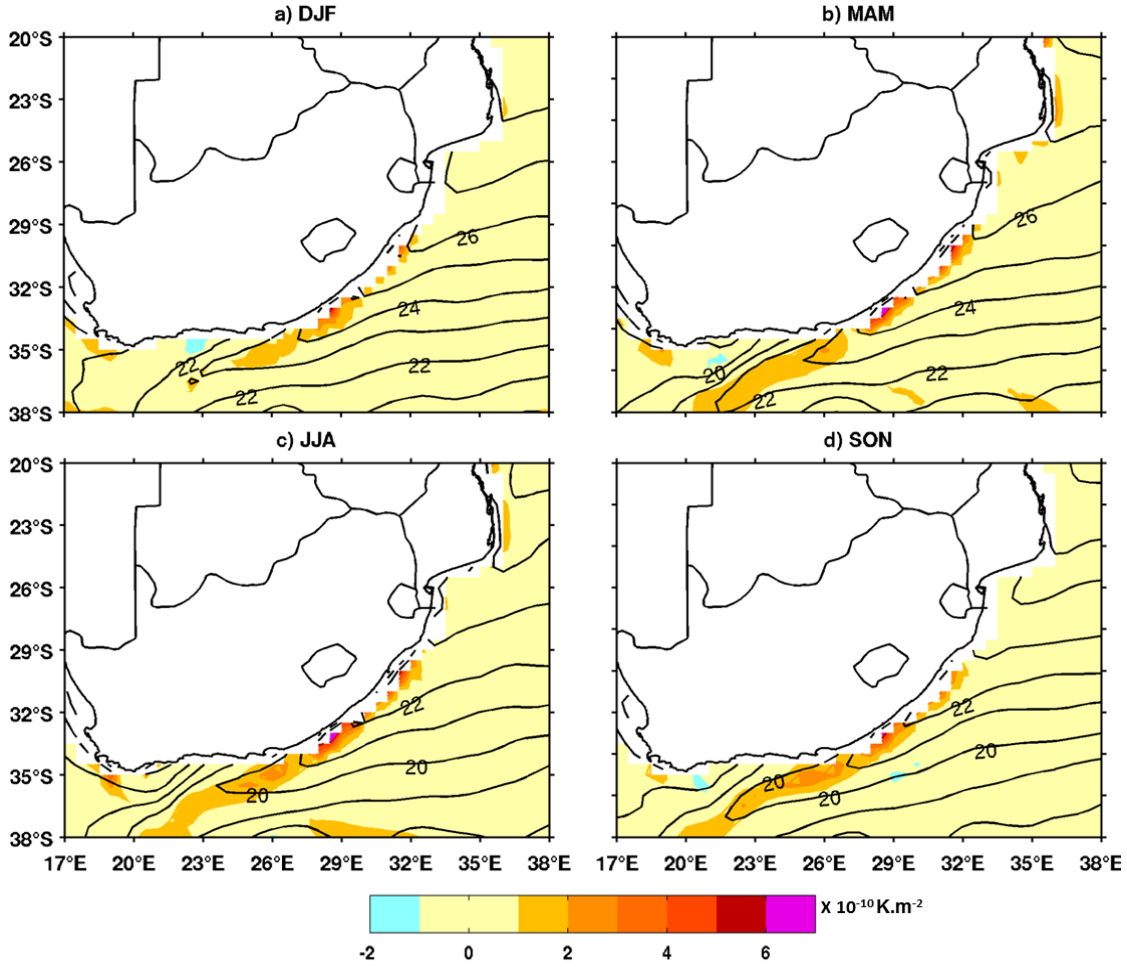

Figure 5.8: Seasonal averages of CFSR sign reversed SST Laplacian: a) summer (DJF), b) autumn (MAM), c) winter (JJA) and d) spring (SON). The patterns of the Agulhas Current along the coast are present for each season. Solid contours represent CFSR seasonal means SST.

We examine the relationship between the sign reversed SST Laplacian, the 10 m wind convergence and the sea level pressure (SLP) Laplacian for each season. The Laplacian acts as a high-pass filter to highlight the regions with strong gradients such as the Agulhas Current. The SST Laplacian, wind convergence and SLP Laplacian are linked by the pressure adjustment mechanism (*Lindzen and Nigam*, 1987; *Minobe et al.* 2008; **Chap. 4**) following **Equations 2.3 and 2.4** of **Chapter 2**,

in which the SST modifies the marine atmospheric boundary layer, and the resultant pressure produces wind convergence over warm SSTs and wind divergence over cold SSTs.

The sign reversed SST Laplacian along the eastern coast of South Africa shows a strong gradient for each season (**Fig. 5.8**). This result is observed for the annual scale (**Chap. 4**). SST Laplacian is large along the coast for each season (between 20-32°E), but in summer (**Fig. 5.8a**) the signal is between 24 and 32°E.

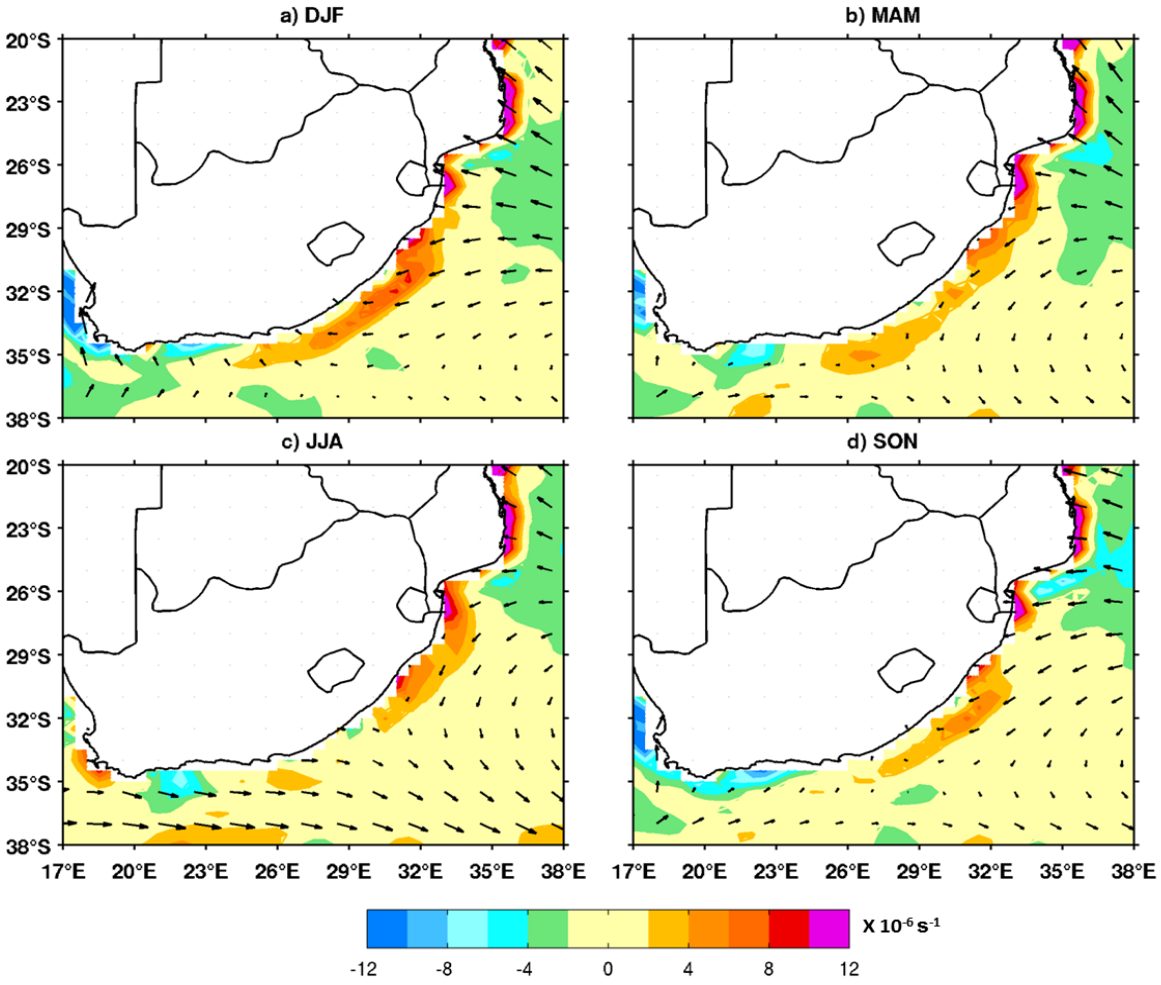

Figure 5.9: Seasonal averages of the CFSR wind convergence (positives values): a) summer (DJF), b) autumn (MAM), c) winter (JJA) and d) spring (SON). Arrows represent the 10 m wind velocities for CFSR, every 2°.

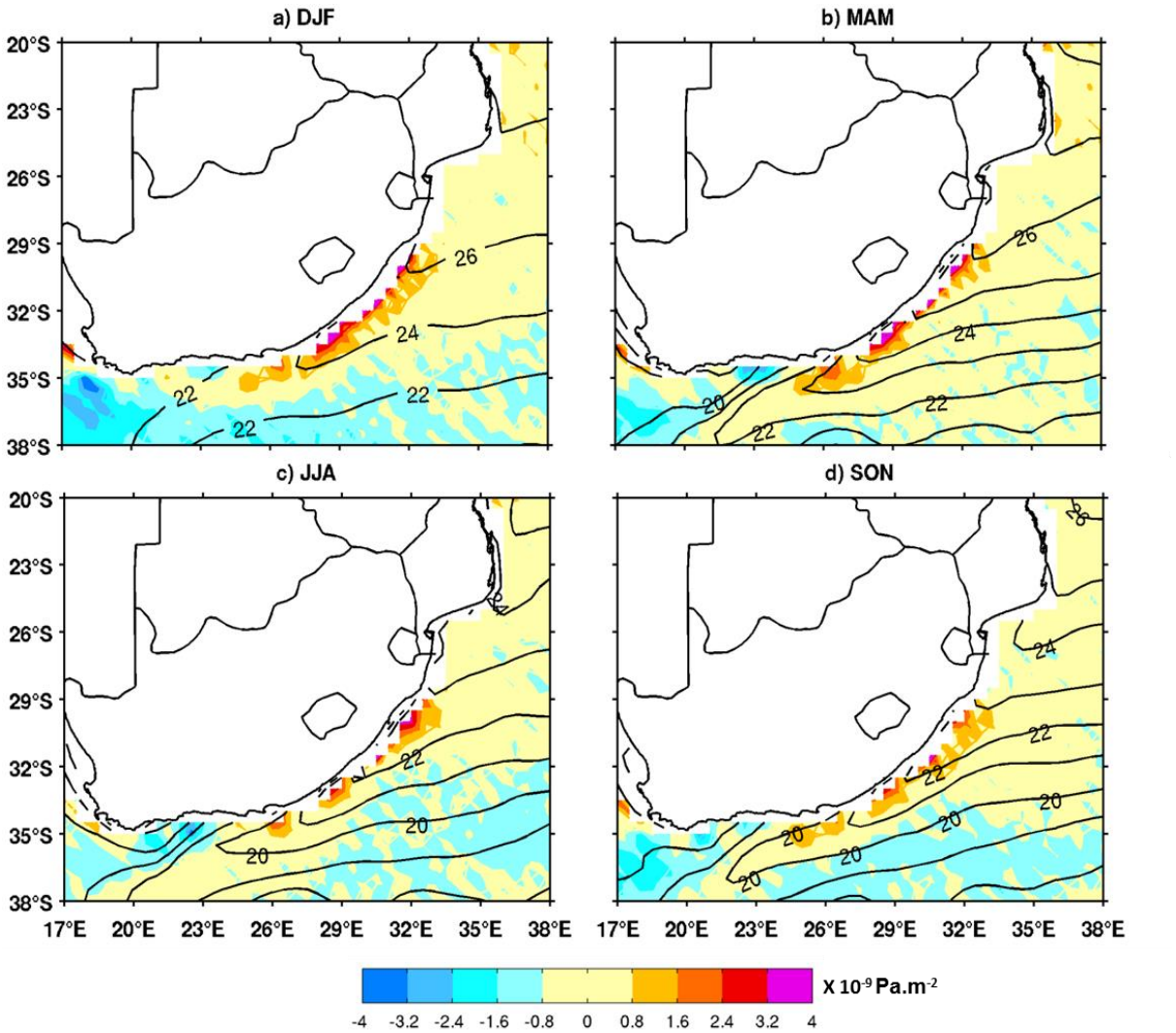

Figure 5.10: Seasonal averages of CFSR SLP Laplacian: a) summer (DJF), b) autumn (MAM), c) winter (JJA) and d) spring (SON). The signature of the Agulhas Current is seen for each season. Solid contours represent CFSR seasonal means SST.

The horizontal distribution of wind convergence (**Fig. 5.9**) is consistent with that in the annual mean analysis of **Chapter 4**, but exhibits a stronger magnitude in summer (DJF) and autumn (MAM), compared to other seasons. In summer, the wind is onshore northeast of South Africa and over the Agulhas Current (**Fig. 5.9a**). It blows from the ocean towards land, bringing moist air from the Indian ocean. This may create orographic rainfall. As in autumn (MAM) and spring (SON) northeast of South Africa, but over the Agulhas Current, the wind is alongshore, decelerates up to 32°S and joins the westerlies (**Fig. 5.9b, d**). In winter, over the Current, the wind coming from the Indian Ocean decelerates (**Fig. 5.9c**). In the Western Cape region, wind convergence is

confined between 33-35°S, 18-19°S and the wind direction is onshore. This creates rainfall due to the effect of the orography. The SLP Laplacian exhibits a strong signal above the core of the Agulhas compared to the surrounding ocean for each season (**Fig. 5.10**).

Correlation between SLP Laplacian and wind convergence, and correlation between SLP Laplacian and SST Laplacian for each season, within the boxes 28-37°S and 23-34°E are shown in **Figure 5.11** as in **Chapter 4**. The SLP and SST Laplacian are highly correlated for each season, with correlations between 0.6 and 0.85, significant at the 95% confidence level (**Fig. 5.11a**). These significant correlations are consistent with our findings on the annual scale (**Chap. 4**). A strong correlation is found between SLP Laplacian and wind convergence (significant at the 95% level) in December-January-February, and September-November, leading to a high correlation in summer (DJF, 0.6) and spring (SON, 0.5) respectively (**Fig. 5.11b**). Meanwhile, a weak but significant correlation in May and August leads to fair good correlations (~0.4) in autumn and winter. This result indicates that the pressure adjustment might contribute to enhancing seasonal precipitation above the Current along the coast where the Current is adjacent to the coast as shown in former chapter.

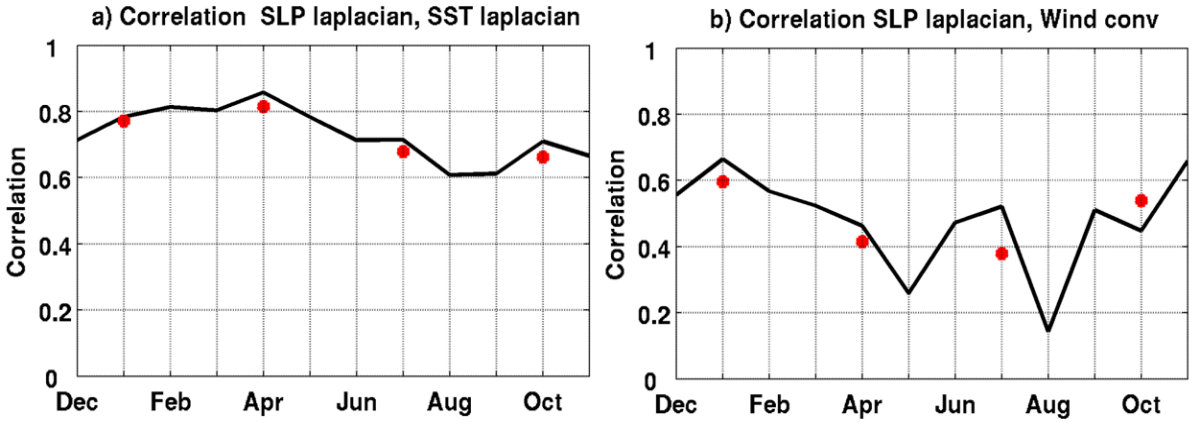

Figure 5.11: Correlations based on monthly climatology within the region 28–37°S, 23–34°E between: a) SLP Laplacian and SST Laplacian, b) SLP Laplacian and wind convergence. Red dots represent the seasonal correlations significant at the 95% confidence level.

To summarise this section, a good correspondence among the SST Laplacian, SLP Laplacian, and wind convergence are found each season, between 28–37°S and 23–34°E (**Figs. 5.8, 5.9,** and **5.10**). This indicates that the pressure adjustment mechanism could enhance the band of precipitation above the Agulhas Current for each season.

5.2 NUMERICAL EXPERIMENTS

In this section, we look at the impact of the warm SST due to the Agulhas Current on South Africa rainfall. The analysis is mostly based on the difference between the WRF control experiment (CTL), and the experiment with a smoothed SST (SMTH), to unveil the impact of smoothing the SST gradients in the Agulhas Current region.

5.2.1 Surface parameter difference

5.2.1.1 Sea surface temperature and latent heat flux

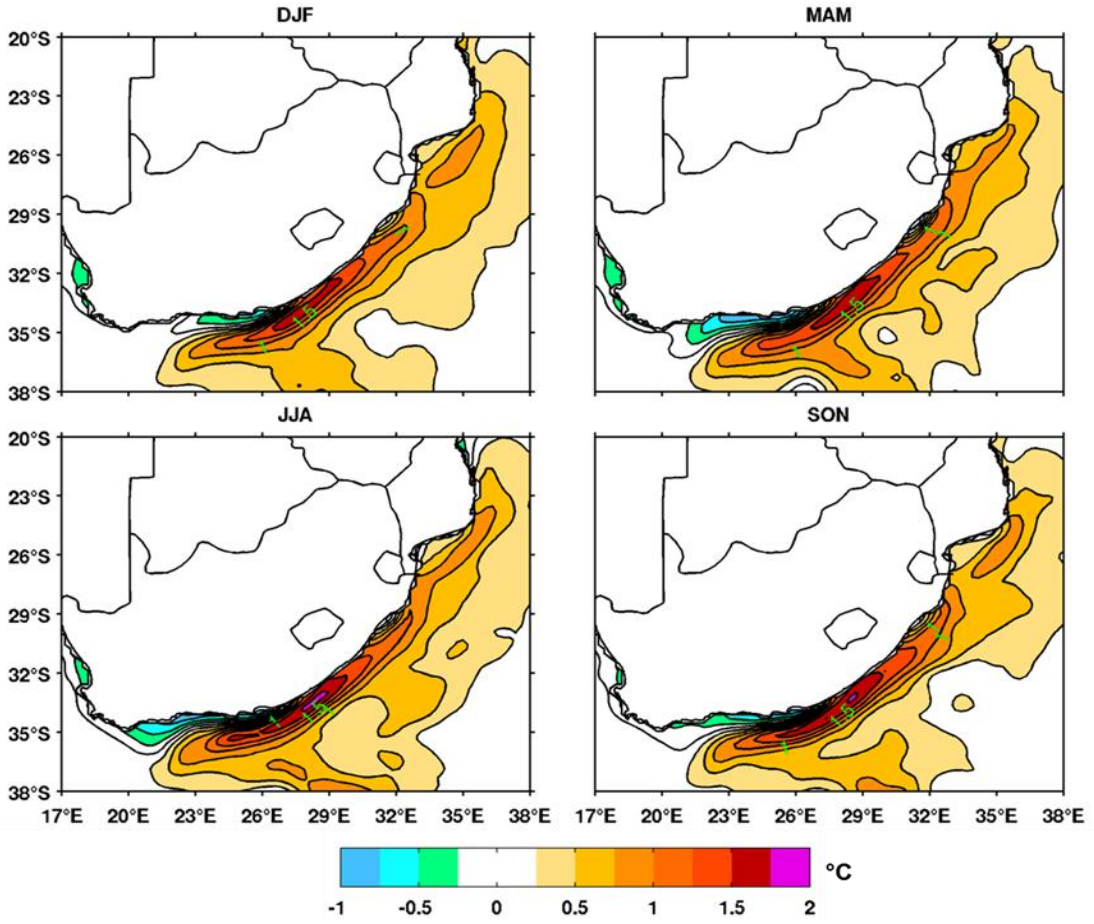

Figure 5.12: Seasonal SST differences between control and smooth SST experiments, with 0.25°C intervals overlaid: a) summer (DJF), b) autumn (MAM), c) winter (JJA) and d) spring (SON).

The SST difference between the two simulations is up to 2°C along the coast, and presents a weak seasonality because the differences are more or less the same for each season (**Fig. 5.12**). The maximum difference is found in the core of the Agulhas Current, around 33-35°S and 27-30°E. Smoothing the SST also leads to a 1°C cooler SST around the Western Cape region (31-33°S, 18°E) and the "garden route" (34°S, 20-26°E) for each season.

The LHF difference between the two simulations exhibits a maximum along the coast (**Fig. 5.13**), consistent with the SST difference (**Fig. 5.12**). The LHF difference is ±65 W.m^{-2}. Thus, SST reduced by ~2°C leads to 55 W.m^{-2} decline of LHF. This result is consistent with the findings of **Chapter 4**. Over the landmass, north of South Africa, the LHF difference is up to 25 W.m^{-2} in summer, autumn, and spring (**Figs. 5.12a, b** and **d**).

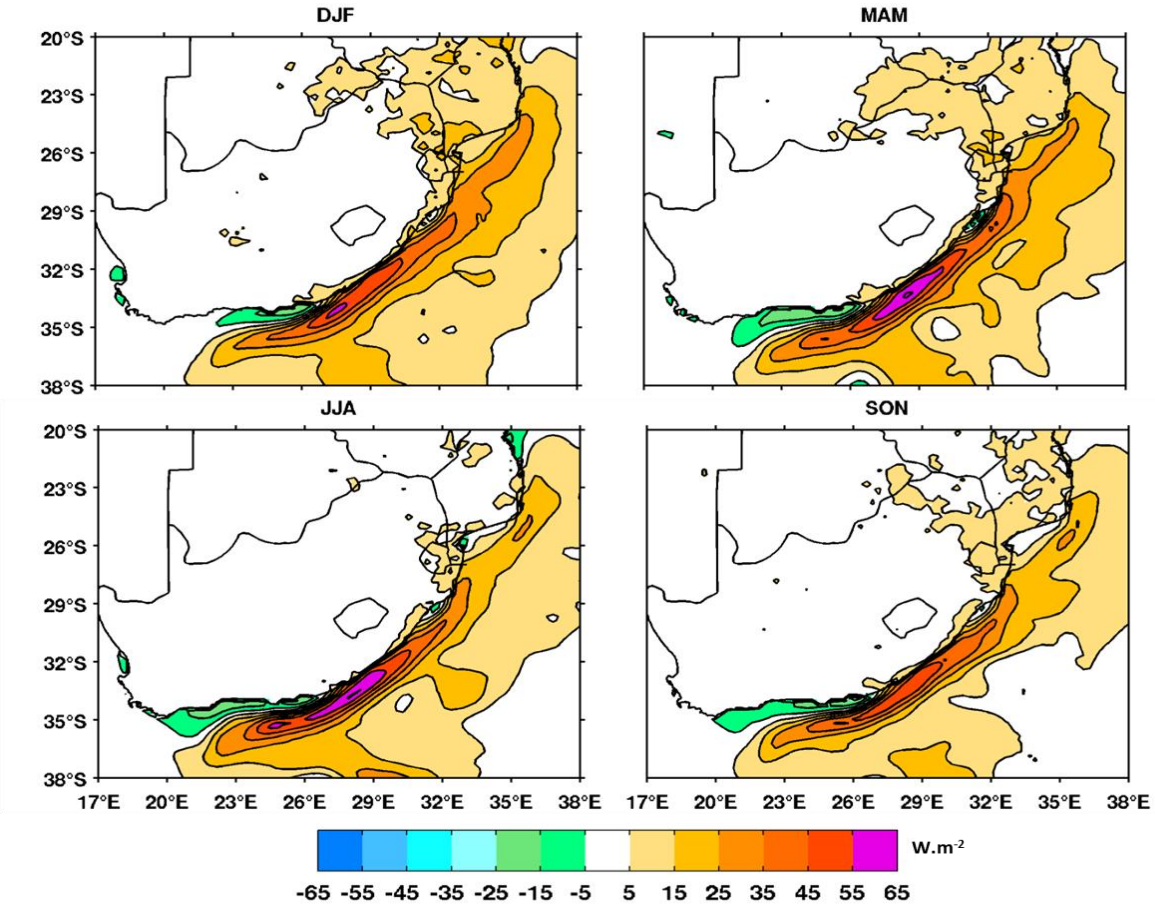

Figure 5.13: Seasonal latent heat flux (W.m^{-2}) differences between control and smooth SST experiments, with 10 W.m^{-2} intervals overlaid: a) summer (DJF), b) autumn (MAM), c) winter (JJA) and d) spring (SON).

5.2.1.2 Precipitation and evaporation

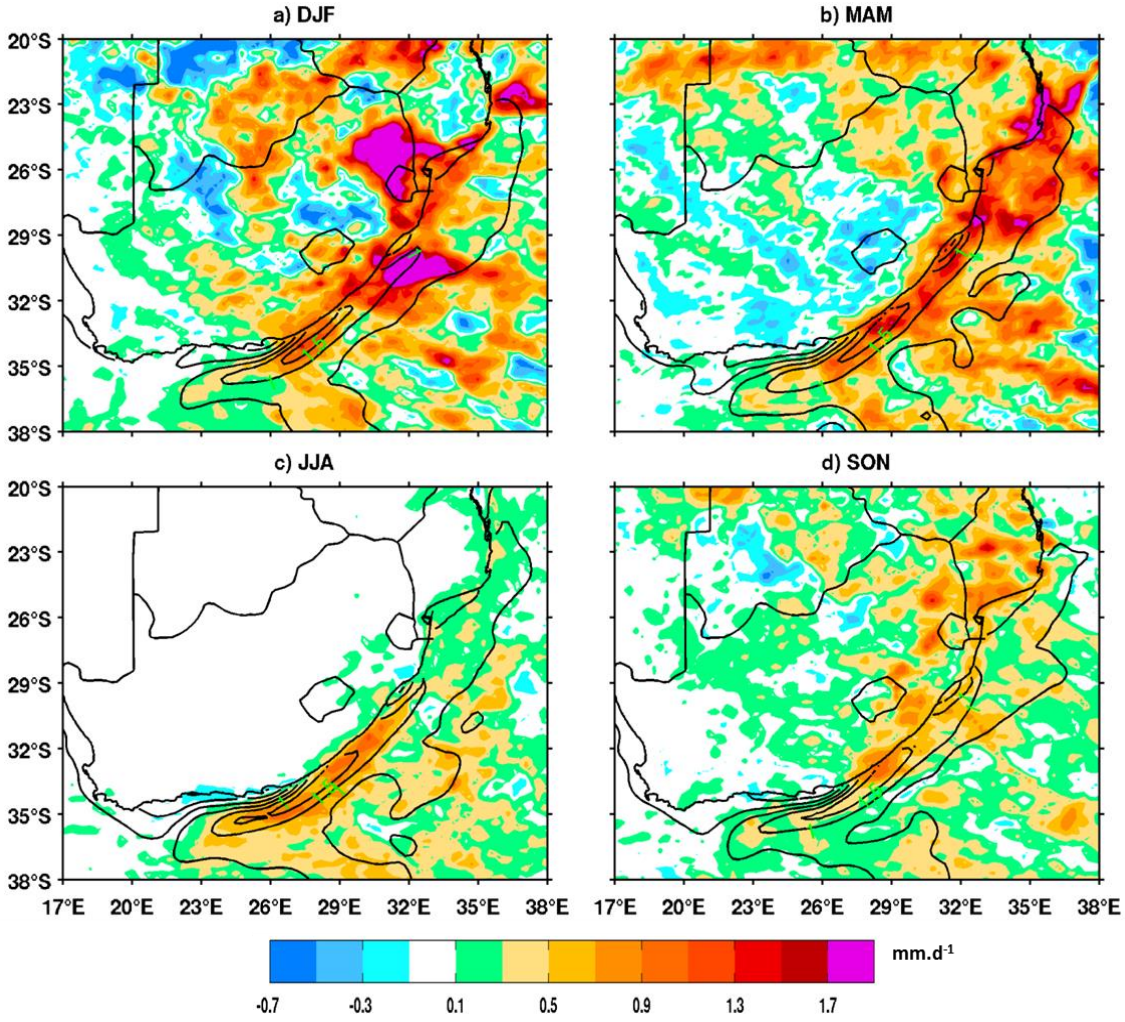

Figure 5.14: Seasonal rainfall differences ($mm.d^{-1}$) between control and smoothed SST experiments: a) summer (DJF), b) autumn (MAM), c) winter (JJA) and d) spring (SON). Overlaid are SST differences between the two simulations.

Figure 5.14 illustrates the WRF rain rate difference for each season. The rainband anchored by the Agulhas Current is mostly due to cumulus convective rain (not shown). Maximum terrestrial precipitation difference is found in summer (DJF) over the northeast of South Africa, around Mpumalanga (24-27°S, 30-33°E). Maximum oceanic rainfall difference occurs off Durban (30-32°S, 31-33°E) (**Fig. 5.14a**) and above the core of the Agulhas Current. This result is consistent

with the SST and LHF differences in the Agulhas Current (**Figs. 5.12, 5.13**). In autumn (MAM), precipitation difference is reduced along the coast compared to summer (DJF), but positive rain difference extends far west in the land area between 20 and 23°S (**Fig. 5.14b**). In winter (JJA), positive precipitation difference occurs along the east coast (**Fig. 5.13c**) and the Agulhas Current. The land precipitation in JJA is almost identical for both simulations with values close to 0. In spring (SON), maximum precipitation difference is along the coast and northeast of Southern Africa (**Fig. 5.14d**).

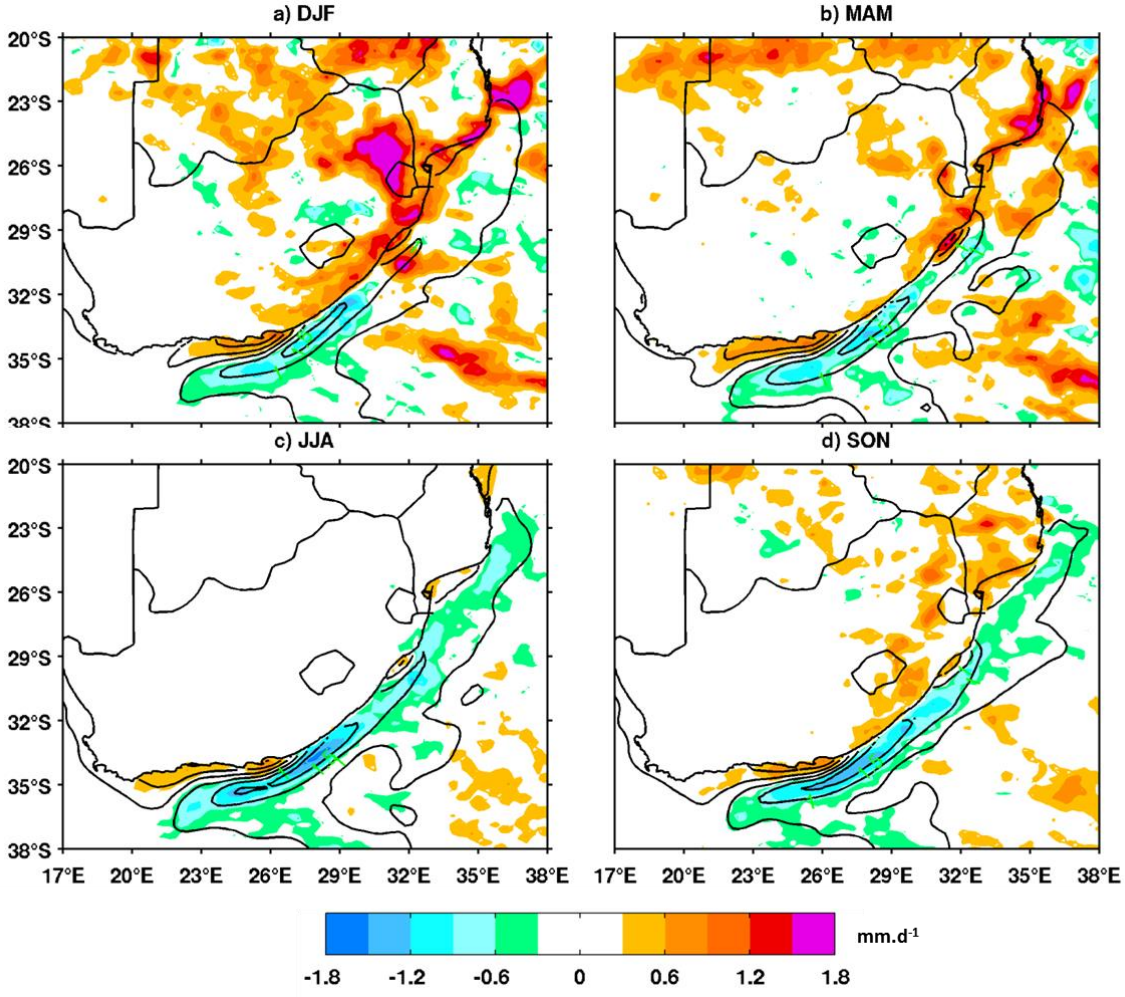

Figure 5.15: Seasonal differences of precipitation minus evaporation (P–E, mm.d^{-1}) between control and smoothed SST experiments: a) summer (DJF), b) autumn (MAM), c) winter (JJA) and d) spring (SON). Overlaid are SST differences between the two simulations.

The horizontal distribution of precipitation minus evaporation budget (P–E) for the difference between the control and the smoothed SST run is shown in **Figure 5.15**. P–E is a useful quantity for understanding the regional variability of water balances. Positives values of P–E mean that a region is becoming wetter. Negatives P–E values indicate less precipitation and more evaporation. Note that evaporation over landmass is underestimated in the WRF model, but is useful for the analysis. In summer (DJF), autumn (MAM) and spring (SON), positive P–E is found over land (**Fig. 5.15a**) corresponding to maximum precipitation (**Fig. 5.14a, b, c**). Positive P–E is also apparent along the "garden route" for each season. This might be due to the orography, as suggested in **section 5.1.3**. Negative P–E (1.5 $mm.d^{-1}$) is confined to the warm core of the Agulhas Current for each season, where SST and LHF differences are maximum. This indicates that a loss of ~2°C SST and ~55$W.m^{-2}$ LHF lead to ~1.5 $mm.d^{-1}$ decrease of P–E. Thus, smoothing the SST leads to precipitation and evaporation decline above the Current. To understand the mechanisms at the origin of these changes in precipitation and evaporation, we analyse the vertically integrated moisture flux differences between both simulations (see **section 5.2**).

5.2.1.3 Low-level convergence

The difference between both simulations of the sign reversed SST Laplacian has the same seasonality as the reanalysis CFSR (not shown), with a maximum along the eastern coast of South Africa for each season. The wind convergence difference (**Fig. 5.16**) and the associated SLP Laplacian difference (**Fig. 5.17**) are collocated with the rain band difference over the Agulhas Current. **Figure 5.16** also shows the wind direction along the coast, marked by the convergence of westerlies and winds coming from the Indian Ocean especially in autumn (**Fig. 5.16b**) and winter (**Fig. 5.16c**). This convergence occurs just above the Agulhas Current. Therefore, seasonally, the 2°C difference between the control and the smooth SST run leads to a decrease of the SLP Laplacian, SST Laplacian and wind convergence. Moreover, the low-level wind difference enhances the observed rainband difference along the east coast of South Africa for each season. Results of the WRF numerical experiments are consistent with those of CFSR reanalysis.

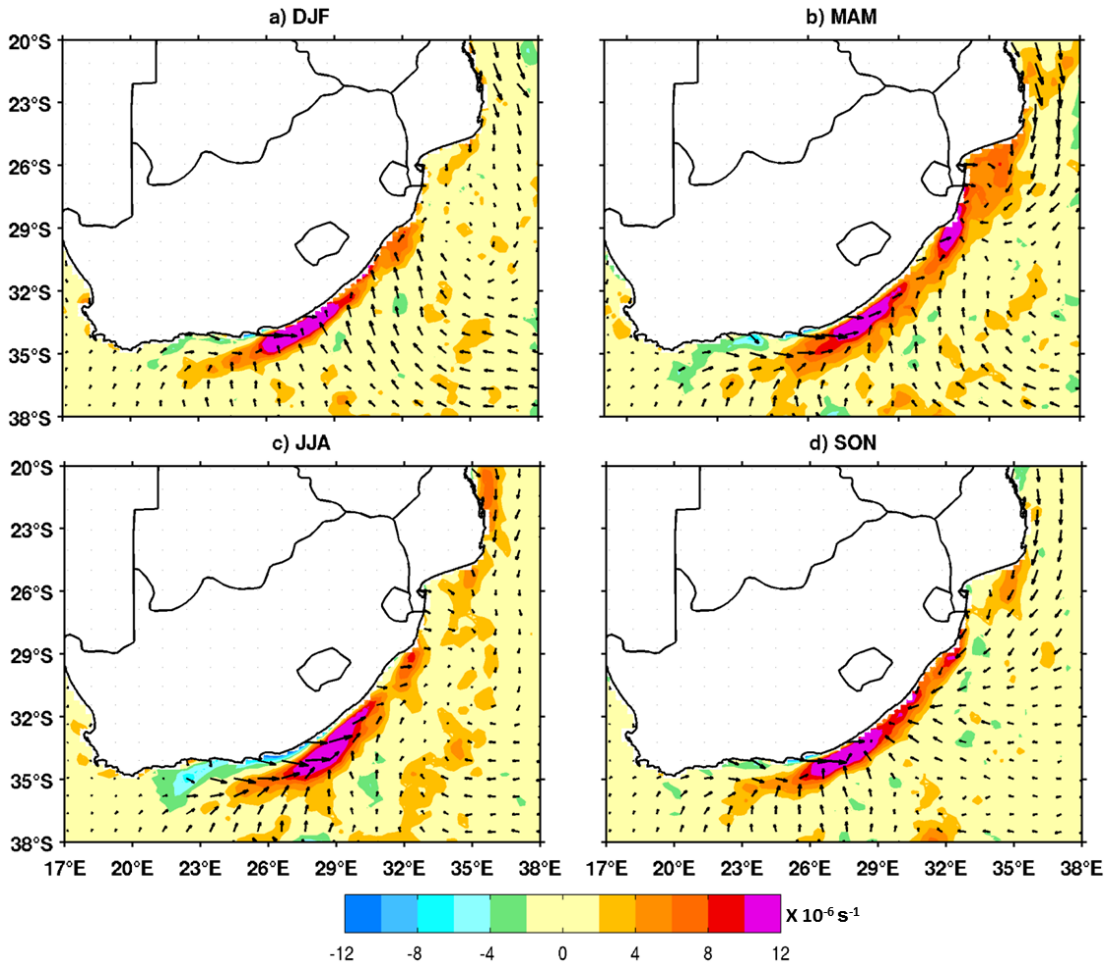

Figure 5.16: Seasonal differences of wind convergence (positive values) between control and smoothed SST experiments: a) summer (DJF), b) autumn (MAM), c) winter (JJA) and d) spring (SON). Superimposed arrows are the 10 m wind direction difference between the two simulations.

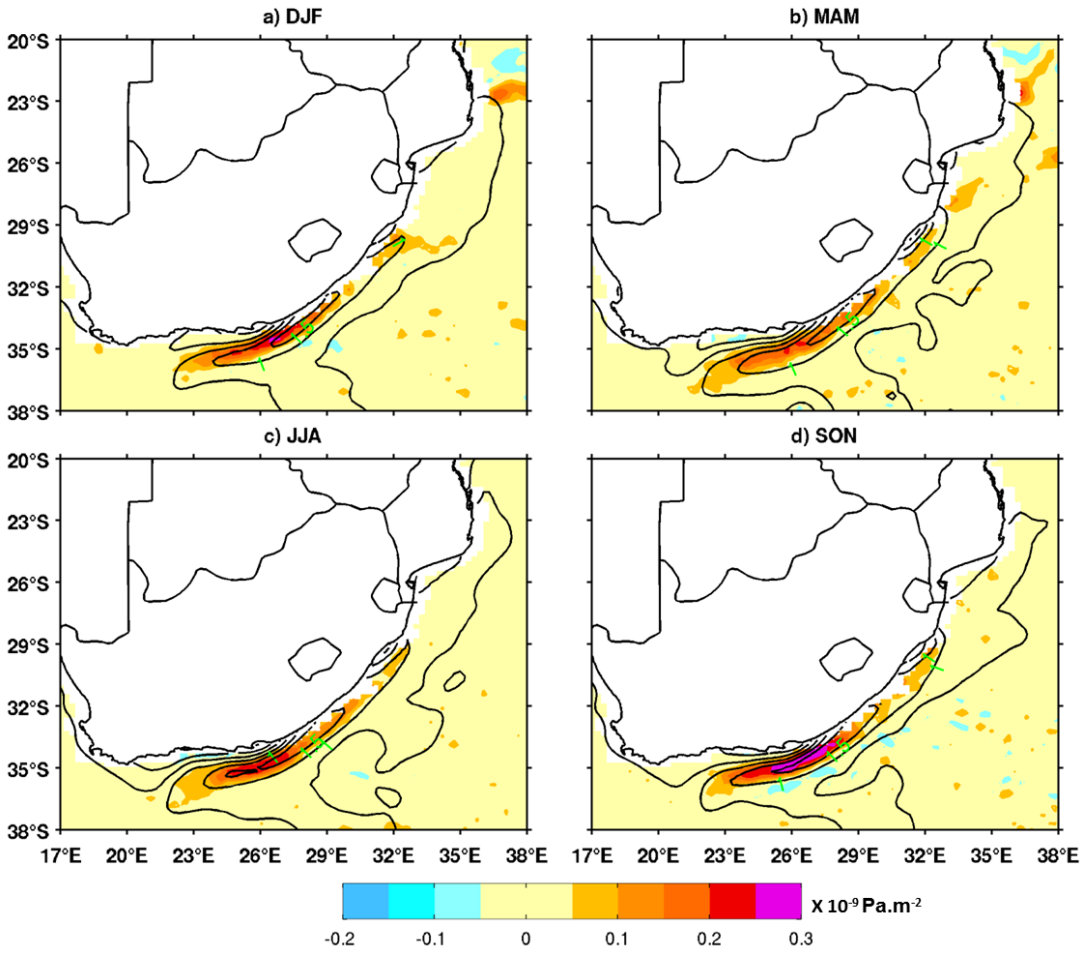

Figure 5.17: Seasonal differences of SLP Laplacian between control and smoothed SST experiment, with the overlaid SST differences: a) summer (DJF), b) autumn (MAM), c) winter (JJA) and d) spring (SON).

5.2.2 Atmospheric parameters

5.2.2.1 Geopotential height

The geopotential height is the height above mean sea level of a given pressure in the atmosphere. **Figures 5.18, 5.19, 5.20,** and **5.21** represent the geopotential heights at 950, 850, 700 and 500 hPa respectively, simulated in the control experiment. From low to middle troposphere, the high-pressure system is apparent in the Indian Ocean and above the continent for each season. Warm and moist air rises in the equatorial regions, especially over the ocean, generating precipitation,

which increases the ascending motion of air. Cool air is then pushed poleward and sinks in the subtropical region where southern Africa sits, creating high-pressure and subsidence which is not favorable to precipitation. Thus, the climate of southern Africa is arid to semi-arid. From low to middle troposphere (950-700 hPa) in summer (DJF), geopotential heights are lower than any other seasons (**Figs. 5.18a, 5.19a,** and **5.20a,**). Meanwhile, in winter (JJA) geopotential heights are higher than other seasons (**Figs. 5.18c, 5.19c,** and **5.20c**). Conversely, at 500 hPa, geopotential heights are the lowest corresponding to the impact of mid-latitude systems (**Fig. 5.21c**).

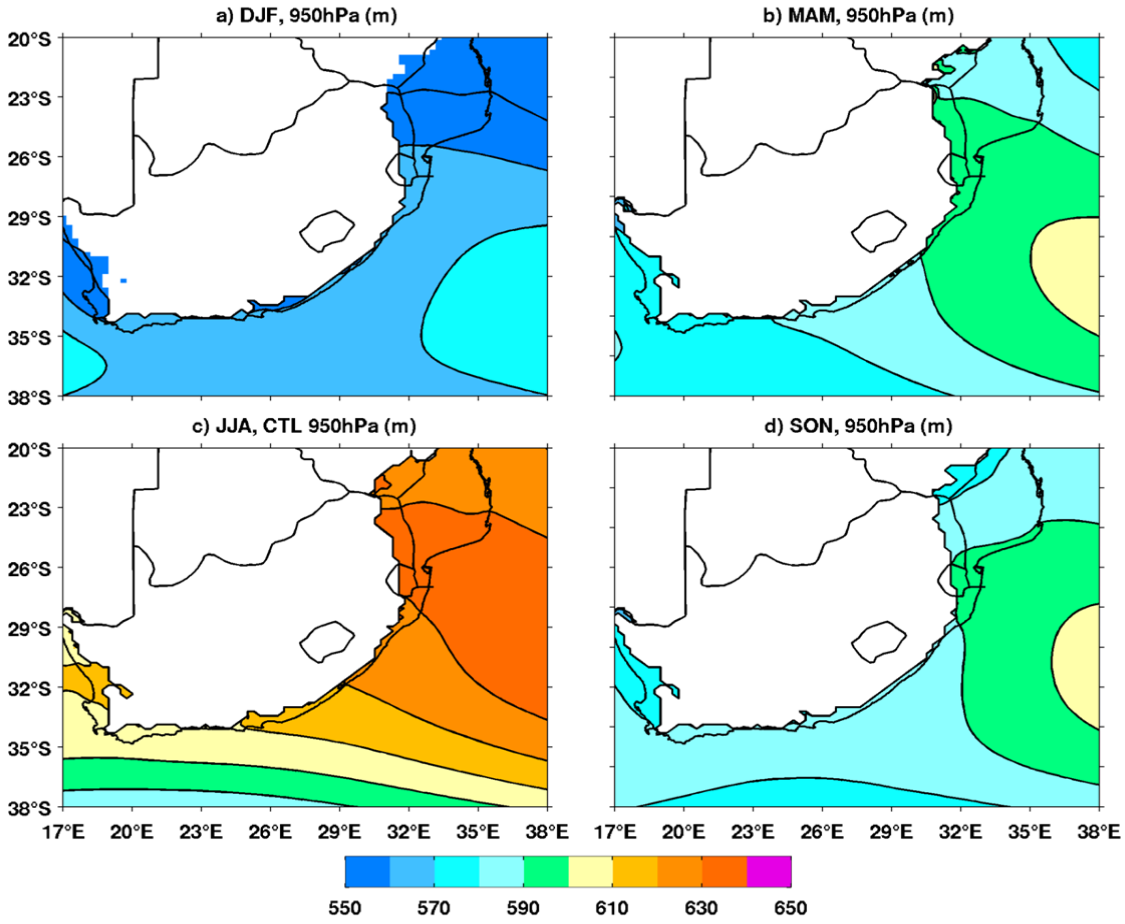

Figure 5.18: Seasonal means of 950 hPa geopotential heights simulated by the control experiment with contours of 10 m intervals: a) summer (DJF), b) autumn (MAM), c) winter (JJA) and d) spring (SON).

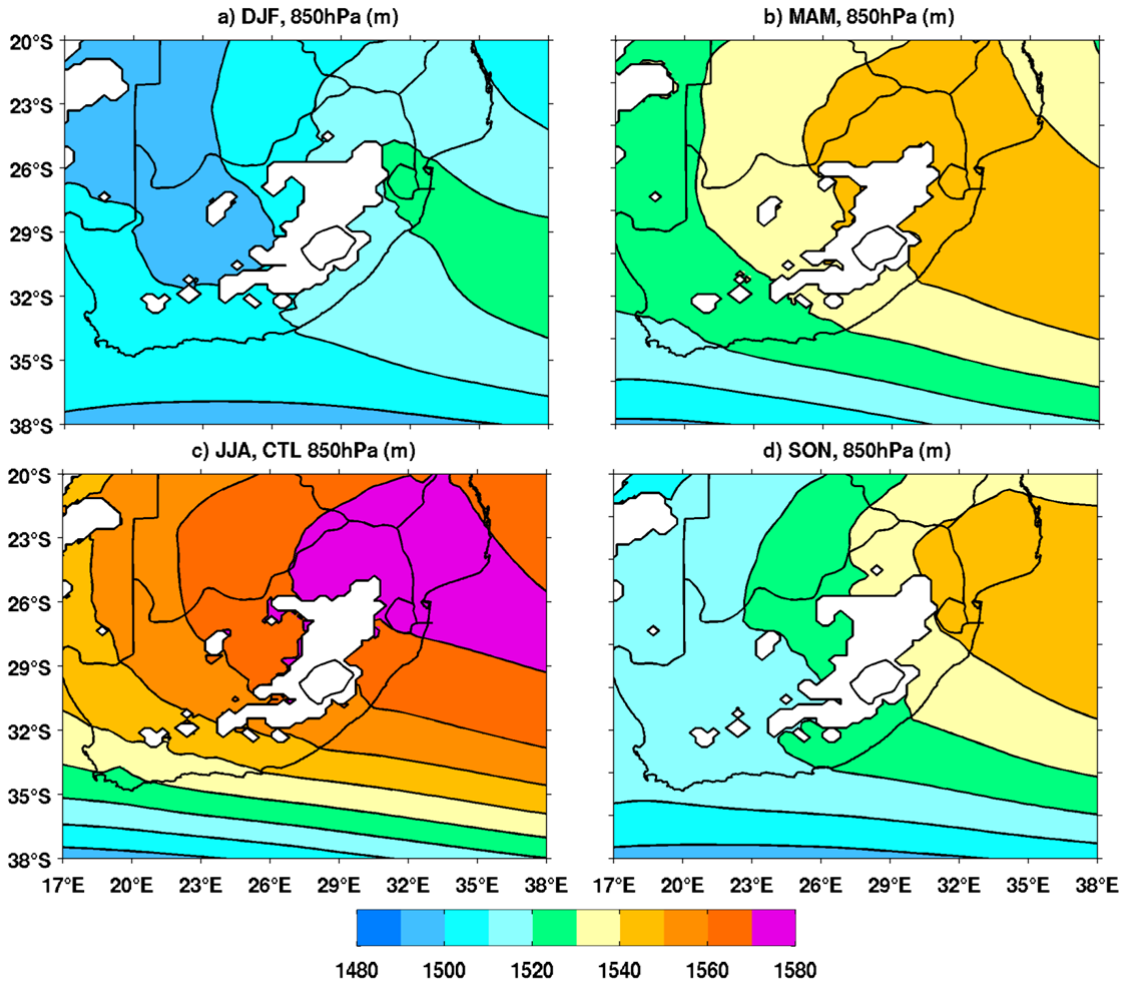

Figure 5.19: Seasonal means of 850 hPa geopotential heights simulated by the control experiment with contours of 10 m intervals: a) summer (DJF), b) autumn (MAM), c) winter (JJA) and d) spring (SON).

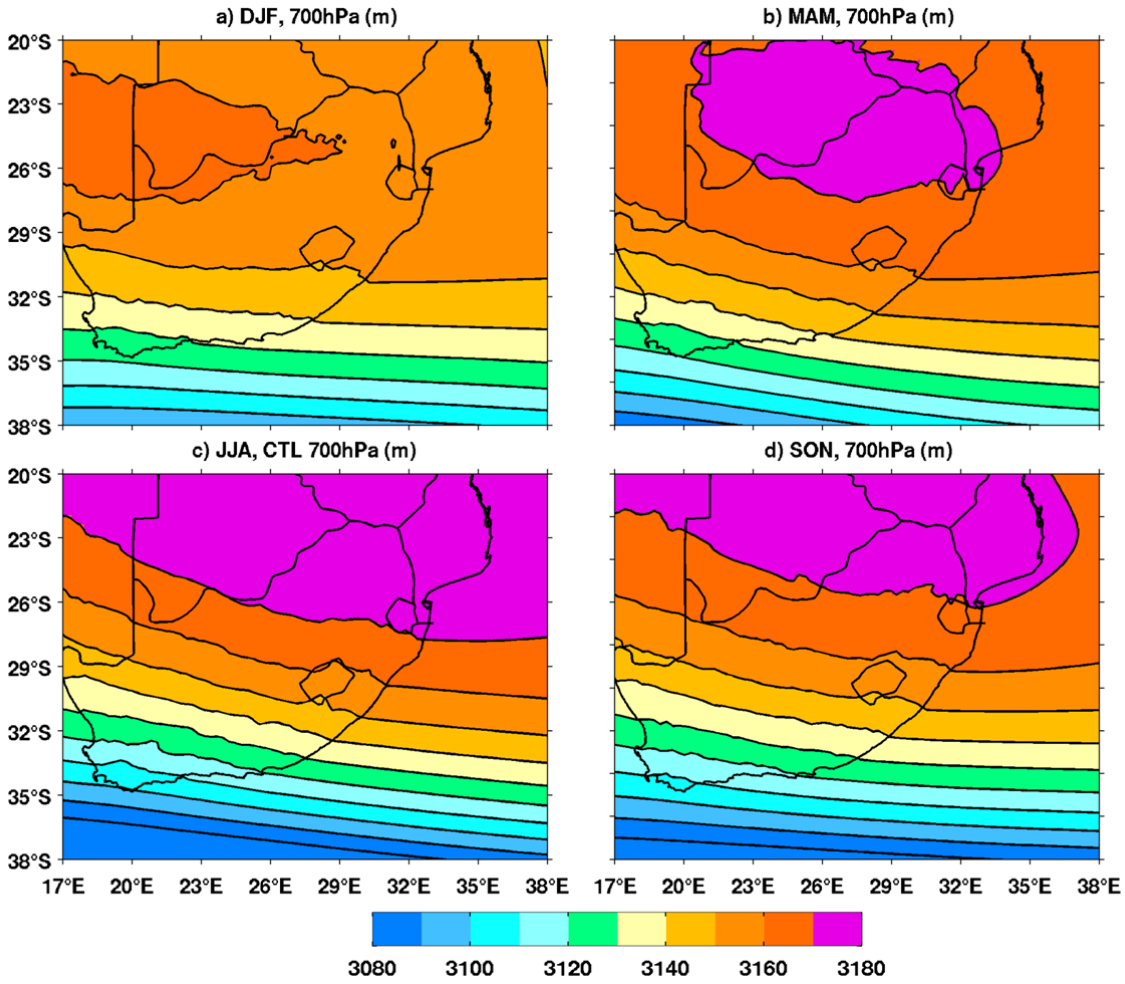

Figure 5.20: Seasonal means of 700 hPa geopotential heights simulated by the control experiment with contours of 10 m intervals: a) summer (DJF), b) autumn (MAM), c) winter (JJA) and d) spring (SON).

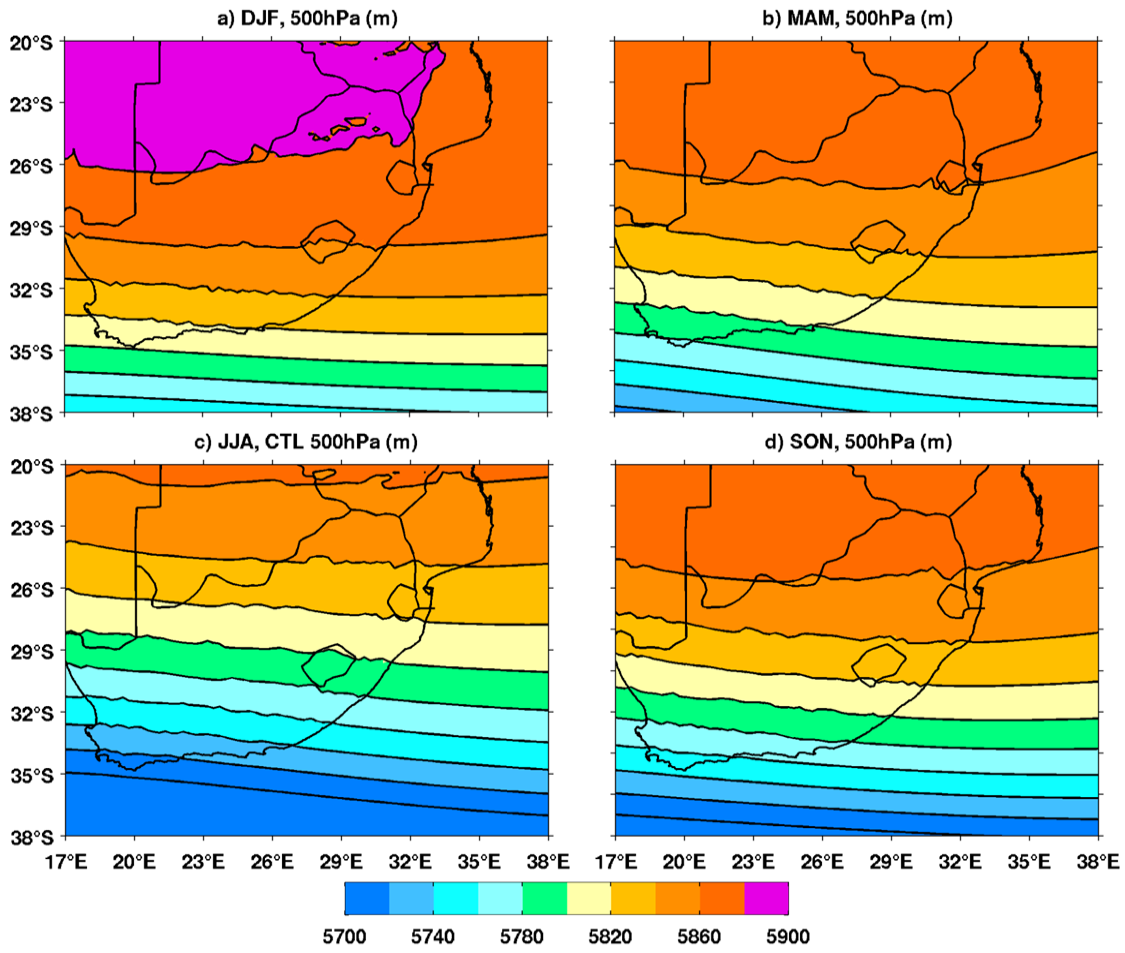

Figure 5.21: Seasonal means of 500 hPa geopotential heights simulated by the control experiment with contours of 20 m intervals: a) summer (DJF), b) autumn (MAM), c) winter (JJA) and d) spring (SON). The highest height is in summer (approximately 6000 m).

Geopotential height anomalies are represented by **Figures 5.22, 5.23, 5.24** and **5.25**. Anomalies are calculated from the difference between the control experiment and the smoothed SST experiment where the impact of the Agulhas Current is reduced. From 950 to 700 hPa in summer and autumn geopotential height anomalies result in a low pressure anomaly. Reducing the SST strengthen the high pressure system of the smooth experiment, resulting in a low pressure anomaly between the control and smooth SST experiments.

At 950 hPa, this low pressure anomaly is over the southeast coast of South Africa (**Fig. 5.22a,b**) and is due to be the effect of the SST of the Agulhas Current.

At 850 and 700 hPa, the geopotential heights anomaly is from coastal area to the south and Indian ocean to the north, extending to land area (**Figs. 5.23a,b** and **5.24a,b**).

At 500 hPa, during summer, the geopotential heights anomaly is shifted futher inland than other levels (**Fig. 5.25a**). In autumn, the anomaly is zonally elongated between 17-35°E (**Fig. 5.25b**). In winter and spring, positive geopotential heights difference is dominant.

Thus, in summer and autumn, a 2°C SST anomaly created by the control run results to a low-pressure anomaly, corresponding to positive precipitation anomalies over the landmass, and along the east coast of South Africa (**Fig. 5.14a,b**).

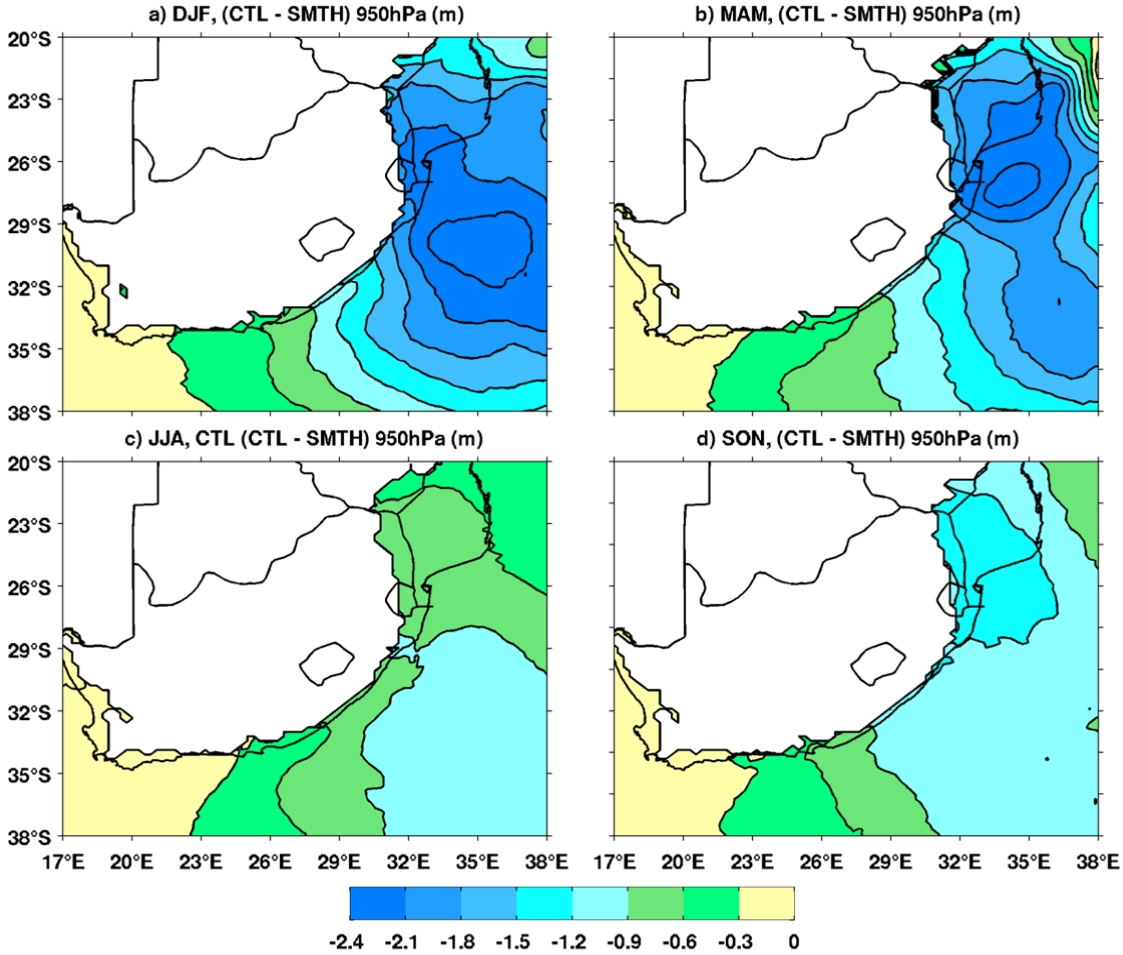

Figure 5.22: Seasonal differences of 950 hPa geopotential heights between control and smoothed SST experiments, with contours of 0.3 m intervals: a) summer (DJF), b) autumn (MAM), c) winter (JJA) and d) spring (SON). Cyclonic geopotential heights anomalies around the Indian ocean, in summer and autumn seasons.

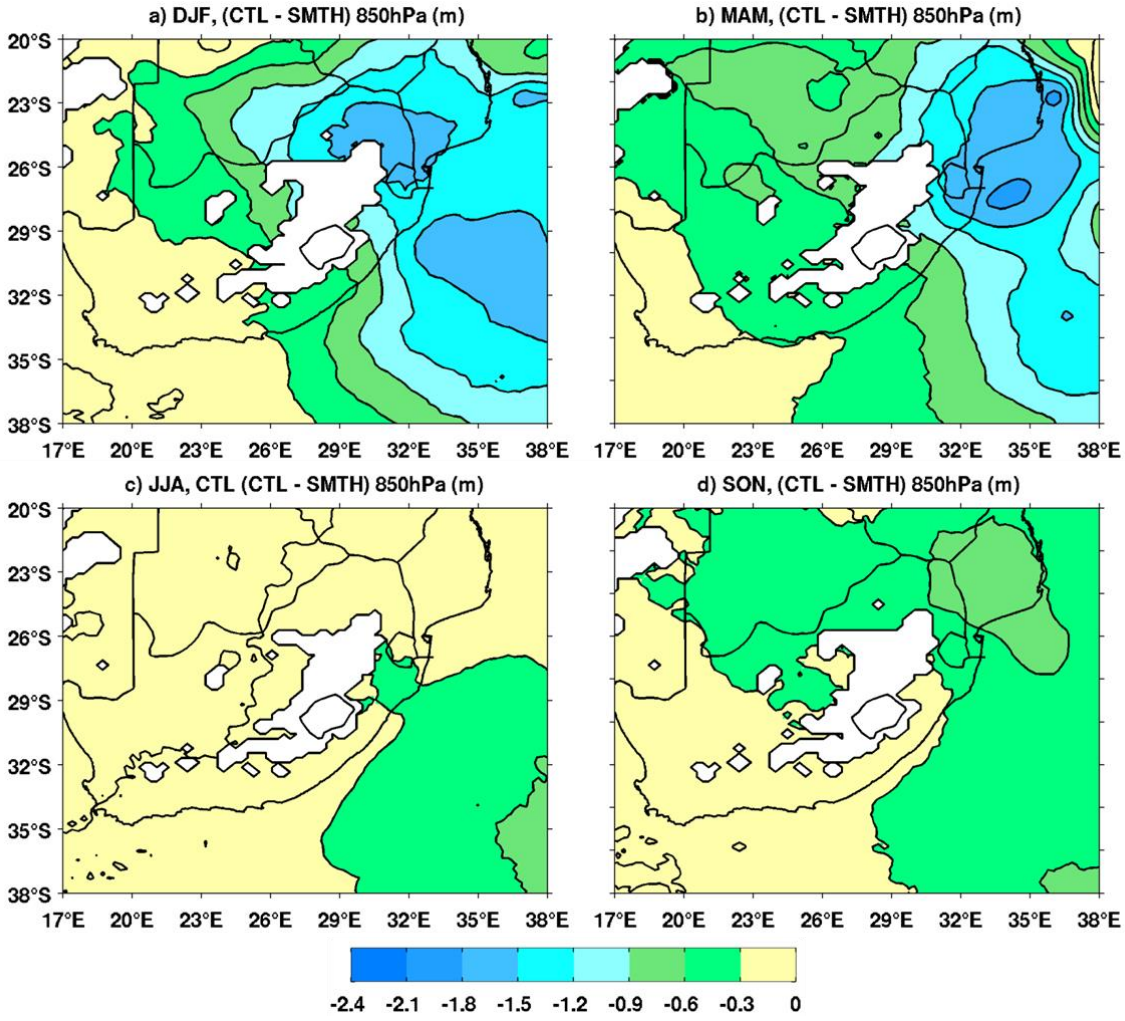

Figure 5.23: Seasonal differences of 850 hPa geopotential heights between control and smoothed SST experiments, with contours of 0.3 m intervals: a) summer (DJF), b) autumn (MAM), c) winter (JJA) and d) spring (SON). Cyclonic geopotential heights anomalies in the Indian ocean, extending inland in summer and autumn.

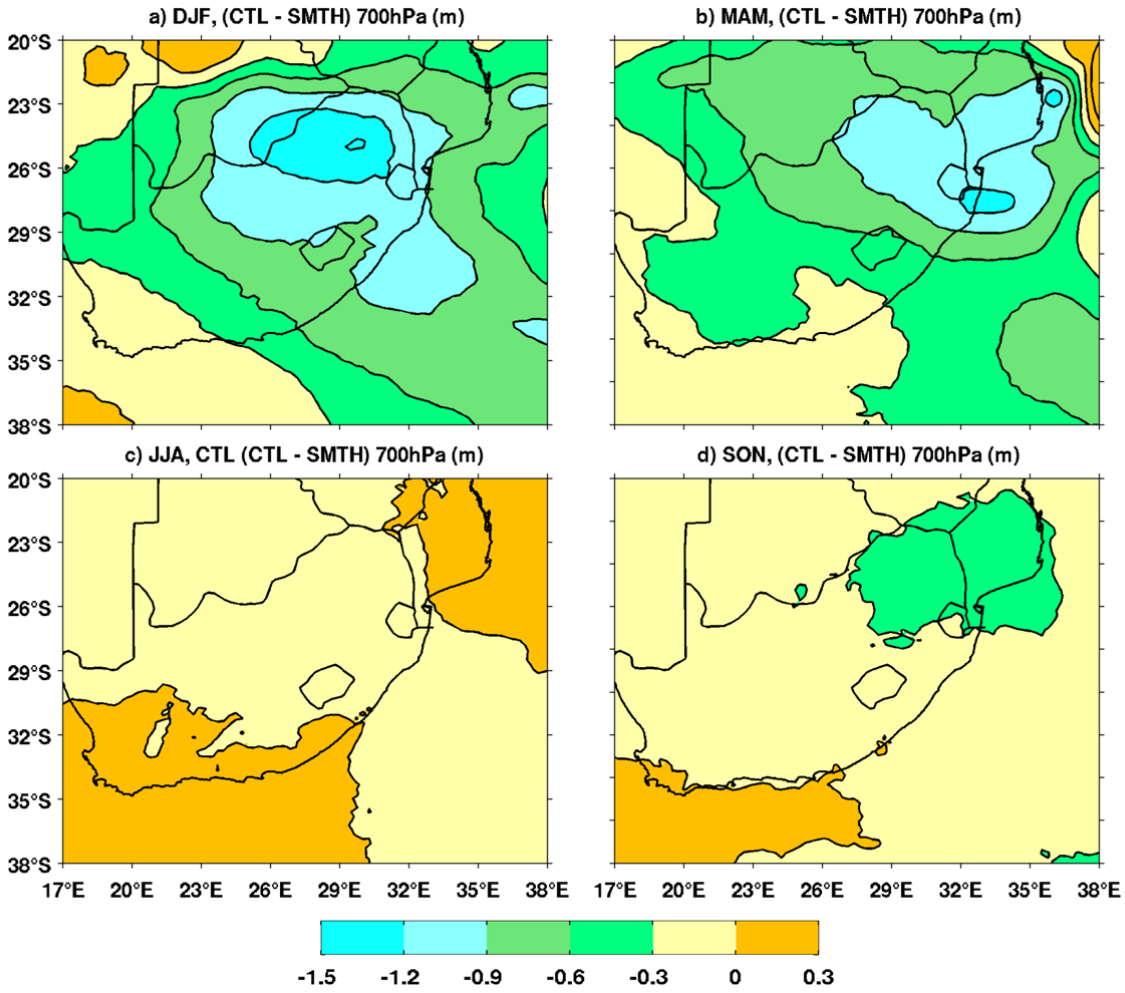

Figure 5.24: Seasonal differences of 700 hPa geopotential heights between control and smoothed SST experiments, with contours of 0.3 m intervals: a) summer (DJF), b) autumn (MAM), c) winter (JJA) and d) spring (SON). Cyclonic geopotential heights anomalies around central South Africa, in summer and autumn.

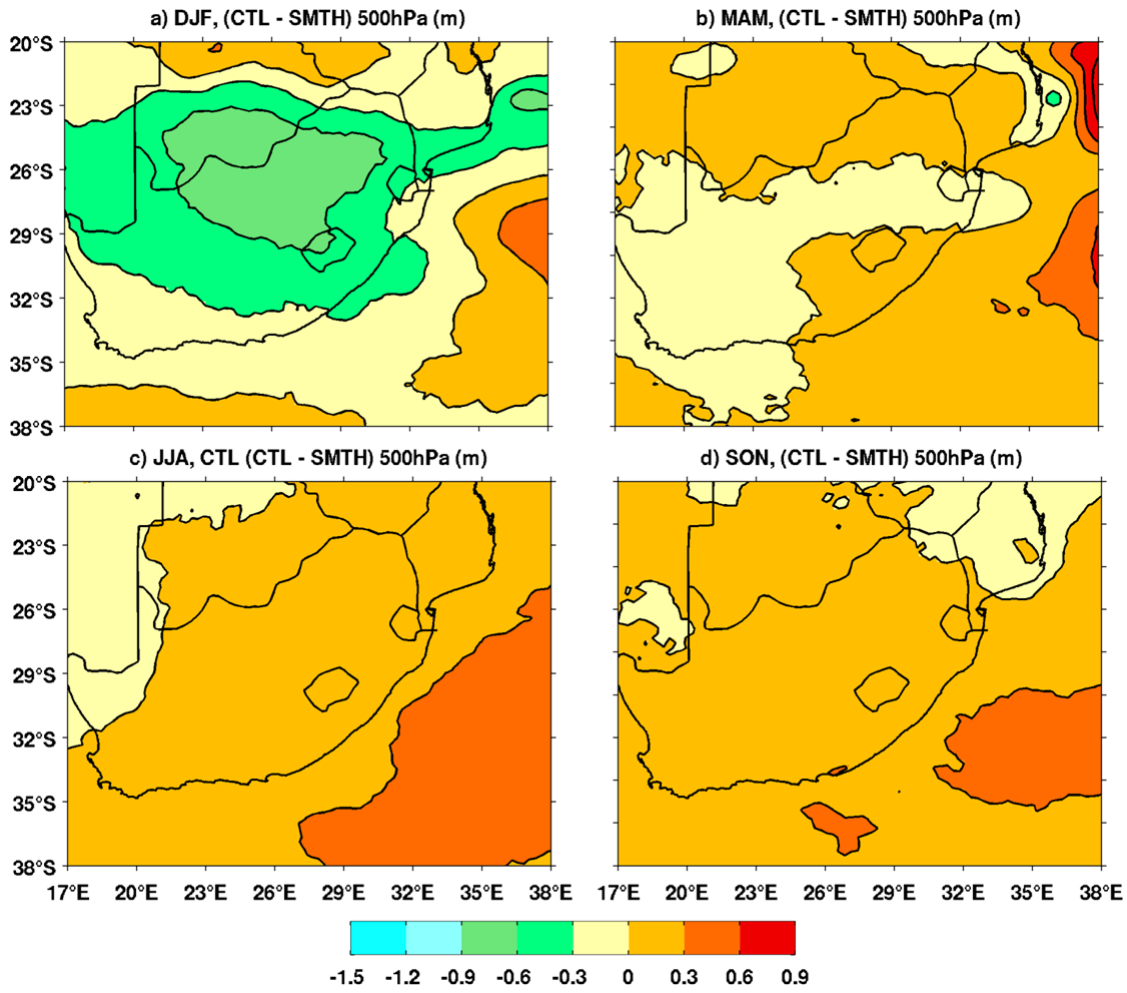

Figure 5.25: Seasonal differences of 500 hPa geopotential heights between control and smoothed SST experiments, with contours of 0.3 m intervals: a) summer (DJF), b) autumn (MAM), c) winter (JJA) and d) spring (SON). Cyclonic geopotential heights anomalies over South Africa in summer.

5.2.2.2 Moisture flux

The moisture flux intensity is evaluated as a product of the specific humidity and the wind, following the equation:

$$Moist(uq, vq) = \sqrt{(uq)^2 + (vq)^2} \text{..... Eq. 5.1}$$

Where $Moist$ is the moisture flux, q is the 3D specific humidity, with specific humidity defined as the ratio between the mass of the water vapor and the mass of the moist air. u and v are respectively the 3D zonal and meridional wind components.

Moisture flux is then computed at 950, 850, 700 and 500 hPa (**Figs. 5.26, 5.27, 5.28,** and **5.29**). The direction of the moisture transport is given by the wind direction. At 950 hpa, an intense flux of moisture originating from the Indian ocean penetrates South Africa via the Mozambique Channel, and the other part flows along the coast just above the Agulhas Current (**Fig. 5.26**). The western Indian Ocean is the major moisture source for southern Africa (*Vigaud et al.*, 2007). Moisture flux is less intense in winter along the coast compared to other season, and ranges between 0 to 32 $g.kg^{-1}.m.s^{-1}$ there, half value of summer moisture (**Fig. 5.26c**). Along the "garden route", in winter the moisture flux is more intense compared to other seasons, with a dominance of westerlies. At 850 hPa, the moisture flux maximum is shifted inland, around central South Africa (**Fig. 5.27**), with the highest intensity in summer between 22-25°S and 26-33°E (**Fig. 5.27a**). From 700 to 500 hPa, a large quantity of moisture flux originates from the Atlantic ocean (with a maximum around the Drakensberg) and leaves the landmass over the coast (**Figs. 5.28** and **5.29**). The South Atlantic is considered as a secondary source of moisture (*Preston-Whyte and Tyson* 1988, *D'Abreton and Lindesay* 1993) for southern African climate variability (*Cook et al.* 2004, *Reason et al.* 2006). At 700 hPa, part of the moisture coming from the land mass penetrates the continent via the Mozambique channel in an anticyclonic circulation.

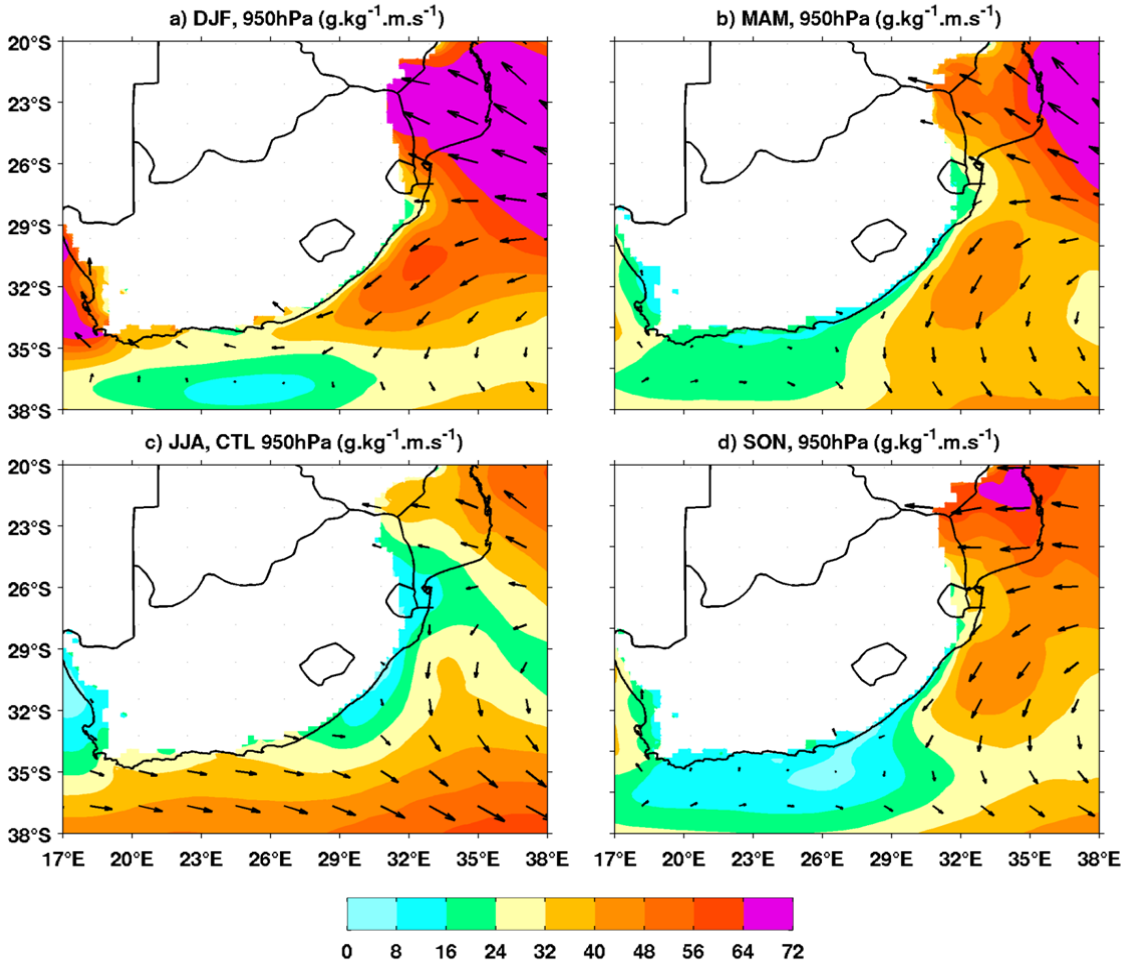

Figure 5.26: Seasonal means of 950 hPa moisture flux simulated by the control experiment: a) summer (DJF), b) autumn (MAM), c) winter (JJA) and d) spring (SON). Arrows represent the direction of the moisture transport every 2°.

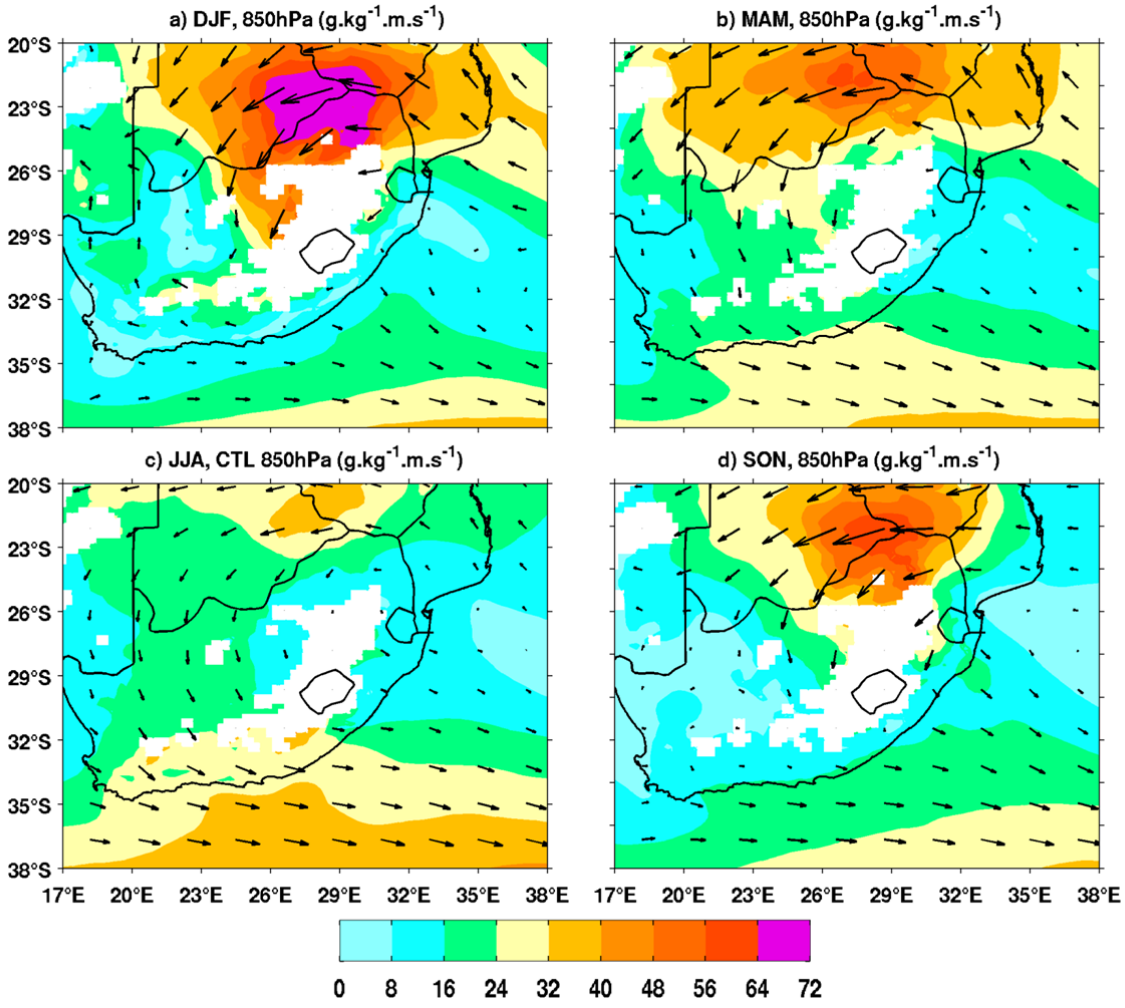

Figure 5.27: Seasonal means of 850 hPa moisture flux simulated by the control experiment: a) summer (DJF), b) autumn (MAM), c) winter (JJA) and d) spring (SON). Arrows represent the direction of the moisture transport every 2°.

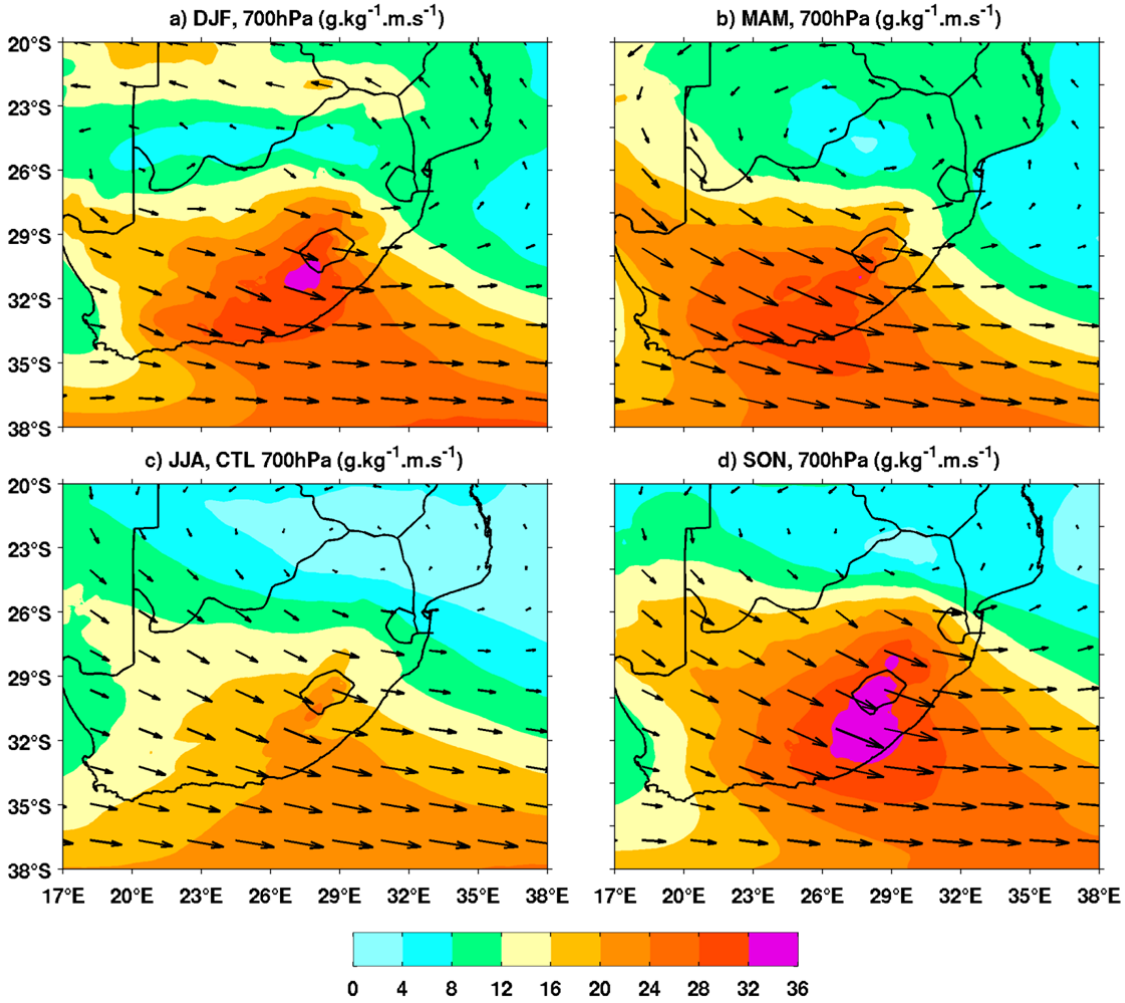

Figure 5.28: Seasonal means of 700 hPa moisture flux simulated by the control experiment: a) summer (DJF), b) autumn (MAM), c) winter (JJA) and d) spring (SON). Arrows represent the direction of the moisture transport every 2°.

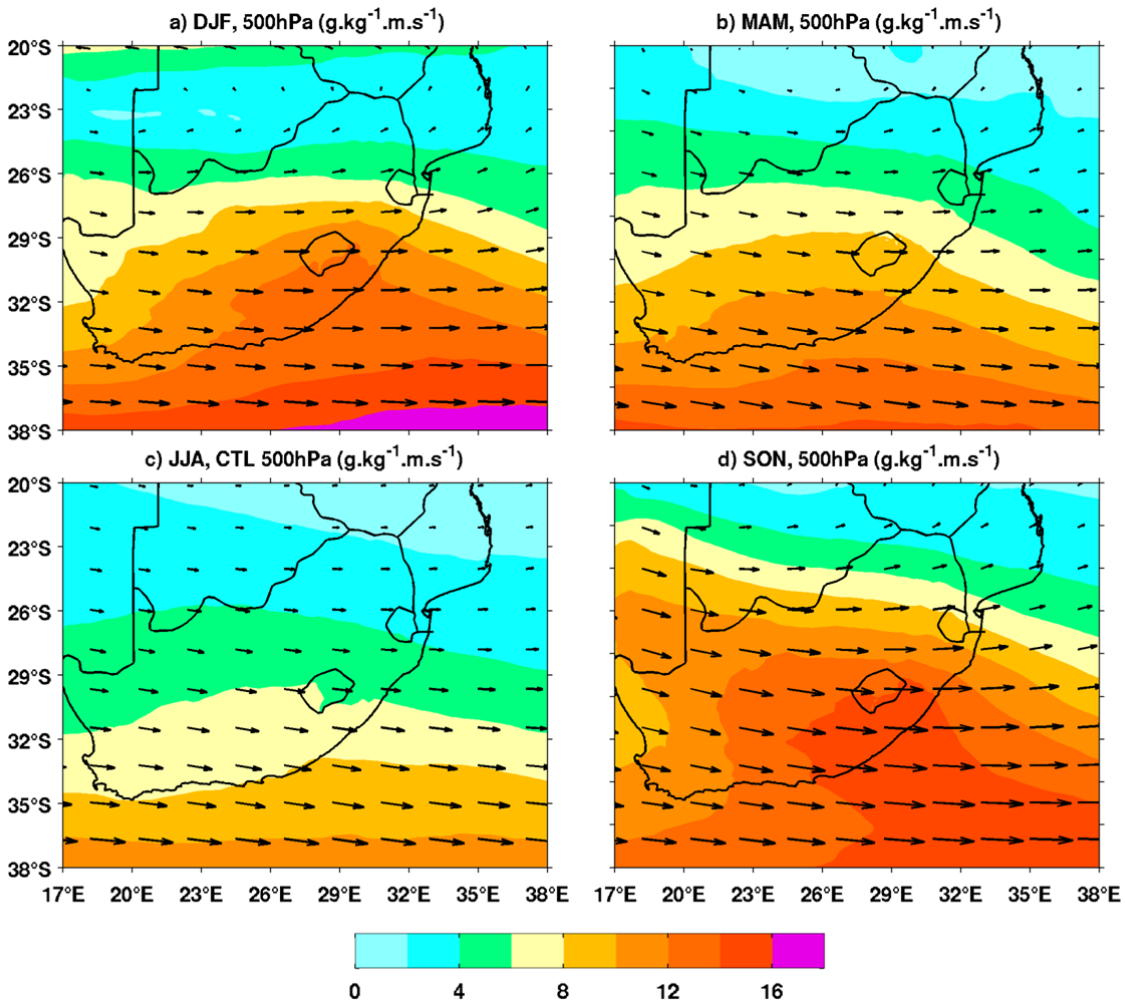

Figure 5.29: Seasonal means of 500 hPa moisture flux simulated by the control experiment: a) summer (DJF), b) autumn (MAM), c) winter (JJA) and d) spring (SON). Arrows represent the direction of the moisture transport every 2°.

Moisture flux anomalies are shown in **Figures 5.30, 5.31, 5.32** and **5.33**. Anomalies are obtained from the difference between the two simulations. This difference leads to a cyclonic moisture flux anomaly leading to an import of moisture from the South and an export of moiture from the Northeast of the continent.

At 950 hPa, a 2°C warm SST creates 10 $g.kg^{-1}.m.s^{-1}$ more moisture flux from the South in control run than smooth SST experiment, especially in summer and autumn southwest of the Indian Ocean and along the east coast (**Fig. 5.30a,b**). The moisture flux is stopped by the orography at the the surface. In summer, autumn and spring, moisture flux anomalies penetrate the continent

where the Agulhas Current is adjacent to the coast (**Fig. 5.30a, b,** and **c**). The cyclonic motion of moisture anomalies is in good agreement with the negative geopotential heights anomaly (**Figs. 5.22** and **5.30**). This indicates that a 2°C decline of SST decreases the inflow of moisture flux. In winter, moisture flux anomalies are between 1 and 3 $g.kg^{-1}.m.s^{-1}$, indicating that smoothing the SST of the Agulhas Current does not affect the moisture flux much compared to other seasons.

At 850 hPa, moisture flux anomalies have a cyclonic motion, as in 950 hPa, and penetrate the continent futher than at 950 hPa across the east coast of South Africa in summer and autumn (**Figs. 5.31a, b**). Still in summer, a band of anomalies of moisture flux transport converges in the Agulhas Current region. In winter and spring, the moisture flux anomalies are eastward (**Fig. 5.31c,d**). This indicates that the inflow moisture flux from the Indian Ocean is weakened when the SST is reduced.

From 700 to 500 hPa, positive moisture anomalies present a maximum mostly above the continent in central southern Africa in summer between 20-23°S and 22-26°E (**Figs. 5.32a** and **5.33a**), in a cyclonic motion. This is in aggreement with the geopotential heights anomaly, and where isolines of this anomaly are tight. In winter, moisture flux anomalies are eastward (**Figs. 5.31c** and **5.33c**). The absence of marked anomalies of geopotential above the ocean and the flux of moisture anomalies together with rainfall anomalies suggest that the moisture anomalies at the surface help to increase rainfall above the continent which would generate further geopotential anomalies at 700 and 500 hPa and more cyclonic rainfall anomalies.

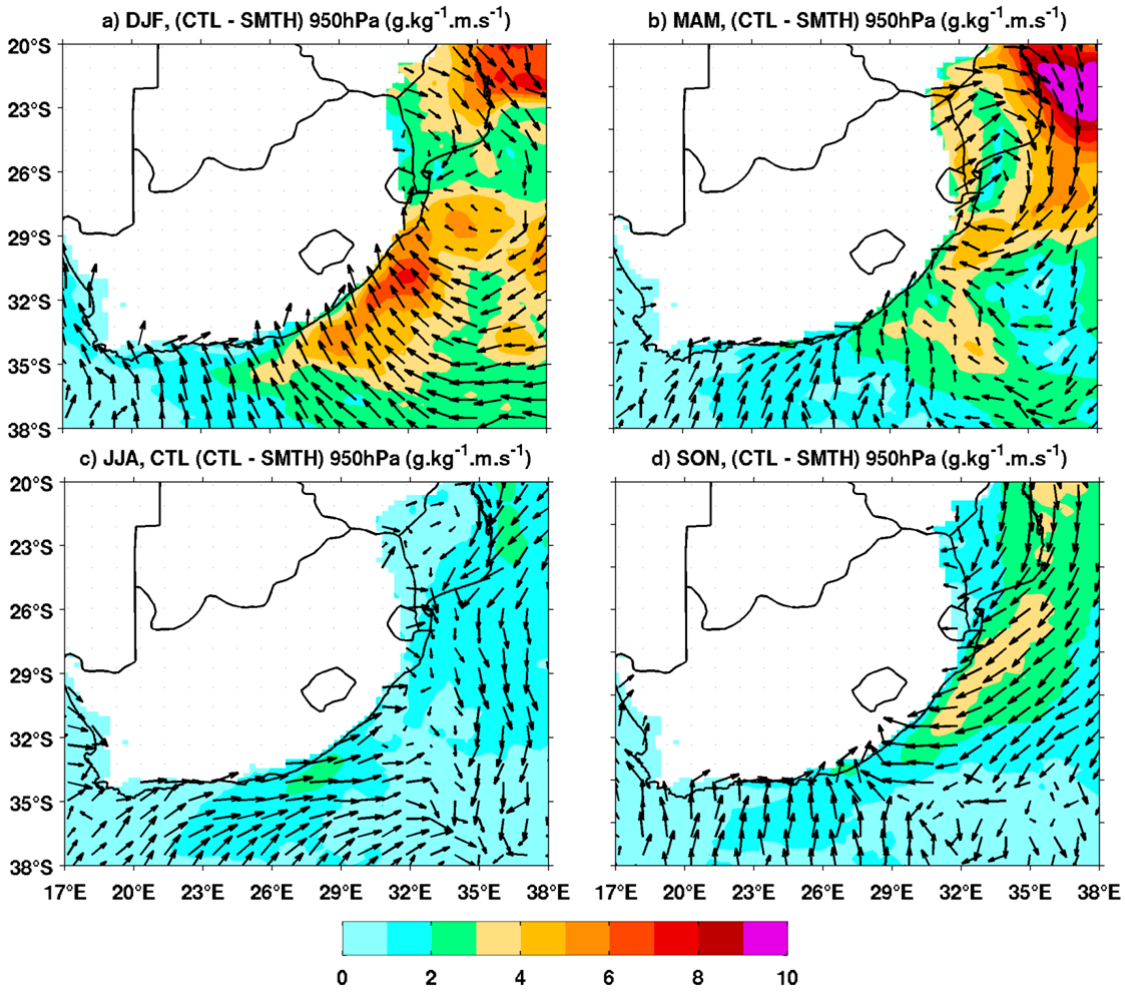

Figure 5.30: Seasonal differences of 950 hPa moisture flux between control and smoothed SST experiments: a) summer (DJF), b) autumn (MAM), c) winter (JJA) and d) spring (SON). Arrows represent the direction of the moisture transport every 1°.

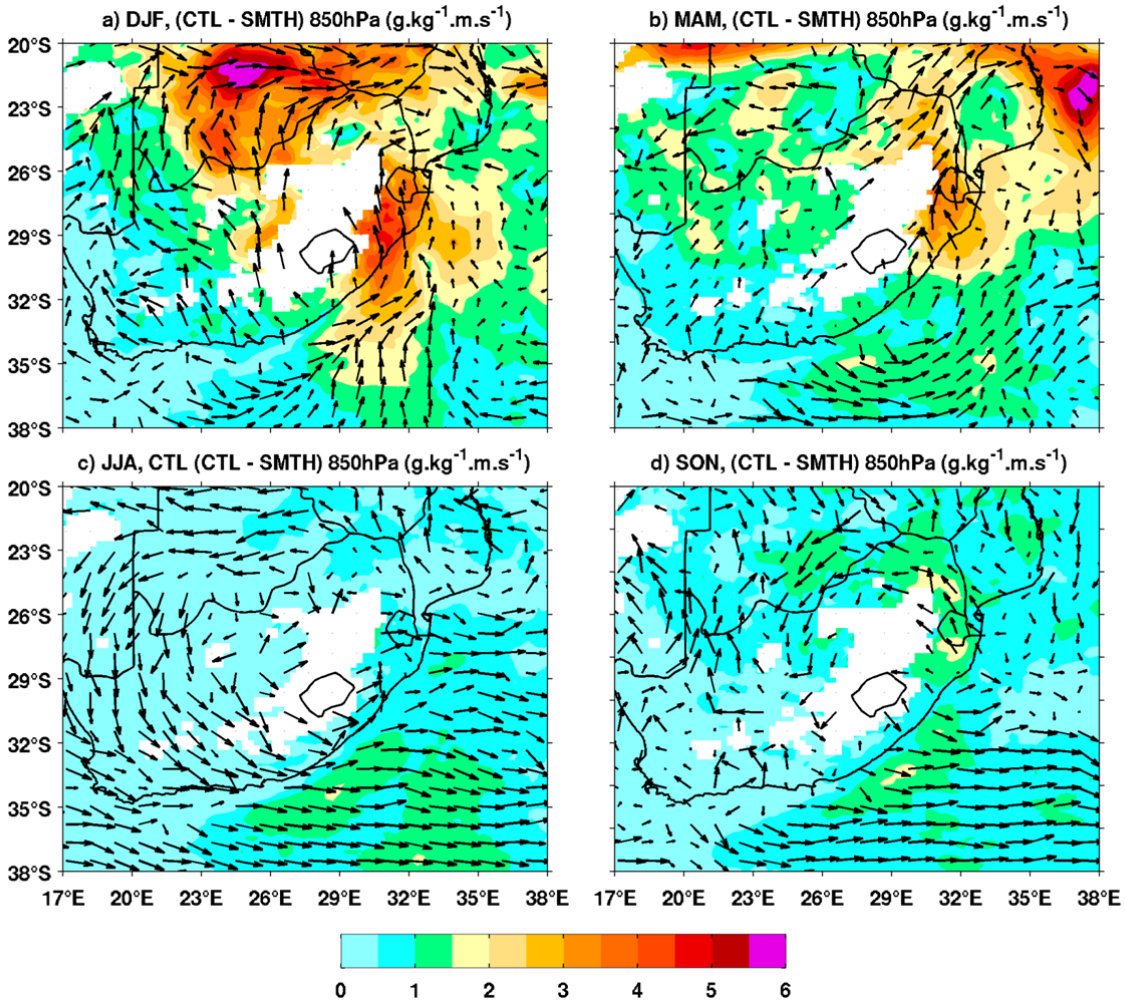

Figure 5.31: Seasonal differences of 850 hPa moisture flux between control and smoothed SST experiments: a) summer (DJF), b) autumn (MAM), c) winter (JJA) and d) spring (SON). Arrows represent the direction of the moisture transport every 1°.

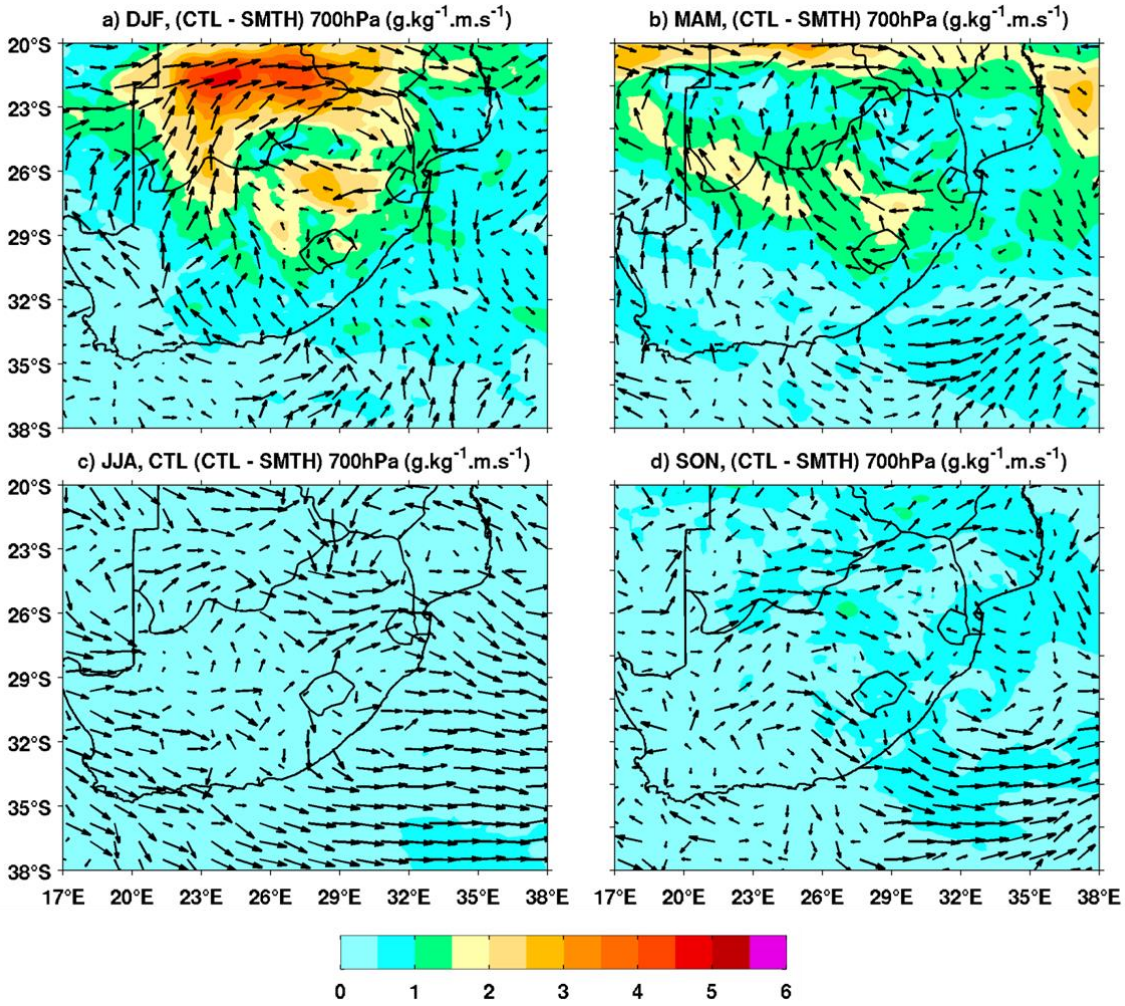

Figure 5.32: Seasonal differences of 700 hPa moisture flux between control and smoothed SST experiments: a) summer (DJF), b) autumn (MAM), c) winter (JJA) and d) spring (SON). Arrows represent the direction of the moisture transport every 1°.

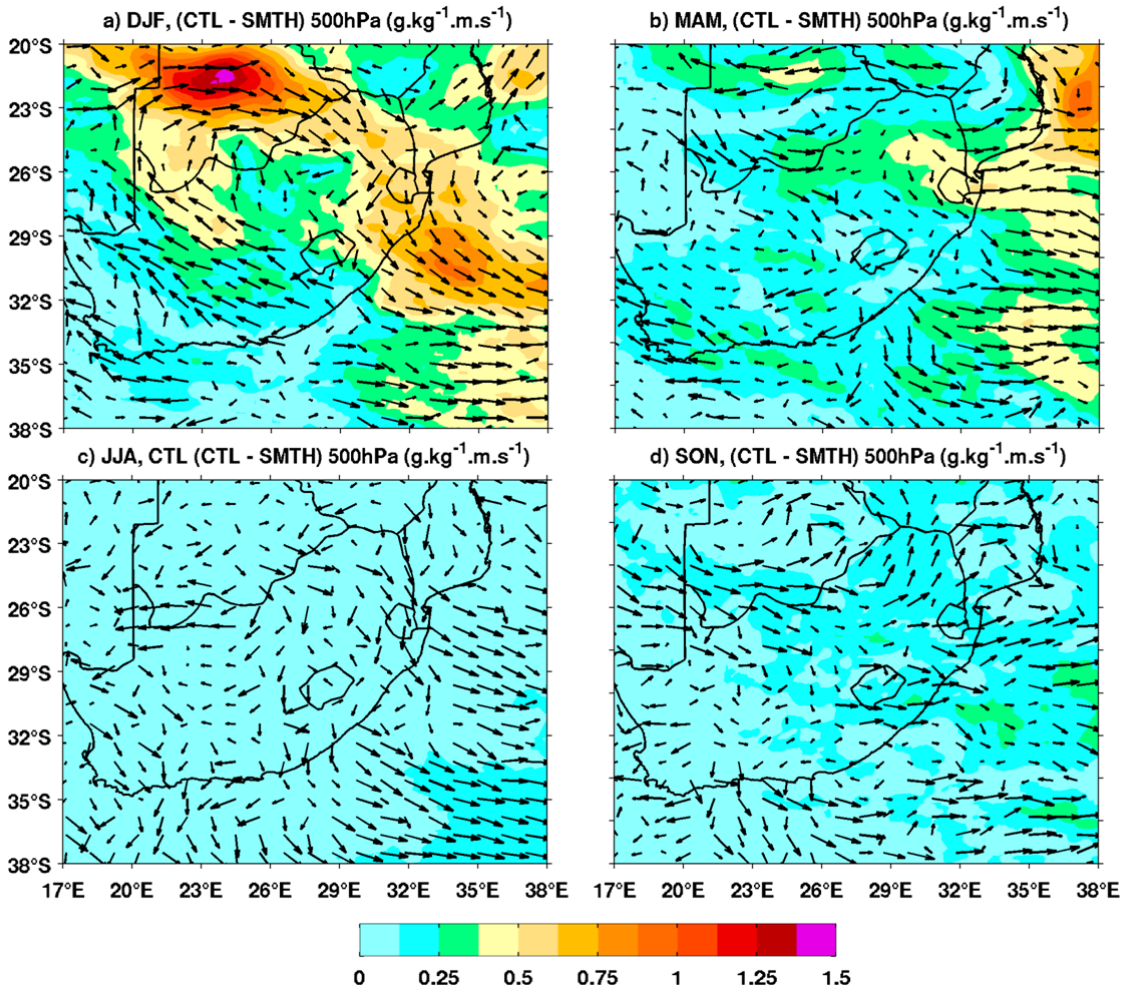

Figure 5.33: Seasonal differences of 500 hPa moisture flux between control and smoothed SST experiments: a) summer (DJF), b) autumn (MAM), c) winter (JJA) and d) spring (SON). Arrows represent the direction of the moisture transport every 1°.

5.2.2.3 Vertically integrated moisture flux

The vertical structure of the moisture distribution is a key factor for analysing the ocean-atmosphere variability in synoptic-scale systems (*Liu and Niiler*, 1984). The moisture flux convergence is a term in the conservation of water vapor equation and was first calculated in the 1950s as a vertically integrated quantity to forecast the rainfall associated with synoptic-scale systems (*Banacos and Schultz* 2004). **Figure 5.34** shows the horizontal distribution of the

vertically integrated moisture flux convergence (positive values) and divergence (negative values), with the vertically integrated moisture transports overlaid (arrows). The moisture is integrated from the surface to 100 hPa, over the air column. As in precipitation minus evaporation budget, moisture convergence indicates a wetter region, and moisture divergence results in a region with less rain or more evaporation.

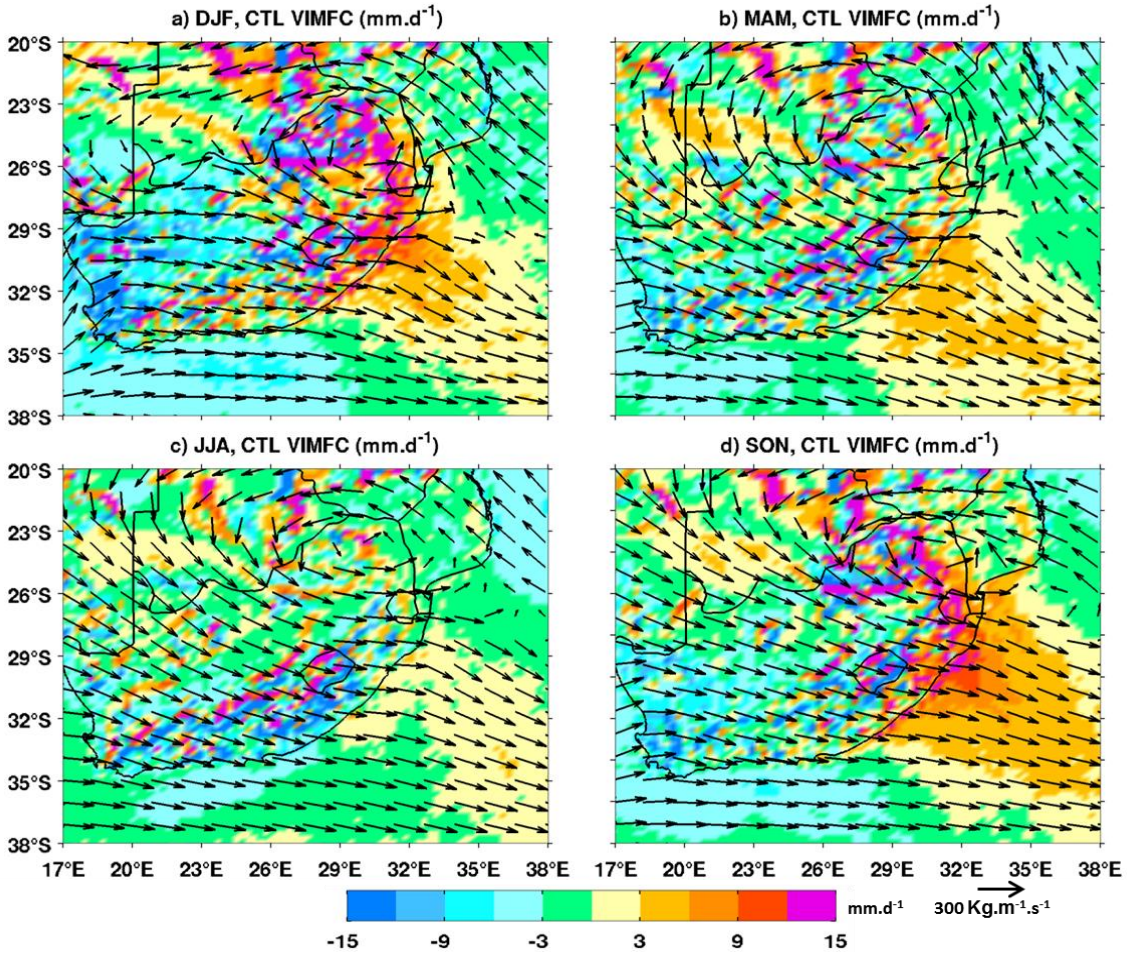

Figure 5.34: Seasonal means of vertically integrated moisture flux convergence (positive values) of control experiment: a) summer (DJF), b) autumn (MAM), c) winter (JJA), and d) spring (SON). Arrows represent the direction of the vertically integrated moisture transport every 1°.

The vertically integrated moisture flux convergence (VIMFC) occurs over the land mostly in summer, autumn and spring (**Fig. 5.34a,b,d**) where the rainfall is dominant over the ocean and east of southern Africa (**Fig. 5.6a,b,d**). Meanwhile, the southwest has a dominance of vertically

integrated moisture flux divergence (VIMFD) (**Fig. 5.34a,b,d**). Over the maritime areas, the VIMFC follows the pathway of the South Indian Convergence Zone (SICZ) for the whole seasons. *Cook* (2000) defined the SICZ as a region of enhanced precipitation extending off the southeast coast of southern Africa. Our results confirm the studies done by *Cook* (2000) and *Ratnam et al.* (2015) for the summer season. The VIMF transport represented by arrows show an import of the VIMF to the north through the Mozambique Channel for each season. This moisture forms an anticyclonic flow over the northeast of South Africa (24-27°S, 25-31°E), with the moisture originating from the South Atlantic Ocean, and is exported to the southeast coast of South Africa. *Vigaud et al.*, (2007, 2009) show that the south Atlantic SSTs partially influence moisture fluxes between the south Atlantic Ocean and southern Africa regions.

The difference between both simulations of the VIMFC must be analysed along with the $P-E$ difference. Change in $P-E$ is balanced by change in atmospheric moisture convergence (*Seager et al.* 2007; *Seager and Vicchi* 2010). In this study, we compare the $P-E$ differences between control and smoothed SST runs ($P-E$ anomalies) (**Fig. 5.15**), and the VIMFC differences between the two simulations (VIMFC anomalies) (**Fig. 5.35**). They are linked by the following equation:

$$P-E=\int_{Ps}^{100hPa}\rho_{air}H*(\nabla.(\bar{q}\Delta\bar{u})+\nabla.(\bar{u}\Delta\bar{q})+\nabla.(\Delta\bar{q}\Delta\bar{u})+\nabla.(u'q')dP \quad \text{....(Eq. 5.2)}$$

P, E, P_s, ρ_{air}, and H are respectively precipitation, evaporation, surface pressure, air density (kg.m^{-3}) and geopotential height (m); $\bar{u}$ is the monthly averaged climatological wind (zonal and meridional) in m.s^{-1}, u' is the wind anomaly for one experiment; $\bar{q}$ is the monthly averaged climatological of specific humidity in g.kg^{-1}, q' is the anomaly of the specific humidity for one experiment. ∇ is the horizontal divergence operator.

We mainly focuse on summer (DJF) and autumn (MAM) where the VIMFC anomalies and $P-E$ anomalies are strong. Northeast of South Africa, the VIMFC anomalies are predominant over land (**Fig. 5.35a, b**), corresponding to positive $P-E$ anomalies (more precipitation) (**Fig. 5.15a, b**). This is consistent with the moisture flux anomalies maximum at 850, 700 and 500 hPa (**Figs. 5.31a,b, 5.32a,b,** and **5.33a,b**). Some horizontal patches of VIMFC anomalies are present over maritime areas along the northeast coast, corresponding to more precipitation as well. VIMFD

anomalies occur over the northwest and southwest of southern Africa in summer, and over South Africa country in autumn, corresponding to regions where $P - E$ is almost 0 (**Fig. 5.15a, b**). In these regions, the moisture flux anomalies are weak (**Figs. 5.31a,b, 5.32a,b,** and **5.33a,b**). **Figure 5.35a,b** also show the export of VIMF anomalies to the north, and the import of VIMF anomalies to the south along the east coast. This indicates that a 2°C decline of SST weakens the import of moisture flux to the north and the export of the moisture through the coast.

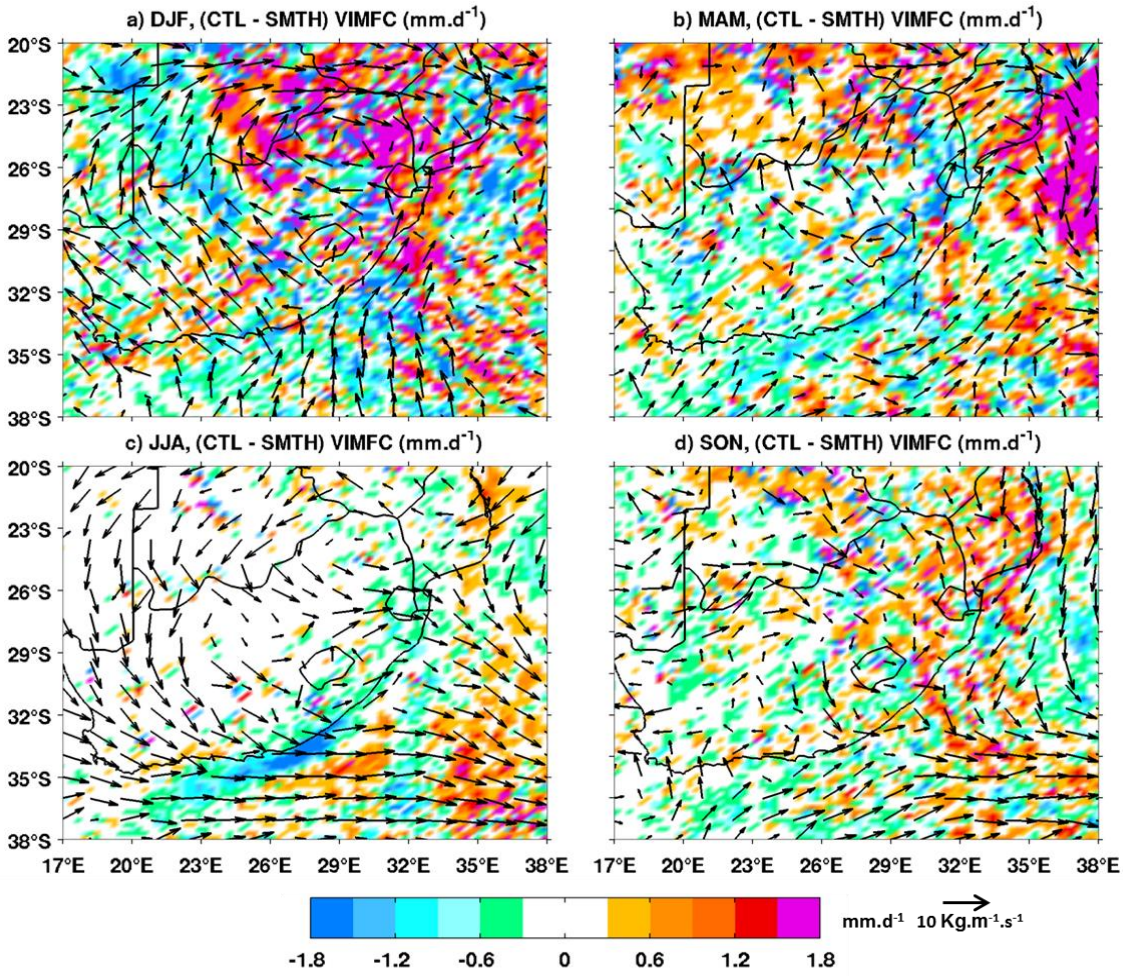

Figure 5.35: Seasonal differences (CTL – SMTH) of vertically integrated moisture flux convergence (positive values): a) summer (DJF), b) autumn (MAM), c) winter (JJA), and d) spring (SON). Arrows represent the direction of the vertically integrated moisture transport every 1°.

To assess whether the VIMF anomalies are due to climatological wind (circulation) anomalies or specific humidity anomalies, we decompose **Equation 5.2** following the approach given by *Seager et al.* (2007):

$\int_{Ps}^{100hPa} \rho_{air} H * \nabla.(\bar{q}\Delta\bar{u})\, dP$……. (**Eq. 5.3**) is the convergence term and is estimated by the climatological wind difference between the two experiments, with the specific humidity of smooth SST experiment.

$\int_{Ps}^{100hPa} \rho_{air} H * \nabla.(\bar{u}\Delta\bar{q})\, dP$……. (**Eq. 5.4**) is the advection term and is estimated by the climatological specific humidity difference between the two experiments with the smooth SST wind.

$\int_{Ps}^{100hPa} \rho_{air} H * \nabla.(\Delta\bar{u}\Delta\bar{q}) dP$ ……. (**Eq. 5.5**) represents the climatological wind and specific humidity differences. This term is found to be negligible compared to the convergence and advection terms (not shown).

$\int_{Ps}^{100hPa} \rho_{air} H * \nabla.(u'q')\, dP$ ……. (**Eq. 5.6**) is the eddy transient and represents the anomalies (deviation from the mean) differences of VIMF between both simulations.

Equations 5.2, 5.3, 5.4, and **5.6** correspond to **Figures 5.35, 5.36, 5.37** and **5.38** respectively, and are analysed together. In summer and autumn, over land area, the VIMFC anomalies (**Fig. 5.35a,b**) closely resemble the horizontal distribution of VIMFC anomalies due to the wind difference between the two simulations (**Fig. 5.36a,b**). The moisture transports anomalies have also similar directions (**Figs. 5.35a,b** and **5.36a,b**). Along the southeast coast of South Africa, over the Agulhas Current, the VIMFD anomalies are dominant, due to the specific humidity difference (**Fig. 5.37a,b**). This result implies that a 2°C warm SST anomalies creates the moisture convergence anomalies over land due to wind anomalies, and this is favourable to more precipitation anomalies; and moisture divergence along the coast due to specific humidity difference and leading to less rainfall more evaporation anomalies. In summer and autumn (**Fig. 5.38a,b**) eddy transient moisture anomalies contribute to increasing the VIMFD anomalies along

the northeastern coast of Southern African regions. This increase in VIMFD cancels out with the VIMFC due to the specific humidity difference (**Fig. 5.37a,b**).

To summarise this section, in summer and autumn, the control experiment creates a 2°C warm SST anomaly, leading to a low-pressure system anomaly. This weakens the high pressure system and creates a cyclonic motion anomaly, transporting moisture anomalies from the ocean to the interior. The moisture flux penetrates the land through the South and eastern coast of South Africa, esecially where the Agulhas Current hugs the coast. The VIMFC differences and the $P - E$ differences are balanced, and this relationship shows the VIMFC anomalies due to wind anomalies. This leads to more precipitation anomaly in southern Africa. This result indicates that the Agulhas Current influences southern Africa precipitation. Over the ocean, the VIMFD anomalies due to specific humidity anomalies results in negative $P - E$ anomalies (evaporation) with the overall effect being more continental precipitation. More precipitation above the continent will result in more geopotential anomaly up to 500 hPa leading to more cyclonic moisture flux anomalies.

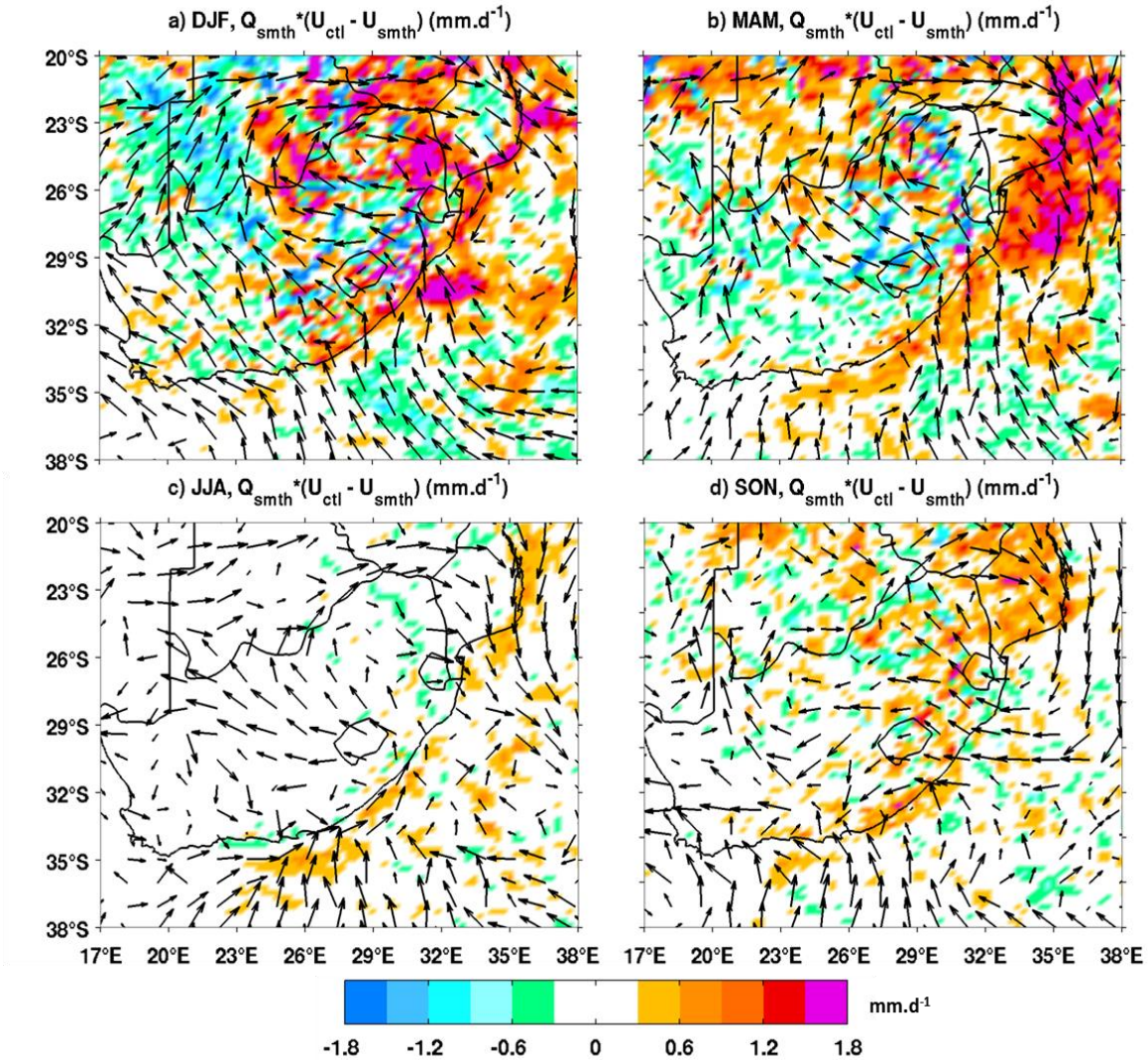

Figure 5.36: Seasonal means of the convergence (positive values) of the smooth specific humidity (Q_{Smth}) multiplied with the horizontal wind difference between the control experiment and the experiment with the smoothed SST ($U_{Ctl} - U_{Smth}$), computed following **Equation 5.3**. Overlaid are the corresponding vertically integrated moisture transports (arrows every 1°): a) DJF, b) MAM, c) JJA, and d) SON.

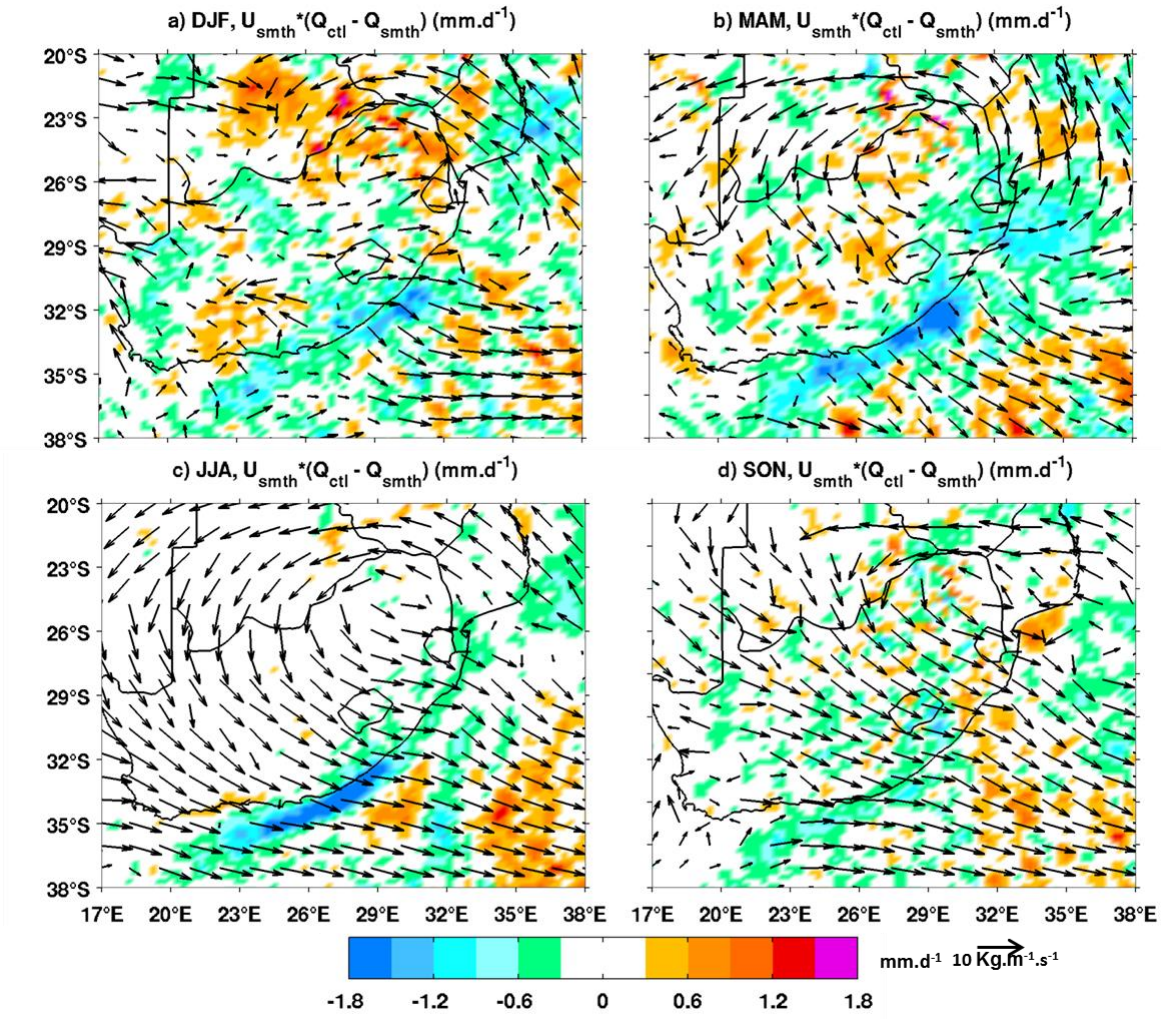

Figure 5.37: Seasonal averages of the convergence (negative values) of the SMTH wind (U_{Smth}), multiplied with the horizontal specific humidity difference between the control experiment and the experiment with the smoothed SST ($Q_{Ctl} - Q_{Smth}$), computed following **Equation 5.4**. Overlaid are the corresponding vertically integrated moisture transports (arrows): a) DJF, b) MAM, c) JJA, and d) SON.

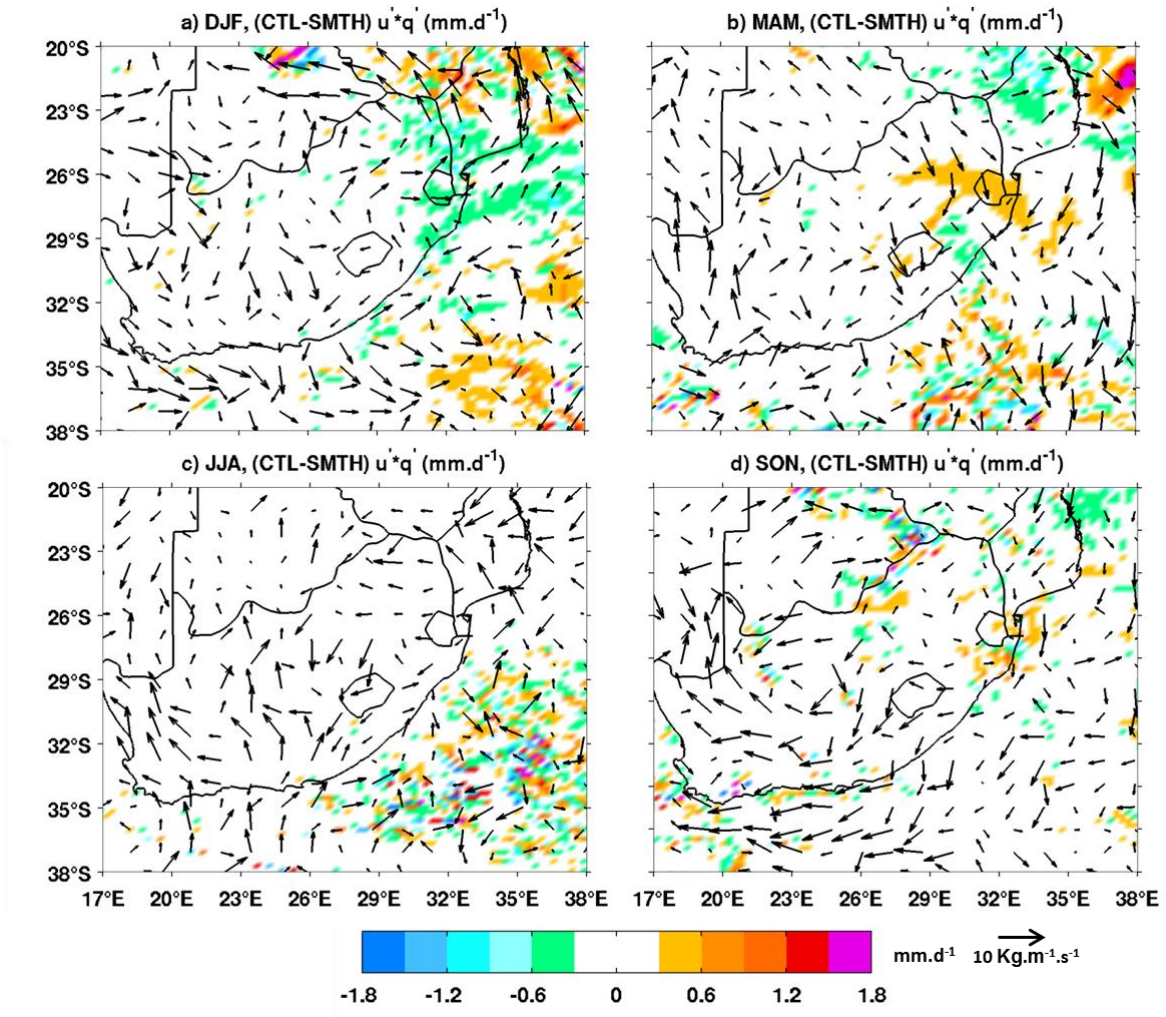

Figure 5.38: Seasonal transient eddy moisture difference between the control and the smoothed SST run of the vertically integrated moisture flux anomalies, computed following **Equation 5.6**. Overlaid are corresponding vertically integrated moisture transports (arrows).

5.3 DISCUSSION AND SUMMARY

In this study, we have investigated the seasonal impact of the Agulhas Current using satellite data, the CFSR reanalysis (*Saha et al*. 2010), and two experiments of the WRF regional model (*Skamarock and Klemp* 2008). We have first validated the WRF and CFSR precipitation using a 50-year climatology of *Hewitson and Crane* (2005), for land precipitation, and using TRMM PR

for maritime rainfall. WRF model overestimates the land precipitation for all seasons. This might be due to the sensitivity of WRF to the topography (see **Chap. 4**). In winter, WRF underestimates the rain along the coast above the Agulhas Current. This could be due to the understimation of the Agulhas Current by WRF, a common problem with atmospheric models. CFSR underestimates precipitation over land and ocean.

We then investigate the seasonal impact of the Agulhas Current on low-level convergence and rainfall of South Africa. The first method is focused on the analysis of the pressure adjustment as in **Chapter 4**. The second method is based on the analysis of geopotential heights, moisture flux, and the approach given by *Seager et al.* (2007), in order to identify whether changes in moisture convergence between the two simulations are due to changes in climatological wind or climatological specific humidity. From the first analysis, we found a relationship between SST Laplacian, SLP Laplacian, and wind convergence for each season (see also **Chap. 4**). Thus, above the Agulhas region and adjacent coastline, the band of precipitation could be explained by the pressure adjustment at all season. We note a 45% increase of precipitation above the Agulhas Current in summer (DJF) and autumn (MAM) and a 35% increase of rainfall over the inland coast (not shown), and up to 25% increase of rain in winter (JJA) and spring (SON). As WRF model overestimates the land precipitation, this result could be link to the sensitivity of WRF to the topography.

The second part of this chapter demonstrates that in summer and autumn, the Agulhas Current creates a low-pressure anomaly above the ocean extending to the land, weakening the anticyclonic motion of the Indian Ocean high pressure system. At 500 and 700 hPa, this anomaly is shifted inland probably because of the increase rainfall inland due to the increase transport of moisture flux from the ocean and the Agulhas Current to the interior. The $P - E$ difference between the two simulations, and the vertically integrated moisture flux (VIMF) difference reveal that the VIMFC anomalies are due to the wind difference. We suggest that the warm SST due to the Agulhas Current is a key driver of this wind difference. The resultant positive $P - E$ difference leads to more precipitation anomalies. This indicates that over land in summer and autumn a 2°C created by the SST of the control run leads to more moisture flux convergence and therefore more precipitation. Thus, the Agulhas Current plays an important role in enhancing precipitation over the interior of southern Africa, by bringing more moisture flux to the interior, and along the coast by the pressure adjustment mechanism.

As modeling studies reproduce results in regard to input data, our main results could be due to the SST prescribed or our smoothing method. As futher work, it will be interesting to do the same analysis with the new climate reanalysis data such as MERRA-2 or the Japanese 55-year Reanalysis, to confirm our main findings.

CHAPTER 6

6 DISCUSSION, CONCLUSIONS AND PERSPECTIVES

The Agulhas Current is the strongest western boundary current in the Southern Hemisphere. The aim of this thesis is to investigate the impact of this warm Current on the South African region. We define four seasons: the austral summer (DJF), autumn (MAM), winter (JJA) and spring (SON). A first assessment is to evaluate whether the new climate reanalyses do represent the intense exchanges of ocean-atmosphere interactions, and to identify the drivers of the annual cycle of the turbulent flux of moisture (as known as turbulent latent heat flux (LHF)). To do that, we use high-resolution satellite data sets, *in-situ* observations, and climate reanalyses. The second part of the thesis is based on the annual influence of the Agulhas Current on South Africa precipitation, using high-resolution data sets, a climate reanalysis and a numerical model. The last part of this study is a follow up of the role of the Agulhas Current on precipitation, at the seasonal scale.

We investigate the seasonal cycle of the turbulent flux of moisture in **Chapter 3** from 2003 to 2007. We find that in the Agulhas Current region, LHF is large all year long, but the highest values are during winter (~250 $W.m^{-2}$) around the Agulhas Retroflection region (19-20°E; 38-39°S), and the lowest are during summer (~150 $W.m^{-2}$) off Port Elizabeth (25-26°E; 34.5-35.5°S) (**Fig. 3.1**). Our result is consistent with the study of *Liu et al.* (2011) who showed that large LHFs were encountered in the Agulhas Retroflection region. We compare the new climate reanalyses and the observations of the National Oceanography Centre Southampton (NOCS, *Berry and Kent*, 2011) with satellite data sets. We find that the Climate Forecast System Reanalysis (CFSR, *Saha et al.* 2010) and the Modern-Era Retrospective analysis for Research and Applications (MERRA-2, *Gelaro et al.* 2017) do represent the intense exchange of moisture from ocean to atmosphere well, when compared to the high-resolution air-sea turbulent fluxes (SEAFLUX, *Curry et al.* 2004). ERA-Interim reanalysis (*Dee et al.* 2011) underestimates the LHF, and the annual cycle of NOCS LHF is reversed, with a maximum in summer and a minimum in winter, when compared to SEAFLUX. *Rouault et al.* (2003) showed that models tend to underestimate the LHF if they are unable to adequately represent the air-sea fluxes over the warmest waters in the Agulhas Current

system. The recent study of *Parker* (2016) shows that reanalyses are closer to observations even though they have limitations due to observational constraints. There is not a "reference" for the LHF, but it is worthy to note that SEAFLUX could be considered as a reference, because of its high-resolution, and the good representation of the SST and wind speed when compared to satellite products.

To estimate uncertainties within the products, we use the high-resolution satellite products Moderate Resolution Imaging Spectroradiometer data set (MODIS, *Kilpatrick et al.* 2015) as a reference for SST, and the Scatterometer Climatology of Ocean Winds (SCOW, *Risien and Chelton*, 2008) as a reference for surface wind speed and direction. CFSR, MERRA-2, ERA-Interim, and NOCS SST are similar to MODIS SST (**Fig. 3.6**), and their corresponding surface specific humidities (Qsst) are well represented compared to MODIS Qsst (**Fig. 3.10**). We recalculate the wind speed of CFSR, MERRA-2, ERA-Interim and NOCS to 10 m equivalent neutral wind using the Bourassa-Vincent-Wood neutral (BVWN) algorithm (*Bourassa et al.* 1999) for a better comparison with the satellite remote sensing SCOW. In the Agulhas region, CFSR and MERRA-2 wind speed compare well with SCOW wind speed, ERA-Interim is weaker than SCOW, and NOCS is stronger in summer and weaker in winter compared to SCOW (**Fig. 3.9**). Therefore, ERA-Interim, and NOCS underestimate the LHF, due to their lower wind speed, especially in winter. There is no reference for the air specific humidity (Qa). However, we use SEAFLUX Qa to evaluate the air specific humidity of reanalyses. We readjust CFSR and ERA-Interim Qa from 2 m to 10 m height using the BVW algorithm. MERRA-2 and NOCS Qa are available at 10 m. We note that Qa is different between products (**Fig. 3.11**), and constitutes a major source of uncertainty in the calculation of LHF. Other sources of specific uncertainties for the reanalyses are incomplete accounts of the surface current speed. Looking at the annual mean of the Agulhas Current from the GlobCurrent data repository, the surface current speed can be more than 1.5 $m.s^{-1}$. During the Agulhas Current Air-Sea Exchange Experiment (ACASEX, *Rouault et al.* (1995)), surface current speeds of up to 2 $m.s^{-1}$ were measured. Thus neglecting a 2 $m.s^{-1}$ current speed at a near-surface wind speed of 4 $m.s^{-1}$ may lead to a 50% error in the LHF estimation. The differences in LHF can also be explained by the diversity of algorithms; different bulk flux algorithms (e.g., *Brunke et al.* (2003)); different sources of the input meteorological state variables (e.g., *Curry et al.* (2004)); differences in the boundary conditions, and differences in the procedures for *in-situ* data collection. Differences can, moreover, arise from the averaging

methodology to obtain monthly means. For the satellite-based products, the retrievals of air temperature and air specific humidity at the surface continue to be problematic in regions with strong vertical gradients (*Smith* et al. 2011).

To identify the drivers of the annual cycle of LHF within the Agulhas Current system, we use the SEAFLUX product. We recalculate the LHF using a) a monthly climatology of the difference in specific humidity (Qsst-Qa) and the annual mean of wind speed (LHF_Qclim), and b) a monthly climatology of wind speed and the annual mean of Qsst-Qa (LHF_Uclim) (**Fig. 3.15**). We selected three locations of 1° longitude and 1° latitude: off Durban (31.5-32.5°E; 30-31°S) representing the eastern part of the Agulhas Current; off Port Elizabeth (25-26°E; 34.5-35.5°S) representing the middle of the Agulhas Current and the Retroflection area (19-20°E; 38-39°S). The analysis of SEAFLUX product within the three locations show that the main driver of the annual cycle of LHF off Durban is the specific humidity, with a correlation of between 0.96 LHF and LHF_Qclim, while it is the wind speed in the Retroflection region with a correlation of 0.85 between LHF and LHF_Uclim, and a combination of the wind speed and specific humidity between Durban and the Retroflection region. CFSR reanalysis is used for the second part of the study because it represents the ocean-atmosphere interactions well in the Southern Ocean compared to other reanalyses.

We use the reanalysis CFSR (from 2001 to 2005), numerous satellite data sets and two experiments of the Weather Research and Forecasting model (WRF, *Skamarock & Klemp*, 2008) to understand how the warm SST associated with the Agulhas Current affects the low-level atmosphere and rainfall annually (**Chapter 4**) and seasonally (**Chapter 5**). The two numerical experiments used over the period 2001 to 2005 are one with a high-resolution SST in the core of the Agulhas Current, and the other with the SST reduced by ~2°C in the Agulhas region. Using the high-resolution Tropical Rainfall Measuring Mission Precipitation Radar (TRMM PR, *Biasutti et al.* 2012), we show that there is a rainband above the Agulhas Current, also observed with the CFSR reanalysis and the WRF control experiment. This is consistent with the measurements of *Lutjeharms et al.* (1986), and *Rouault et al.* (2000) who observed a cloud line just above the Agulhas Current, around 1500 m in the lower troposphere, and concluded that this cloudband is due to the Agulhas Current. Our results indicate that the sharp SST gradients are responsible for the formation of the rainband and drive a local narrow overturning circulation in the lower troposphere. *Berthou et al.* (2016) studied the submonthly impact of air–sea coupling on precipitation in the Western Mediterranean basin. They found that the sensitivity of precipitation

to SST changes is due to low-level wind changes related to changes in surface heat fluxes. A closer study made on the region of Valencia (Spain) showed that there are lagged influence of mistral wind on heavy precipitation over the region through ocean-atmosphere coupling (*Berthou et al.* 2018). From a diagnostic of the pressure adjustment mechanism (*Lindzen and Nigam,* 1987; *Minobe et al.* 2008), we found that SST Laplacian, SLP Laplacian, and wind convergence are linked (**Figs. 4.3** and **4.5**). This relationship contributes to enhancing a band of precipitation along and above the Current also found by *Minobe et al.* (2008) above the Gulf Stream. Recent studies, however, indicate that the anchoring of precipitation over the Gulf Stream front is mainly associated with atmospheric frontal precipitation associated with synoptic-scale extratropical cyclones (*O'Neill et al.* 2017; *Parfitt et al.* 2016, *Sheldon et al.* 2017; *Vannière et al.* 2017, *Small et al.* 2018). A similar mechanism probably acts over the Agulhas Current, as a large part of the rainfall here is also related to atmospheric fronts (*Catto et al.* 2012). From the numerical experiments, we found that annually, ~2°C decline of SST leads to ~40% reduction of maritime precipitation along the eastern coast of South Africa above the Agulhas Current, and ~20% reduction of rainfall along the inland coast. Thus, it is important to resolve the fine structure of the Agulhas Current in order to quantify its impact on the regional climate.

Finally, in **Chapter 5**, we validate the seasonal cycle of WRF and CFSR precipitation, and we investigate the pressure adjustment mechanism, as well as the relationship between geopotential heights, moisture flux, and $P - E$ budget according to *Seager et al*. (2007). The WRF model overestimates by 3 $mm.d^{-1}$ the land precipitation for all seasons (**Fig. 5.6**), compared to the climatology of *Hewitson and Crane* (2005). This is due to the sensitivity of WRF to the topography. In winter, WRF underestimates the rain above the Agulhas Current by 2 $mm.d^{-1}$, compared to TRMM Precipitation Radar. CFSR reanalysis (**Fig. 5.7**) underestimates the precipitation over land and ocean compared to the climatology of *Hewitson and Crane* (2005) and TRMM Precipitation radar. The analysis of the pressure adjustment reveals a strong SST Laplacian, wind convergence and SLP Laplacian for all seasons (summer, autumn, winter, and spring), corresponding to the rainband above the Agulhas Current during these seasons. This causes enhanced precipitation over the maritime and inland coastal regions. The analysis of WRF shows that a 2°C SST decline weakens the SST Laplacian, SLP Laplacian and wind convergence. This leads to less precipitation along the coast. The model studies of *Small et al.* (2018) and *Desbiolles et al.* (2018) in summertime using high and low-resolution SST showed the strong

control of the high-resolution SST on the summer precipitation in the Southern Ocean. This is also observed in our study, using the two WRF experiments. Moreover, *Small et al.* (2018) showed that summer precipitation over the major western boundary currents is due to storm tracks over these regions. This could strengthen the anchoring of the rainband above the Agulhas Current. To improve the seasonal forecasts over South Africa, Ratnam et al. (2016) carried out a dynamical downscaling of the Scale Interaction Experiment–Frontier Research Center for Global Change (SINTEX-F2v CGCM) forecasts using WRF Model. The WRF Model was forced by the mean bias-corrected SINTEX-F2v CGCM fields. The mean bias correction was to replace the SINTEX-F2v 6-hourly climatology with the corresponding 6-hourly ERA-Interim climatological fields. Ratnam et al. (2016) showed that the WRF Model driven by the bias-corrected SINTEX-F2v fields had the higher skill in precipitation forecast compared to both the SINTEX-F2v and the WRF Model forced by the uncorrected SINTEX-F2v fields, and the last simulation showed higher skill compared to the SINTEX-F2v.

Reason et al. (2006) showed that the moisture flux enters Southern Africa through three different coastal areas: the tropical western Indian Ocean, the southwestern Indian Ocean, and the southeastern Atlantic Ocean. In this study, we are interested in the sources of moisture across the southwestern Indian Ocean, surrounding the northeastern part of southern Africa, and the moisture source from the southeastern Atlantic Ocean. At 950 hPa in summer and autumn, the moisture flux flows from southwestern Indian Ocean to the landmass, and along the coast above the Agulhas Current (**Fig. 5.26a, b**). At 850 hPa, the moisture circulation is landward northeast of South Africa, but in the core of the Agulhas Current, the moisture leaving the continent tends to balance the quantity entering South Africa (**Fig. 5.27a, b**). During winter, the moisture flux comes from the Atlantic Ocean (**Fig. 5.27c**). At 700 and 500 hPa, the large incoming moisture source is the southeast Atlantic Ocean for all seasons (**Figs. 5.28** and **5.29**). We found good relationships between the geopotential height anomalies and the moisture flux transport anomalies at 950, 850, 700 and 500 hPa. Negative geopotential height anomalies form a low-pressure system, resulting in a cyclonic motion extending from Indian Ocean to landmass. This phenomenon brings positive moisture flux anomalies from the Agulhas Current across the east coast of South Africa to the interior, with a maximum in central South Africa. Moisture flux anomalies then disappear through the Mozambique Channel. Thus, a 2°C decrease in SST weakens the inflow of moisture, entering South Africa from the Agulhas Current, and therefore less precipitation.

Finally, we calculate the vertically integrated moisture flux convergence (VIMFC) from the surface to 100 hPa. The VIMFC is transported from the southwest Indian Ocean to the southern African landmass. *Ratnam et al.* (2015) have shown the same result in the Southern Ocean, by using ERA-Interim reanalysis. In addition, based on the method of *Seager et al.* (2007), we show that in summer and autumn, the VIMFC difference between the two simulations correspond to positive $P - E$ anomalies over land (**Figs. 5.15** and **5.35**) and lead to more precipitation anomalies there. The VIMFC anomalies correspond to the VIMFC anomalies due to the wind difference between the two simulations (**Fig. 5.36**). Meanwhile, above the Agulhas Current, the VIMFD anomalies indicate negative anomalies of $P - E$ and therefore more evaporation (**Figs. 5.15** and **5.33**). In this case, the VIMFD anomalies correspond to the VIMFD anomalies due to the specific humidity difference between the two experiments (**Fig. 5.37**). The limitation of this study is that I have not been able to run more than two simulations for my study. But interestingly, there are some studies done with more WRF simulations by *Koseki and Demissie* (2018) and *Koseki et al.* (2018), as follow up *of Nkwinkwa Njouodo et al.* (2018). In the former study, *Koseki et al.* (2018) investigated the diurnal cycle of precipition in Southern Africa using 3 WRF simulations: one with the Agulhas Current, one with the Smoothed SST and the last simulation without the Drakengsberg mountain. They concluded that the diurnal cycle is mostly due to the Drakengsberg during the day, and the Agulhas Current plays a second role in producing rainfall along the inland east coast of South Africa from midnight to early morning.

With regard to the turbulent latent heat flux, further work will involve investigating the influence of the difference between satellite and equivalent neutral wind versus real wind, on the turbulent latent heat flux estimation, and on the associated seasonal variability. Moreover, it is necessary to examine the increase in turbulent latent heat flux derived from the products, its impact on extreme events, as well as the relationship between the heat flux derived from each product and variability of the Agulhas Current. To do that, climate reanalyses and modeling studies are recommended to take into account the core of the Agulhas Current speed that is 1.5 $m.s^{-1}$, and to quantify well the specific humidity east of the Agulhas Current, the wind speed in the Retroflection area, and both parameters in between. Concerning our model study, the convective-radiative feedback has not been activated following *Alapaty et al.* (2012). This could deeply modify latent heat fluxes under cloud cover and alter in the end the estimation of the Agulhas Current effects on the regional climate and rainfall. As future work, we will run a simulation that considers this effect, to have a

more accurate rainfall as the WRF model tends to overestimate precipitation. It will be useful to run a high-resolution simulation with and without the influence of El Nino Southern Oscillation, to ascertain whether the decrease of precipitation in South Africa is due to the strongest western boundary current in the Southern Hemisphere. It is also important to study the impact of the Agulhas Current on tropical temperate through, cold fronts and low-pressure systems that form offshore Durban. As further work, we also think of a long-term analysis of current and future effects of the Agulhas Current on the region, by using CFSR reanalysis since 1979 and high-resolution coupled model that allow to represent the Agulhas Current as outputs used for climate projections do not include the Agulhas Current. Also by using outputs of the climate projections taken from Coupled Model Intercomparaison Project version 5 or 6 (CMIP5/6) that could include changes in regional sea surface temperature, latent heat fluxes and atmospheric circulation under increasing anthropogenic influence, if these models represent well the Agulhas Current.

BIBLIOGRAPHY

Alapaty, K., Herwehe, J.A., Otte, T.L., Nolte, C.G., Bullock, O.R., Mallard, M.S., Kain, J.S. and Dudhia, J. (2012). Introducing subgrid-scale cloud feedbacks to radiation for regional meteorological and climate modeling. *Geophysical Research Letters*, *39*(24).

Andersson, A., Fennig, K., Klepp, C., Bakan, S., Graßl, H. and Schulz, J. (2010). The Hamburg ocean atmosphere parameters and fluxes from satellite data–HOAPS-3. *Earth System Science Data*, *2*, 215-234.

Andersson, A., Klepp, C., Fennig, K., Bakan, S., Grassl, H. and Schulz, J. (2011). Evaluation of HOAPS-3 ocean surface freshwater flux components. *Journal of Applied Meteorology and Climatology*, *50*(2), 379-398.

Back, L.E. and Bretherton, C.S. (2009). On the relationship between SST gradients, boundary layer winds, and convergence over the tropical oceans. *Journal of Climate*, *22*(15), 4182-4196.

Beal, L.M. and Bryden, H.L. (1997). Observations of an Agulhas undercurrent. *Deep Sea Research Part I: Oceanographic Research Papers*, *44*(9-10), 1715-1724.

Beal, L.M. and Bryden, H.L., 1999. The velocity and vorticity structure of the Agulhas Current at 32 S. *Journal of Geophysical Research: Oceans*, *104*(C3), 5151-5176.

Beal, L.M., Ffield, A. and Gordon, A.L. (2000). Spreading of Red Sea overflow waters in the Indian Ocean. *Journal of Geophysical Research: Oceans*, *105*(C4), 8549-8564.

Beal, L.M., Chereskin, T.K., Lenn, Y.D. and Elipot, S. (2006). The sources and mixing characteristics of the Agulhas Current. *Journal of physical oceanography*, *36*(11), 2060-2074.

Beal, L.M., De Ruijter, W.P., Biastoch, A., Zahn, R., Cronin, M., Hermes, J., Lutjeharms, J., Quartly, G., Tozuka, T., Baker-Yeboah, S. and Bornman, T. (2011). On the role of the Agulhas system in ocean circulation and climate. *Nature*, *472*(7344), 429.

Beal, L.M., Elipot, S., Houk, A. and Leber, G.M. (2015). Capturing the transport variability of a western boundary jet: Results from the Agulhas Current Time-Series Experiment (ACT). *Journal of Physical Oceanography*, *45*(5), 1302-1324.

Bentamy, A., Piollé, J.F., Grouazel, A., Danielson, R., Gulev, S., Paul, F., Azelmat, H., Mathieu, P.P., Von Schuckmann, K., Sathyendranath, S. and Evers-King, H. (2017). Review and assessment of latent and sensible heat flux accuracy over the global oceans. *Remote Sensing of Environment*, *201*, 196-218.

Banacos, P.C. and Schultz, D.M. (2005). The use of moisture flux convergence in forecasting convective initiation: Historical and operational perspectives. *Weather and Forecasting*, *20*(3), 351-366.

Berry, D.I. and Kent, E.C. (2009). A new air–sea interaction gridded dataset from ICOADS with uncertainty estimates. *Bulletin of the American Meteorological Society, 90*(5), 645-656.

Berry, D.I. and Kent, E.C. (2011). Air–sea fluxes from ICOADS: The construction of a new gridded dataset with uncertainty estimates. *International Journal of Climatology, 31*(7), 987-1001.

Berthou, S., Mailler, S., Drobinski, P., Arsouze, T., Bastin, S., Béranger, K., Flaounas, E., Lebeaupin Brossier, C., Somot, S. and Stéfanon, M., (2016). Influence of submonthly air–sea coupling on heavy precipitation events in the Western Mediterranean basin. *Quarterly Journal of the Royal Meteorological Society, 142*, 453-471.

Berthou, S., Mailler, S., Drobinski, P., Arsouze, T., Bastin, S., Béranger, K. and Brossier, C.L. (2018). Lagged effects of the Mistral wind on heavy precipitation through ocean-atmosphere coupling in the region of Valencia (Spain). *Climate dynamics*, *51*(3), 969-983.

Betts, A.K., (1986). A new convective adjustment scheme. Part I: Observational and theoretical basis. *Quarterly Journal of the Royal Meteorological Society, 112*(473), 677-691.

Biastoch, A. and Krauss, W. (1999). The role of mesoscale eddies in the source regions of the Agulhas Current. *Journal of Physical Oceanography, 29*(9), 2303-2317.

Biastoch, A., Böning, C.W. and Lutjeharms, J.R.E. (2008). Agulhas leakage dynamics affects decadal variability in Atlantic overturning circulation. *Nature, 456*(7221), 489.

Biastoch, A., Böning, C.W., Schwarzkopf, F.U. and Lutjeharms, J.R.E. (2009). Increase in Agulhas leakage due to poleward shift of Southern Hemisphere westerlies. *Nature, 462*(7272), 495.

Biasutti, M., Yuter, S.E., Burleyson, C.D. and Sobel, A.H. (2012). Very high resolution rainfall patterns measured by TRMM precipitation radar: seasonal and diurnal cycles. *Climate dynamics, 39*(1-2), 239-258.

Bosilovich, M.G., Lucchesi, R. and Suarez, M. (2016). MERRA-2: File specification GMAO Office Note No. 9 (Version 1.1).

Bourassa, M.A., Vincent, D.G. and Wood, W.L. (1999). A flux parameterization including the effects of capillary waves and sea state. *Journal of the Atmospheric Sciences, 56*(9), 1123-1139.

Brunke, M.A., Fairall, C.W., Zeng, X., Eymard, L. and Curry, J.A. (2003). Which bulk aerodynamic algorithms are least problematic in computing ocean surface turbulent fluxes?. *Journal of Climate, 16*(4), 619-635.

Bryden, H.L., Beal, L.M. and Duncan, L.M. (2005). Structure and transport of the Agulhas Current and its temporal variability. *Journal of Oceanography, 61*(3), 479-492.

Casey, K.S. (2004). *Global AVHRR 4 km SST for 1985-2001, Pathfinder V5. 0, NODC* (No. 0001763-0001864). RSMAS, Technical report, NOAA National Oceanographic Data Center, Silver Spring, Maryland. NODC Accession.

Catto, J.L., Jakob, C., Berry, G. and Nicholls, N., 2012. Relating global precipitation to atmospheric fronts. *Geophysical Research Letters*, *39*(10).

Cayan, D.R. (1992). Latent and sensible heat flux anomalies over the northern oceans: Driving the sea surface temperature. *Journal of Physical Oceanography*, *22*(8), 859-881.

Chan, P.K. and Gao, B.C. (2005). A comparison of MODIS, NCEP, and TMI sea surface temperature datasets. *IEEE geoscience and remote sensing letters*, *2*(3), 270-274.

Chelton, D.B., Esbensen, S.K., Schlax, M.G., Thum, N., Freilich, M.H., Wentz, F.J., Gentemann, C.L., McPhaden, M.J. and Schopf, P.S. (2001). Observations of coupling between surface wind stress and sea surface temperature in the eastern tropical Pacific. *Journal of Climate*, *14*(7), 1479-1498.

Chelton, D.B., Schlax, M.G., Freilich, M.H. and Milliff, R.F. (2004). Satellite measurements reveal persistent small-scale features in ocean winds. *science*, *303*(5660), 978-983.

Chelton, D.B., (2005). The impact of SST specification on ECMWF surface wind stress fields in the eastern tropical Pacific. *Journal of climate*, *18*(4), 530-550.

Chelton, D.B. and Wentz, F.J. (2005). Global microwave satellite observations of sea surface temperature for numerical weather prediction and climate research. *Bulletin of the American Meteorological Society*, *86*(8), 1097-1116.

Chelton, D.B. and Xie, S.P. (2010). Coupled ocean-atmosphere interaction at oceanic mesoscales. *Oceanography*, *23*(4), 52-69.

Chen, F. and Dudhia, J. (2001). Coupling an advanced land surface–hydrology model with the Penn State–NCAR MM5 modeling system. Part I: Model implementation and sensitivity. *Monthly Weather Review*, *129*(4), 569-585.

Chou, S.H., Nelkin, E., Ardizzone, J. and Atlas, R.M. (2004). A comparison of latent heat fluxes over global oceans for four flux products. *Journal of climate*, *17*(20), 3973-3989.

Clark, N.E., Eber, L., Laurs, R.M., Renner, J.A. and Saur, J.F.T. (1974). *Heat exchange between ocean and atmosphere in the eastern North Pacific for 1961-1971*. US Department of Commerce.

Clayson, C.A., J. B. Roberts and A. Bogdanoff, (2013). SEAFLUX Version 1: a new satellitebased ocean-atmosphere turbulent flux dataset. *International Journal of Climatologie* (in revision).

Cook, K.H. (2000). The South Indian convergence zone and interannual rainfall variability over southern Africa. *Journal of Climate*, *13*(21), 3789-3804.

Cook, C., Reason, C.J. and Hewitson, B.C. (2004). Wet and dry spells within particularly wet and dry summers in the South African summer rainfall region. *Climate Research*, *26*(1), 17-31.

Cook, K.H. (2001). A Southern Hemisphere wave response to ENSO with implications for southern Africa precipitation. *Journal of the Atmospheric Sciences*, *58*(15), 2146-2162.

Curry, J.A., Bentamy, A., Bourassa, M.A., Bourras, D., Bradley, E.F., Brunke, M., Castro, S., Chou, S.H., Clayson, C.A., Emery, W.J. and Eymard, L. (2004). Seaflux. *Bulletin of the American Meteorological Society*, *85*(3), 409-424.

d'Abreton, P.C. and Lindesay, J.A. (1993). Water vapour transport over southern Africa during wet and dry early and late summer months. *International Journal of Climatology*, *13*(2), 151-170.

Dee, D.P., Uppala, S.M., Simmons, A.J., Berrisford, P., Poli, P., Kobayashi, S., Andrae, U., Balmaseda, M.A., Balsamo, G., Bauer, D.P. and Bechtold, P. (2011). The ERA-Interim reanalysis: Configuration and performance of the data assimilation system. *Quarterly Journal of the royal meteorological society*, *137*(656), 553-597.

Bentamy, A., Katsaros, K.B., Mestas-Nuñez, A.M., Drennan, W.M., Forde, E.B. and Roquet, H., (2003). Satellite estimates of wind speed and latent heat flux over the global oceans. *Journal of climate*, *16*(4), 637-656.

De Ruijter, W.P., Ridderinkhof, H. and Schouten, M.W. (2005). Variability of the southwest Indian Ocean. *Philosophical Transactions of the Royal Society of London A: Mathematical, Physical and Engineering Sciences*, *363*(1826), 63-76.

Desbiolles, F., Blamey, R., Illig, S., James, R., Barimalala, R., Renault, L. and Reason, C. (2018). Upscaling impact of wind/sea surface temperature mesoscale interactions on southern Africa austral summer climate. *International Journal of Climatology*, *38*(12), 4651-4660.

Dudhia, J. (1989). Numerical study of convection observed during the winter monsoon experiment using a mesoscale two-dimensional model. *Journal of the atmospheric sciences*, *46*(20), 3077-3107.

Donlon, C.J., Martin, M., Stark, J., Roberts-Jones, J., Fiedler, E. and Wimmer, W. (2012). The operational sea surface temperature and sea ice analysis (OSTIA) system. *Remote Sensing of Environment*, *116*, 140-158.

Donners, J. and Drijfhout, S.S. (2004). The Lagrangian view of South Atlantic interocean exchange in a global ocean model compared with inverse model results. *Journal of physical oceanography*, *34*(5), 1019-1035.

Engelbrecht, C.J., Landman, W.A., Engelbrecht, F.A. and Malherbe, J. (2015). A synoptic decomposition of rainfall over the Cape south coast of South Africa. *Climate Dynamics*, *44*(9-10), 2589-2607.

Engelbrecht, C.J. and Landman, W.A. (2016). Interannual variability of seasonal rainfall over the Cape south coast of South Africa and synoptic type association. *Climate dynamics*, *47*(1-2), 295-313.

Fairall, C.W., Bradley, E.F., Hare, J.E., Grachev, A.A. and Edson, J.B. (2003). Bulk parameterization of air–sea fluxes: Updates and verification for the COARE algorithm. *Journal of climate*, *16*(4), 571-591.

Frankignoul, C., Müller, P. and Zorita, E. (1997). A simple model of the decadal response of the ocean to stochastic wind forcing. *Journal of Physical Oceanography*, *27*(8), 1533-1546.

Frankignoul, C., de Coëtlogon, G., Joyce, T.M. and Dong, S. (2001). Gulf Stream variability and ocean–atmosphere interactions. *Journal of physical Oceanography*, *31*(12), 3516-3529.

Frankignoul, C. and Kestenare, E. (2002). The surface heat flux feedback. Part I: Estimates from observations in the Atlantic and the North Pacific. *Climate dynamics*, *19*(8), 633-647.

Geernaert, G. and Katsaros, K.B. (1986). Incorporation of stratification effects on the oceanic roughness length in the derivation of the neutral drag coefficient. *Journal of physical oceanography*, *16*(9), 1580-1584.

Gelaro, R., McCarty, W., Suárez, M.J., Todling, R., Molod, A., Takacs, L., Randles, C.A., Darmenov, A., Bosilovich, M.G., Reichle, R. and Wargan, K. (2017). The modern-era retrospective analysis for research and applications, version 2 (MERRA-2). *Journal of Climate*, *30*(14), 5419-5454.

Gibson, J.K., Kallberg, P., Uppala, S., Hernandez, A., Nomura, A. and Serrano, E. (1997). ERA description. ECMWF Re-Analysis Project Report Series 1, ECMWF. *Reading, UK*, 77.

Gimeno, L., Drumond, A., Nieto, R., Trigo, R.M. and Stohl, A. (2010). On the origin of continental precipitation. *Geophysical Research Letters*, *37*(13).

Gordon, A.L. (1986). Interocean exchange of thermocline water. *Journal of Geophysical Research: Oceans*, *91*(C4), 5037-5046.

Gordon, A. L., Weiss, R. F., Smethie, W. M. and Warner, M. J. (1992), Thermocline and intermediate water communication between the South Atlantic and Indian Oceans. *Journal of Geophysical Research* 97, 7223–7240.

Grell, G.A. and Freitas, S.R. (2014). A scale and aerosol aware stochastic convective parameterization for weather and air quality modeling. *Atmos. Chem. Phys*, *14*(10), 5233-5250.

Griffies, S.M., Harrison, M.J., Pacanowski, R.C. and Rosati, A. (2004). A technical guide to mom4 gfdl ocean group technical report no. 5, NOAA. *Geophysical Fluid Dynamics Laboratory*, *339*.

Hand, R., Keenlyside, N., Omrani, N.E. and Latif, M. (2014). Simulated response to inter-annual SST variations in the Gulf Stream region. *Climate dynamics*, *42*(3-4), 715-731.

Hart-Davis, M.G., Backeberg, B.C., Halo, I., van Sebille, E. and Johannessen, J.A. (2018). Assessing the accuracy of satellite derived ocean currents by comparing observed and virtual buoys in the Greater Agulhas Region. *Remote Sensing of Environment*.

Hewitson, B.C. and Crane, R.G. (2005). Gridded area-averaged daily precipitation via conditional interpolation. *Journal of Climate*, *18*(1), 41-57.

http://seaflux.org/seaflux_data/DOCUMENTATION/SeaFluxDocumentationV12.pdf

Hólm, E.V. (2002), July. Revision of the ECMWF humidity analysis: Construction of a Gaussian control variable. In *Proceedings of the ECMWF/GEWEX Workshop on humidity analysis* 8-11.

Hong, S.Y. and Lim, J.O.J. (2006). The WRF single-moment 6-class microphysics scheme (WSM6). *J. Korean Meteor. Soc*, *42*(2), 129-151.

Hong, S.Y., Noh, Y. and Dudhia, J. (2006). A new vertical diffusion package with an explicit treatment of entrainment processes. *Monthly weather review*, *134*(9), 2318-2341.

Hoskins, B.J. and Hodges, K.I. (2005). A new perspective on Southern Hemisphere storm tracks. *Journal of Climate*, *18*(20), 4108-4129.

Johannessen, J.A., Chapron, B., Collard, F., Rio, M.H., Piollé, J.F., Gaultier, L., Quartly, G., Shutler, J., Raj, R., Donlon, C. and Danielson, R. (2016), September. GlobCurrent: Multisensor synergy for surface current estimation. ESA.

Josey, S.A., Kent, E.C. and Taylor, P.K. (1999). New insights into the ocean heat budget closure problem from analysis of the SOC air–sea flux climatology. *Journal of Climate*, *12*(9), 2856-2880.

Jury, M.R., Valentine, H.R. and Lutjeharms, J.R. (1993). Influence of the Agulhas Current on summer rainfall along the southeast coast of South Africa. *Journal of Applied Meteorology*, *32*(7), 1282-1287.

Jury, M.R. (1994). A thermal front within the marine atmospheric boundary layer over the Agulhas Current south of Africa: Composite aircraft observations. *Journal of Geophysical Research: Oceans*, *99*(C2), 3297-3304.

Jury, M.R., Pathack, B., Rautenbach, C.D.W. and Vanheerden, J. (1996). Drought over South Africa and Indian Ocean SST: statistical and GCM results. *The Global Atmosphere and Ocean System*, *4*(1), 47-63.

Jury, M.R. (2015). Passive suppression of South African rainfall by the Agulhas Current. *Earth Interactions*, *19*(13), 1-14.

Kalnay, E., Kanamitsu, M., Kistler, R., Collins, W., Deaven, D., Gandin, L., Iredell, M., Saha, S., White, G., Woollen, J. and Zhu, Y. (1996). The NCEP/NCAR 40-year reanalysis project. *Bulletin of the American meteorological Society*, *77*(3), 437-472.

Kanamitsu, M., Ebisuzaki, W., Woollen, J., Yang, S.K., Hnilo, J.J., Fiorino, M. and Potter, G.L. (2002). Ncep–doe amip-ii reanalysis (r-2). *Bulletin of the American Meteorological Society*, *83*(11), 1631-1644.

Kain, J.S. (2004). The Kain–Fritsch convective parameterization: an update. *Journal of applied meteorology*, *43*(1), 170-181.

Kain, J.S., Weiss, S.J., Levit, J.J., Baldwin, M.E. and Bright, D.R. (2006). Examination of convection-allowing configurations of the WRF model for the prediction of severe convective weather: The SPC/NSSL Spring Program 2004. *Weather and Forecasting*, *21*(2), 167-181.

Kent, E.C. and Kaplan, A. (2006). Toward estimating climatic trends in SST. Part III: Systematic biases. *Journal of Atmospheric and Oceanic Technology*, *23*(3), 487-500.

Kilpatrick, K.A., Podesta, G.P. and Evans, R. (2001). Overview of the NOAA/NASA advanced very high resolution radiometer Pathfinder algorithm for sea surface temperature and associated matchup database. *Journal of Geophysical Research: Oceans*, *106*(C5), 9179-9197.

Kilpatrick, K.A., Podestá, G., Walsh, S., Williams, E., Halliwell, V., Szczodrak, M., Brown, O.B., Minnett, P.J. and Evans, R., (2015). A decade of sea surface temperature from MODIS. *Remote Sensing of Environment*, *165*, 27-41.

Kistler, R., Kalnay, E., Collins, W., Saha, S., White, G., Woollen, J., Chelliah, M., Ebisuzaki, W., Kanamitsu, M., Kousky, V. and van den Dool, H. (2001). The NCEP–NCAR 50-year reanalysis: monthly means CD-ROM and documentation. *Bulletin of the American Meteorological society*, *82*(2), 247-268.

Knorr, G. and Lohmann, G. (2003). Southern Ocean origin for the resumption of Atlantic thermohaline circulation during deglaciation. *Nature*, *424*(6948), 532.

Koseki, S. and Watanabe, M. (2010). Atmospheric boundary layer response to mesoscale SST anomalies in the Kuroshio Extension. *Journal of Climate*, *23*(10), 2492-2507.

Koseki, S. and Demissie, T., (2018). Does the Drakensberg dehydrate southwestern Africa?. *Journal of Arid Environments*, *158*, 35-42.

Koseki, S., Pohl, B., Bhatt, B.C., Keenlyside, N. and Nkwinkwa Njouodo, A.S. (2018). Insights into the Summer Diurnal Cycle over Eastern South Africa. *Monthly Weather Review*, *146*(12), 4339-4356.

Krug, M. and Tournadre, J. (2012). Satellite observations of an annual cycle in the Agulhas Current. *Geophysical Research Letters*, *39*(15).

Kwon, Y.O., Alexander, M.A., Bond, N.A., Frankignoul, C., Nakamura, H., Qiu, B. and Thompson, L.A. (2010). Role of the Gulf Stream and Kuroshio–Oyashio systems in large-scale atmosphere–ocean interaction: A review. *Journal of Climate*, *23*(12), 3249-3281.

Kwon, Y.O., Alexander, M.A., Bond, N.A., Frankignoul, C., Nakamura, H., Qiu, B. and Thompson, L.A. (2010). Role of the Gulf Stream and Kuroshio–Oyashio systems in large-scale atmosphere–ocean interaction: A review. *Journal of Climate*, *23*(12), 3249-3281.

Le Bars, D.L.B., Dijkstra, H.A. and De Ruijter, W.P.M. (2013). Impact of the Indonesian Throughflow on Agulhas leakage. *Ocean Science Discussions*, *10*, 353-391.

Lee-Thorp, A.M., Rouault, M. and Lutjeharms, J.R.E. (1998). Cumulus cloud formation above the Agulhas Current. *South African journal of science*, *94*(7), 351-354.

Lee-Thorp, A.M., Rouault, M. and Lutjeharms, J.R.E. (1999). Moisture uptake in the boundary layer above the Agulhas Current: A case study. *Journal of Geophysical Research: Oceans*, *104*(C1), 1423-1430.

Lindzen, R.S. and Nigam, S. (1987). On the role of sea surface temperature gradients in forcing low-level winds and convergence in the tropics. *Journal of the Atmospheric Sciences*, *44*(17), 2418-2436.

Liu, J., Xiao, T. and Chen, L. (2011). Intercomparisons of air–sea heat fluxes over the Southern Ocean. *Journal of Climate*, *24*(4),1198-1211.

Liu, W.T. and Niiler, P.P. (1984). Determination of monthly mean humidity in the atmospheric surface layer over oceans from satellite data. *Journal of Physical Oceanography*, *14*(9), 1451-1457.

Lorenc, A.C. (1981). A global three-dimensional multivariate statistical interpolation scheme. *Monthly Weather Review*, *109*(4), 701-721.

Lutjeharms, J.R.E., Mey, R.D. and Hunter, I.T. (1986). Cloud lines over the Agulhas Current. *South African Journal of Science*, *82*(11), 635-640.

Lutjeharms, J.R.E. and Roberts, H.R. (1988). The Natal pulse: An extreme transient on the Agulhas Current. *Journal of Geophysical Research: Oceans*, *93*(C1), 631-645.

Lutjeharms, J.R.E. and Van Ballegooyen, R.C. (1988). The retroflection of the Agulhas Current. *Journal of Physical Oceanography*, *18*(11), 1570-1583.

Lutjeharms, J.R.E., Cooper, J. and Roberts, M. (2000). Upwelling at the inshore edge of the Agulhas Current. *Continental Shelf Research*, *20*(7), 737-761.

Lutjeharms, J.R.E. and Rouault, M. (2000). Observations of cloud formation above Agulhas Current intrusions in the Southeast Atlantic. *South African Journal of Science*, *96*.

Lutjeharms, J.R. (2006). *The agulhas current* (Vol. 2). Berlin: Springer.

Maloney, E.D. and Chelton, D.B. (2006). An assessment of the sea surface temperature influence on surface wind stress in numerical weather prediction and climate models. *Journal of climate*, *19*(12), 2743-2762.

Marean, C.W., Bar-Matthews, M., Bernatchez, J., Fisher, E., Goldberg, P., Herries, A.I., Jacobs, Z., Jerardino, A., Karkanas, P., Minichillo, T. and Nilssen, P.J. (2007). Early human use of marine resources and pigment in South Africa during the Middle Pleistocene. *Nature*, *449*(7164), 905.

McCarty, W., Coy, L., Gelaro, R., Huang, A., Merkova, D., Smith, E.B., Sienkiewicz, M. and Wargan, K. (2016). MERRA-2 input observations: Summary and assessment. *NASA Tech. Rep. Series on Global Modeling and Data Assimilation, NASA/TM-2016-104606*, *20*.

Mey, R.D., Walker, N.D. and Jury, M.R. (1990). Surface heat fluxes and marine boundary layer modification in the Agulhas Retroflection region. *Journal of Geophysical Research: Oceans*, *95*(C9), 15997-16015.

Milliff, R.F. and Morzel, J. (2001). The global distribution of the time-average wind stress curl from NSCAT. *Journal of the Atmospheric Sciences*, *58*(2), 109-131.

Minobe, S., Kuwano-Yoshida, A., Komori, N., Xie, S.P. and Small, R.J. (2008). Influence of the Gulf Stream on the troposphere. *Nature*, *452*(7184), 206.

Minobe, S., Miyashita, M., Kuwano-Yoshida, A., Tokinaga, H. and Xie, S.P. (2010). Atmospheric response to the Gulf Stream: Seasonal variations. *Journal of Climate*, *23*(13), 3699-3719.

Mlawer, E.J., Taubman, S.J., Brown, P.D., Iacono, M.J. and Clough, S.A. (1997). Radiative transfer for inhomogeneous atmospheres: RRTM, a validated correlated-k model for the longwave. *Journal of Geophysical Research: Atmospheres*, *102*(D14), 16663-16682.

Murray, F.W. (1966). *On the computation of saturation vapor pressure* (No. P-3423). RAND CORP SANTA MONICA CALIF.

Nakamura, H. and Kazmin, A.S. (2003). Decadal changes in the North Pacific oceanic frontal zones as revealed in ship and satellite observations. *Journal of Geophysical Research: Oceans*, *108*(C3).

Nakamura, H., Sampe, T., Tanimoto, Y. and Shimpo, A. (2004). Observed associations among storm tracks, jet streams and midlatitude oceanic fronts. *Earth's Climate: The Ocean–Atmosphere Interaction, Geophys. Monogr*, *147*, 329-345.

Nkwinkwa Njouodo, A.S., Koseki, S., Keenlyside, N. and Rouault, M. (2018). Atmospheric signature of the Agulhas Current. *Geophysical Research Letters*.

O'Neill, L.W., Chelton, D.B. and Esbensen, S.K. (2003). Observations of SST-induced perturbations of the wind stress field over the Southern Ocean on seasonal timescales. *Journal of Climate*, *16*(14), 2340-2354.

O'neill, L.W., Chelton, D.B., Esbensen, S.K. and Wentz, F.J. (2005). High-resolution satellite measurements of the atmospheric boundary layer response to SST variations along the Agulhas Return Current. *Journal of Climate*, *18*(14), 2706-2723.

O'Neill, L.W., Haack, T., Chelton, D.B. and Skyllingstad, E. (2017). The Gulf Stream convergence zone in the time-mean winds. *Journal of the Atmospheric Sciences*, *74*(7), 2383-2412.

O'Neill, L.W., Haack, T., Chelton, D.B. and Skyllingstad, E. (2017). The Gulf Stream convergence zone in the time-mean winds. *Journal of the Atmospheric Sciences*, *74*(7), 2383-2412.

Parfitt, R. and Czaja, A. (2016). On the contribution of synoptic transients to the mean atmospheric state in the Gulf Stream region. *Quarterly Journal of the Royal Meteorological Society*, *142*(696), 1554-1561.

Parfitt, R., Czaja, A., Minobe, S. and Kuwano-Yoshida, A. (2016). The atmospheric frontal response to SST perturbations in the Gulf Stream region. *Geophysical Research Letters*, *43*(5), 2299-2306.

Park, S., Deser, C. and Alexander, M.A. (2005). Estimation of the surface heat flux response to sea surface temperature anomalies over the global oceans. *Journal of climate*, *18*(21), 4582-4599.

Park, K., Cornillon, P. and Codiga, D.L. (2006). Modification of surface winds near ocean fronts: Effects of Gulf Stream rings on scatterometer (QuikSCAT, NSCAT) wind observations. *Journal of Geophysical Research: Oceans*, *111*(C3).

Parker, W.S. (2016). Reanalyses and observations: What's the difference?. *Bulletin of the American Meteorological Society*, *97*(9), 1565-1572.

Peeters, F.J., Acheson, R., Brummer, G.J.A., De Ruijter, W.P., Schneider, R.R., Ganssen, G.M., Ufkes, E. and Kroon, D. (2004). Vigorous exchange between the Indian and Atlantic oceans at the end of the past five glacial periods. *Nature*, *430*(7000), 661.

Philippon, N., Rouault, M., Richard, Y. and Favre, A. (2012). The influence of ENSO on winter rainfall in South Africa. *International Journal of Climatology*, *32*(15), 2333-2347.

Pohl, B., Rouault, M. and Roy, S.S. (2014). Simulation of the annual and diurnal cycles of rainfall over South Africa by a regional climate model. *Climate dynamics*, *43*(7-8), 2207-2226.

Preston-Whyte, R.A. and Tyson, P.D. (1988). *Atmosphere and weather of southern Africa*. Oxford University Press.

Qiu, B. (2003). Kuroshio Extension variability and forcing of the Pacific decadal oscillations: Responses and potential feedback. *Journal of Physical Oceanography*, *33*(12), 2465-2482.

Ratnam, J.V., Morioka, Y., Behera, S.K. and Yamagata, T. (2015). A model study of regional air-sea interaction in the austral summer precipitation over southern Africa. *Journal of Geophysical Research: Atmospheres*, *120*(6), 2342-2357.

Ratna, S.B., Behera, S., Ratnam, J.V., Takahashi, K. and Yamagata, T. (2013). An index for tropical temperate troughs over southern Africa. *Climate dynamics*, *41*(2), 421-441.

Reason, C.J.C. (2001). Evidence for the influence of the Agulhas Current on regional atmospheric circulation patterns. *Journal of Climate*, *14*(12), 2769-2778.

Reason, C.J.C. (2001). Subtropical Indian Ocean SST dipole events and southern African rainfall. *Geophysical Research Letters*, *28*(11), 2225-2227.

Reason, C.J.C. (2002). Sensitivity of the southern African circulation to dipole sea-surface temperature patterns in the south Indian Ocean. *International Journal of Climatology*, *22*(4), 377-393.

Reason, C.J.C., Landman, W. and Tennant, W. (2006). Seasonal to decadal prediction of southern African climate and its links with variability of the Atlantic Ocean. *Bulletin of the American Meteorological Society*, *87*(7), 941-956.

Reed, R.K (1977). On estimating insolation over the ocean. *Journal of Physical Oceanography*, *7*(3), 482-485.

Renault, L., Molemaker, M.J., Gula, J., Masson, S. and McWilliams, J.C. (2016). Control and stabilization of the Gulf Stream by oceanic current interaction with the atmosphere. *Journal of Physical Oceanography*, *46*(11), 3439-3453.

Renault, L., McWilliams, J.C. and Penven, P. (2017). Modulation of the agulhas current retroflection and leakage by oceanic current interaction with the atmosphere in coupled simulations. *Journal of Physical Oceanography*, *47*(8), 2077-2100.

Reynolds, R.W. and Smith, T.M. (1994). Improved global sea surface temperature analyses using optimum interpolation. *Journal of climate*, *7*(6), 929-948.

Reynolds, R.W., Smith, T.M., Liu, C., Chelton, D.B., Casey, K.S. and Schlax, M.G. (2007). Daily high-resolution-blended analyses for sea surface temperature. *Journal of Climate*, *20*(22), 5473-5496.

Rienecker, M.M., Suarez, M.J., Gelaro, R., Todling, R., Bacmeister, J., Liu, E., Bosilovich, M.G., Schubert, S.D., Takacs, L., Kim, G.K. and Bloom, S. (2011). MERRA: NASA's modern-era retrospective analysis for research and applications. *Journal of climate*, *24*(14), 3624-3648.

Rio, M.H., Mulet, S. and Picot, N. (2014). Beyond GOCE for the ocean circulation estimate: Synergetic use of altimetry, gravimetry, and in situ data provides new insight into geostrophic and Ekman currents. *Geophysical Research Letters*, *41*(24), 8918-8925.

Risien, C.M. and Chelton, D.B. (2008). A global climatology of surface wind and wind stress fields from eight years of QuikSCAT scatterometer data. *Journal of Physical Oceanography*, *38*(11), 2379-2413.

Roberts, J.B., Clayson, C.A., Robertson, F.R. and Jackson, D.L. (2010). Predicting near-surface atmospheric variables from Special Sensor Microwave/Imager using neural networks with a first-guess approach. *Journal of Geophysical Research: Atmospheres*, *115*(D19).

Ropelewski, C.F. and Halpert, M.S. (1989). Precipitation patterns associated with the high index phase of the Southern Oscillation. *Journal of climate*, *2*(3), 268-284.

Rouault, M., Lee-Thorp, A.M., Ansorge, I. and Lutjeharms, J.R.E. (1995). Agulhas Current air-sea exchange experiment. *South African Journal of Science*, *91*, 493-496.

Rouault, M. and Lee-Thorp, A.M. (1996). Fine-time resolution measurements of atmospheric boundary layer properties between Cape Town and Marion Island. *South African Journal of Marine Science*, *17*(1), 281-296.

Rouault, M. and Lutjeharms, J.R.E. (2000). Air–sea exchange over an Agulhas eddy at the subtropical convergence. *Global Atmos. Ocean Syst*, *7*, 125-150.

Rouault, M., Lee-Thorp, A.M. and Lutjeharms, J.R.E. (2000). The atmospheric boundary layer above the Agulhas Current during alongcurrent winds. *Journal of physical oceanography*, *30*(1), 40-50.

Rouault, M., White, S.A., Reason, C.J.C., Lutjeharms, J.R.E. and Jobard, I. (2002). Ocean–atmosphere interaction in the Agulhas Current region and a South African extreme weather event. *Weather and Forecasting*, *17*(4), 655-669.

Rouault, M., Reason, C.J.C., Lutjeharms, J.R.E. and Beljaars, A.C.M. (2003). Underestimation of latent and sensible heat fluxes above the Agulhas Current in NCEP and ECMWF analyses. *Journal of Climate*, *16*(4), 776-782.

Rouault, M. and Lutjeharms, J.R.E. (2003). Microwave satellite remote sensing of SST around Southern Africa. *S. Afr. J. Sci*, *99*, 489-494.

Rouault, M. and Richard, Y. (2005). Intensity and spatial extent of droughts in southern Africa. *Geophysical Research Letters*, *32*(15).

Rouault, M., Penven, P. and Pohl, B. (2009). Warming in the Agulhas Current system since the 1980's. *Geophysical Research Letters*, *36*(12).

Rouault, M.J. and Penven, P. (2011). New perspectives on Natal Pulses from satellite observations. *Journal of Geophysical Research: Oceans*, *116*(C7).

Rouault, M., Roy, S.S. and Balling, R.C. (2013). The diurnal cycle of rainfall in South Africa in the austral summer. *International Journal of Climatology*, *33*(3), 770-777.

Rouault, M., Verley, P. and Backeberg, B. (2016). Wind changes above warm Agulhas Current eddies. *Ocean Science*, *12*(2), 495-506.

Saha, S., Moorthi, S., Pan, H.L., Wu, X., Wang, J., Nadiga, S., Tripp, P., Kistler, R., Woollen, J., Behringer, D. and Liu, H. (2010). The NCEP climate forecast system reanalysis. *Bulletin of the American Meteorological Society*, *91*(8), 1015-1058.

Sasaki, Y.N., Minobe, S., Asai, T. and Inatsu, M. (2012). Influence of the Kuroshio in the East China Sea on the early summer (baiu) rain. *Journal of Climate*, *25*(19), 6627-6645.

Sheldon, L., Czaja, A., Vannière, B., Morcrette, C., Sohet, B., Casado, M. and Smith, D. (2017). A 'warm path'for Gulf Stream–troposphere interactions. *Tellus A: Dynamic Meteorology and Oceanography*, *69*(1), 1299397.

Seager, R., Ting, M., Held, I., Kushnir, Y., Lu, J., Vecchi, G., Huang, H.P., Harnik, N., Leetmaa, A., Lau, N.C. and Li, C. (2007). Model projections of an imminent transition to a more arid climate in southwestern North America. *Science*, *316*(5828), 1181-1184.

Seager, R. and Vecchi, G.A. (2010). Greenhouse warming and the 21st century hydroclimate of southwestern North America. *Proceedings of the National Academy of Sciences*, *107*(50), 21277-21282.

Shimada, T. and Minobe, S. (2011). Global analysis of the pressure adjustment mechanism over sea surface temperature fronts using AIRS/Aqua data. *Geophysical Research Letters*, *38*(6).

Simmons, A. (2006). ERA-Interim: New ECMWF reanalysis products from 1989 onwards. *ECMWF newsletter*, *110*, 25-36.

Singh, R., Joshi, P.C. and Kishtawal, C.M. (2005). A new technique for estimation of surface latent heat fluxes using satellite-based observations. *Monthly weather review*, *133*(9), 2692-2710.

Sirven, J., Frankignoul, C., De Coetlogon, G. and Taillandier, V. (2002). Spectrum of wind-driven baroclinic fluctuations of the ocean in the midlatitudes. *Journal of physical oceanography*, *32*(8), 2405-2417.

Skamarock, W.C. and Klemp, J.B. (2008). A time-split nonhydrostatic atmospheric model for weather research and forecasting applications. *Journal of Computational Physics*, *227*(7), 3465-3485

Small, R.J., Xie, S.P., O'Neill, L., Seo, H., Song, Q., Cornillon, P., Spall, M. and Minobe, S., (2008). Air–sea interaction over ocean fronts and eddies. *Dynamics of Atmospheres and Oceans*, *45*(3-4), 274-319.

Smirnov, D., Newman, M., Alexander, M.A., Kwon, Y.O. and Frankignoul, C. (2015). Investigating the local atmospheric response to a realistic shift in the Oyashio sea surface temperature front. *Journal of Climate*, *28*(3), 1126-1147.

Smith, S.D. (1980). Wind stress and heat flux over the ocean in gale force winds. *Journal of Physical Oceanography*, *10*(5), 709-726.

Smith, S.D. (1988). Coefficients for sea surface wind stress, heat flux, and wind profiles as a function of wind speed and temperature. *Journal of Geophysical Research: Oceans*, *93*(C12), 15467-15472.

Smith, S.R., Hughes, P.J. and Bourassa, M.A. (2011). A comparison of nine monthly air–sea flux products. *International Journal of Climatology*, *31*(7), 1002-1027.

Storm, B., Dudhia, J., Basu, S., Swift, A. and Giammanco, I. (2009). Evaluation of the weather research and forecasting model on forecasting low-level jets: Implications for wind energy. *Wind Energy: An International Journal for Progress and Applications in Wind Power Conversion Technology*, *12*(1), 81-90.

Stramma, L. and Lutjeharms, J.R. (1997). The flow field of the subtropical gyre of the South Indian Ocean. *Journal of Geophysical Research: Oceans*, *102*(C3), 5513-5530.

Sturges, W., Hong, B.G. and Clarke, A.J. (1998). Decadal wind forcing of the North Atlantic subtropical gyre. *Journal of physical oceanography*, *28*(4), 659-668.

Taguchi, B., Xie, S.P., Schneider, N., Nonaka, M., Sasaki, H. and Sasai, Y. (2007). Decadal variability of the Kuroshio Extension: Observations and an eddy-resolving model hindcast. *Journal of Climate*, *20*(11), 2357-2377.

Taguchi, B., Nakamura, H., Nonaka, M. and Xie, S.P. (2009). Influences of the Kuroshio/Oyashio Extensions on air–sea heat exchanges and storm-track activity as revealed in regional atmospheric model simulations for the 2003/04 cold season. *Journal of Climate*, *22*(24), 6536-6560.

Takahashi, T., Sutherland, S.C., Wanninkhof, R., Sweeney, C., Feely, R.A., Chipman, D.W., Hales, B., Friederich, G., Chavez, F., Sabine, C. and Watson, A. (2009). Climatological mean and decadal change in surface ocean pCO2, and net sea–air CO2 flux over the global oceans. *Deep Sea Research Part II: Topical Studies in Oceanography*, *56*(8-10), 554-577.

Tanimoto, Y., Nakamura, H., Kagimoto, T. and Yamane, S. (2003). An active role of extratropical sea surface temperature anomalies in determining anomalous turbulent heat flux. *Journal of Geophysical Research: Oceans*, *108*(C10).

Taylor, K.E., Williamson, D. and Zwiers, F. (2000). *The sea surface temperature and sea-ice concentration boundary conditions for AMIP II simulations*. Program for Climate Model Diagnosis and Intercomparison, Lawrence Livermore National Laboratory, University of California.

Thomas, B.R., Kent, E.C., Swail, V.R. and Berry, D.I. (2008). Trends in ship wind speeds adjusted for observation method and height. *International Journal of Climatology: A Journal of the Royal Meteorological Society*, *28*(6), 747-763.

Tokinaga, H., Tanimoto, Y. and Xie, S.P., (2005). SST-induced surface wind variations over the Brazil–Malvinas confluence: Satellite and in situ observations. *Journal of climate*, *18*(17), 3470-3482.

Tokinaga, H., Tanimoto, Y., Xie, S.P., Sampe, T., Tomita, H. and Ichikawa, H. (2009). Ocean frontal effects on the vertical development of clouds over the western North Pacific: In situ and satellite observations. *Journal of climate*, *22*(16), 4241-4260.

Toole, J.M. and Warren, B.A. (1993). A hydrographic section across the subtropical South Indian Ocean. *Deep Sea Research Part I: Oceanographic Research Papers*, *40*(10), 1973-2019.

Tyson, P.D., Preston-Whyte, R.A. and Schulze, R.E. (1976). *The climate of the Drakensberg* (Vol. 31). Town and Regional Planning Commission.

Tyson D., and Preston-White R.A. (2000), The weather and Climate of Southrn Africa, *Oxford universityPress: South Africa*

Uppala, S.M., Kållberg, P.W., Simmons, A.J., Andrae, U., Bechtold, V.D.C., Fiorino, M., Gibson, J.K., Haseler, J., Hernandez, A., Kelly, G.A. and Li, X. (2005). The ERA-40 re-analysis. *Quarterly Journal of the royal meteorological society*, *131*(612), 2961-3012.

Valentine, H.R., Lutjeharms, J.R.E. and Brundrit, G.B. (1993). The water masses and volumetry of the southern Agulhas Current region. *Deep Sea Research Part I: Oceanographic Research Papers*, *40*(6), 1285-1305.

Vannière, B., Czaja, A., Dacre, H. and Woollings, T. (2017). A "Cold Path" for the Gulf Stream–Troposphere Connection. *Journal of Climate*, *30*(4), 1363-1379.

Vigaud, N., Richard, Y., Rouault, M. and Fauchereau, N. (2007). Water vapour transport from the tropical Atlantic and summer rainfall in tropical southern Africa. *Climate dynamics*, *28*(2-3), 113-123.

Vigaud, N., Richard, Y., Rouault, M. and Fauchereau, N. (2009). Moisture transport between the South Atlantic Ocean and southern Africa: relationships with summer rainfall and associated dynamics. *Climate Dynamics*, *32*(1),113-123.

Walker, J.A. (1989). Preliminary observations of oceanic influences on the February March 1988 floods in central South Africa. *South African Journal of Science*, *85*(3), 164.

Wallace, J.M., Mitchell, T.P. and Deser, C. (1989). The influence of sea-surface temperature on surface wind in the eastern equatorial Pacific: Seasonal and interannual variability. *Journal of Climate*, *2*(12), 1492-1499.

Wang, H., Yu, E. and Yang, S. (2011). An exceptionally heavy snowfall in Northeast China: Large-scale circulation anomalies and hindcast of the NCAR WRF model. *Meteorology and Atmospheric Physics*, *113*(1-2), 11-25.

Weijer, W., De Ruijter, W.P., Sterl, A. and Drijfhout, S.S. (2002). Response of the Atlantic overturning circulation to South Atlantic sources of buoyancy. *Global and Planetary Change*, *34*(3-4), 293-311.

Woodruff, S.D., Slutz, R.J., Jenne, R.L. and Steurer, P.M (1987). A comprehensive ocean-atmosphere data set. *Bulletin of the American meteorological society*, *68*(10), 1239-1250.

Xie, S.P. (2004). Satellite observations of cool ocean–atmosphere interaction. *Bulletin of the American Meteorological Society*, *85*(2), 195-208.

Xu, H., Xu, M., Xie, S.P. and Wang, Y. (2011). Deep atmospheric response to the spring Kuroshio over the East China Sea. *Journal of Climate*, *24*(18), 4959-4972.

Yang, H., Lohmann, G., Wei, W., Dima, M., Ionita, M. and Liu, J. (2016). Intensification and poleward shift of subtropical western boundary currents in a warming climate. *Journal of Geophysical Research: Oceans*, *121*(7), 4928-4945.

Young, G.S. and Sikora, T.D. (2003). Mesoscale stratocumulus bands caused by Gulf Stream meanders. *Monthly Weather Review*, *131*(9), 2177-2191.